U.S. Department of Transportation
Federal Railroad Administration

Office of Research and Development

Washington, D.C. 20590

An Experimental Evaluation of a Full-Scale Single-Sided Linear Induction Motor with Different Reaction Rails

Volume I: Test Results

Garrett AiResearch Manufacturing Company
2525 W. 190th St. Torrance, California 90509

FRA/ORD-81/27-1

DECEMBER 1981

R.J.A. Bevan

NOTICE

This document is disseminated under sponsorship of the United States Department of Transportation in the interest of information exchange. The United States Government assumes no liability for its contents or use thereof.

The contents of this report reflect the view of the AiResearch Manufacturing Company of California, which is responsible for the facts and the accuracy of the data presented herein. The contents do not necessarily reflect the official views or policy of the Department of Transportation. This report does not constitute a standard, specification, or regulation.

The United States Government does not endorse products or manufacturers. Trade or manufacturer names appear herein solely because they are considered essential to the object of this report.

PREFACE

Performance of the work described herein was sponsored by the Office of Research and Development (ORD), Federal Railroad Administration, U.S. Department of Transportation. Mr. Matthew Guarino, Jr., Manager, Electrical Traction R&D, ORD, was the Contracting Officer's Technical Representative and provided substantial guidance, direction, and support of the program.

Program responsibility at AiResearch Manufacturing Company was vested in Mr. R. Shull, Program Manager, and Dr. G. Kalman, Technical Manager. Senior program personnel were Mr. R. Bevan, System Engineer; Mr. J. McConville, Chief Test Engineer; Mr. H. Holley, Test Site Manager; Mr. S. Mitchell, Data Processing Engineer; Mr. F. Weigand, Mechanical Engineer; Dr. H. Lee, Theoretical Modeling; and Mr. Y. Willer, Safety Engineer.

Particular recognition and thanks are extended to the field test crew, including Messrs. C. Bachhuber, L. Burton, R. Graff, G. Mitchell, W. Sloan, and P. Vollbehr, whose efforts and resourcefulness were critical in the operation and maintenance of the vehicle, data van, and other supporting equipment.

The assistance of the following personnel is also gratefully achknowledged: Dr. J. Stickler, Transportation Systems Center, whose experimental measurements appear as an appendix to this report; Mr. K. Grunwald and Mr. W. McCutcheon of the Transportation Test Center at Pueblo, Colorado.

Technical Report Documentation Page

1. Report No.	2. Government Accession No.	3. Recipient's Catalog No.
FRA/ORD-80/77-I		

4. Title and Subtitle
AN EXPERIMENTAL EVALUATION OF A FULL-SCALE SINGLE-SIDED LINEAR INDUCTION MOTOR WITH DIFFERENT REACTION RAILS
VOLUME I - TEST RESULTS

5. Report Date
December 1981

6. Performing Organization Code

7. Author(s)
R.J.A. Bevan

8. Performing Organization Report No.
79-16095-1

9. Performing Organization Name and Address
AiResearch Manufacturing Company of California
A Division of The Garrett Corporation
2525 West 190th Street
Torrance, California 90509

10. Work Unit No. (TRAIS)

11. Contract or Grant No.
DOT-FR-64226

12. Sponsoring Agency Name and Address
Department of Transportation
Federal Railroad Administration
Office of Research and Development
Washington, D.C. 20590

13. Type of Report and Period Covered
Final Report

14. Sponsoring Agency Code

15. Supplementary Notes

16. Abstract

This document is the final volume in a series of reports presenting the results of an extensive test program involving the linear induction motor research vehicle (LIMRV). Specifically, this report describes the final LIMRV test activity with a single-sided linear induction motor (SLIM). The principal objective was to evaluate motor performance with two types of reaction rails: aluminum plus solid iron (baseline configuration) and solid iron only. The test program encompassed measurement of SLIM propulsion characteristics, distributed parameters, track fluxes and associated parameters, and vertical force distribution. The test results showed that: (1) extending the primary iron structure beyond the ends of the stator winding has little effect on motor performance; (2) more saturation occurs over the solid iron reaction rail than over the baseline rail; (3) measuring track flux penetration in solid iron by coarsely laminating the backiron is valid only for the baseline reaction rail; (4) SLIM output characteristics with constant voltage excitation differ considerably from those at the rated constant current excitation, though less with the solid reaction rail; (5) peak efficiency is not severely compromised with the removal of the aluminum, but the power factor is significantly lower for the solid iron reaction rail; and (6) SLIM baseline tests indicate lower peak efficiency and power factor than that of earlier double-sided LIM's, though comparison is difficult because of the different nature of the reaction rails. Supplementary data is presented in Volume II.

17. Key Words	18. Distribution Statement
High-speed ground transportation, Rail car propulsion systems, Linear induction motors	Document is available to the public through the National Technical Information Service, Springfield, Virginia 22151

19. Security Classif. (of this report)	20. Security Classif. (of this page)	21. No. of Pages	22. Price
Unclassified	Unclassified	307	

CONTENTS

CONTENTS (Continued)

ILLUSTRATIONS

ILLUSTRATIONS (Continued)

ILLUSTRATIONS (Continued)

ILLUSTRATIONS (Continued)

ILLUSTRATIONS (Continued)

ILLUSTRATIONS (Continued)

TABLES

TABLES (Continued)

SECTION 1

INTRODUCTION AND SUMMARY

INTRODUCTION

This document is the final volume in a series of reports presenting the results of an extensive test program involving the linear induction motor research vehicle (LIMRV). This Federal Railroad Administration sponsored program, carried out as part of the Department of Transportation's long-range ground transportation plan, is aimed at establishing a technological base for various candidate propulsion subsystems.

Since 1965 the Office of Research and Development, and its predecessor, the Office of High Speed Ground Transportation, have been actively engaged in electric traction and propulsion research and development for ground transportation systems. This R&D effort encompassed the study of a wide variety of propulsion concepts, with potential applications to both near-term as well as long-range deployment. Results of this study revealed the need for environmentally acceptable propulsion systems that can operate at vehicle speeds higher than those presently practical with the traditional rotating electric traction equipment, and yet are not dependent on futuristic technologies. The linear induction motor bridges that gap; hence the creation of the LIMRV program.

In accordance with these aims, the LIMRV program was primarily intended to generate analytical and experimental data on linear induction motors (LIM). This effort necessitated the development of a full-scale, 2500-hp linear motor and associated test equipment, including a 30-ton test vehicle capable of operating at speeds up to 112 m/s, a 10-km-long high-speed test track, and a telemetry link for remote operation and data transmission. Thus, the hardware developed under the LIMRV program represented a major advancement in transportation research.

As a result of the information produced to date through the experimental verification of several theoretical models with full-scale hardware, the LIMRV program helped to establish a requisite design baseline for the potential deployment of LIM-type propulsion systems. While many of the socioeconomic and technical problems related to high-speed ground transportation are as yet unresolved, the success of the LIMRV program enabled DOT to assess realistically, with a high design confidence, the linear induction motor for any future application in ground transportation.

LIMRV Program Overview

This report describes the final LIMRV test activity with a single-sided linear induction motor (SLIM) installed, during the period of August 1978 to March 1979, and therefore it is necessarily concerned only with the documentation of this last series of tests. For interested readers, however, a brief overview of the entire LIMRV program from inception to completion is provided with appropriate references.

Subject	Reference
• Initial analytical feasibility study (1967)	(1)
• Model test using rotary disk (1969)	(2)
• Full-scale hardware development (1969)	(3)
• Acquisition of first DLIM electrical performance data (1972)	(4)
• Wheel/rail adhesion test (1974)	(5)
• Addition of J52 jet engines for thrust augmentation (1974)	(6)
• DLIM electrical braking test (1975)	(7)
• Mechanical speed upgrading of LIMRV to 112 m/s (1975)	(8)
• Reaction rail current and airgap flux distribution measurements (1976)	(9)
• Final DLIM configuration tests (1977)	(10)
• Hardware modification: LIMRV converted to SLIM configuration (1977)	(11)
• Final SLIM configuration tests (1978)	--

Objective

The principal objective was to evaluate motor performance with two types of reaction rails. Detailed measurements were made of flux distributions in a specially instrumented portion of the reaction rail. Eddy current braking was also investigated. Considerable data was acquired to evaluate comparative double-sided and single-sided LIM performance.

Background

Investigations prior to August 1977 were concerned with full-scale testing of the double-sided motor installed in the LIMRV (6, 9, 10, 12, and 13)*. In addition to a comprehensive test program, extensive theoretical support of the test results has been provided by AiResearch and others (14, 15, 16, 17, and 18) for the double-sided LIM (DLIM). The reader may consult the referenced publications for detailed background on DLIM research and the LIMRV test facility.

*Numbers in parentheses denote references, which are listed in Section 11.

In August 1977 modifications were performed on the LIMRV and its propulsion system to ready the vehicle for SLIM tests. Briefly, the statement of work included:

- Mechanical modification of the motor from double-sided to single-sided configuration.
- Design, analysis, and fabrication of the motor support system.
- Analysis of the existing LIMRV powerplant to ensure a satisfactory operating envelope.
- Design and analysis of the intended reaction rail configurations.
- Supporting theoretical analyses of the SLIM to ensure satisfactory operation of the entire vehicle/track system.

The design and analysis effort is described in detail elsewhere [11].

This report is intended to be complementary to the previous report on DLIM test results [10], which represented the initial part of this experimental program.

This report contains experimental data in a form compatible with prior DLIM reportage. For reader convenience, highlights of DLIM testing are also summarized when relevant. And, although no detailed theoretical analysis is presented herein because it is already covered in another document [11], some expedient analytical methods are suggested, and are used in interpretation of the test data.

Dynamic testing accomplished during this program has been limited to study of SLIM performance as affected by the finite length of the electrical and magnetic primary circuits. Some static testing has been performed on the transverse edge effects [19], and this work is described later in this volume.

Therefore, the dynamic data represents a spatial average over the width of the motor, and the reader should consider the detailed flux measurements of lateral primary flux distribution when interpreting the dynamic data.

The scope of work includes the following tasks:

Task	Description	Significance
1	Measure SLIM propulsion characteristics (thrust, power factor, efficiency) for 10-pole excitation.	Provides basic data for comparison with DLIM.
2	Measure distributed parameters (pole flux, power per pole, kVA per pole, voltage per pole) at different motor speeds.	Provides SLIM flux signature and data on effect of finite length primary.

Task	Description	Significance
3	Measure track fluxes and associated parameters.	Provides data for establishing effectiveness of solid iron reaction rail backiron.
4	Investigate SLIM performance with two different reaction rails.	Evaluation of cost-effective reaction rail design.
5	Measure SLIM vertical force distribution.	Evaluation of data required for system design.

In addition, analytical effort was expended to support the test results.

Report Organization

This report comprises two volumes, arranged as follows:

Volume 1, 11 sections plus Appendices A through I.

Section 1 places the present series of tests in historical perspective.

Section 2 defines the guidelines that led to formation of a SLIM test plan.

Section 3 describes the test facility used in acquiring the data.

Section 4 delineates test objectives.

Sections 5 and 6 describe the tests performed and the methods employed.

Section 7 introduces the test data.

Section 8 contains onboard data for the SLIM with an aluminum/steel reaction rail (hereafter referred to as the baseline reaction rail).

Section 9 contains onboard data for the SLIM with the aluminum cover removed from the reaction rail, solid iron only (hereafter referred to as the solid iron reaction rail).

Section 10 contains track flux data for both the baseline and the solid iron reaction rails, together with a mathematical model for track flux analysis.

Section 11 lists documents cited in earlier sections.

Volume II (5 sections) contains all processed and plotted data acquired during the SLIM test series so that independent investigators may conveniently refer to additional secondary material not presented in Volume 1.

SUMMARY

The first tests involved measurement of SLIM parameters for three primary configurations (10 poles, 5 active poles leading, and 5 active poles trailing) in conjunction with the baseline reaction rail, with a single value of airgap width. The aluminum cover was then removed, and 10-pole tests were run on the solid iron reaction rail at the same entrefer (i.e., airgap between primary and secondary backiron). Finally, tests were repeated on the solid iron reaction rail in the 10-pole configuration at a reduced airgap width.

The ac tests were conducted at an excitation frequency of 94.3 $\pm$1 Hz. Various excitation levels were applied, but data in general was normalized to 0.346 V/Hz/pole and 1400 A. Dc excitation tests (eddy current braking) were performed at maximum excitation levels within the limitations of the vertical force measuring system.

Table 1-1 summarizes airgap data for this test series. The actual airgap differs from the specified airgap due to the difficulty of precise adjustment.

TABLE 1-1

AIRGAP WIDTHS

Reaction Rail	Primary Connection	Physical Airgap, mm		Entrefer, mm
		Specified	Actual	
Baseline	10-pole	25.4	24.5	28.5
Baseline	5-pole	25.4	24.5	28.5
Solid iron (1)	10-pole	26	28.5	28.5
Solid iron (2)	10-pole	18	14.5	14.5

Propulsion Characteristics

Some performance degradation on a per-pole basis must be expected when the number of active poles is reduced, since end effects become more prominent. The test results plotted in Figures 1-1 and 1-2 support this prediction. Figure 1-1 shows the thrust per pole of the 10-pole SLIM with data normalized to 0.346 V/Hz/pole. Comparable data for the motor in a 5-pole configuration is shown in Figure 1-2 on a per-pole basis. The effect is manifested by a given thrust per pole being developed at a greater value of slip for the 5-pole configuration than for the 10-pole connection, with a consequent loss of efficiency.

Figures 1-3 and 1-4 display the different thrust characteristics of a solid iron rail. Despite a change of airgap width from 28.5 to 14.5 mm, the thrust only increases from a peak of 0.42 to 0.49 kN/pole, indicating that heavy track saturation is present.

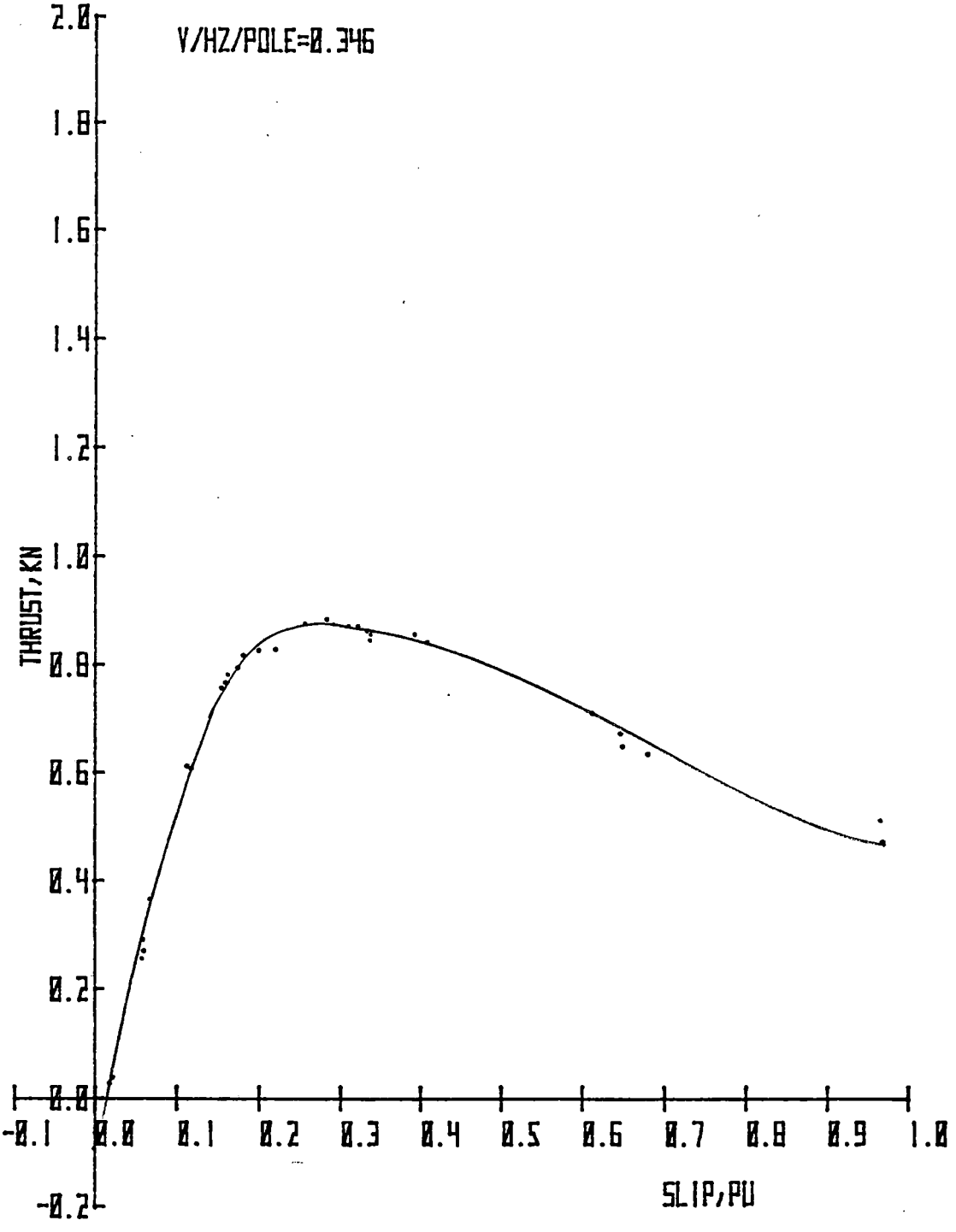

Figure 1-1. Thrust per Pole vs Slip, 10-Pole SLIM, Baseline Reaction Rail

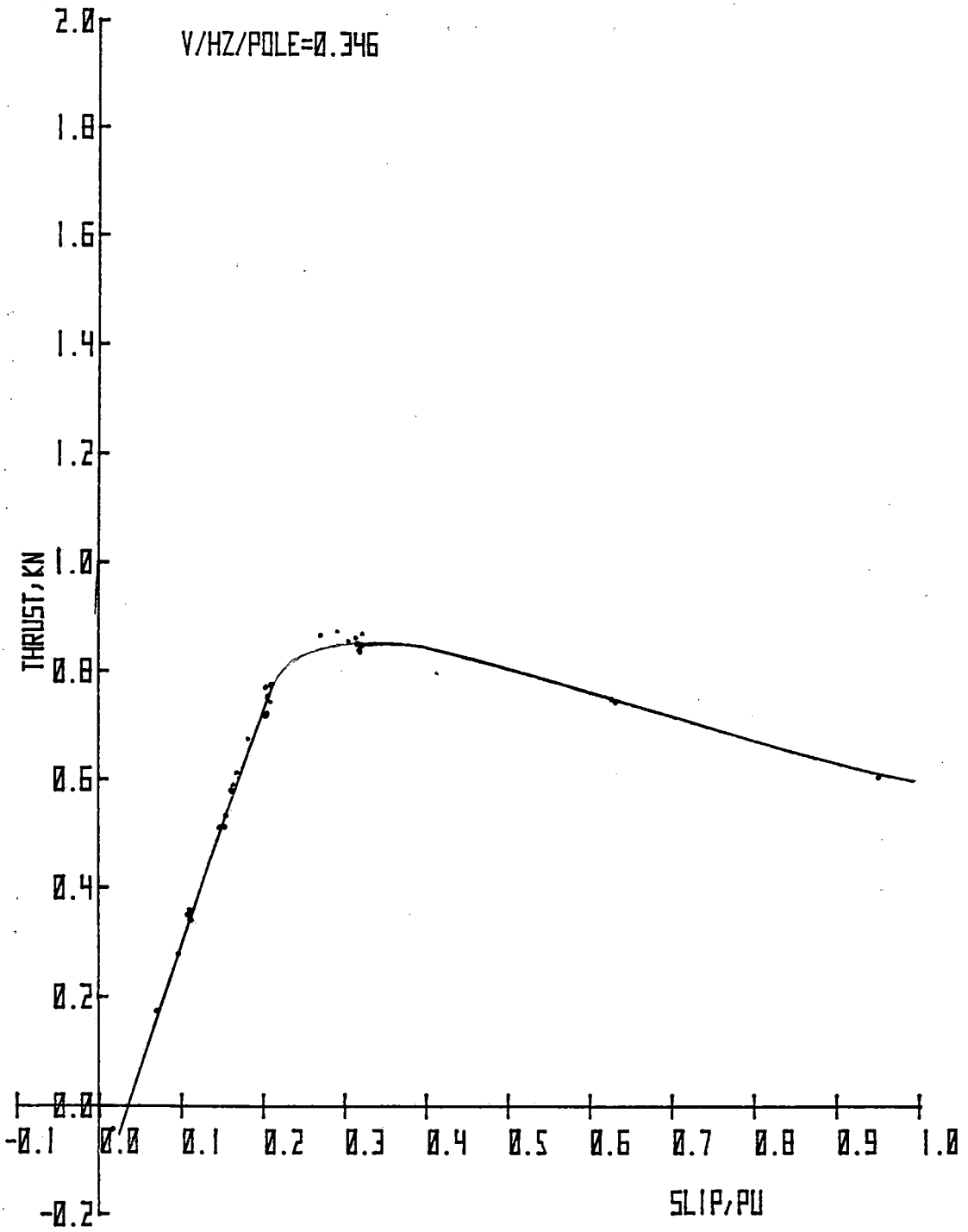

Figure 1-2. Thrust per Pole vs Slip, 5-Pole (Leading) SLIM, Baseline Reaction Rail

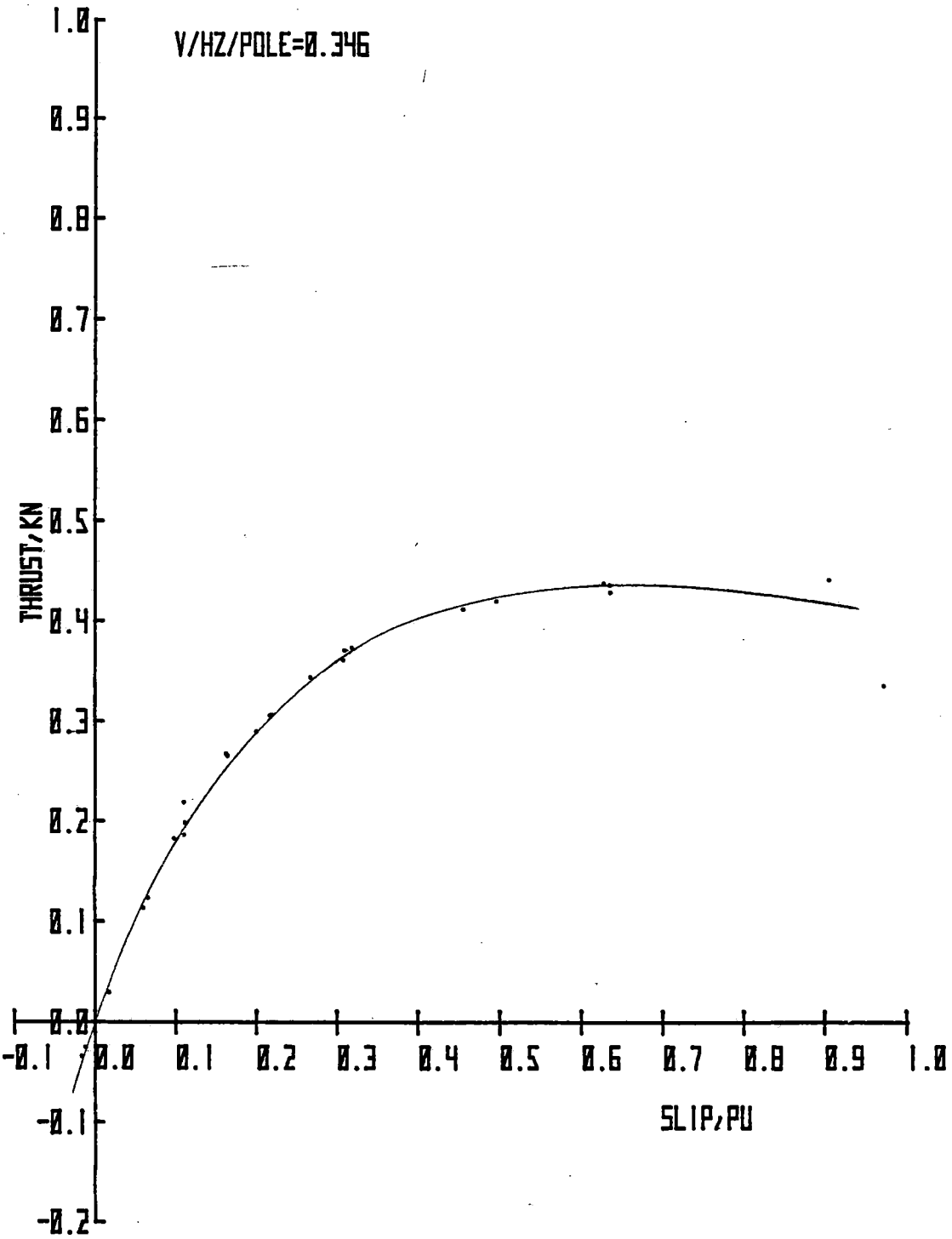

Figure 1-3. Thrust per Pole vs Slip, 10-Pole SLIM, Solid Iron Reaction Rail, 26-mm Airgap

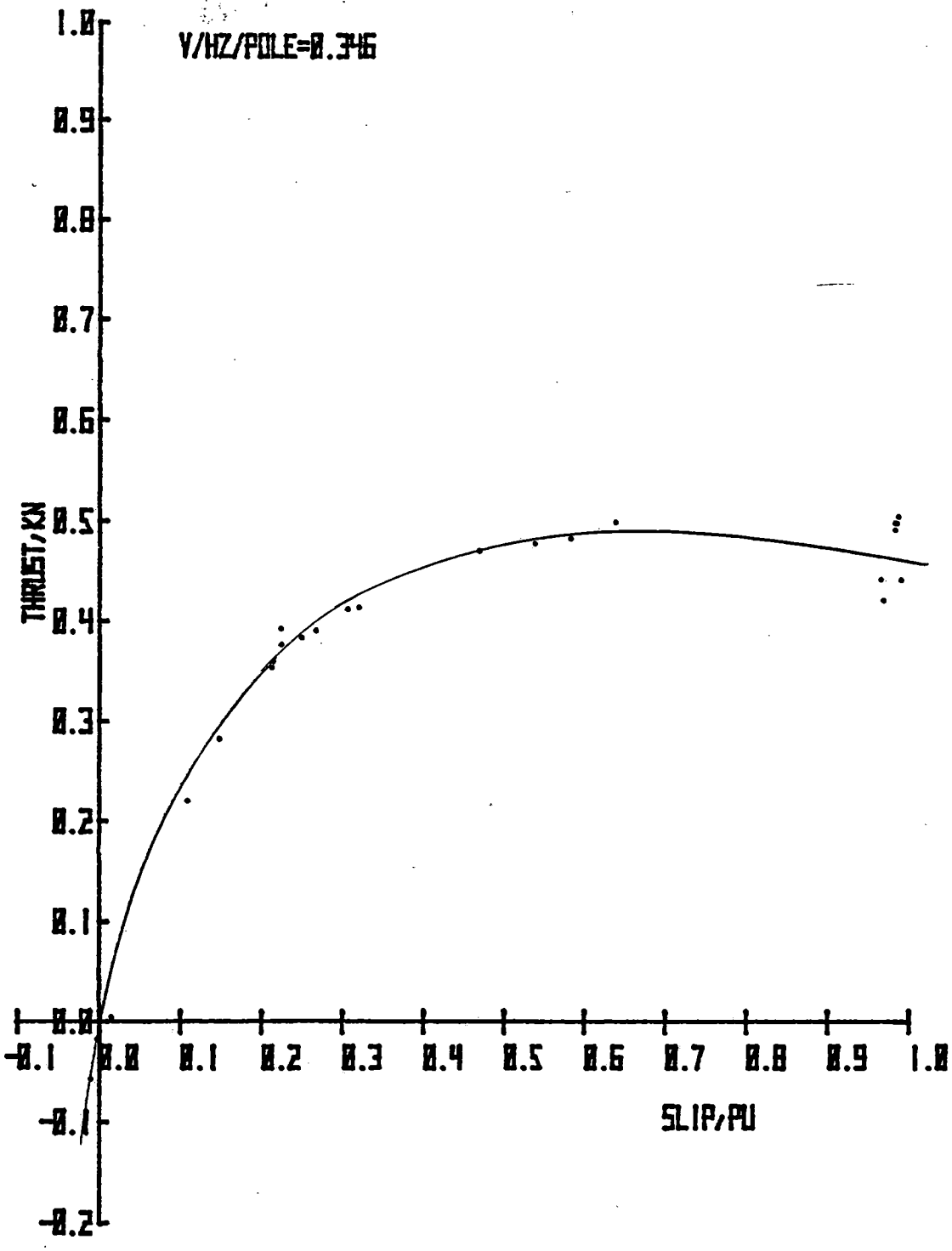

Figure 1-4. Thrust per Pole vs Slip, 10-Pole SLIM, Solid Iron Reaction Rail, 18-mm Airgap

Power factor is plotted against slip in Figure 1-5. Peak power factor for the 10-pole SLIM with baseline reaction rail is 49 percent. For the 5-pole configuration, peak power factor is 46 percent, as shown in Figure 1-6. The solid iron reaction rail exhibits a lower power factor with a flat characteristic over much of the slip range (Figures 1-7 and 1-8). A small increase in power factor (32 to 36 percent) is achieved when the airgap is approximately halved. This indicates that motor performance is substantially affected by characteristics of the solid iron secondary, and losses due to airgap magnetizing power are small.

Effect of Extended Primary Iron

An item of considerable interest is the effect of iron extending beyond the bounds of the primary winding. Some LIM analytical models assume infinite length iron with a finite length winding; others treat the motor with a finite length iron. The DLIM tests offered the first opportunity for an experimental comparison of these two approaches. The comparison was based on tests with five leading poles vs five trailing poles of the LIM energized. Thrust differences were seen to be only marginal, as were the differences in other performance characteristics (efficiency, real power, and reactive power). Similar tests were conducted on the SLIM to determine if the use of solid saturated backiron affected the validity of this assumption.

Again, only marginal performance differences were detected between the two configurations, with the exception of vertical force measurements, during which the magnetic flux wake caused a significant vertical force in the unexcited region. Figures 1-9 and 1-10 are plots of vertical force vs slip for the 5-pole (leading) and 5-pole (trailing) configurations, respectively. Therefore, the proximity of iron at the rear of the excited primary winding must be considered when calculating total vertical forces between a SLIM primary with its supporting structure and the reaction rail.

Track Flux

This report describes a method of measuring track flux in a solid backiron, in which a coarsely laminated special track section is used. Validity of this method is examined with reference to test results obtained with the baseline and the solid iron reaction rails. Tests showed that the method was useful when the backiron was covered by a heavily conducting plate. However, in tests using a solid backiron only, this method has limited validity. Difficulties were experienced with remanent flux levels in the steel. A mathematical treatment of flux penetration in the track section is included herein.

Eddy Current Braking

Tests were performed on various primary/secondary configurations with two phases of the motor excited with direct current in order to determine properties of the motor during usage as an eddy current brake. In addition to providing fundamental data on the generation of forces with low dynamic end effect, these tests also yielded experimental data on the maximum vertical forces to be sustained by a SLIM-propelled vehicle operating with this type of braking.

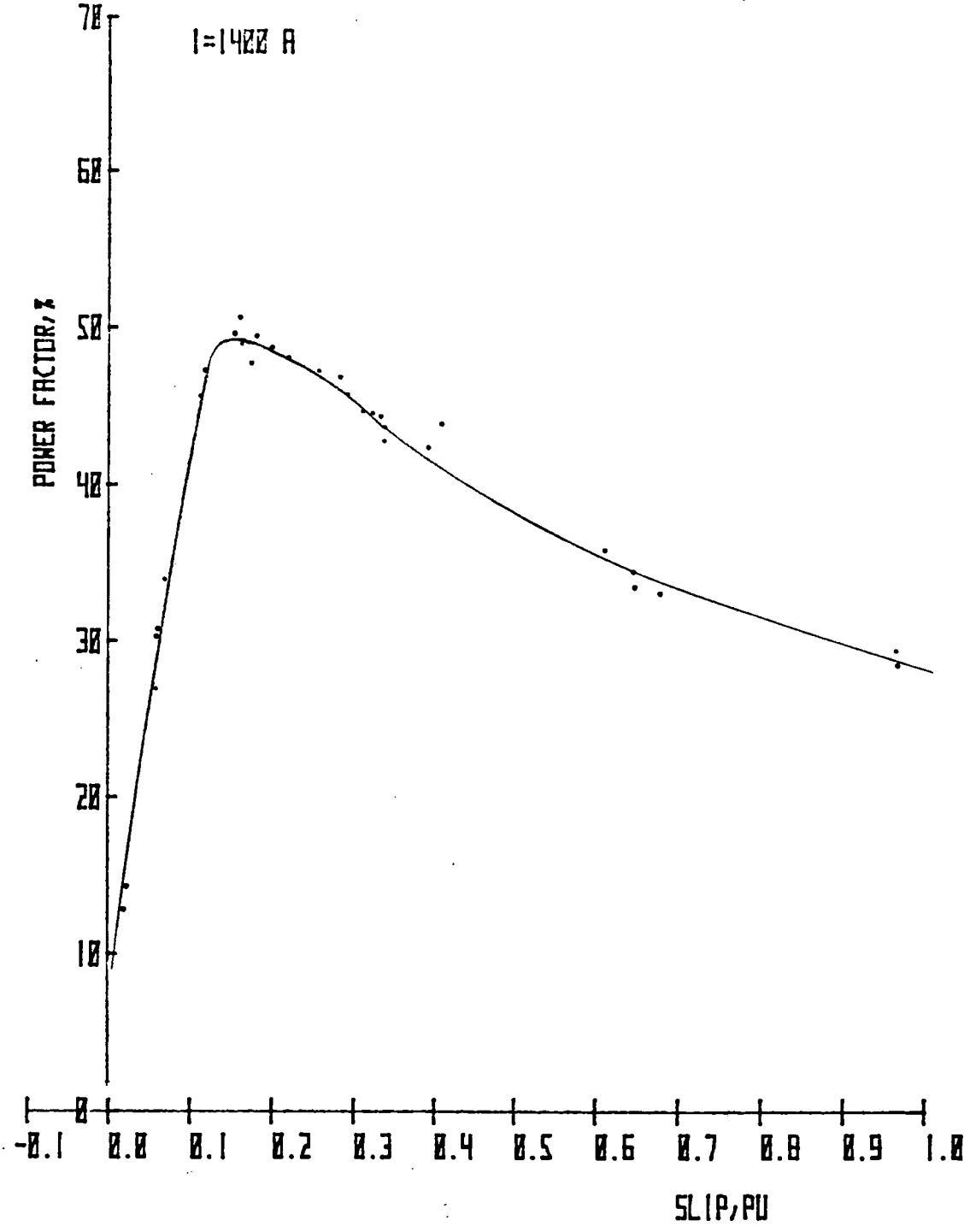

Figure 1-5. Power Factor vs Slip, 10-Pole SLIM, Baseline Reaction Rail

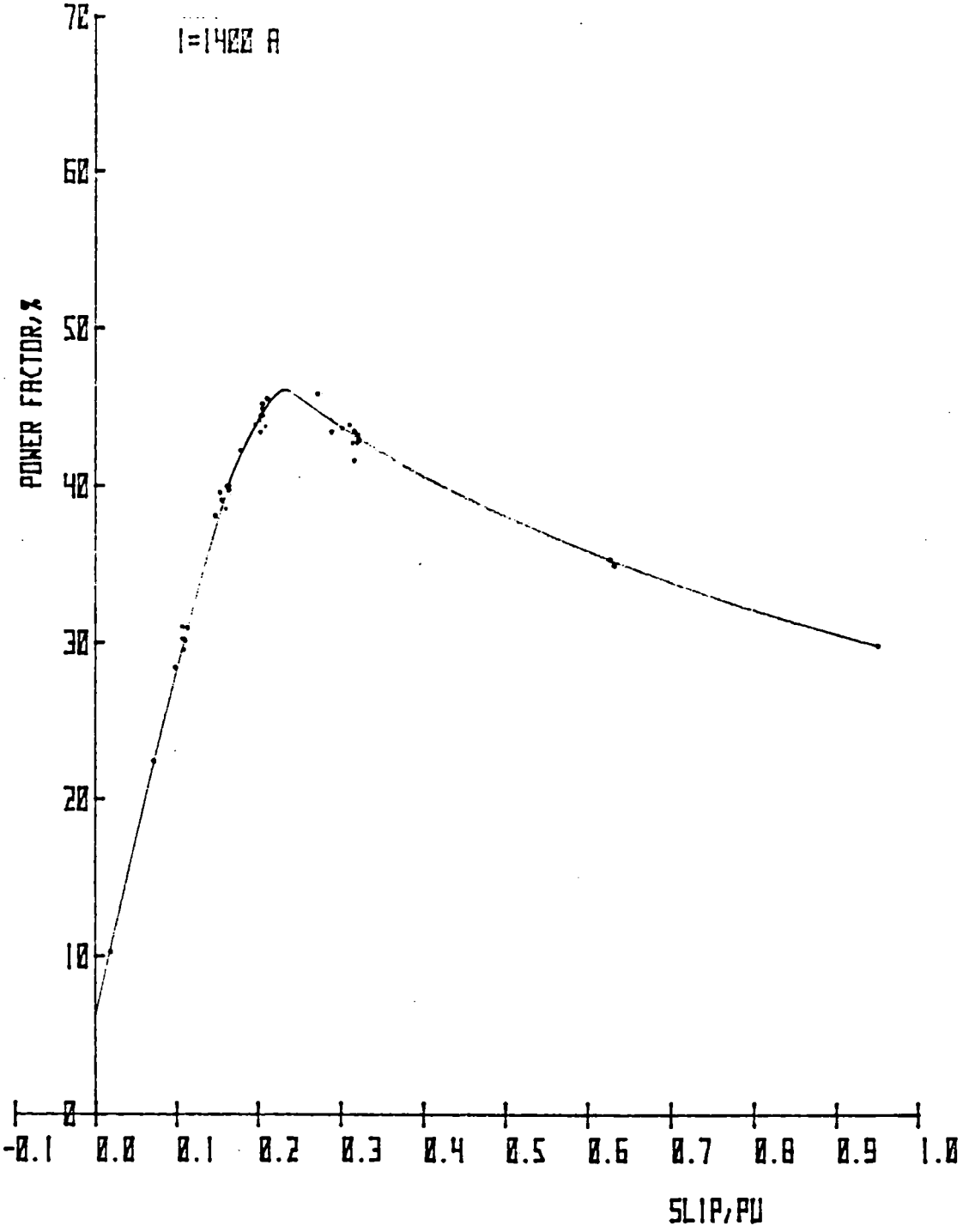

Figure 1-6. Power Factor vs Slip, 5-Pole (Leading) SLIM, Baseline Reaction Rail

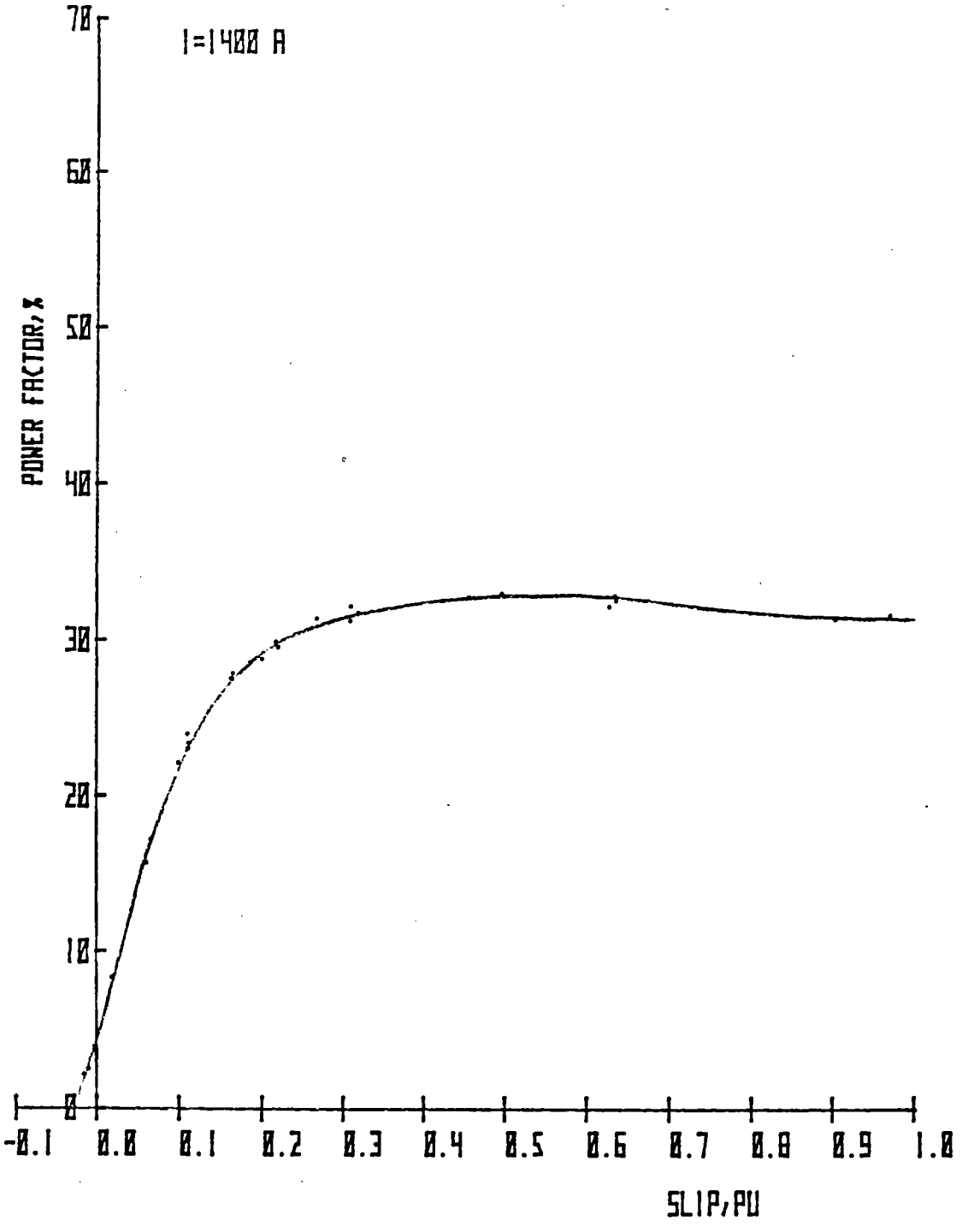

Figure 1-7. Power Factor vs Slip, 10-Pole SLIM, Solid Iron Reaction Rail, 26-mm Airgap

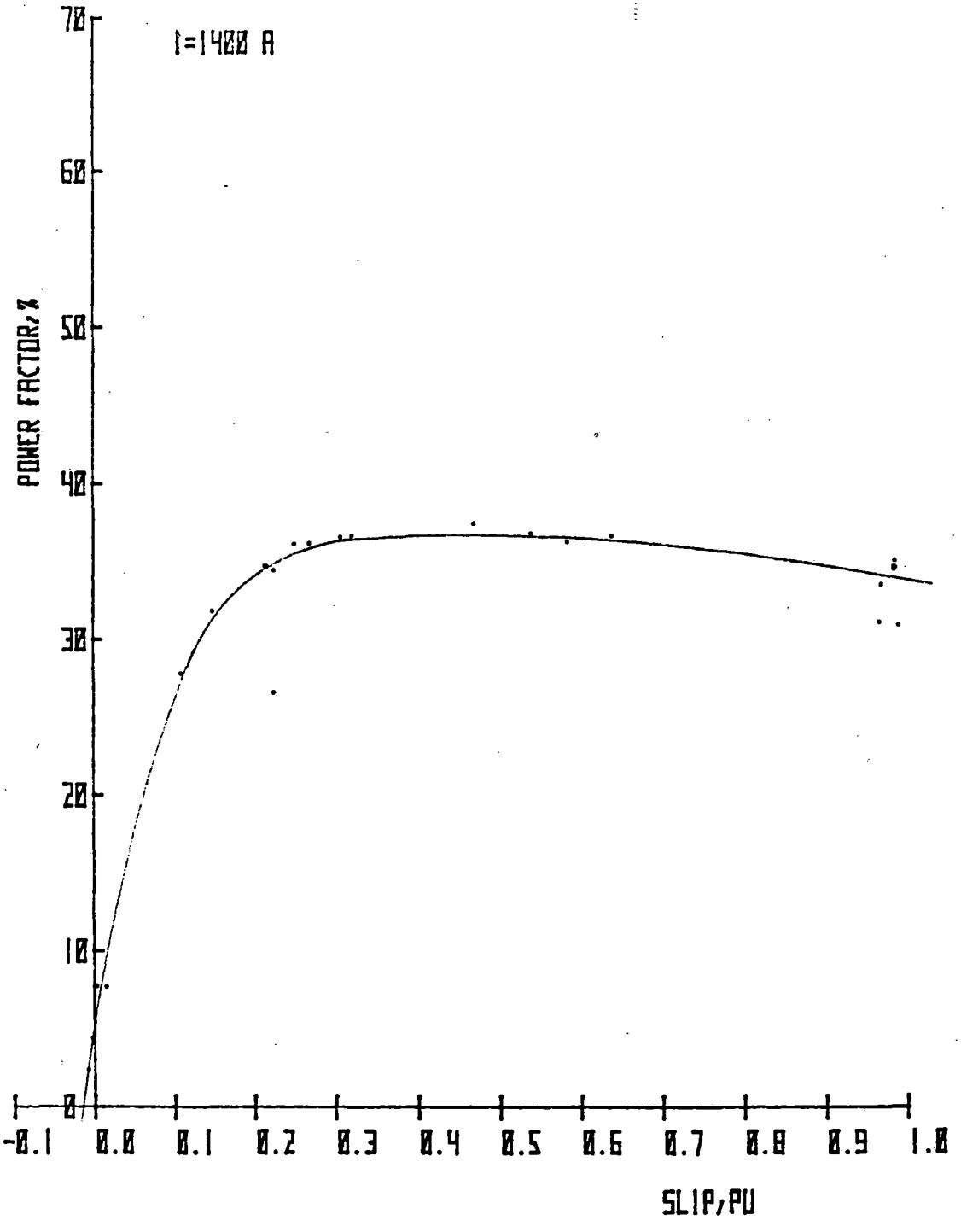

Figure 1-8. Power Factor vs Slip, 10-Pole SLIM, Solid Iron Reaction Rail, 18-mm Airgap

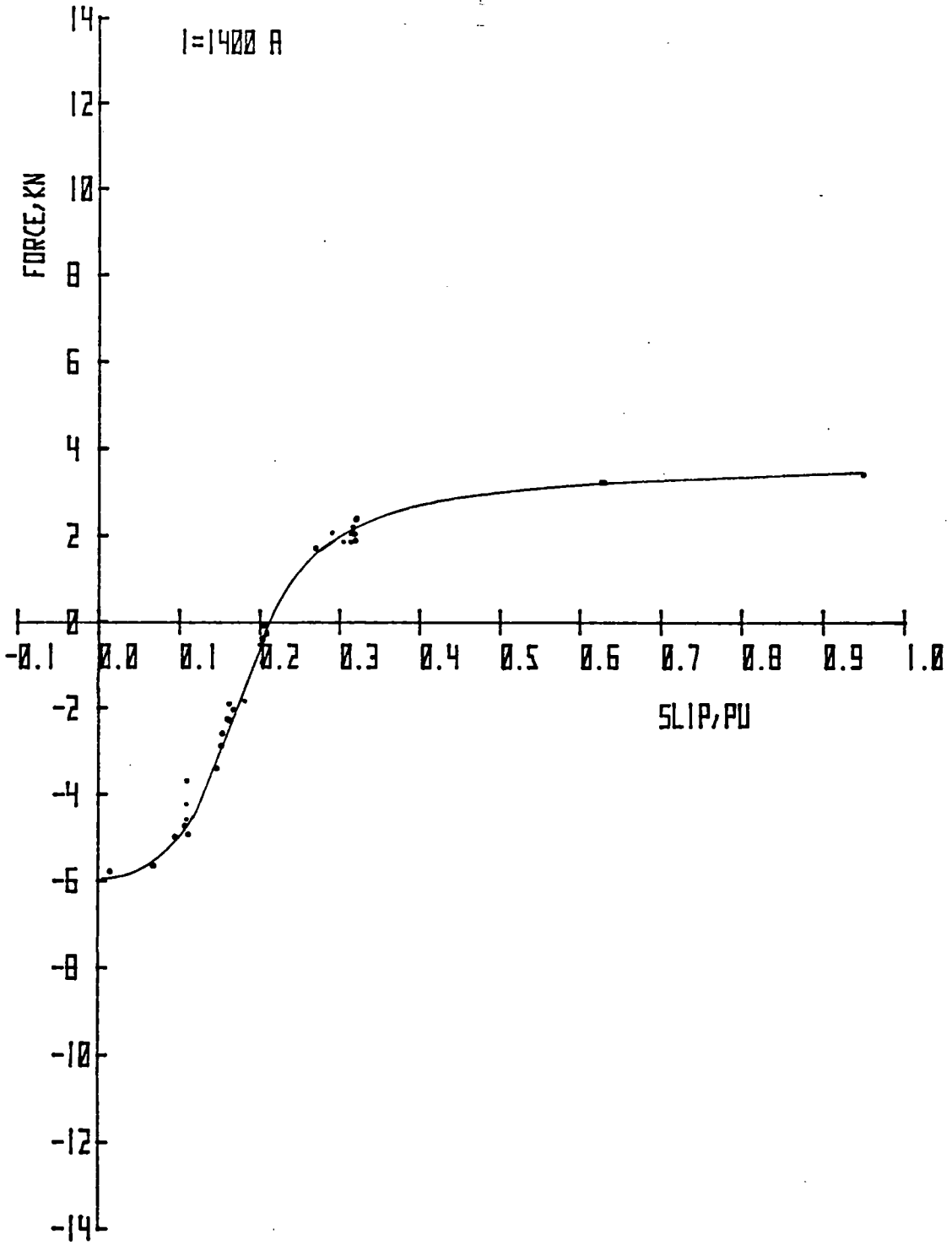

Figure 1-9. Total Vertical Force vs Slip, 5-Pole (Leading) SLIM, Baseline Reaction Rail

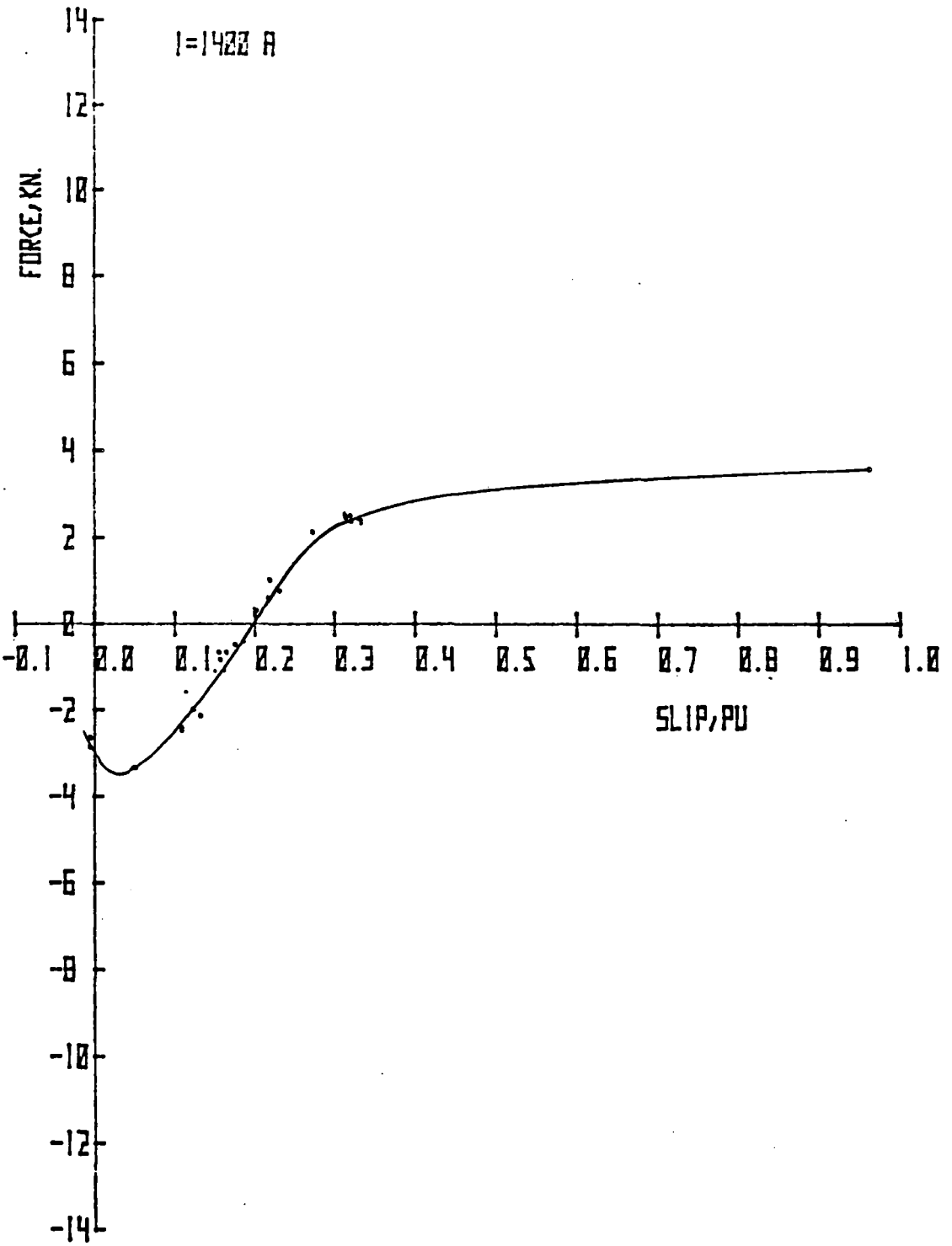

Figure 1-10. Total Vertical Force vs Slip, 5-Pole (Trailing) SLIM, Baseline Reaction Rail

CONCLUSIONS

The following general conclusions were derived from the SLIM test data.

- Extending the primary iron structure beyond the ends of the stator winding has little effect on motor performance. However, the magnetic wake causes a significant attraction between the primary iron and the reaction rail aft of the motor. This also would include structural steel in near proximity to the aft end of the primary.

- A certain degree of saturation was noted during tests with the baseline reaction rail. A much more significant effect was noted over the solid iron reaction rail.

- The method of measuring track flux penetration in solid iron by coarsely laminating the backiron has validity only for the baseline reaction rail tests. Additional tests would be required to establish the initial and final states of magnetization in the reaction rail.

- SLIM output characteristics with constant voltage excitation differ considerably from those at the rated constant current excitation. However, the solid iron reaction rail appeared to match primary current and voltage requirements more exactly.

- Table 1-2 shows comparative performance criteria for tests with and without the aluminum cover.

TABLE 1-2

REACTION RAIL PERFORMANCE

	Aluminum Plus Solid Iron (Entrefer = 28.5 mm)	Solid Iron Only (Entrefer = 28.5 mm)	Solid Iron Only (Entrefer = 14.5 mm)
Peak efficiency, percent	73	69.5	71
Peak power factor, percent	49	33	36

Peak efficiency is not severely compromised by removal of the aluminum cover. However, the power factor is significantly lower for the solid iron reaction rail. As previously stated, an appreciable degree of saturation is present between the two solid iron candidates, as the differences in efficiency and power factor are negligible.

- Comparison of these SLIM test results with earlier DLIM test results (Table 1-3) is not easily accomplished due to the different nature of the reaction rails. However, the SLIM baseline tests indicate lower peak efficiency and power factor for the DLIM tests. The performance degradation was due to a combination of larger airgap per side, and higher magnetic saturation, reflecting real compromises to be made when operating the SLIM in the same environment as the DLIM.

TABLE 1-3

COMPARATIVE DLIM AND SLIM PERFORMANCE

Parameter	1978-1979 SLIM with Baseline Reaction Rail	1977 DLIM
Peak efficiency, percent	73	75
Peak power factor, percent	49	67

SECTION 2

TEST PLAN GUIDELINES

INTRODUCTION

Prior to testing the LIMRV in its single-sided configuration, extensive tests were completed with the motor configured in a double-sided topology [10]. The DLIM investigation generated much valuable information and insight for developing not only a suitable theoretical analysis of linear induction motors, but also for the acquisition of test and field experience on a full-size traction unit. These tests clearly identified the most valuable tests to be performed on the SLIM. Accordingly, a test plan was devised [20] for acquiring additional data relevant to the different characteristics of the SLIM. The theoretical and practical considerations that underlined this test program are examined in this section.

RELEVANCE OF DLIM TESTING

DLIM tests that proved applicable in the formulation of a SLIM test program are discussed below.

Ac Electrical Performance Tests

Electrical performance data is defined as measured thrust and associated parameters (power, efficiency, power factor, voltage, and current, for example) that enable evaluation of the LIM as a propulsion unit. DLIM test data was acquired at a nominal excitation frequency of 94.3 Hz over the motoring slip range. Thus, for the SLIM tests, a meaningful comparison can be made by specifying the same excitation frequency of 94.3 Hz over the motoring slip range.

Distributed Electrical Parameters, Pole-by-Pole

Although airgap flux and reaction rail current distribution were measured during the original LIMRV test series by using flux coils and linear couplers installed on a section of reaction rail [9], attaining the specified test conditions at a specific guideway location was found to be difficult and expensive. An alternative approach was identified, whereby related parameters could be measured onboard the test vehicle.

Providing voltage measurement taps in the series-connected LIM winding enabled the distribution of voltage, power, power factors, and reactive power to be measured along the length of the motor. Measurement of these parameters in various pole configurations provided additional data that enhanced understanding of linear induction motors.

Theoretical work was developed that supported the results of these tests.

It was decided that the existing instrumentation could be used to acquire data for the SLIM in a manner similar to that used for the DLIM. Additionally, the scope of the distributed parameter measurement could be expanded to include

measurement of pole flux, as existing flux search coils had been damaged during the DLIM test period.

Distributed Electrical Parameters in an Extended Iron Configuration

In the previous test series, data was acquired on the effect of extended iron in the motor primary by testing the motor in two five-pole configurations. While this data serves mainly to assist the theoretical analysis of LIMs, it appeared advisable to perform similar tests on SLIM with the baseline reaction rail to provide additional theoretical support for ongoing analytical work.

Braking Characteristics with Dc Excitation

A natural extension from electrical performance tests with ac excitation is excitation of the motor with direct current in order to examine braking characteristics. This aspect was investigated and reported for the DLIM [6]. However, these tests may be conveniently included in the SLIM test series.

Saturation Effect Tests

In order to set steady-state conditions during acquisition of a data point, a variance from the intended point must be tolerated. The effect of saturation must be examined during testing to check the validity of normalizing test data to a common excitation level. This aspect was covered in previous DLIM testing, but it assumes greater importance in SLIM testing due to the reduced magnetic cross section in the secondary.

TEST ASPECTS UNIQUE TO SLIM

Conversion of the LIMRV to the single-sided configuration necessitated the design and construction of an entirely new reaction rail. This had profound electrical performance implications, and in addition required a complete modification of the motor suspension and force measuring system. Some of the wider implications of a change in motor topology are discussed below, with particular reference to the formulation of a SLIM test plan.

- Complex destabilizing normal and lateral forces are generated between primary and secondary under various test conditions. These forces are of interest in integrating this type of LIM into a vehicle system. Variation of these motor forces during operation of the SLIM as a motoring/braking unit affects the dynamics of potential vehicle systems. While of interest primarily in the areas of safety and ride comfort, this aspect also is important in evolving more basic data required for major subsystem design. Measurement of motor forces for a given excitation level with respect to electrical slip provides fundamental data. Variations in motor forces due to other variables include the effect of excitation level (saturation), the effect of change in airgap, and the relative lateral position between motor primary and reaction rail.

- The reaction rail itself represents a new area of investigation. Practical cost considerations dictate that the reaction rail design specification prescribe, if at all possible, common grade materials. Candidate reaction rail configurations include composite aluminum/steel (Figure 2-1), and solid steel; an opportunity exists to investigate both configurations with minimum modification. Significant material and fabrication savings may be effected by adopting a solid iron secondary, albeit at the expense of electrical performance. Tests must therefore be oriented toward comparative evaluation of these two candidates. Also, measurement of the utilization of reaction rail material (including the degree of saturation of the backiron) is required for optimization of rail material cost. Another element of reaction rail cost is the required accuracy of rail alignment. Unavoidable variations in mechanical airgap between primary and secondary are caused by vehicle dynamics and reaction rail alignment. This imposes a constraint on the minimum mechanical airgap below which the SLIM cannot be operated without significant primary/secondary contact. This implies a theoretical efficiency and power factor maximum determined by mechanical interface problems, peculiar to the SLIM configuration. The optimum gap for the tests described herein is not necessarily the optimum gap for other SLIM-propelled vehicle systems, and it will be determined by reaction rail characteristics in addition to the SLIM primary dynamic movement. However, the nature of the LIMRV primary suspension is such that airgap variations are caused primarily by reaction rail roughness, and thus valuable data will be obtained on the effect of a practical reaction rail, on SLIM performance, and on the minimum airgap width at which a SLIM with this type of rail cannot be operated. Other studies [21, 22] show that vehicle and/or SLIM primary dynamic movements can also be significant for other advanced tracked vehicles. The effect of different operating airgaps on motor performance should also form an essential part of the program for the reasons mentioned above.

OTHER CONSIDERATIONS

It was emphasized earlier that the reaction rail design heavily influences vehicle testing program philosophy. Adoption of a new motor topology depends upon a successful theoretical analysis and understanding, and the test data must provide, in addition to practical performance data, an insight into motor behavior so that convenient mathematical models may be developed. Although a comprehensive analysis for the motor in its DLIM configuration [10] has been modified for use in the SLIM configuration [11], certain assumptions were required whose validities were unattested. In addition, alternative analytical approaches, while lacking the sophistication of the aforementioned analysis, offer expedient solutions to many application problems. Test data provides an opportunity to explore such assumptions, and develop alternative analyses.

In summary, the basic objectives of the testing program are to:

- Determine SLIM electrical performance characteristics and compare them with those of the DLIM.

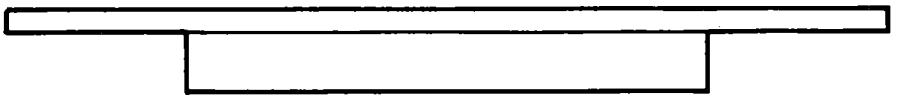

a. COMPOSITE ALUMINUM/SOLID IRON RAIL (BASELINE)

b. SOLID IRON RAIL

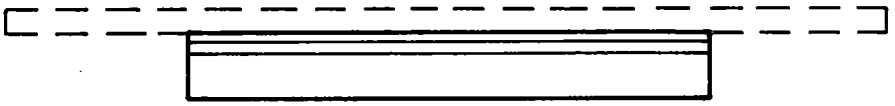

c. SPECIAL 6.7-M LAMINATED SECTION FOR INVESTIGATION OF FLUX PENETRATION

S-40189

Figure 2-1. Reaction Rail Candidates

- Examine aspects of a practical reaction rail.
- Provide data for integrating the SLIM into potential vehicle systems.
- Acquire data for validating theoretical models to analyze LIMs.

These broad goals are subdivided into more specific objectives for translation into actual test procedures. The description of tests includes a section that correlates the objectives with test details.

SECTION 3

SYSTEM DESCRIPTION

TEST FACILITY

All testing reported herein was conducted at the U. S. Department of Transportation Test Center, Pueblo, Colorado. Figure 3-1 shows the geographical layout of the site. Appendix A contains a detailed description of the test facility, including reaction rail design data and electrical particulars on the SLIM primary.

The LIM secondary (reaction rail) is attached to the wooden ties that support the standard-gauge railroad track. The LIMRV track extends for approximately 10 km, of which 2.4 km is fitted with the SLIM reaction rail, at an average 1-percent downhill grade from the LIMRV building. The length of reaction rail was considered adequate for testing up to vehicle speeds of 70 m/s, thus affording a 10-second data window---on the assumption that two J52 booster jet engines mounted outboard the LIMRV would provide thrust augmentation. The track includes 4.8 km of curves, banked at 8 deg, with a 4-km radius. The track was constructed to specific geometric requirements, and it is rigorously maintained to permit safe high-speed operation.

The LIMRV is housed and serviced in a building at the north end of the track. The data van, located 3.7 km from the LIMRV building, contains the data acquisition and remote control systems. Appendix C describes the data acquisition system in detail.

LIM SUSPENSION MODIFICATIONS

A substantial redesign of the motor mounting concept was required to convert the LIMRV from its original double-sided LIM configuration. This design effort is discussed elsewhere [11]; only design highlights relevant to this report are included herein.

The left half of the original double-sided linear induction motor became the single-sided motor. The SLIM was bolted to a strongback assembly along its length for strength and support.

The strongback was suspended at either end from a subframe via four strain-gaged load links. In addition, the center of the strongback was attached to the truck sideframe center pivot by a center hanger, which permitted limited lateral movement. The subframe comprised two side members bolted front and back to cross trusses; this arrangement provided a safety backup in the event of support link failure. The subframe was attached to the truck side members in the vicinity of the journal bearings via journal struts.

MOTOR CONNECTIONS

Previous LIMRV tests [10] investigated the effect of connecting different numbers of active poles, and in particular the effect of extended primary

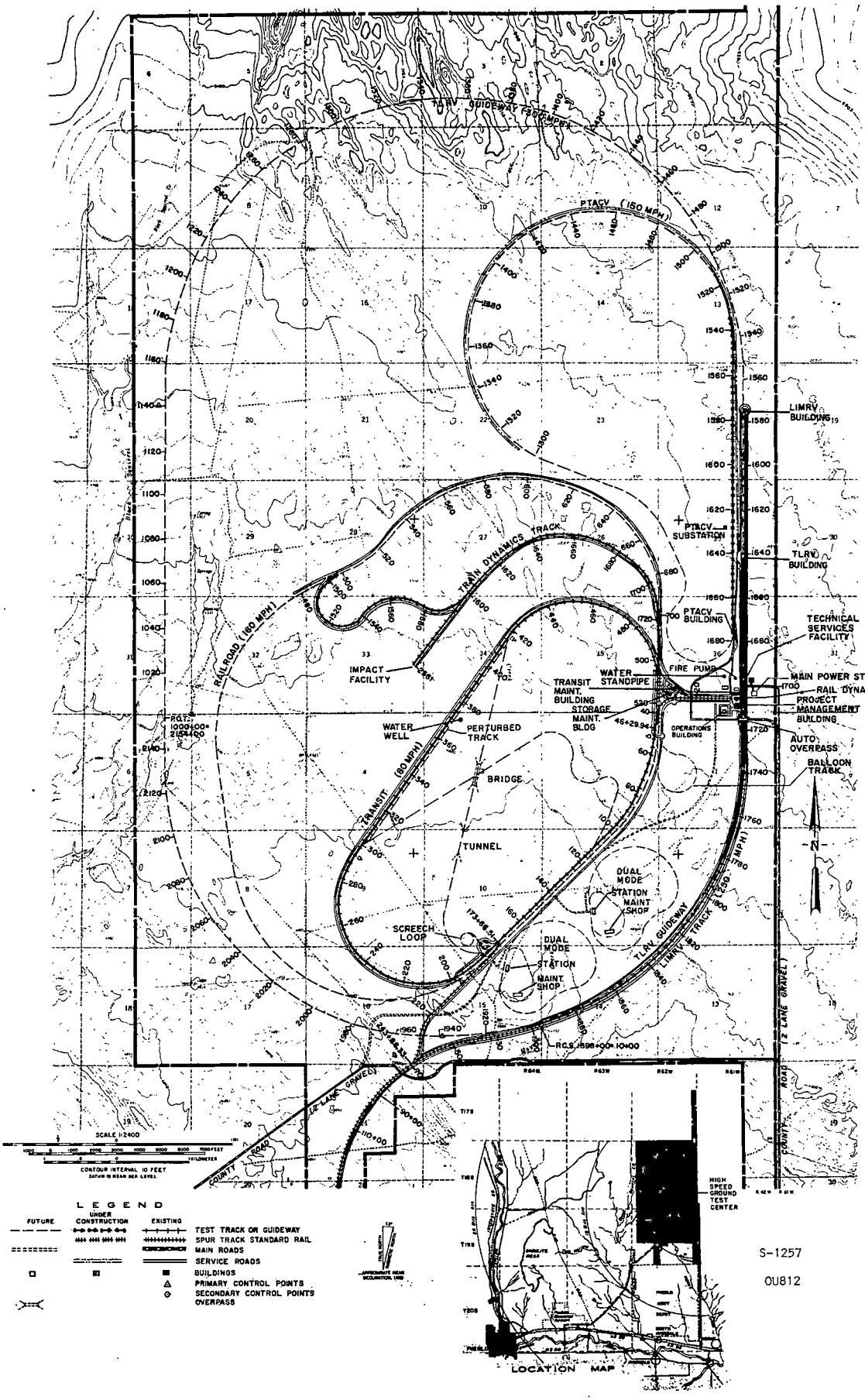

Figure 3-1. Transportation Test Center

iron in the 5-pole configuration. The 10-pole motor provides the same opportunity for testing in the single-sided configuration, and the implications may well be different for extended iron in the SLIM configuration.

Figure 3-2 shows the primary motor connections for testing in the 10-pole and 5-pole configurations. Also shown are the instrumentation connections for measurement of distributed phase-belt parameters.

Table 3-1 lists the high-voltage lead wire designations for the pair of lead wires connected to the voltage taps of each phase belt. One additional high-voltage instrument lead designated NR, connected to the LIM neutral, was brought out from the LIM to a terminal box to make 31 points available for monitoring phase-belt voltages and related parameters.

ANCILLARY INSTRUMENTATION

During the prevous LIMRV test series, instrumentation was provided to measure distributed electrical performance parameters. Instrumentation was therefore provided for voltage and power measurements of 12 phase belts so that a survey could be made of all phase belts in a given phase, or of all three phases in four poles. This additional instrumentation is described in the following paragraphs, and the instrumentation common to the left half of the DLIM is relevant for SLIM tests.

Input Power Measurement

Figure 3-3 is a schematic wiring diagram of the propulsion system. The power source for the LIM was a gas-turbine-driven, 3-phase, wye-connected, ungrounded-neutral alternator. The LIM had 3-phase, wye-connected, ungrounded-neutral windings. The instrumentation described herein was installed in the vehicle to obtain data on the effect of the number of poles on distributed parameters such as phase-belt voltages, power, and flux.

Total power input to the LIM is a significant parameter in assessing LIM performance, since it enters directly into the determination of LIM efficiency. In the LIMRV instrumentation system, the common reference point for the power transducers measuring total LIM input power was the neutral of the LIM windings.

Voltage Measurement

Thirty-one high-voltage instrumentation leads (as defined in Table 3-1 and Figure 3-3) were brought out from the LIM and terminated in a terminal box. Fifteen potential transformers were provided to condition selected voltages from the LIM to the input voltage level required by the instrumentation system. Three of these potential transformers were dedicated to the measurement of individual overall phase voltage for the active poles of a winding. The remaining transformers measured up to 12 phase-belt voltages (three phase belts in each of four poles) or all phase belts in a given phase.

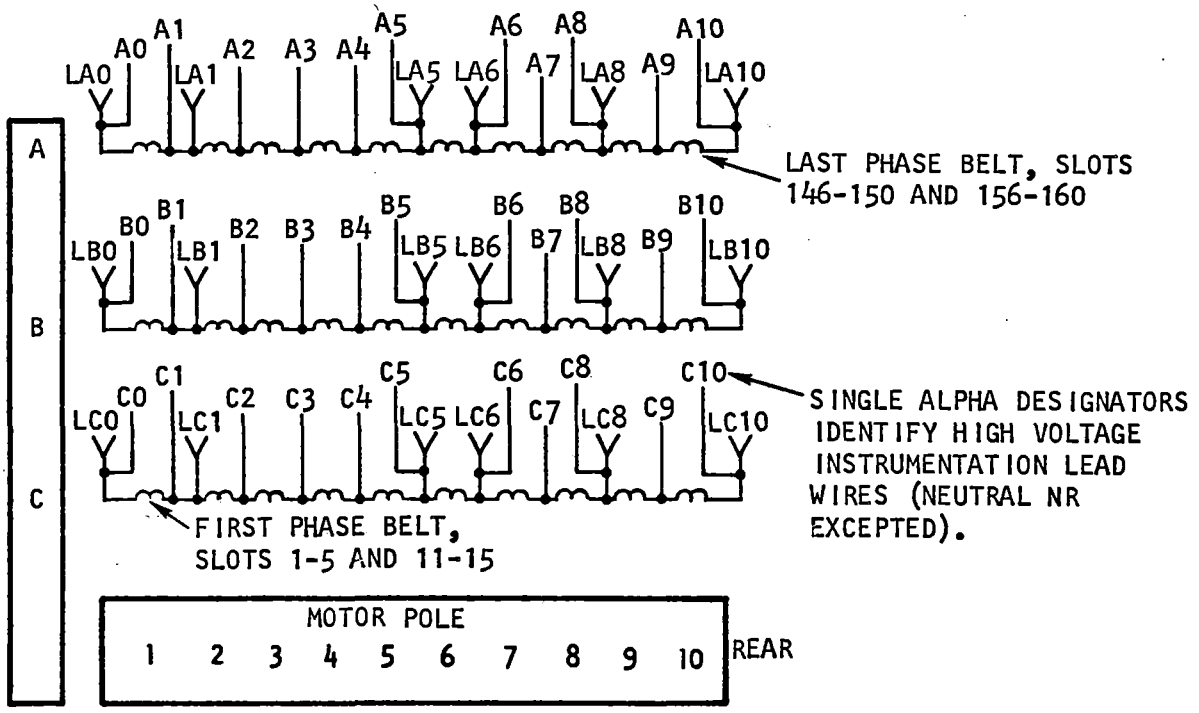

Motor Configuration	Description	Phase			Neutral Jumpers
		A	B	C	
10	All poles active	LA0	LB0	LC0	LA10 LB10 LC10
05	5 rear poles active	LA5	LB5	LC5	LA10 LB10 LC10
55	5 forward poles active	LA0	LB0	LC0	LA5 LB5 LC5

S-23754

Figure 3-2. Primary Power and Instrumentation Connections

TABLE 3-1

VOLTAGE TAP CONNECTIONS

Pole Number	Phase		
	A	B	C
1	A0 - A1	B0 - B1	C0 - C1
2	A1 - A2	B1 - B2	C1 - C2
3	A2 - A3	B2 - B3	C2 - C3
4	A3 - A4	B3 - B4	C3 - C4
5	A4 - A5	B4 - B5	C4 - C5
6	A5 - A6	B5 - B6	C5 - C6
7	A6 - A7	B6 - B7	C6 - C7
8	A7 - A8	B7 - B8	C7 - C8
9	A8 - A9	B8 - B9	C8 - C9
10	A9 - A10	B9 - B10	C9 - C10

Current Measurement

Figure 3-3 shows the location of the 12 existing current sensors. Six of the LIM current sensor signals provided information for the measurement of LIM performance parameters; the remaining six were available for vehicle operation. The three LIM current signals were then input to the data acquisition system.

SIGNAL CONDITIONING

Figure 3-4 identifies the electrical performance parameters required for this test. Adjustable gain signal conditioning is shown for both current and voltage signals. Gain changes were accomplished by means of plug-in gain cards, each having a fixed gain.

The three conditioned current signals, three input voltage signals, and 12 phase-belt voltage signals were output to 18 high-sample-rate (1000 sps) DAS channels to provide alternative data as backup to the onboard analog-computed performance data.

FORCE MEASURING SYSTEM

Figure 3-5 shows the front portion of the SLIM supported in its subframe by vertical and lateral load links. The SLIM is additionally restrained by a thrust load cell operating in compression.

Vertical Force Measurement

Five vertical load links support the SLIM, four of which are located near each corner of the airgap surface, and operate in tension and compression only due to the spherical rod ends at the ends of each link. The center of the SLIM is additionally supported by the center support link. Theory of operation is as follows: The link monitors vertical forces by means of strains developed axially. Lateral movements of up to 3.2 mm (0.125 in.) are allowed by the bending of the link in the Y-Y plane before a snubber restricts further lateral movement of the SLIM center. The total vertical force acting on the SLIM is the sum of all five vertical force transducer indications.

Lateral Force Measurement

Five load links, including the center support link, restrain and monitor lateral forces between the SLIM and the truck. The lateral load links at the four corners of the SLIM operate in tension and compression only (as do the vertical load links), and are preloaded in tension to minimize mechanical play. The lateral force acting on the center support link is monitored by means of strains developed in the bending axis. The total lateral force is the sum of the five lateral transducer indications.

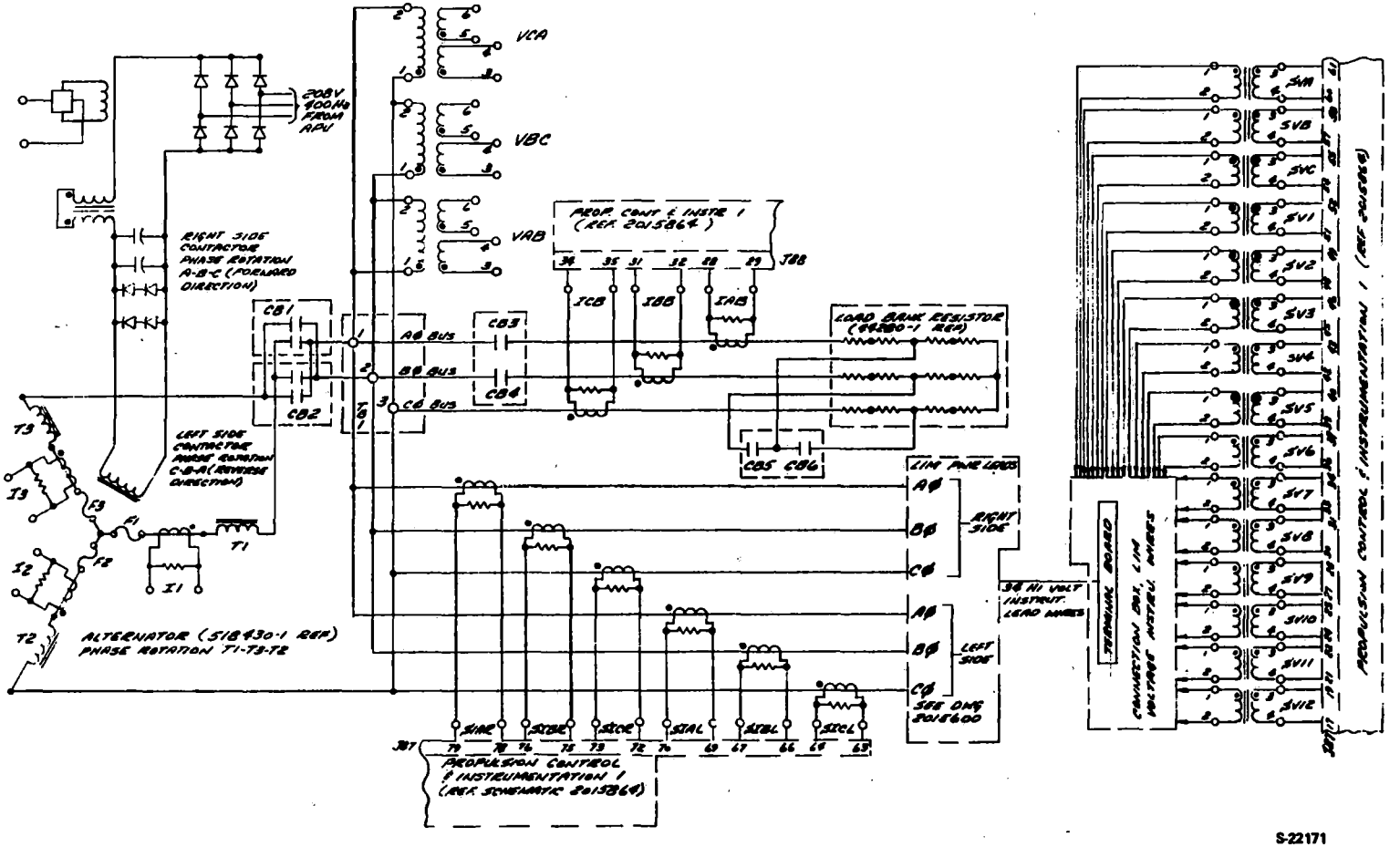

Figure 3-3. LIMRV Propulsion System

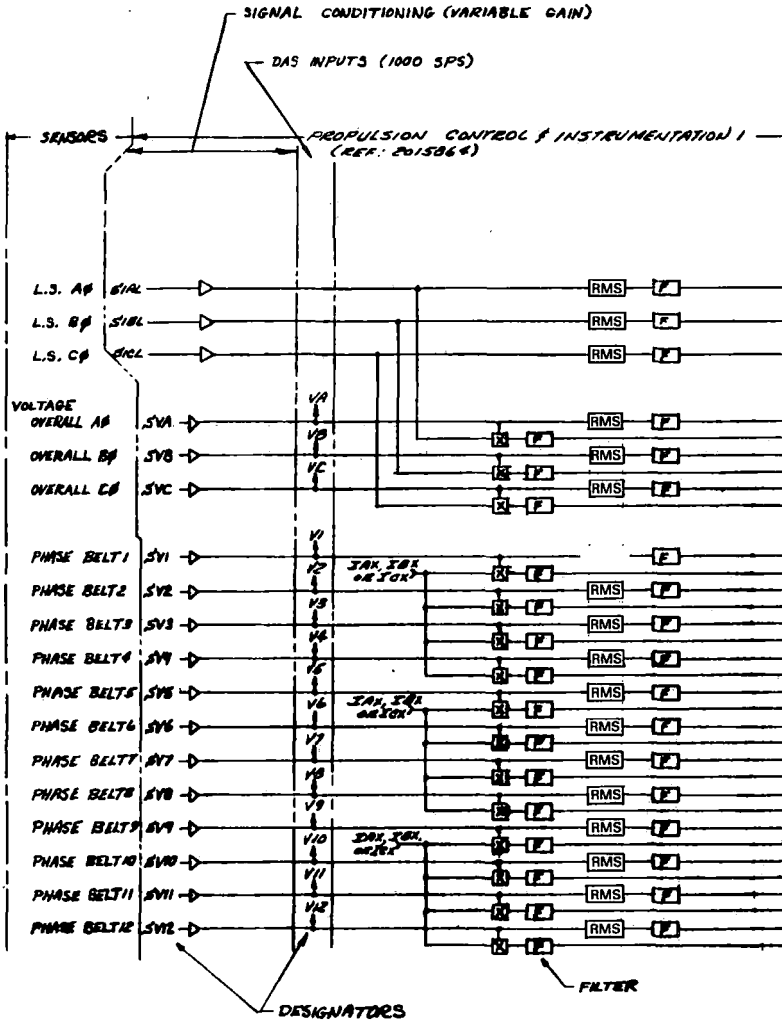

Figure 3-4. Electrical

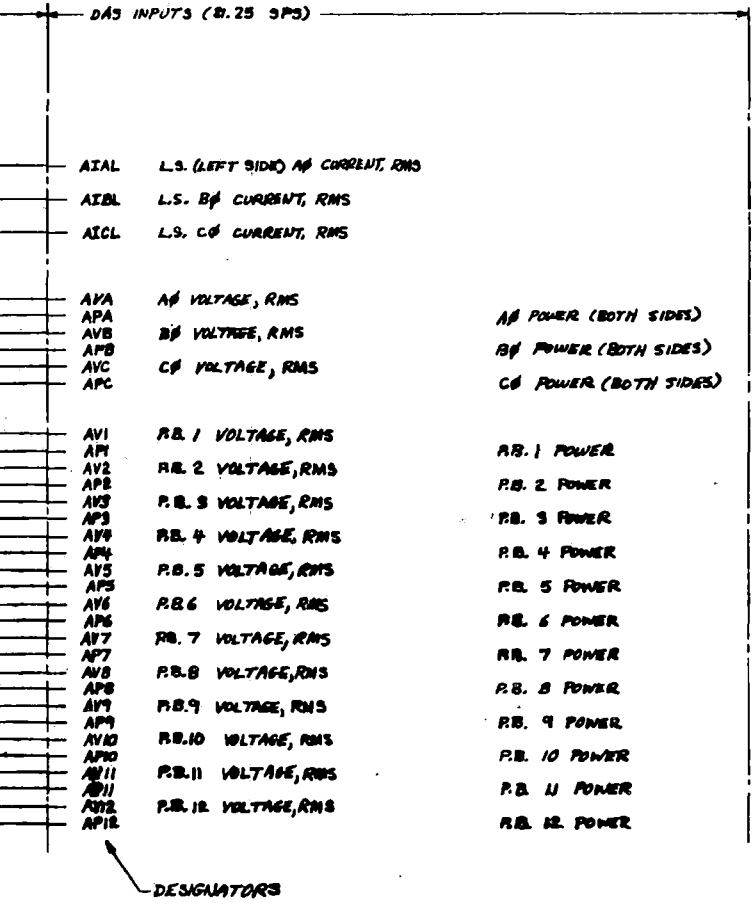

S-22172

Performance Parameters

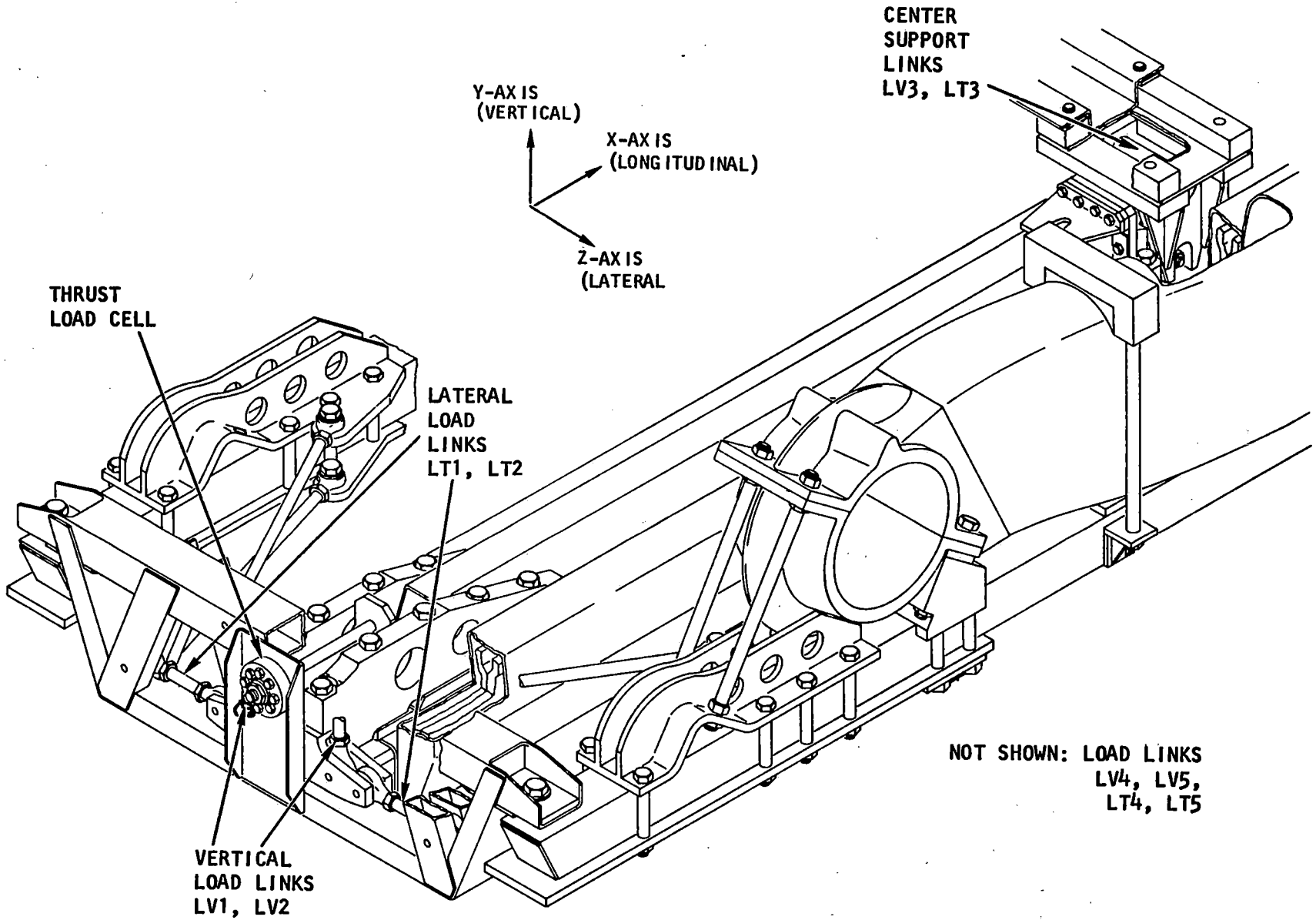

Figure 3-5. SLIM Support Structure

Thrust Measurement

Thrust is monitored by a compression load cell mounted on the SLIM subframe. The force is transmitted between the transducer and the SLIM by a compression link.

Load Cell and Strain Gage Signal Conditioning

The combination of the 11 force transducers to indicate total vertical force, total lateral force, thrust, and pitching moment is shown in Appendix C, Figure C-4.

Calibration of Force Measuring System

The redundancy inherent in this force measuring system implies a significant degree of cross coupling. To calibrate the force measuring system, and to qualify the cross coupling effects, each transducer was calibrated individually, and as part of the total system. The difference between the individual calibrations and the system calibration quantifies the degree of cross coupling that exists in the X, Y, and Z directions. Calibration procedures are described in Appendix C.

These same 18 signals were input to the onboard analog computing system, which generated a total of 33 signals for input to low-sample-rate (31.25 sps) DAS channels. Three current signals and 15 voltage signals were input to root-mean-square (RMS) devices and then filtered to provide RMS values of the input parameters. Fifteen power signals were generated by analog multiplication of a single voltage signal by a single current signal. The resulting output signal was filtered before input to the DAS. The filtered responses of all the signals were matched to attain a measure of comparability under dynamic conditions.

SECTION 4

SUMMARY OF TESTS AND TEST OBJECTIVES

TEST SUMMARY

Table 4-1 shows a summary of tests performed in the SLIM configuration. All dynamic tests (with ac excitation) were performed at a nominal frequency of 94.3 Hz to facilitate comparison with previous DLIM data. Although many different test configurations were examined, two distinct modes of testing were employed.

- Dc eddy current tests with different reaction rail configurations.
- Ac excitation tests with different reaction rail configurations and motor connections.

DC EDDY CURRENT TEST OBJECTIVES

Evaluate the braking characteristic as a function of speed and dc excitation.

Evaluate vertical force distribution as a function of speed and dc excitation.

Evaluate the effects of saturation, especially in the backiron.

Evaluate the effectiveness of current jumpers (baseline reaction rail only).

Provide experimental data to assist in the modeling of linear induction motors with various secondaries.

AC EXCITATION TEST OBJECTIVES

All ac tests were performed at a nominal excitation frequency of 94.3 Hz to facilitate convenient comparison with previous DLIM tests.

Acquire electrical performance data (variations of thrust and associated electrical data) as a function of electrical slip.

Acquire vertical force data as a function of electrical slip.

Acquire data on distributed parameters (volts per pole, power per pole, kVA per pole, and pole flux) as a function of slip.

Investigate the effects of saturation in the normalizing of data.

Acquire data on the penetration and magnitude of flux in the reaction rail backiron.

Investigate the effect of a change in airgap (solid iron reaction rail only).

Compare data, where applicable, with previous DLIM data, including the tests with extended primary iron.

TABLE 4-1

SLIM TEST SUMMARY

Specified Airgap, mm	Motor Configuration*	Reaction Rail	Type of Test	Active Poles	Active Pole Location
25.4	10	Baseline	Eddy current braking	10	All
25.4	10	Baseline	Dynamic	10	All
25.4	10	Baseline	Dynamic track flux	10	All
25.4	05	Baseline	Dynamic	5	Trailing
25.4	55	Baseline	Dynamic	5	Leading
26	10	Solid iron	Eddy current braking	10	All
26	10	Solid iron	Dynamic	10	All
26	10	Solid iron	Dynamic track flux	10	All
18	10	Solid iron	Eddy current braking	10	All
18	10	Solid iron	Dynamic	10	All

*10 = All poles active
05 = 5 rear poles active
55 = 5 forward poles active

SECTION 5

TEST CONDITIONS

TEN-POLE TESTS WITH BASELINE REACTION RAIL

Tables 5-1, 5-2, and 5-3 summarize conditions for tests performed on 10-pole configurations with the baseline reaction rail. Appendix D cross references the test condition numbers with unique run numbers assigned by the Chief Test Engineer.

EDDY CURRENT BRAKING TESTS

SLIM braking characteristics were investigated when two phases of the motor primary were excited with direct current. The tests were conducted at two levels of excitation to investigate the effects of saturation (Table 5-1). In addition, the effect of secondary discontinuities on motor performance was assessed during the B-100 test series.

Transient variations in vertical force, pitching force, and longitudinal force were noted on the high-frequency force channels with the electrical current jumpers in place. The tests were repeated with the electrical current jumpers removed.

The following parameters were recorded during a dc test of the motor in its 10-pole configuration.

Time (arbitrary origin)

Position (station number)

Primary current (two phases in series)

Total vertical force

Pitching moment

Longitudinal force (braking)

Front airgap

Other parameters in the data acquisition system were not recorded.

TESTS AT 94.3 HZ EXCITATION FREQUENCY

The full motoring characteristic over the slip range $1 > S > 0$ was investigated. The required test conditions are shown in Tables 5-2 and 5-3. For the B-2 test series, phase-belt instrumentation was connected to the B phase of the machine to measure distributed parameters as a function of slip and excitation level. Two levels of excitation were used to quantify the saturation effects. Note that a degree of overlap occurs between Table 5-2 and 5-3. However, the

B-5 test series is intended to acquire data on track fluxes using a trackside oscillograph. The primary use of onboard instrumentation is to correlate the trackside fluxes with the relevant onboard data.

Instrumentation codes for the B-2 and B-5 test series enable all three phase parameters to be monitored for this test series.

TABLE 5-1

EDDY CURRENT BRAKING TESTS,
SLIM CONFIGURATION 10, 25.4-MM AIRGAP, BASELINE REACTION RAIL

Test Condition Number	Vehicle Speed, m/s	mph	Nominal Current, A
B-100	1	2.3	1225
B-101	2	4.5	1225
B-102	3	6.7	1225
B-103	4	8.9	1225
B-104	5	11.2	1225
B-105	7	15.6	1225
B-106	10	22.4	1225
B-107	12.5	28	1225
B-108	15	33.5	1225
B-109	20	44.7	1225
B-110	1	2.3	1715
B-111	2	4.5	1715
B-112	3	6.7	1715
B-113	4	8.9	1715
B-114	5	11.2	1715
B-115	7	15.6	1715
B-116	10	22.4	1715
B-117	12.5	28	1715
B-118	15	33.5	1715
B-119	20	44.7	1715

NOTE: Two phases excited.

TABLE 5-2

DYNAMIC TEST, SLIM
CONFIGURATION 10, 25.4-MM AIRGAP

Test Condition Number	Vehicle Speed, m/s	mph	Slip Freq, Hz	Nominal V/Hz	Motor Voltage, VRMS (L-N)	Instrumentation Code	Selected Data Test Group
B-200	67.1	150	0	3.46	326	2000	B2-1
B-201	65.8	147	3	3.46	326	2000	B2-1
B-202	63.5	142	5	3.46	326	2000	B2-1
B-203	62.5	139	7.5	3.46	326	2000	B2-1
B-204	60	134	10	3.46	326	2000	B2-1
B-205	56.4	126	15	3.46	326	2000	B2-1
B-206	55.4	123	17.5	3.46	326	2000	B2-1
B-207	52.8	118	20	3.46	326	2000	B2-1
B-208	49.3	110	25	3.46	326	2000	B2-1
B-209	45.7	102	30	3.23	304	2000	B2-1
B-210	39.2	87	40	2.93	277	2000	B2-1
B-211	24.4	55	60	2.37	223	2000	B2-1
B-212	3.1	7	90	2.21	208	2000	B2-1
B-213	67.1	150	0	4.16	392	2000	B2-2
B-214	63.5	142	5	4.16	392	2000	B2-2
B-215	61.7	138	7.5	4.16	392	2000	B2-2
B-216	60	134	10	4.16	392	2000	B2-2
B-217	56.4	126	15	4.16	392	2000	B2-2
B-218	49.3	110	25	4.16	392	2000	B2-2
B-219	45.7	102	30	4.16	392	2000	B2-2
B-220	24.4	55	60	3.39	320	2000	B2-2
B-221	3.1	7	90	3.16	298	2000	B2-2

TABLE 5-3

DYNAMIC TRACK FLUX TEST, SLIM
CONFIGURATION 10, 25.4-MM AIRGAP, BASELINE REACTION RAIL

Test Condition Number	Vehicle Speed, m/s	mph	Nominal Slip Freq, Hz*	Nominal V/Hz*	Motor Voltage, VRMS (L-N)	Instrumentation Code	Selected Data Test Group	Reference Voltage Phase
B-500	63.5	142	5	3.46	326	1000	B2-1	B
B-501	60	134	10	3.46	326	1000	B2-1	B
B-502	56.4	126	15	3.46	326	1000	B2-1	B
B-503	52.8	118	20	3.46	326	1000	B2-1	B
B-504	45.7	102	30	3.46	326	1000	B2-1	B
B-505	24.4	55	60	3.39	320	1000	B2-1	B
B-506	3.1	7	90	3.16	298	1000	B2-1	B
B-507	63.5	142	5	4.16	392	3000	B2-2	B
B-508	60	134	10	4.16	392	3000	B2-2	B
B-509	56.4	126	15	4.16	392	3000	B2-2	B
B-510	52.8	118	20	4.16	392	3000	B2-2	B
B-511	45.7	102	30	4.16	392	3000	B2-2	B

*Not subject to selection by anomaly criteria.

PERFORMANCE TESTS WITH EXTENDED PRIMARY IRON (BASELINE REACTION RAIL)

Tables 5-4 and 5-5 show required test conditions for the motor in two 5-pole configurations. Not only do the connections of the primary permit a study of the effect of extended iron aft of the excited portion of the winding, but also the reduced phase voltage for a given current over the 10-pole configuration allows a higher voltage per pole to be applied without exceeding powerplant limits.

For P = 55, selected data test groups B4-1, B4-2, and B4-3 may be used to determine the effects of saturation on electrical parameters. Test groups B3-1, B3-2, and B3-3 provide corresponding information for P = 05. All phase-belt parameters were measured at the low excitation level.

TEN-POLE TESTS WITH SOLID IRON REACTION RAIL (ALUMINUM COVER REMOVED)

Eddy Current Tests

Tests were performed at two airgap widths, and variations of motor forces (vertical and braking forces) were measured as vehicle speed varied. See Tables 5-6 and 5-7. In addition, a standstill magnetizing test was performed to examine the linearity of the vertical force characteristic (and consequently saturation). Excitation levels were adjusted to give the maximum vertical force without overranging the measuring system.

TABLE 5-4

DYNAMIC TEST, SLIM
CONFIGURATION 55, 25.4-MM AIRGAP, BASELINE REACTION RAIL

Test Condition Number	Vehicle Speed, m/s	mph	Slip Freq, Hz	Nominal V/Hz	Motor Voltage VRMS (L-N)	Instru-mentation Code	Selected Data Test Group
B-400	67.1	150	0	1.73	163	2000	B4-1
B-401	63.5	142	5	1.73	163	2000	B4-1
B-402	60	134	10	1.73	163	2000	B4-1
B-403	56.4	126	15	1.73	163	2000	B4-1
B-404	52.9	118	20	1.73	163	2000	B4-1
B-405	49.3	110	25	1.73	163	2000	B4-1
B-406	45.7	102	30	1.73	163	2000	B4-1
B-407	24.4	55	60	1.73	163	2000	B4-1
B-408	3.1	7	90	1.73	163	2000	B4-1
B-409	60	134	10	2.08	204	2000	B4-1
B-410	56.4	126	15	2.08	204	2000	B4-2
B-411	52.9	118	20	2.08	204	2000	B4-2
B-412	45.7	102	30	2.08	204	2000	B4-2
B-413	60	134	10	2.60	245	2000	B4-2
B-414	56.4	126	15	2.60	245	2000	B4-3
B-415	52.9	118	20	2.55	240	2000	B4-3
B-416	45.7	102	30	2.25	212	2000	B4-3
B-417	60	134	10	1.73	163	1000	B4-1
B-418	56.4	126	15	1.73	163	1000	B4-1
B-419	52.9	118	20	1.73	163	1000	B4-1
B-420	45.7	102	30	1.73	163	1000	B4-1
B-421	60	134	10	1.73	163	3000	B4-1
B-422	56.4	126	15	1.73	163	3000	B4-1
B-423	52.9	118	20	1.73	163	3000	B4-1
B-424	45.7	102	30	1.73	163	3000	B4-1

TABLE 5-5

DYNAMIC TEST, SLIM
CONFIGURATION 05, 25.4-MM AIRGAP, BASELINE REACTION RAIL

Test Condition Number	Vehicle Speed, m/s	mph	Slip Freq, Hz	Nominal V/Hz	Motor Voltage VRMS (L-N)	Instru-mentation Code	Selected Data Test Group
B-300	67.1	150	0	1.73	163	2000	B3-1
B-301	63.5	142	5	1.73	163	2000	B3-1
B-302	60	134	10	1.73	163	2000	B3-1
B-303	56.4	126	15	1.73	163	2000	B3-1
B-304	52.9	118	20	1.73	163	2000	B3-1
B-305	49.3	110	25	1.73	163	2000	B3-1
B-306	45.7	102	30	1.73	163	2000	B3-1
B-307	24.4	55	60	1.73	163	2000	B3-1
B-308	3.1	7	90	1.73	163	2000	B3-1
B-309	60	134	10	2.08	204	2000	B3-2
B-310	56.4	126	15	2.08	204	2000	B3-2
B-311	52.9	118	20	2.08	204	2000	B3-2
B-312	45.7	102	30	2.08	204	2000	B3-2
B-313	60	134	10	2.60	245	2000	B3-3
B-314	56.4	126	15	2.60	245	2000	B3-3
B-315	52.9	118	20	2.55	240	2000	B3-3
B-316	45.7	102	30	2.25	212	2000	B3-3
B-317	60	134	10	1.73	163	1000	B3-1
B-318	56.4	126	15	1.73	163	1000	B3-1
B-319	52.9	118	20	1.73	163	1000	B3-1
B-320	45.7	102	30	1.73	163	1000	B3-1
B-321	60	134	10	1.73	163	3000	B3-1
B-322	56.4	126	15	1.73	163	3000	B3-1
B-323	52.9	118	20	1.73	163	3000	B3-1
B-324	45.7	102	30	1.73	163	3000	B3-1

TABLE 5-6

EDDY CURRENT BRAKING TEST,
SLIM CONFIGURATION 10, 26-MM AIRGAP, SOLID IRON REACTION RAIL

Test Condition Number	Vehicle Speed, m/s	mph	Nominal Current, kA
S-100	1	2.3	1.36
S-101	2	4.5	1.36
S-102	3	6.7	1.36
S-103	4	8.9	1.36
S-104	5	11.2	1.36
S-105	7	15.6	1.36
S-106	10	22.4	1.36
S-107	12.5	28	1.36
S-108	15	33.5	1.36
S-109	20	44.7	1.36

NOTE: Two phases excited.

TABLE 5-7

EDDY CURRENT BRAKING TEST,
SLIM CONFIGURATION 10, 18-MM AIRGAP, SOLID IRON REACTION RAIL

Test Condition Number	Vehicle Speed, m/s	mph	Nominal Current, kA
18S-100	1	2.3	0.83
18S-101	2	4.5	0.83
18S-102	3	6.7	0.83
18S-103	4	8.9	0.83
18S-104	5	11.2	0.83
18S-105	7	15.6	0.83
18S-106	10	22.4	0.83
18S-107	12.5	28	0.83
18S-108	15	33.5	0.83
18S-109	20	44.7	0.83
18S-110	0	0	0.2
18S-111	0	0	0.4
18S-112	0	0	0.6
18S-113	0	0	0.8
18S-114	0	0	0.83

NOTE: Two phases excited.

Ac Dynamic Tests

Tests were performed at two different airgap widths. Tables 5-8 and 5-9 show details of the performance tests similar to the baseline reaction rail tests. Track flux (oscillograph) data was acquired for these test points whenever possible. Tests at the smaller gap width are denoted by the 18S- prefix. The 26-mm tests bear only the S- prefix.

TABLE 5-8

DYNAMIC TEST, SLIM CONFIGURATION 10, 26-MM AIRGAP,
SOLID IRON REACTION RAIL (INCLUDES TRACK FLUX TESTS)

Test Condition Number	Vehicle Speed, m/s	mph	Slip Freq, Hz	Nominal V/Hz	Motor Voltage, VRMS (L-N)	Instru-mentation Code	Reference Voltage Phase
S-200	67.1	150	0	4.16	392	2000	B
S-201	65.8	147	3	4.16	392	2000	B
S-202	63.5	142	5	4.16	392	2000	B
S-203	62.5	139	7.5	4.16	392	2000	B
S-204	60	134	10	4.16	392	2000	B
S-205	56.4	126	15	4.16	392	2000	B
S-206	52.8	118	20	4.16	392	2000	B
S-207	49.3	110	25	4.16	392	2000	B
S-208	45.7	102	30	4.16	392	2000	B
S-209	35.5	79	45	4.16	392	2000	B
S-210	24.4	55	60	4.16	392	2000	B
S-211	3.1	7	90	4.16	392	2000	B

TABLE 5-9

DYNAMIC TEST, SLIM CONFIGURATION 10, 18-MM AIRGAP,
SOLID IRON REACTION RAIL (INCLUDES TRACK FLUX TESTS)

Test Condition Number	Vehicle Speed, m/s	mph	Slip Freq, Hz	Nominal V/Hz	Motor Voltage, VRMS (L-N)	Instru-mentation Code
18S-200	67.1	150	0	4.16	392	2000
18S-201	65.8	147	3	4.16	392	2000
18S-202	63.5	142	5	4.16	392	2000
18S-203	62.5	139	7.5	4.16	392	2000
18S-204	60	134	10	4.16	392	2000
18S-205	56.4	126	15	4.16	392	2000
18S-206	52.8	118	20	4.16	392	2000
18S-207	49.3	110	25	4.16	392	2000
18S-208	45.7	102	30	4.16	392	2000
18S-209	35.5	79	45	4.16	392	2000
18S-210	24.4	55	60	4.16	392	2000
18S-211	3.1	7	90	4.16	392	2000

SECTION 6

TEST CONDUCT

TEST PROCEDURE

The relatively short length (2439 m) of the reaction rail necessitated the use of the thrust booster J52 jet engines for most test runs. The acquisition of a data point was essentially the same as in the DLIM testing. V/Hz excitation was approximately set as the vehicle approached the start of the 2439-m-long reaction rail. When the primary was over the reaction rail, final speed, slip frequency, and excitation adjustments were made, using a combination of T64 fuel control, J52 throttle control, and alternator field excitation. At the conclusion of a test run, the vehicle was towed to the north-end start of the track by the track service vehicle.

ACQUISITION OF ONBOARD TEST DATA

Appendix C describes the data acquisition system used for acquiring and processing onboard data. To check the operation of all instrumentation, especially vertical force transducers under no-load conditions, the acquisition of dynamic test data was preceded by a readout of all instrumentation channels for a 1- to 2-second period as the vehicle started moving at the beginning of each test run. This facilitated the testing and correction, when necessary, of instrumentation offsets. Initially, it built confidence in a new force measuring system in conjuction with a hydraulic calibration facility for the motor's vertical, pitching, and thrust forces. The redundancy of the force measuring structure necessitated individual zero adjustments for vertical force measurement during final data reduction at Torrance.

ACQUISITION OF TRACK FLUX DATA

The difficulty of measuring the flux distribution within solid iron prompted the use of a short track section within the main rail section in which the backiron was fabricated in three relatively thick horizontal laminations (Figure 6-2). Such horizontal laminations behave essentially like solid iron, but allow insertion of search coils with no local distortion of flux. The details of the special track section and installation of search coils are discussed in Appendix F.

One aspect of the testing using the laminated rail was to establish the section's behavior relative to the baseline backiron in order to extrapolate track flux measurements for solid iron predictions.

A trackside tape recorder was used to record the output of the search coil integrators. In addition, B phase voltage and A phase current were stripped from the data system to correlate onboard data with the trackside data. The onboard vehicle track position sensors also enabled onboard data to be synchronized to the instant the vehicle passed over the track search coils.

The nature of the LIMRV powerplant precluded accurate setting of test conditions as the vehicle passed over the track flux coils. Every effort was made to ensure that the excitation frequency was close to the base frequency of 94.3 Hz.

REACTION RAIL HEATING

The transient nature of the LIMRV powerplant during excitation of the SLIM at startup precluded accurate reaction rail temperature distribution tests. However, some measurements were mandatory to ensure that reaction rail hot-spot temperatures were not exceeded during low-speed tests. A thermocouple was installed in the instrumented laminated section to monitor track temperatures during startup conditions.

TEST PRIORITIES

It was necessary to complete all baseline reaction rail tests before beginning tests with the aluminum cover removed (solid iron tests). The available investigation time was divided between the baseline reaction rail tests and those with the aluminum cover removed, assuming continued availability of the vehicle. Removal of the aluminum cover was an irrevocable process due to the demanding constraints of time allotted for the completion of testing.

Interest in a solid iron reaction rail centered on its practical, low-cost design. Therefore, the practical aspects of the reaction rail were examined, rather than the more theoretical aspects of the baseline reaction rail test series. Particular features investigated were:

Electrical performance characteristic

Eddy current braking characteristic

Vertical force characteristic

Utilization/behavior of solid backiron

Effect of airgap change on the above features

SECTION 7

PRESENTATION OF DATA

This section describes the organization of test data in the remainder of the report.

- Section 8 highlights baseline reaction rail test data with various motor connection and excitation conditions.
- Section 9 presents solid iron reaction rail data in the 10-pole connection with various airgaps and excitation conditions. A major change in motor characteristics occurred due to removal of the aluminum cover; therefore, the test results are subdivided.
- Section 10 describes measurements made of flux penetration in the solid iron backiron for both baseline and solid iron reaction rail tests. A critical evaluation of these measurements is also included.

Sections 8 and 9 consist of data acquired through the vehicle's onboard data telemetry system, which is described in Appendix C. The following aspects are examined for each motor connection in these sections:

Electrical performance characteristics

Vertical force characteristic

Distributed (pole-by-pole) parameters

Eddy current braking characteristic (10 pole only)

AC EXCITATION TESTS

All ac tests in these sections were run at a nominal excitation frequency of 94.3 $\pm$1 Hz. Data was either normalized to 1400 A (constant current condition) or 0.346 V/Hz/pole (constant voltage condition). To determine the effect of saturation in the normalizing process, tests were run at different excitation levels. All applicable data points acquired during ac tests are identified because they have passed exacting qualifying criteria and are suitable for analysis and presentation.

DC EXCITATION TESTS

Data acquired during dc excitation tests did not require computer processing for selected data. Data is presented in two ways:

- Variation of motor forces with speed (constant current, normalized)

- Variation of motor forces with excitation current (zero speed)

Section 10 consists mainly of oscillographic traces obtained via an FM tape recorder and played back through an oscillograph in the data van. Where necessary, the data is supported with onboard data synchronized by means of the track position sensor.

Only the test results essential for report continuity are included in Volume I. Complete plotted test data is included in Volume II for the benefit of other researchers.

SECTION 8

BASELINE REACTION RAIL TESTS

TEN-POLE DC EDDY CURRENT BRAKING TESTS

Data was acquired from runs 1042 and 1044 for evaluation of the eddy current braking characteristic. Except for the excitation current level, test conditions were identical for the two runs. Table 8-1 lists pertinent details.

TABLE 8-1

BRAKING TEST CONDITIONS

Run	Test Excitation Current, (I_{TEST}), kA	Normalizing Current, (I_{NORM}), kA	Normalizing Ratio (RATI = I_{TEST}/I_{NORM})
1042	1.23	1.71	0.72
1044	1.71	1.71	1.00

Figure 8-1 shows the braking characteristic of the 10-pole SLIM (run 1042) at a test excitation current of 1.23 kA, normalized to 1.71 kA. It should be emphasized that dc eddy current braking test results shown in graphical form have been normalized to a common excitation level to facilitate comparison. The excitation level shown on each graph is the normalizing current. Figure 8-2 shows the braking characteristic of the 10-pole SLIM (run 1044) at a test excitation current of 1.71 kA. Figures 8-3 and 8-4 show the vertical force characteristic as a function of vehicle speed at the same two excitation levels. Table 8-2 provides summarized data on the effects of saturation on braking force and vertical force.

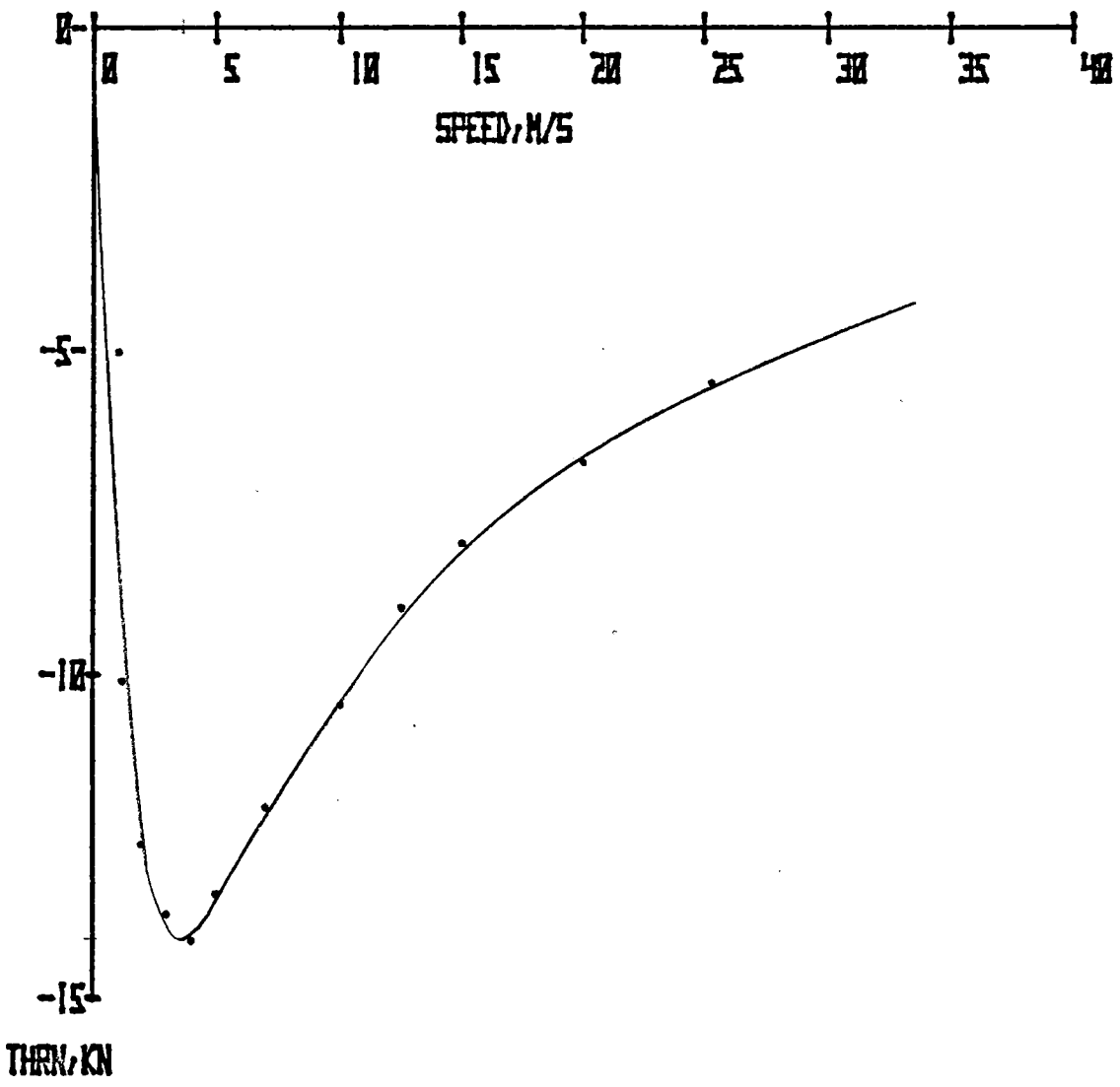

Figure 8-1. Braking Force vs Speed, 10-Pole SLIM, Run 1042

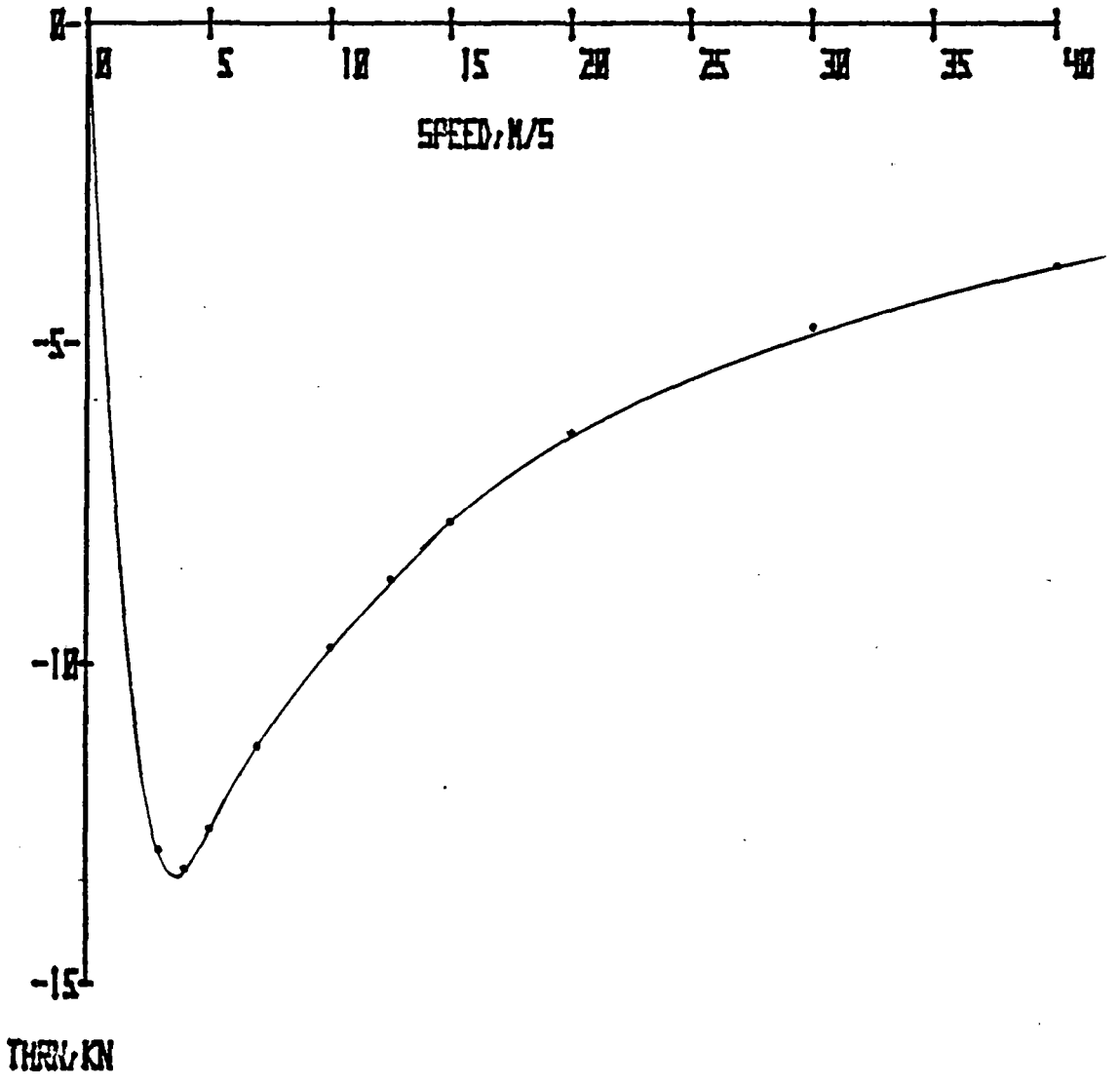

Figure 8-2. Braking Force vs Speed, 10-Pole SLIM, Run 1044

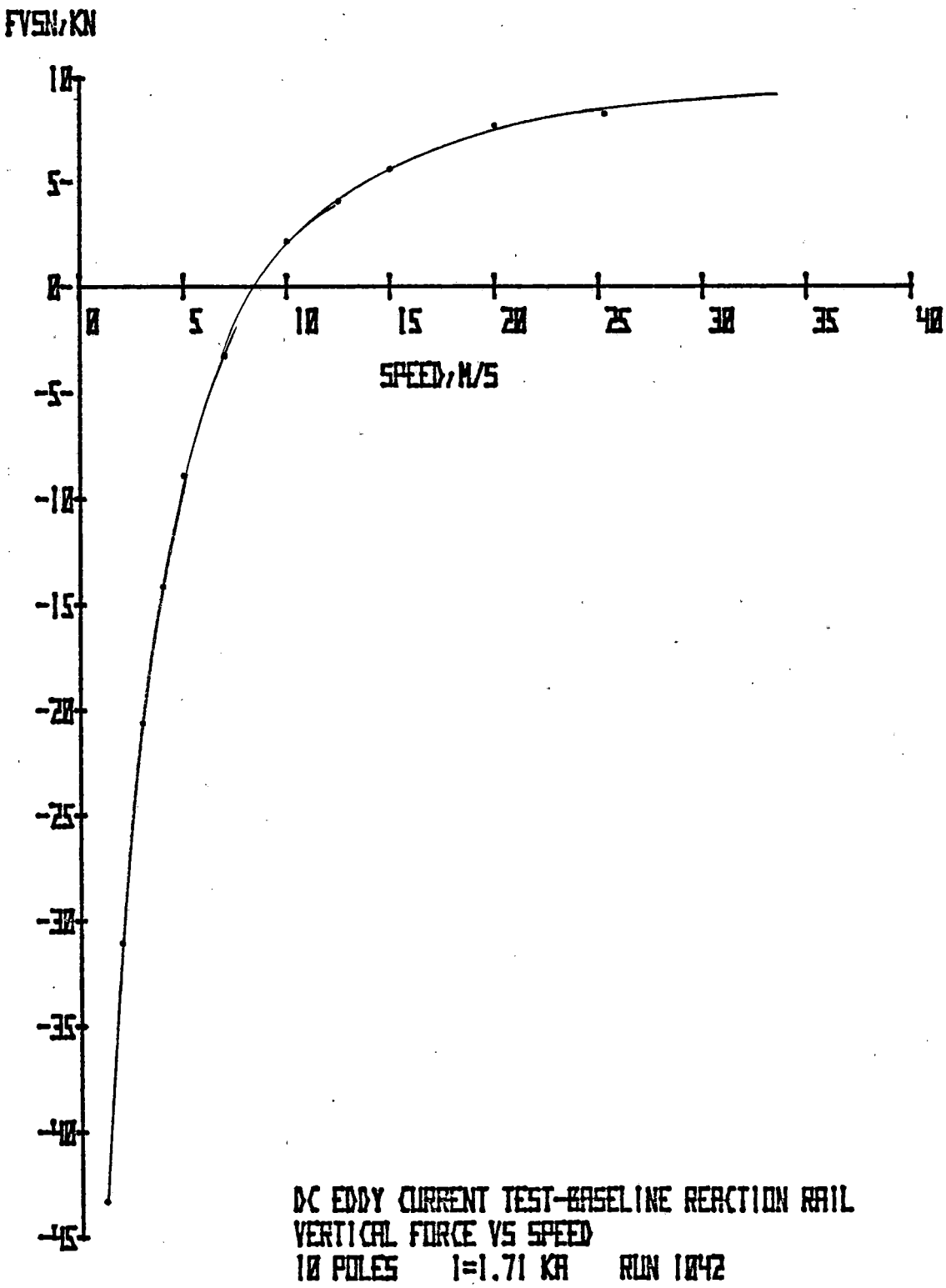

Figure 8-3. Vertical Force vs Speed, 10-Pole SLIM, Run 1042

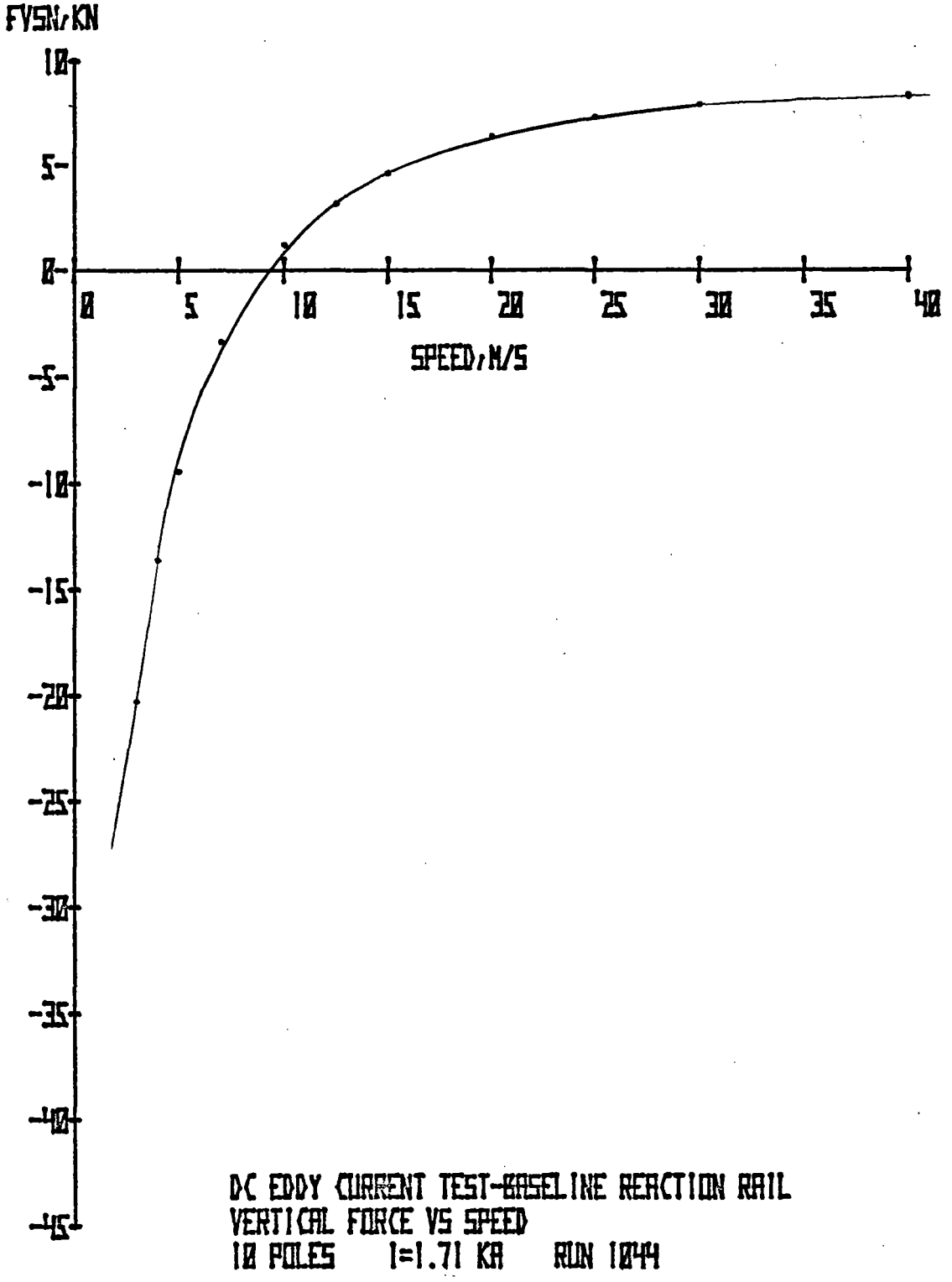

Figure 8-4. Vertical Force vs Speed, 10-Pole SLIM, Run 1044

TABLE 8-2

SATURATION EFFECTS

Run	RATI	Speed, m/s	Peak Braking Force Normalized* to 1.71 kA, kN	Speed at Which Vertical Force Equals Zero, m/s	Normalized Vertical Force at 30 m/s, (Positive)
1042	0.72	3.5	-14.1	8.0	+9.0
1044	1.0	3.5	-13.4	9.2	+7.7

* Forces are normalized according to the relation $F_{NORM} = F_{TEST}/(RATI)^2$.

The data tabulated above gives rise to the following observations:

- Peak thrust and vertical force show significant saturation, and the effect on vertical forces appears to be more noticeable at higher speeds.
- The peak thrust point is unaffected by saturation.
- Vertical force crossover (that is, the speed at which vertical force changes from attraction to repulsion) is dependent upon excitation level.

ELECTRICAL PERFORMANCE TESTS

Thrust vs Slip

Figures 8-5 and 8-6 show the variation of thrust with slip for the motor in its 10-pole and 5-pole leading (5-pole L) configurations, respectively. Thrust measurements here were normalized to a 1400-A excitation level. Thrust of the motor in the 5-pole trailing (5-pole T) configuration is essentially the same as that in the 5-pole L configuration, and is shown in Volume II.

Figure 8-7 shows the 10-pole motor thrust characteristic when the same data noted in Figure 8-5 is normalized to 0.346 V/Hz/pole.

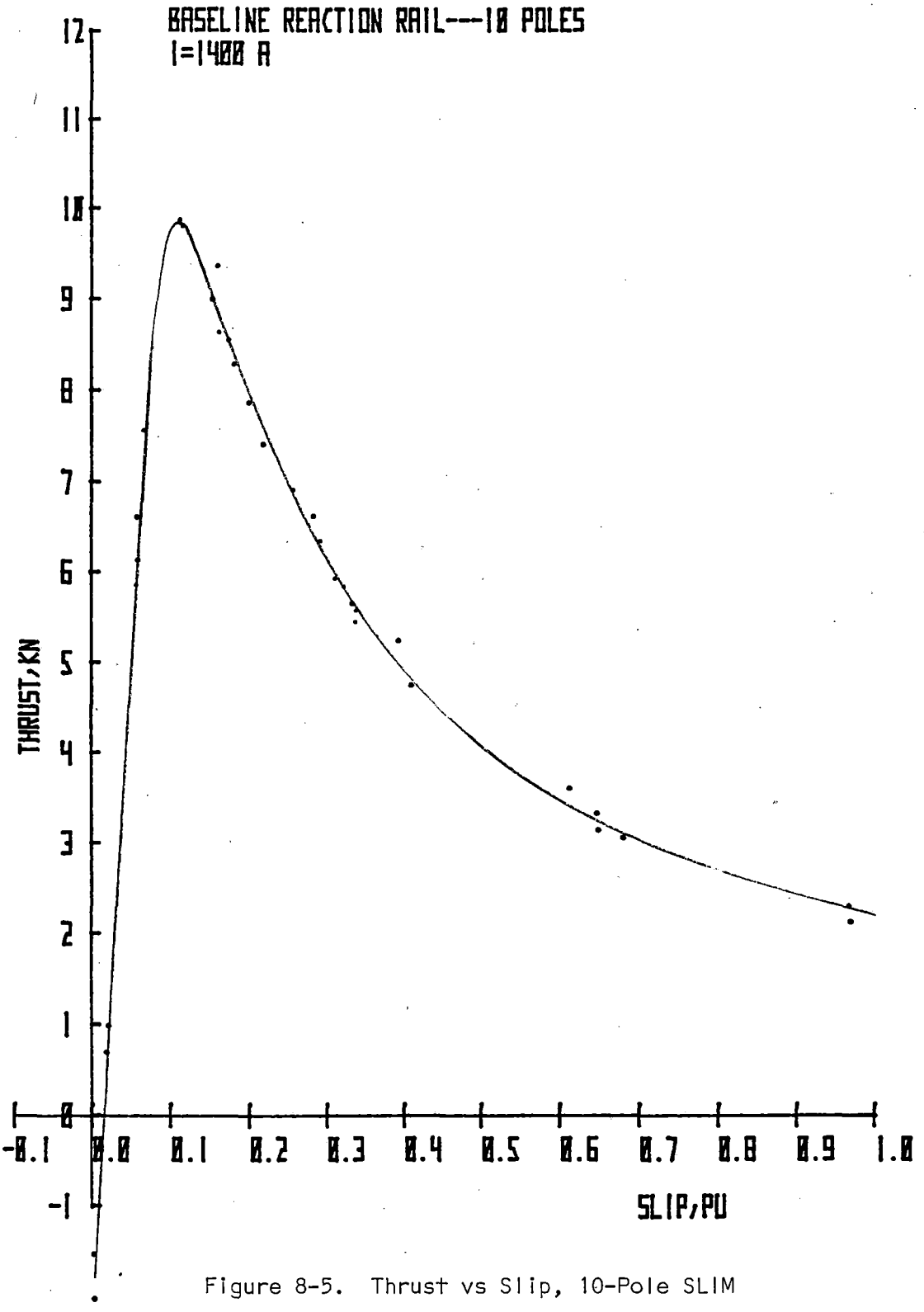

Figure 8-5. Thrust vs Slip, 10-Pole SLIM

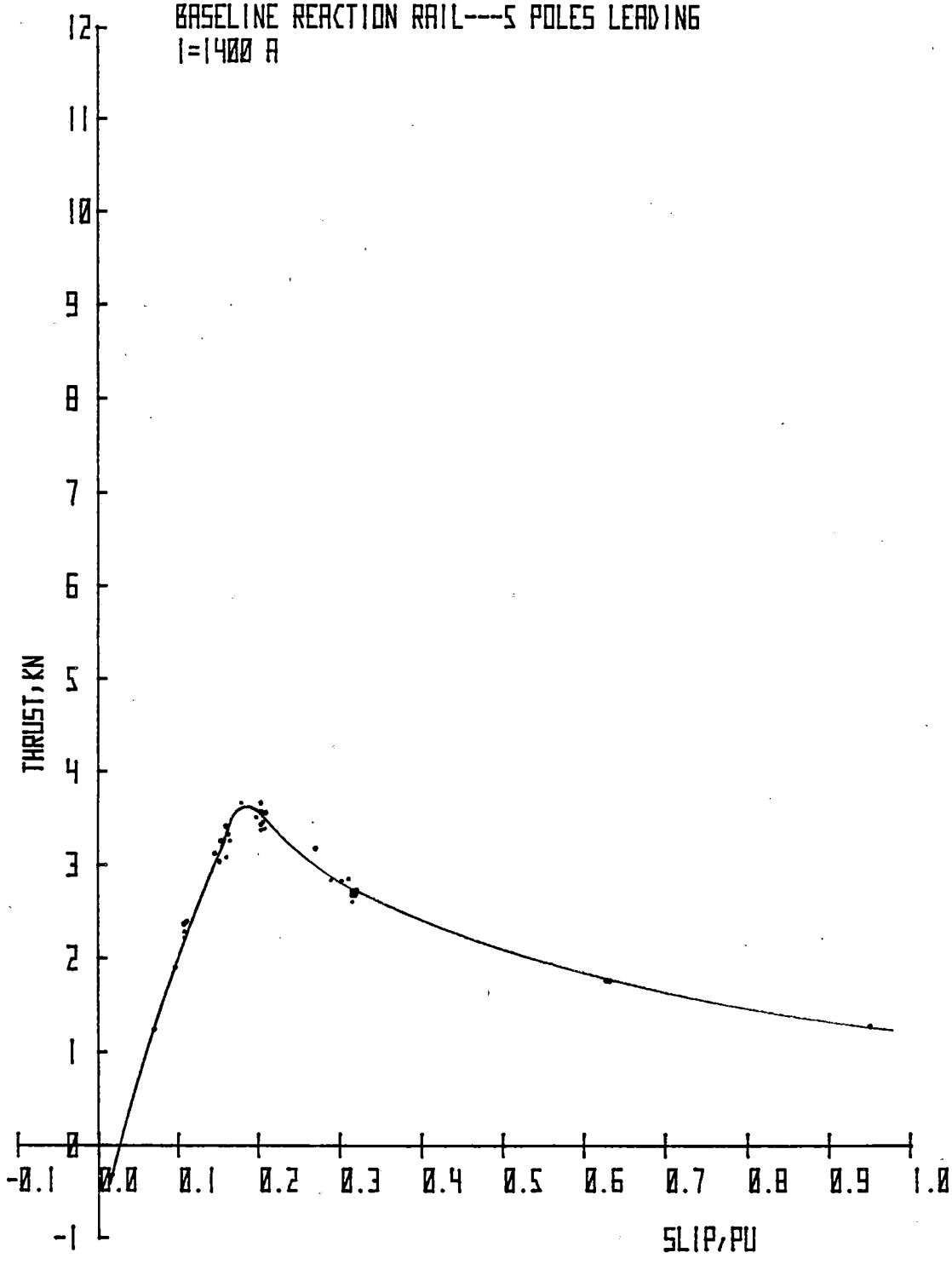

Figure 8-6. Thrust vs Slip, 5-Pole Leading SLIM

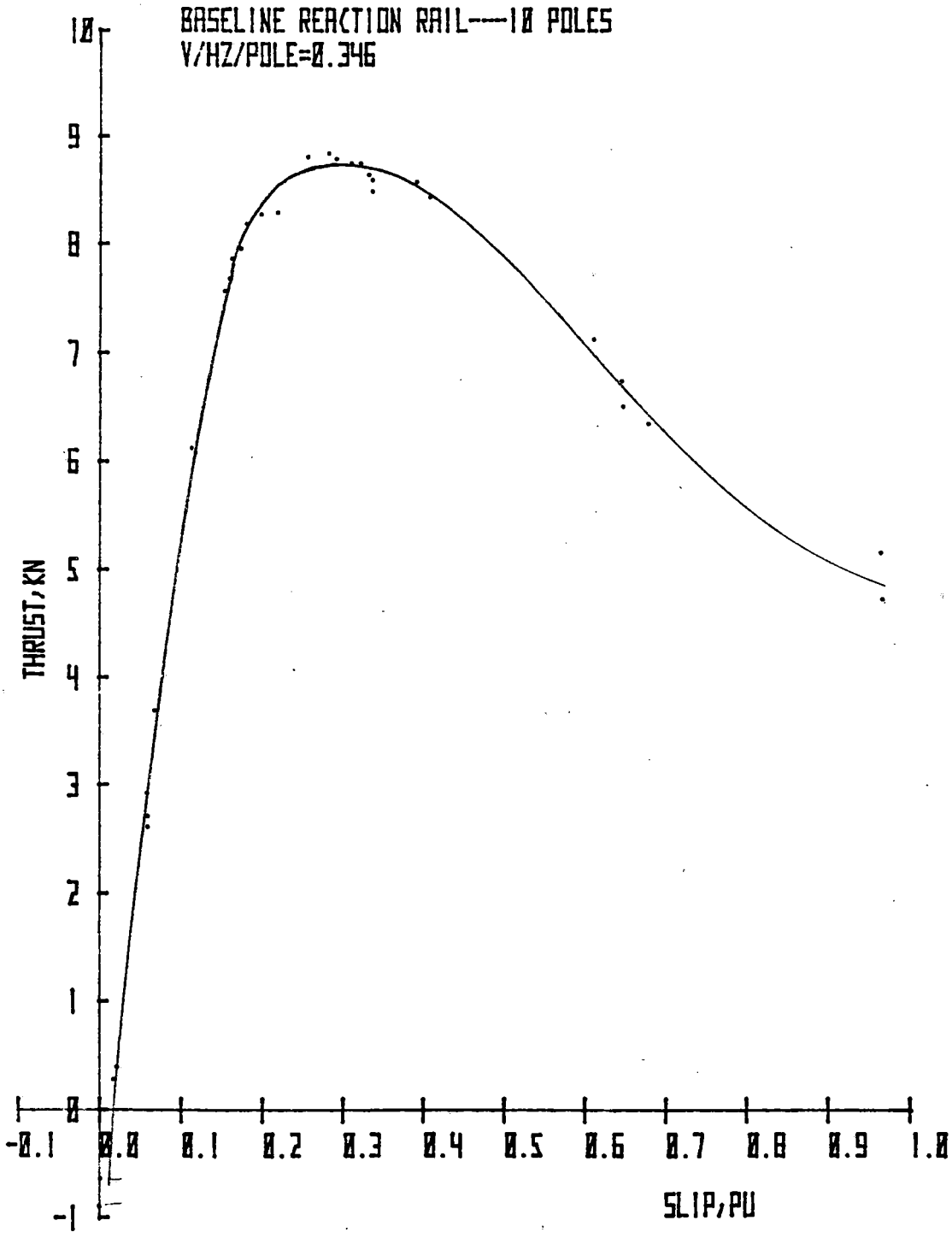

Figure 8-7. Thrust vs Slip, 10-Pole SLIM, 0.346 V/Hz/Pole

Current vs Slip

Figures 8-8 and 8-9 show the variation of primary current with slip for the 10-pole and 5-pole L configurations, respectively, with the data normalized to 0.346 V/Hz/pole. It is evident that the effect of reduced motor length (increased end effect) is manifested by increased magnetizing current for the same average voltage per pole at low slip values. It follows that a greater proportion of the active pole length is affected in the shorter configuration.

The value of primary current at zero slip normally represents only the magnetizing component for a rotary machine. The value of primary current at zero slip, however, includes a contribution from end effect, and may usefully be applied to quantify end effect for different linear motor configurations. This point will be discussed later when all motor configurations are examined.

Figures 8-10 and 8-11 depict the real and imaginary components for current in the 10-pole and 5-pole L configurations, respectively, as primary current locus diagrams. Comparison of these diagrams reveals that reduced active pole length increases the reactive (magnetizing) component of primary current when the voltage per pole is normalized to a constant value. The real component is essentially unaffected by end effect.

Mean Voltage vs Slip

Figures 8-12 and 8-13 show the corresponding variation of primary voltage with slip when the data is normalized to 1400 A. Table 8-3 lists primary voltage per pole at selected values of slip for the 10-pole and 5-pole L configurations.

The obvious trend is that voltage per pole remains independent of end effect at high slip values. Data from 5-pole T tests did not differ significantly from the 5-pole L test data cited above.

Efficiency and Power Factor vs Slip

Figures 8-14 and 8-15 show efficiency vs slip test data for the 10-pole and 5-pole L SLIM configurations, respectively. It can be seen that at slip values greater than 0.2, efficiency is apparently independent of pole configuration. This may be conveniently explained by reference to the equivalent circuit approach. Equivalent circuits do not define LIM performance precisely, but they do provide a useful technique for understanding complex LIM behavior.

At high slip values, no significant difference in performance is detectable between the 10-pole and 5-pole connections on a per-pole basis. The implication is that the equivalent circuit is determined by geometric arrangement of the electrical and magnetic circuit.

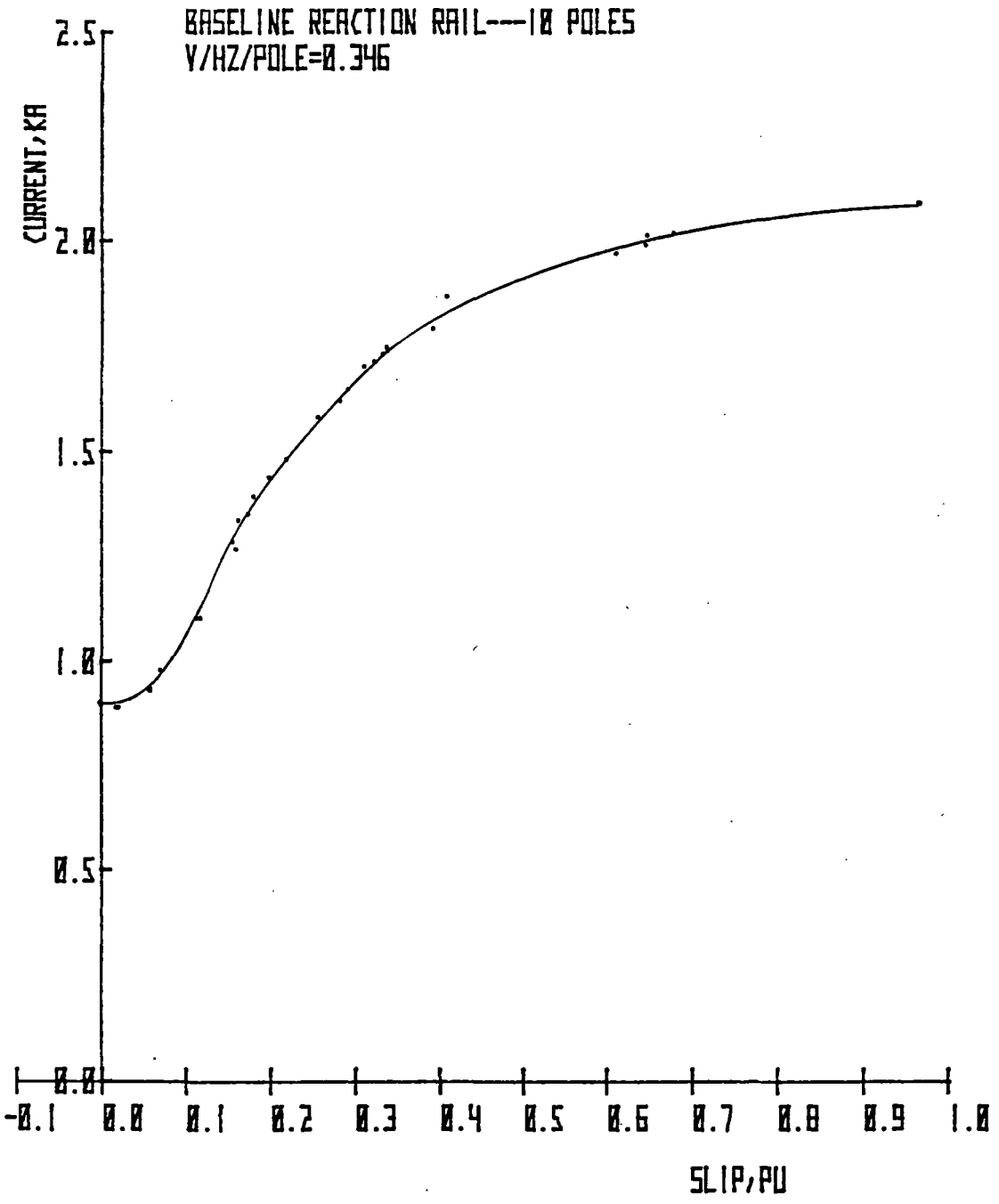

Figure 8-8. Mean Line Current vs Slip, 10-Pole SLIM.

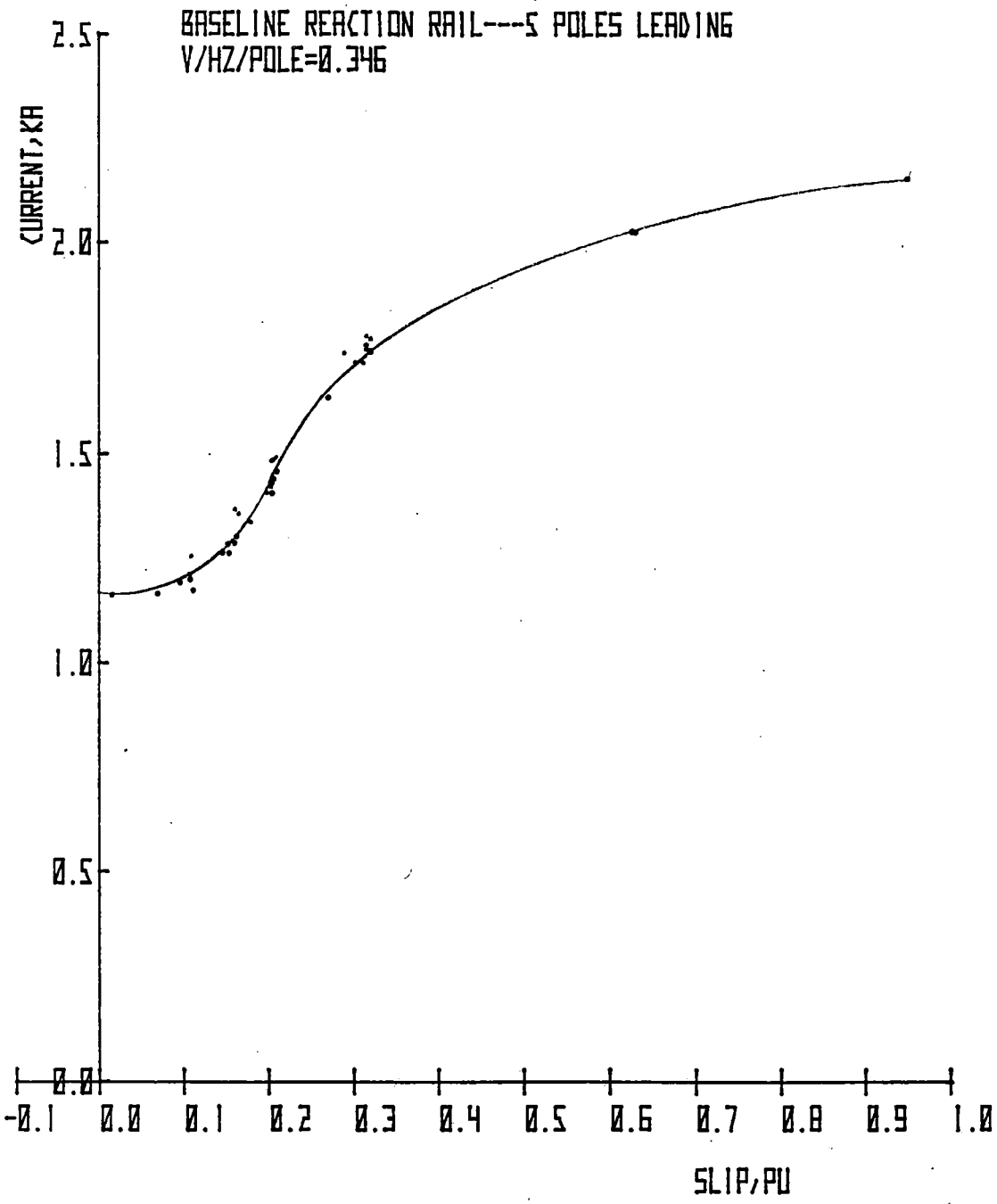

Figure 8-9. Mean Line Current vs Slip, 5-Pole (Leading) SLIM

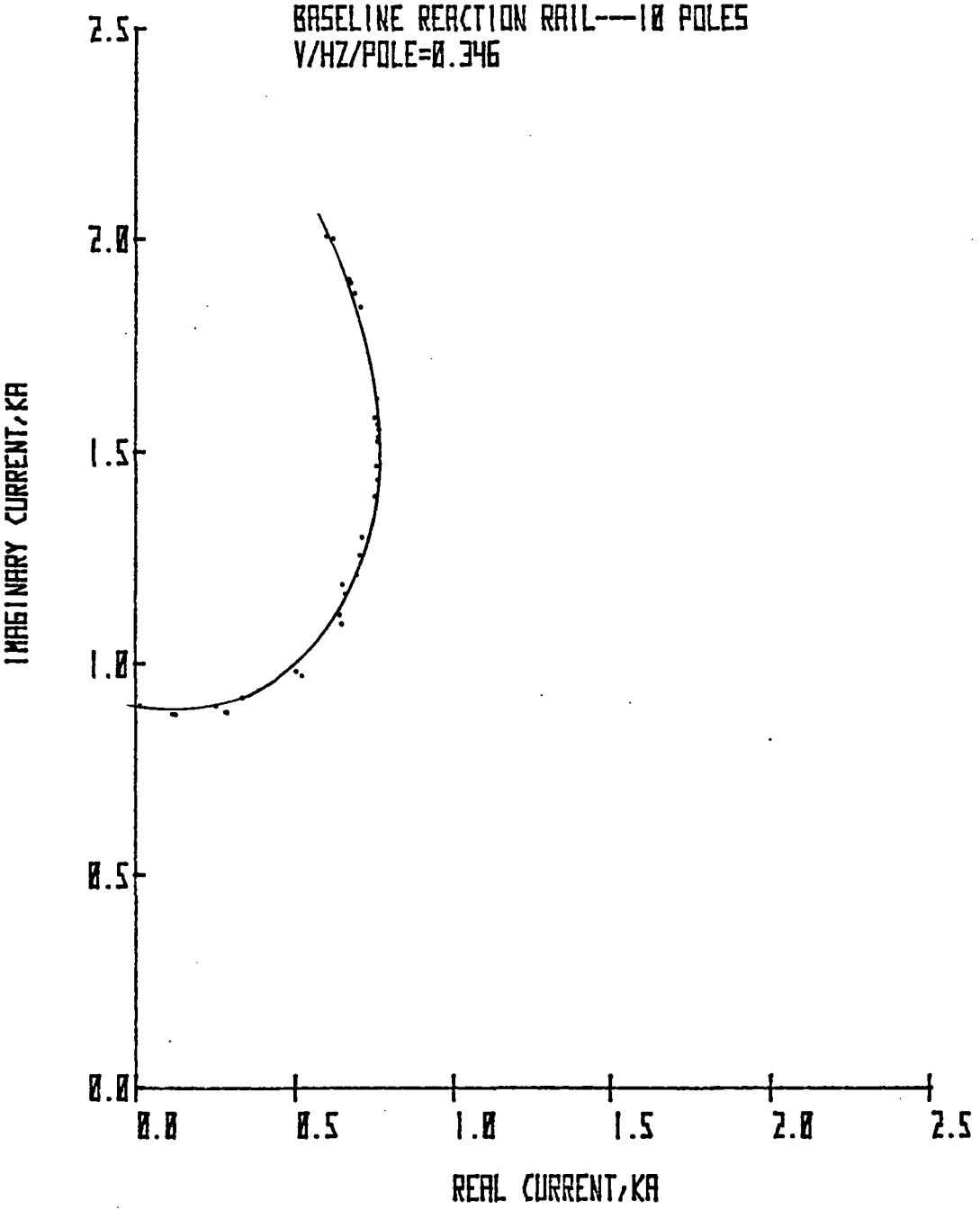

Figure 8-10. LIM Current Locus Diagram, 10-Pole SLIM.

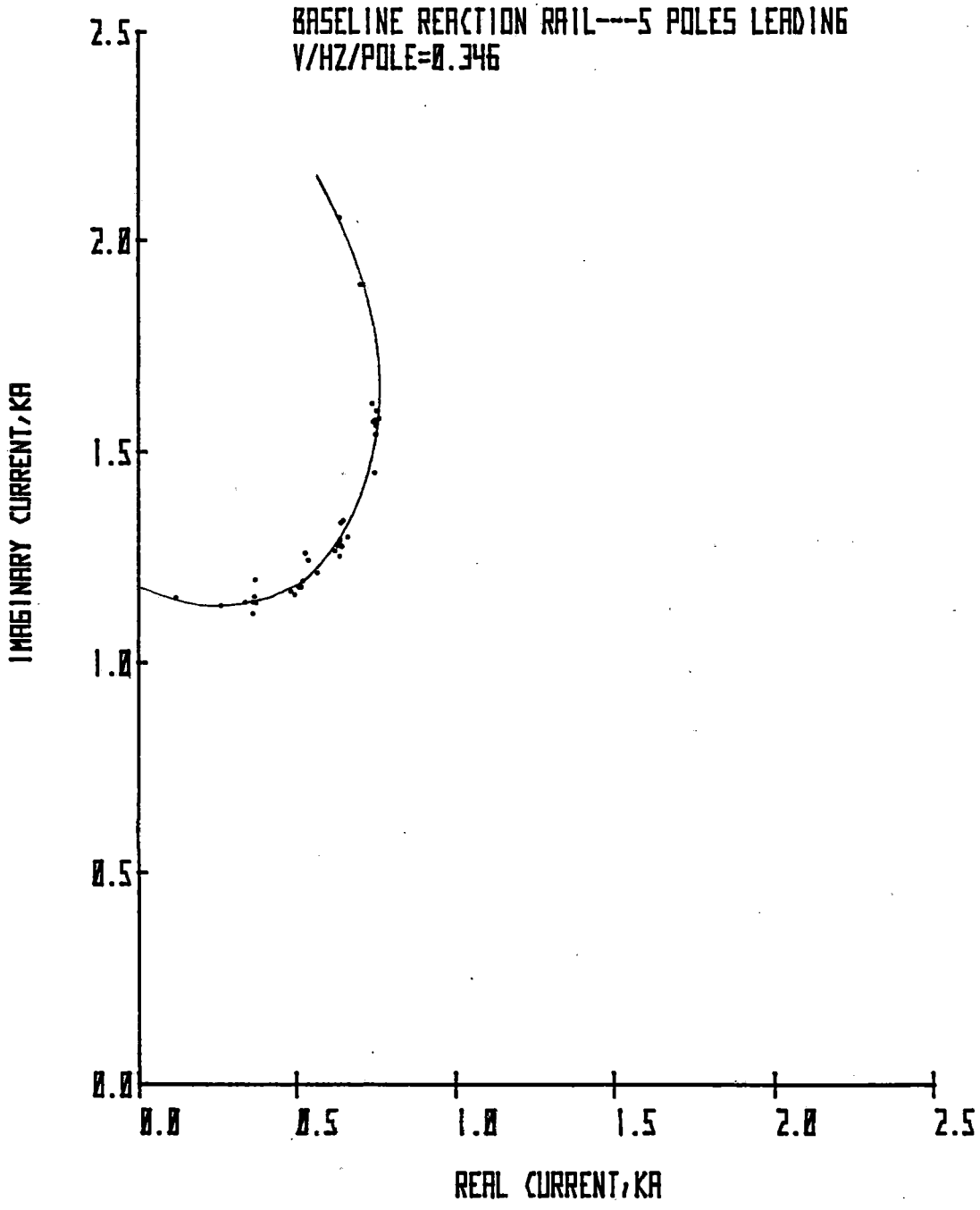

Figure 8-11. LIM Current Locus Diagram, 5-Pole (Leading) SLIM

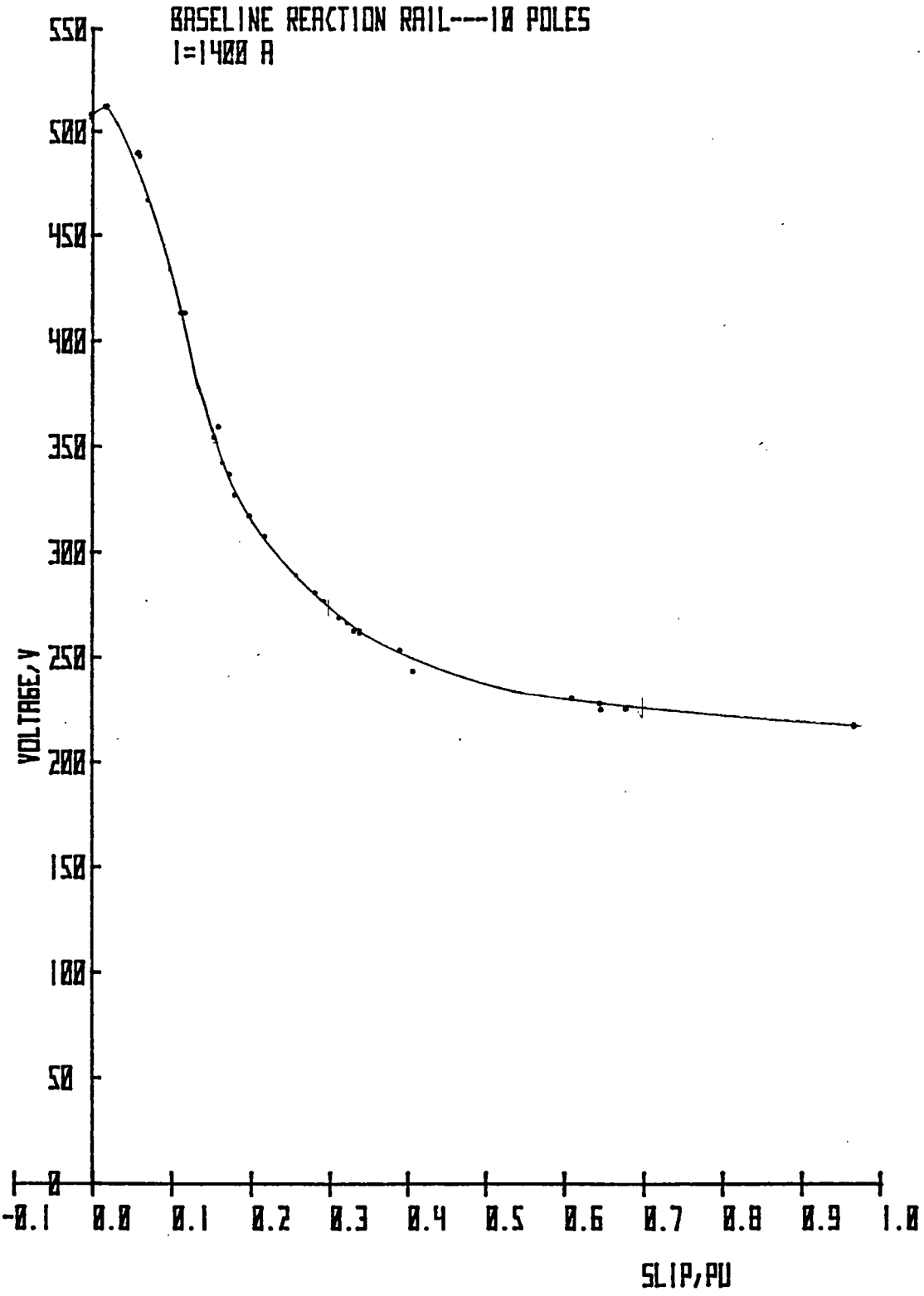

Figure 8-12. Mean Phase Voltage vs Slip, 10-Pole SLIM

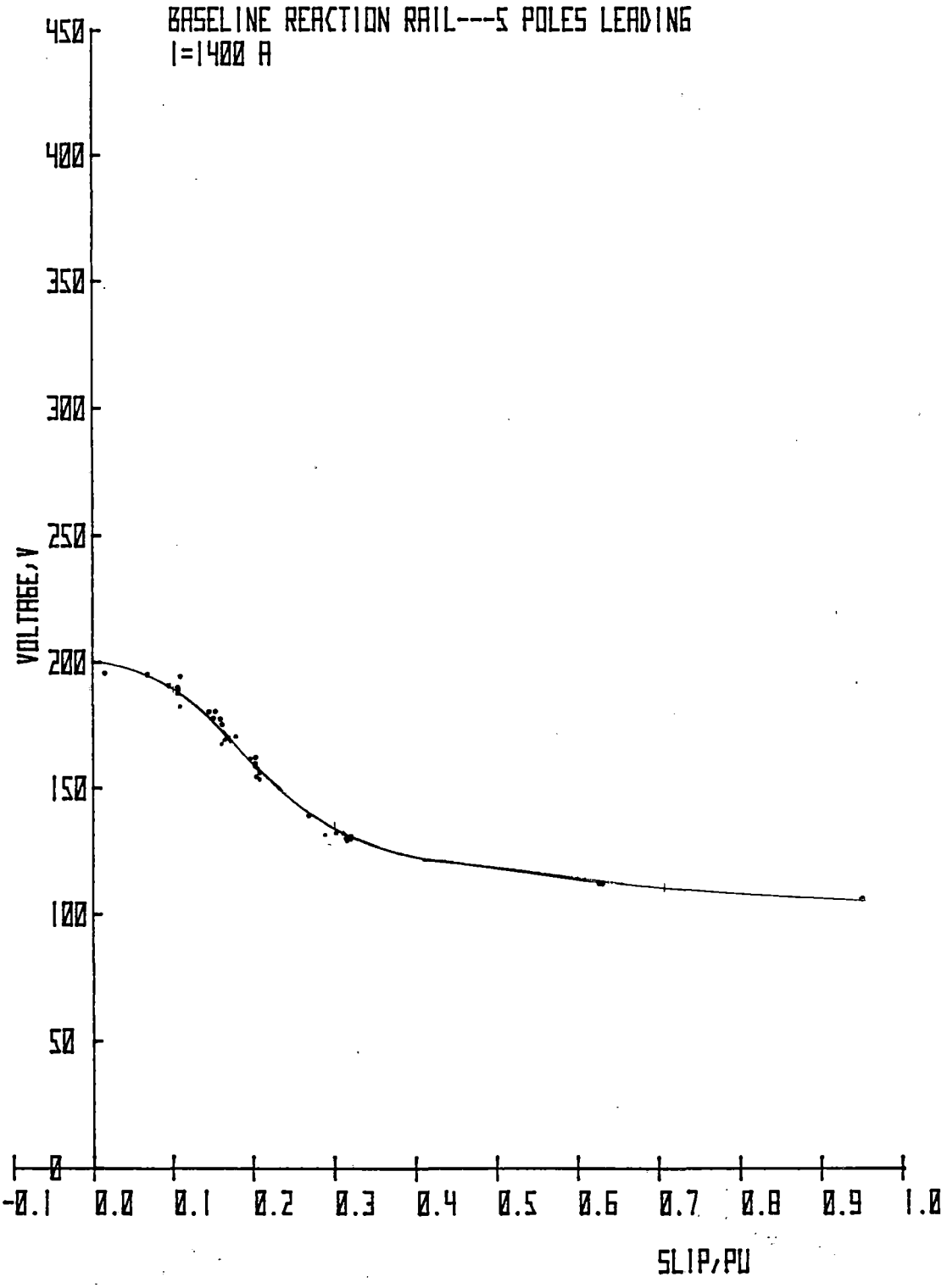

Figure 8-13. Mean Phase Voltage vs Slip, 5-Pole (Leading) SLIM

TABLE 8-3

PRIMARY VOLTAGE

Slip	Voltage per Pole, V	
	10-Pole SLIM	5-Pole L SLIM
0	51.0	40.0
0.1	43.4	37.0
0.3	27.5	25.6
0.7	22.5	22.4
1.0	22.0	21.0

At low slip values, however, end effect causes a greater loss of performance for the 5-pole connection than for the 10-pole version, and on a per-pole basis, the magnetizing reactance is lower. For a constant current condition, therefore, the secondary current is smaller, with lower consequent power for the 5-pole configuration.

Degraded efficiency is therefore seen in the 5-pole connection at lower slip values, since other losses are identical for both connections. Appendix H derives the equation for maximum efficiency based on an equivalent circuit approach.

Figures 8-16 and 8-17 show variations of power factor with slip for the 10-pole and 5-pole L SLIM configurations, respectively. Power factor for the 10-pole motor remains higher than that for the 5-pole motor at slip values less than 0.4.

The product of power factor and efficiency was computed for each data point, and the resultant curves plotted in Figures 8-18 and 8-19 for the 10- and 5-pole configurations, respectively. A significant difference is apparent over a large portion of the operating slip range. These curves are useful in quantifying the full extent of the penalty associated with reduction of the primary active length. Table 8-4 summarizes the graphed data.

TABLE 8-4

EFFICIENCY AND POWER FACTOR MAXIMUM VALUES

Configuration	Maximum Efficiency, Percent	Maximum Power Factor, Percent	Maximum Value of Efficiency x Power Factor, Per Unit
10-pole	73.5 at 0.105 slip	48.7 at 0.15 slip	0.35 at 0.13 slip
5-pole	66.3 at 0.185 slip	46.0 at 0.225 slip	0.285 at 0.2 slip

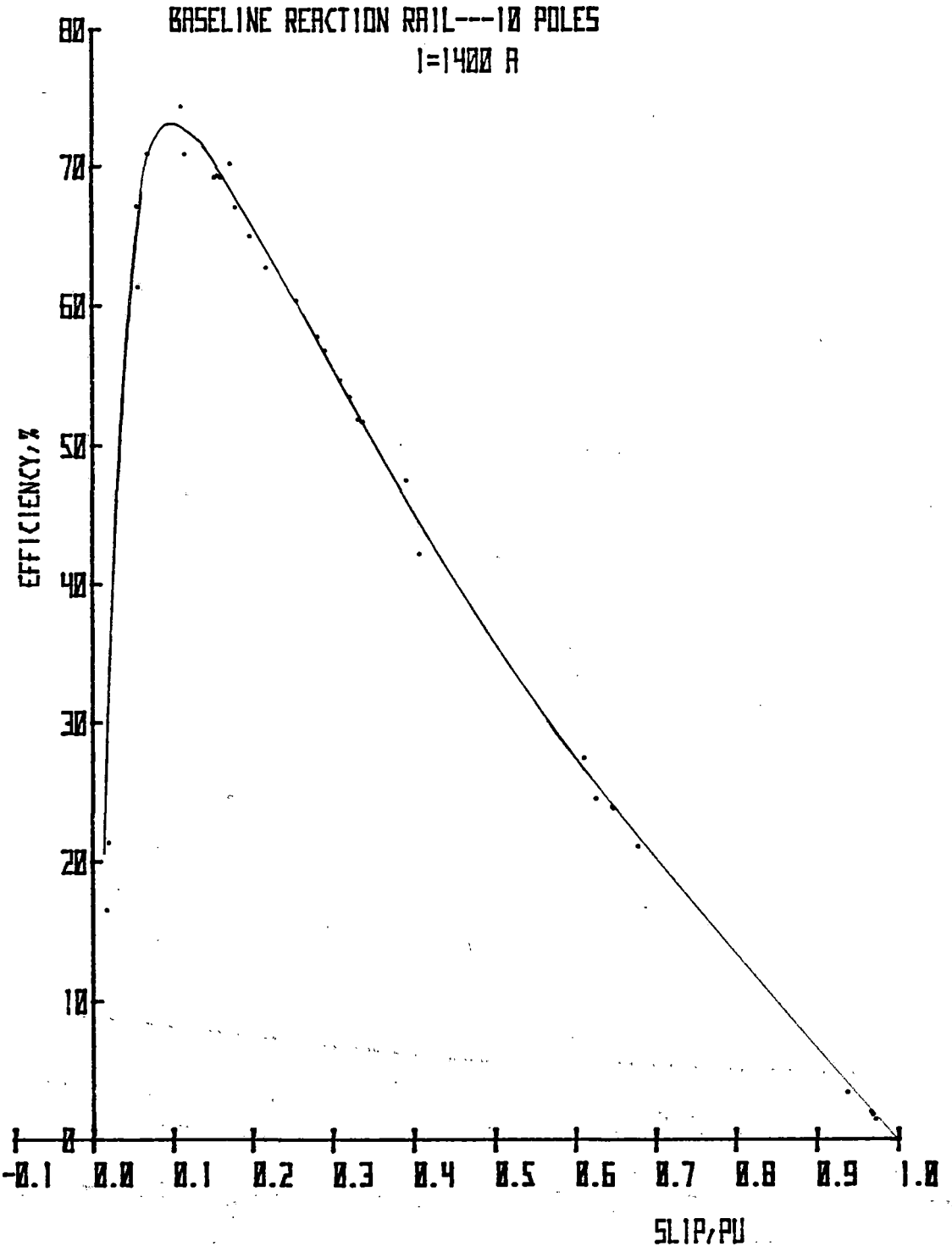

Figure 8-14. Efficiency vs Slip, 10-Pole SLIM

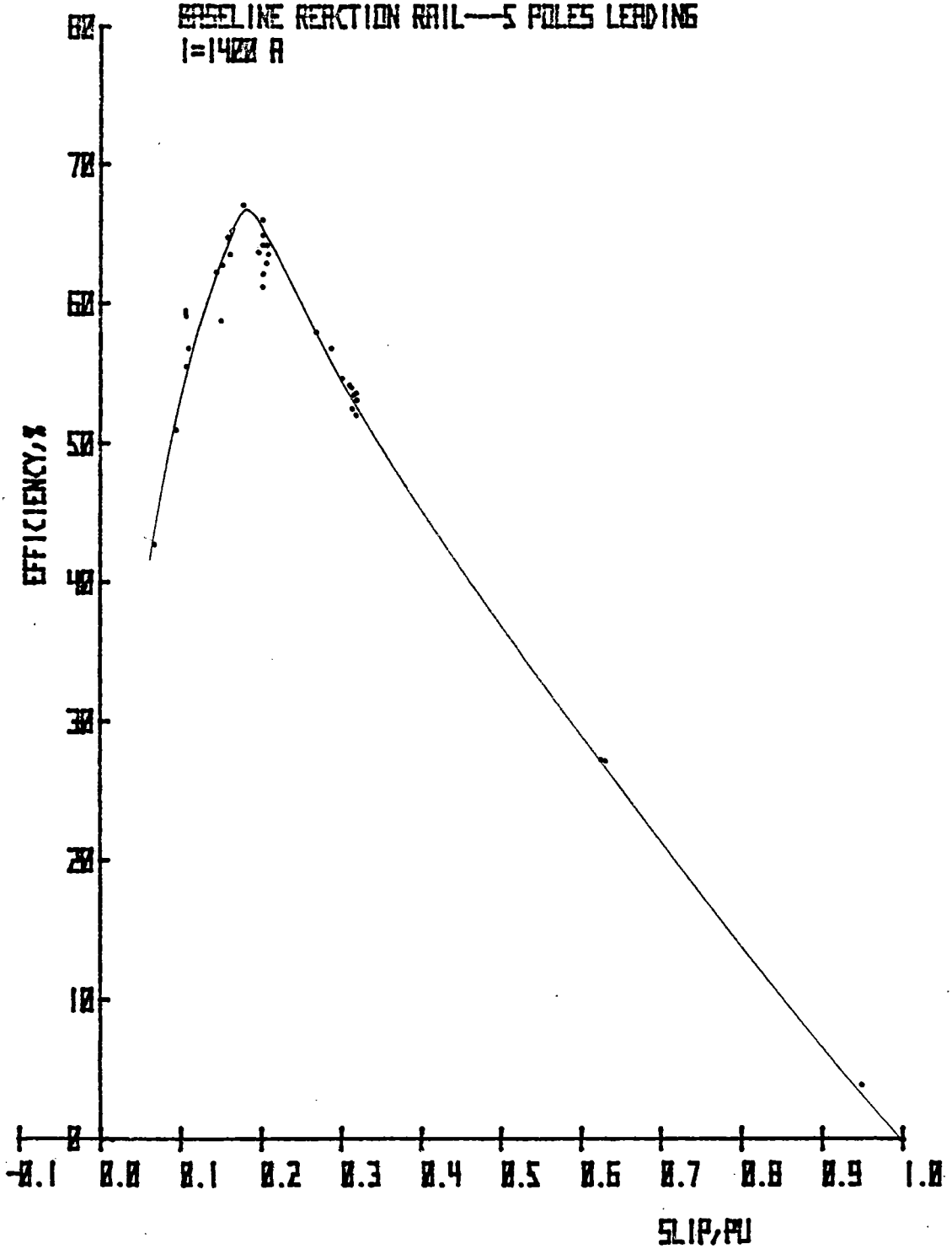

Figure 8-15. Efficiency vs Slip, 5-Pole (Leading) SLIM

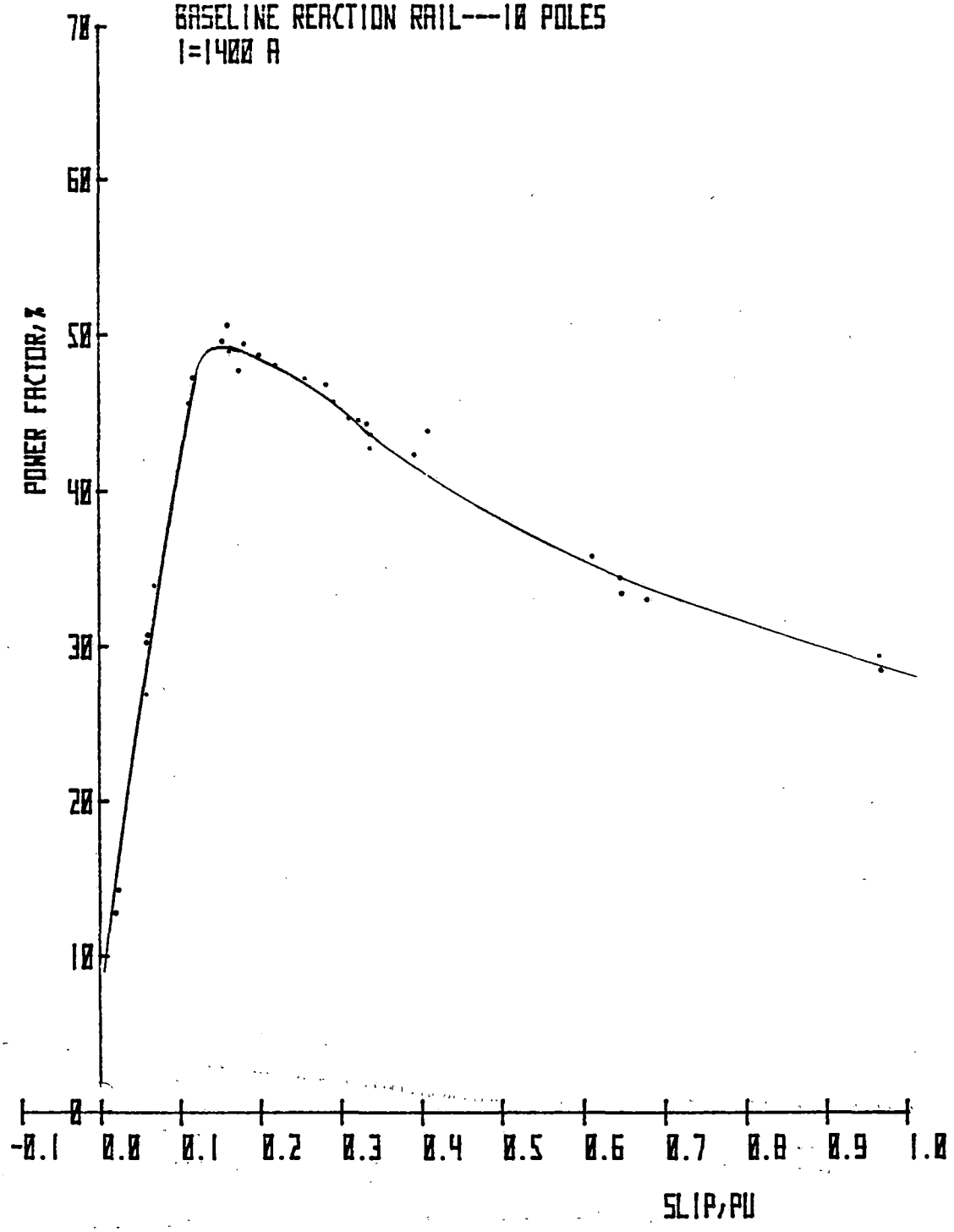

Figure 8-16. Power Factor vs Slip, 10-Pole SLIM

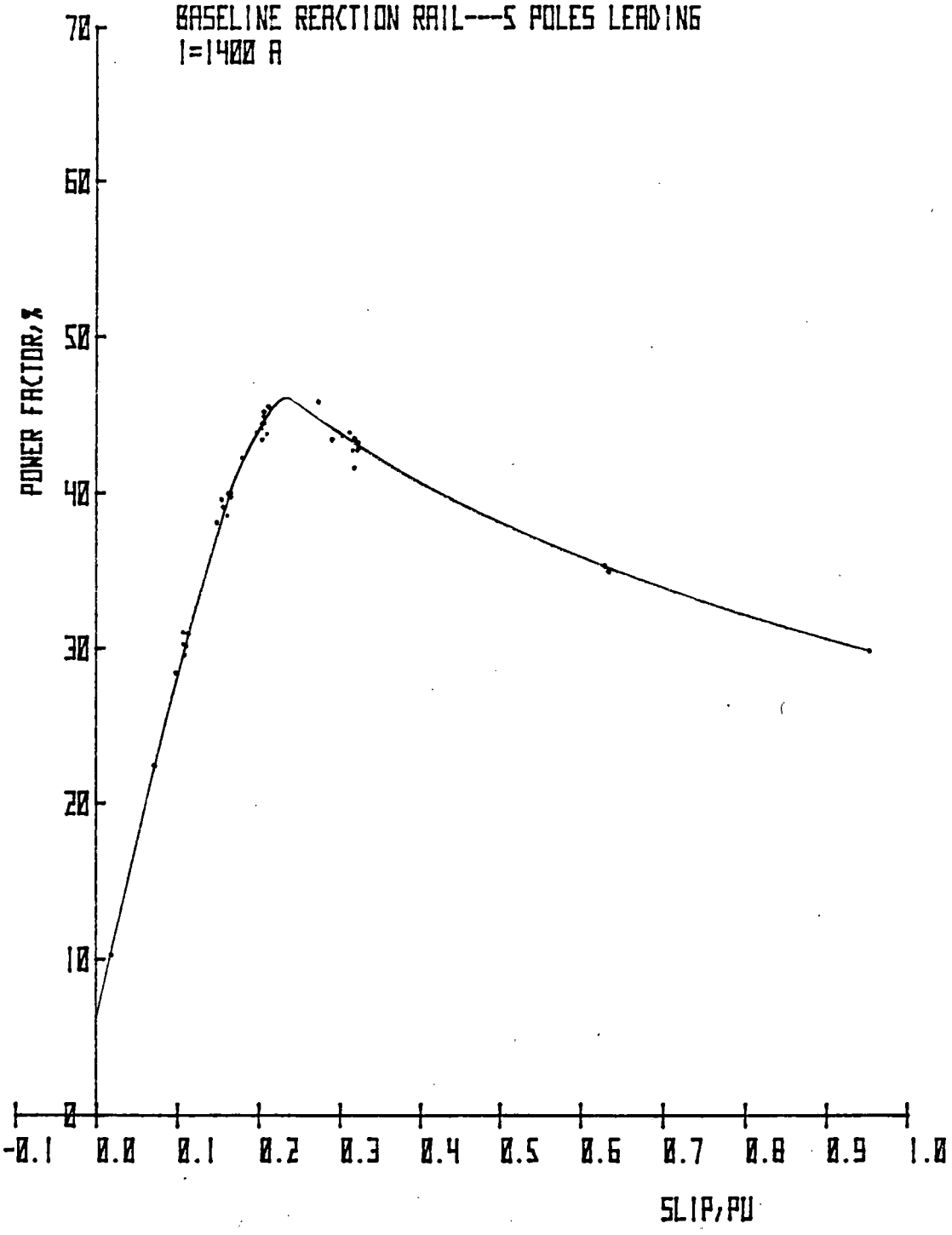

Figure 8-17. Power Factor vs Slip, 5-Pole (Leading) SLIM

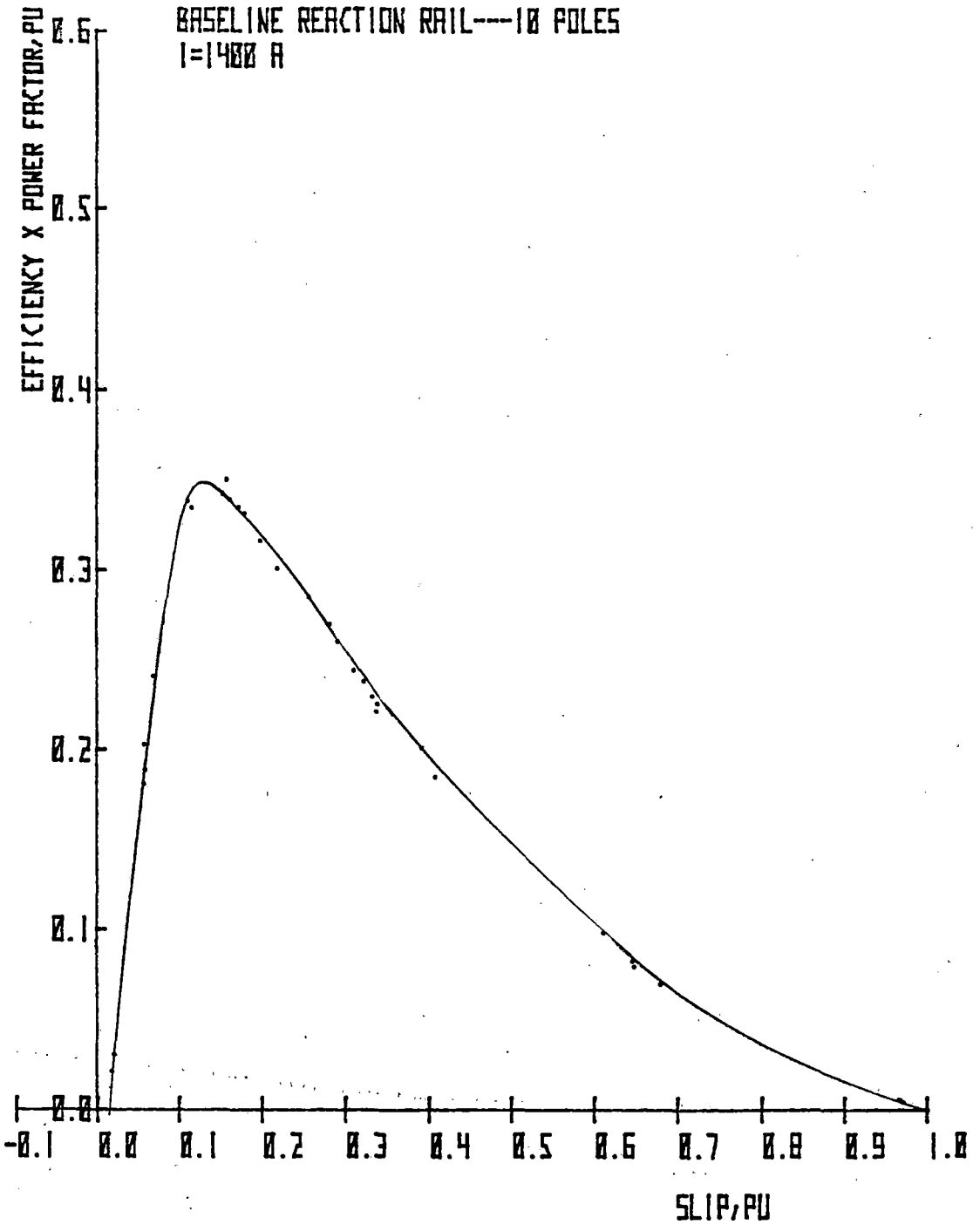

Figure 8-18. Efficiency x Power Factor vs Slip, 10-Pole SLIM

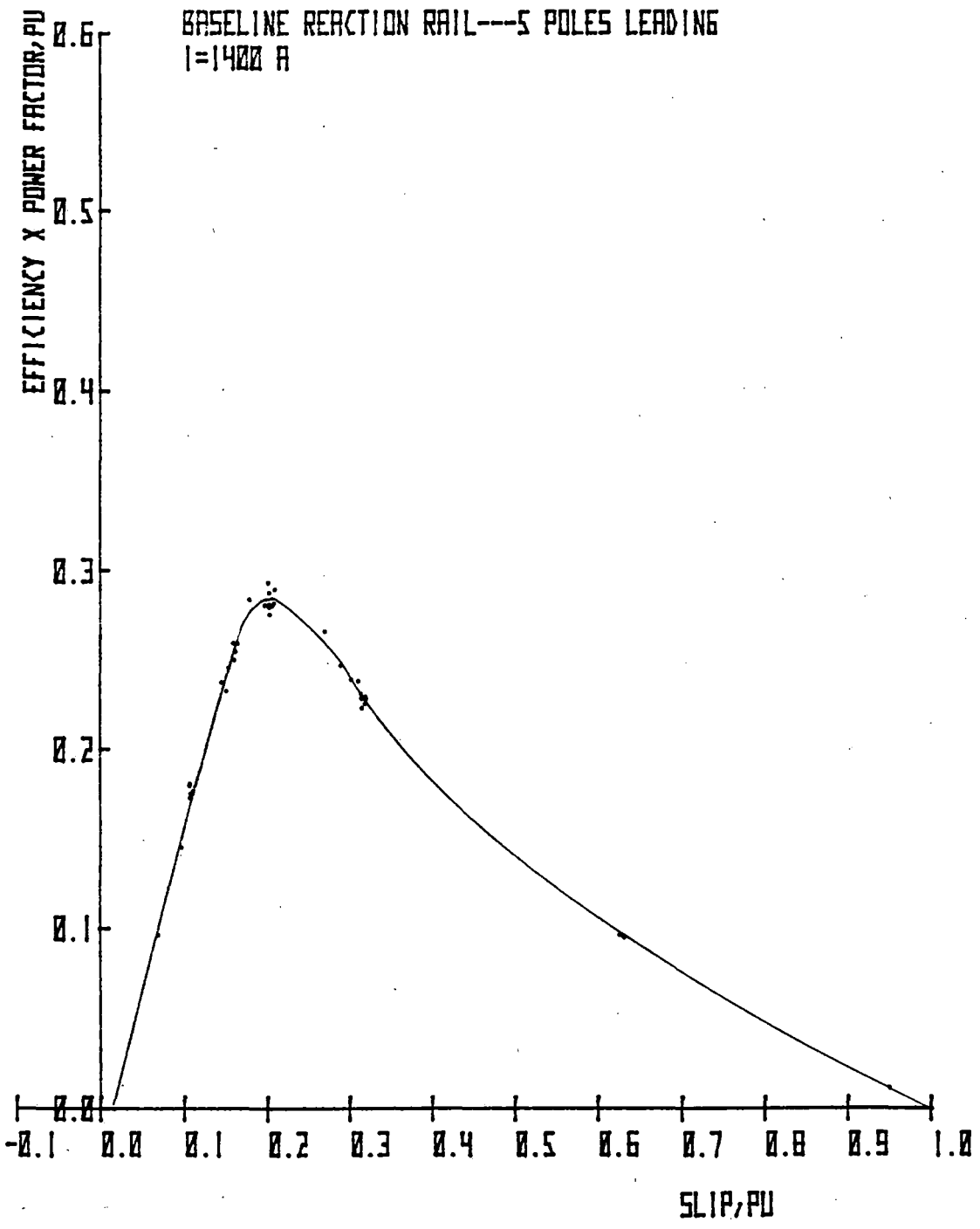

Figure 8-19. Efficiency x Power Factor vs Slip, 5-Pole (Leading) SLIM

Incremental Power Loss Due to End Effect

Simplified rotary induction motor theory defines power loss in the machine as:

$$P_L = 3I_1^2R_1 + W_{Fe} + P_{AG}S$$

where $3I_1^2R_1$ = primary conductor loss (A primary resistance value, R1, of 0.0122 ohm was used, which includes the measured dc winding resistance per phase of 0.01 ohm, and a factor to account for incremental ac losses.)

W_{Fe} = iron core loss

$P_{AG}S$ = airgap power and slip product (secondary loss)

Assuming a mean V/Hz = 3.46 for the motor in its 10-pole configuration, the iron core loss is estimated at 4 W/Kg.

The estimated primary iron mass is 666 kg. The total core loss is therefore 2.6 kW (10-pole configuration). This loss is approximately reduced pro rata for reduced pole excitations. This loss was found to be negligible in the calculation of P_L.

In this case:

$$P_{AG} = P_{IN} - 3I_1^2R_1$$

whence $P_{L(IDEAL)} = 3I_S^2R_1 (1 - S) + P_{IN}S$

This equation for power loss does not include contributions from end effects at the entry and exit edges of the motor primary.

The measured power loss (defined as $P_{MEAS} = P_{IN}$ - THRUST x VELOCITY) may be compared with ideal (rotary equivalent) power loss, and these points were computed for each data point and plotted in Figures 8-20 and 8-21.

VERTICAL FORCE CHARACTERISTICS

Figures 8-22 and 8-23 show the variation of total vertical force* vs slip for the motor in its 10-pole and 5-pole T configurations.

The 5-pole L configuration differs significantly from its 5-pole T counterpart. For purposes of comparison, the 5-pole T data will be shown here, as the presence of flux beyond the exit edge in the 5-pole L configuration leads to a nontypical force distribution. Comparative 5-pole data is shown later in this section.

* -ve force indicates attractive force between primary and secondary.

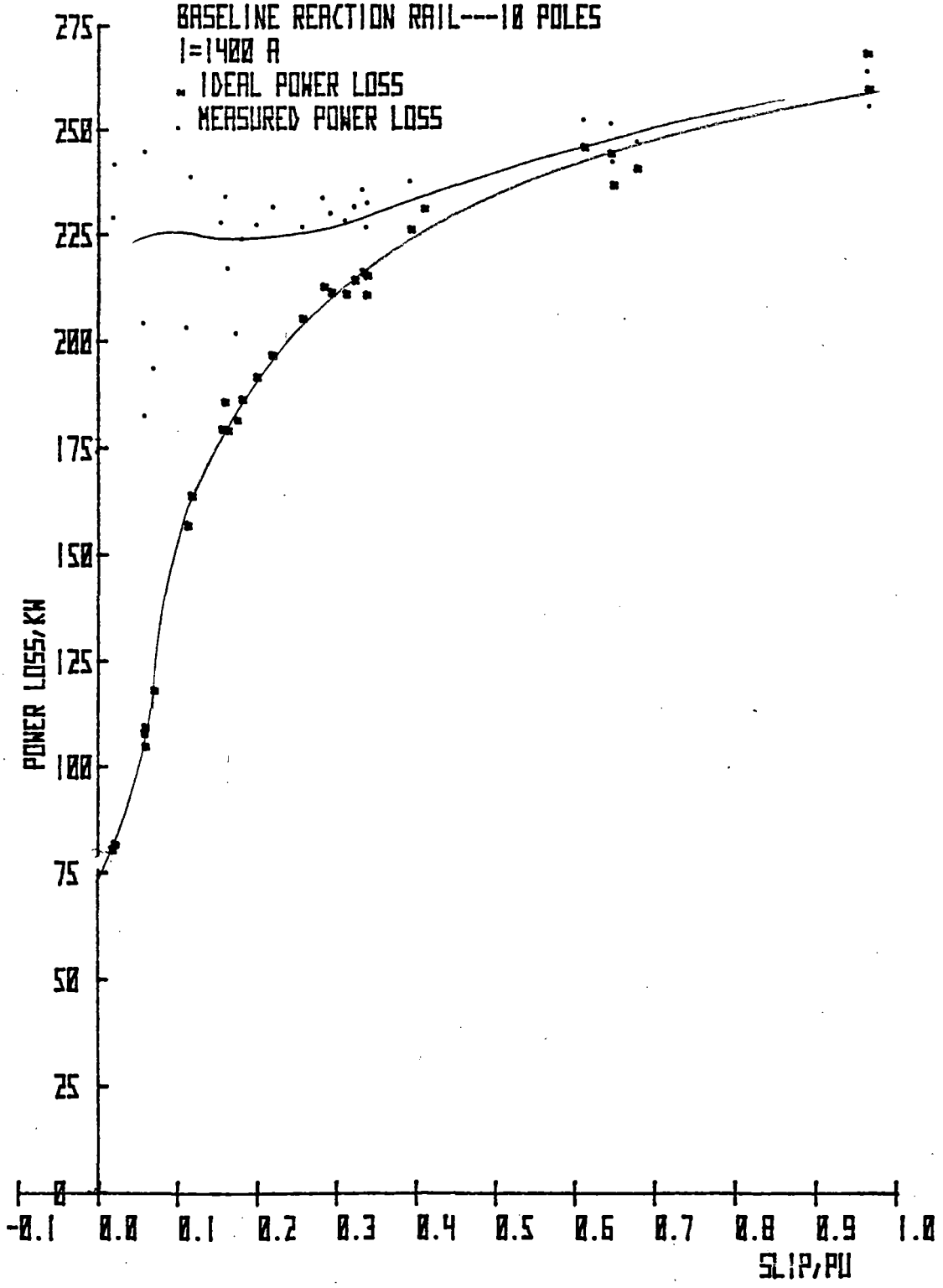

Figure 8-20. Ideal and Measured Power Loss vs Slip, 10-Pole SLIM

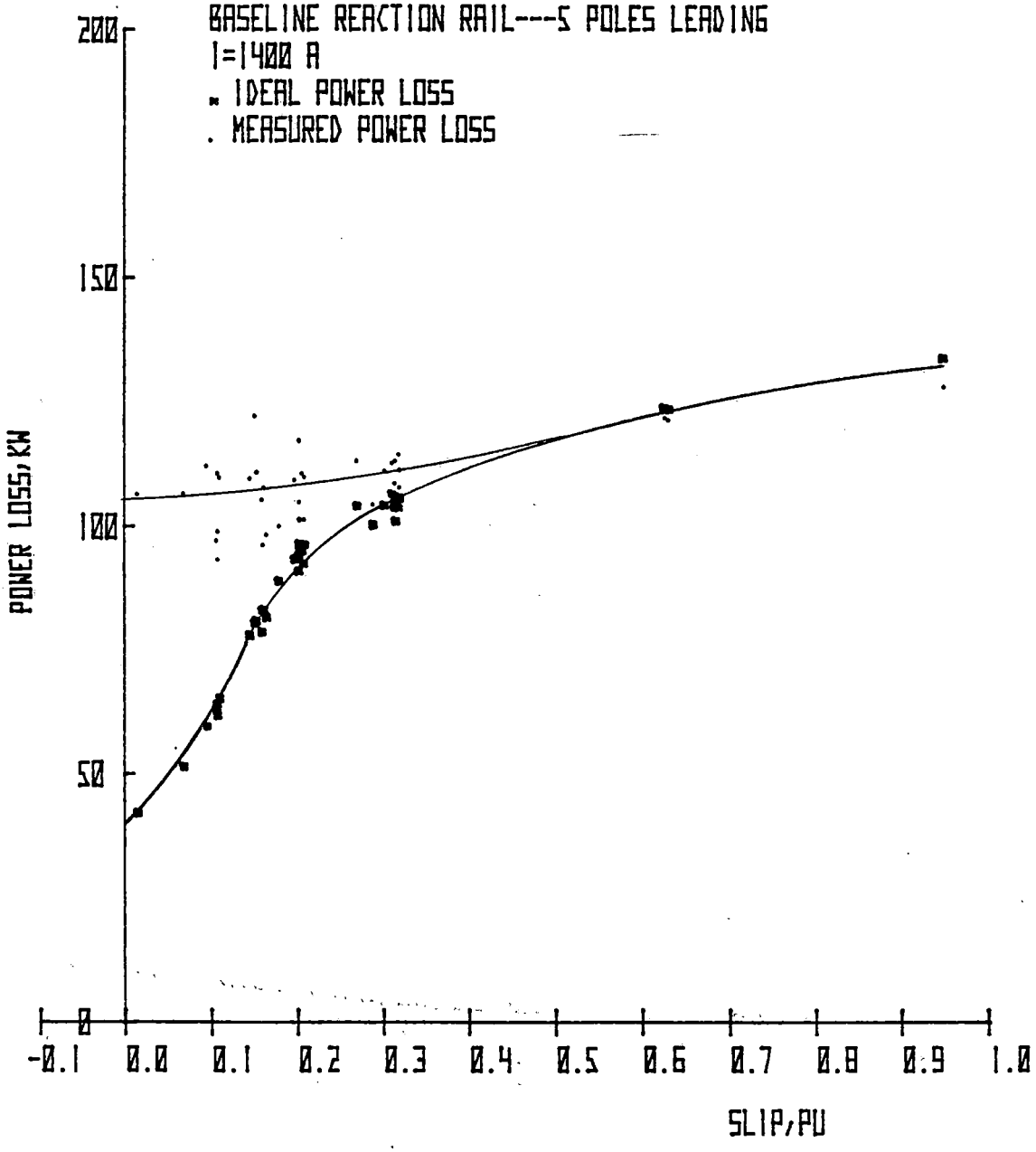

Figure 8-21. Ideal and Measured Power Loss vs Slip, 5-Pole (Leading) SLIM

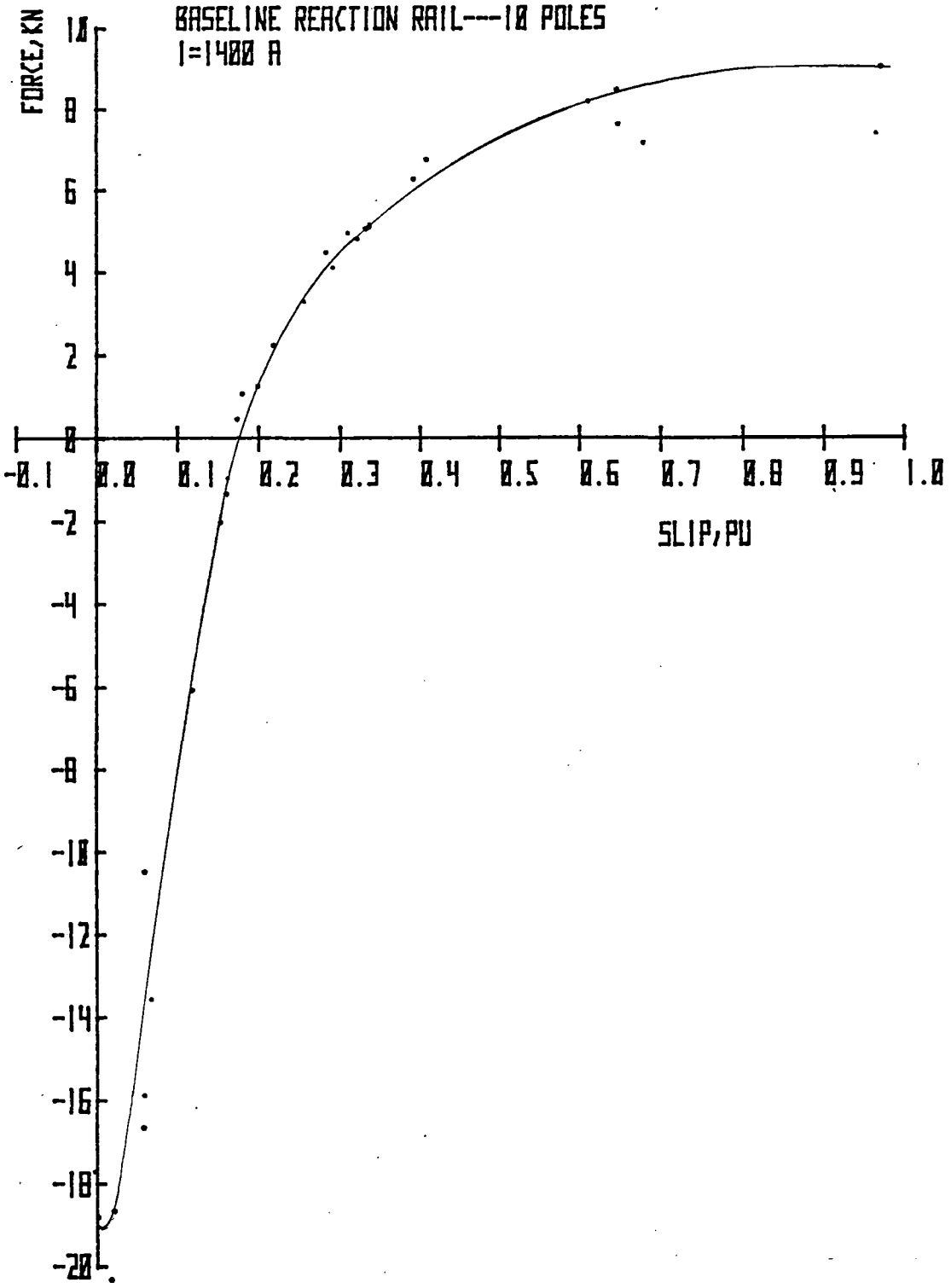

Figure 8-22. Total Vertical Force vs Slip, 10-Pole SLIM

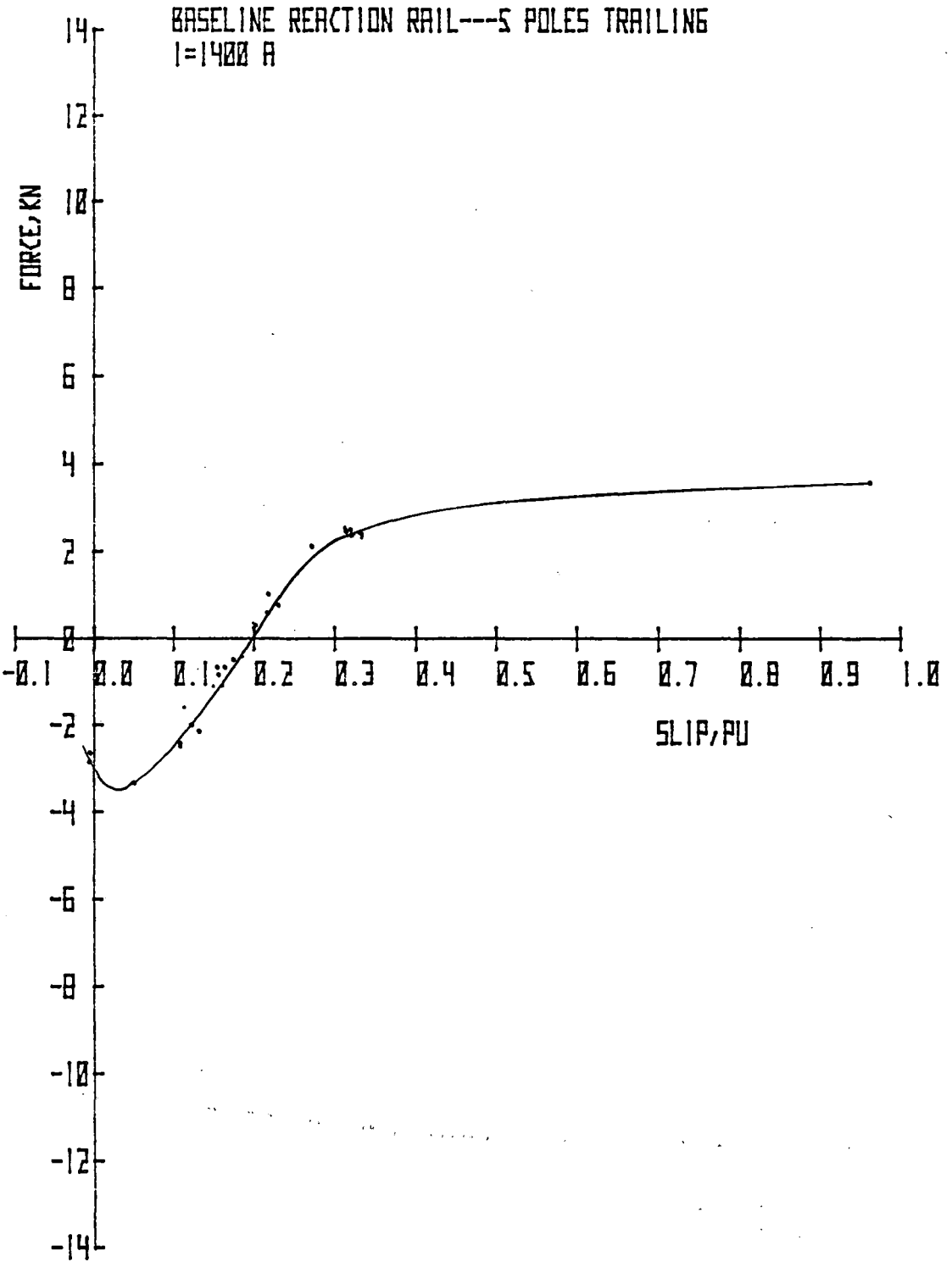

Figure 8-23. Total Vertical Force vs Slip, 5-Pole (Trailing) SLIM

The vertical force data shown is normalized to 1400 A.

At zero slip, a significant difference exists between the vertical forces for the 10-pole and 5-pole configurations on a per-pole basis. This variance is caused by a comparatively high magnetizing current at zero slip for the 5-pole configuration, as shown earlier in Figure 8-9. When the vertical force data is consequently normalized to constant current for both configurations, a significant adjustment is required.

It can be seen that the measured power loss in the low-slip region is unreliable due to measurement error. At low slips, the thrust and input power decrease to low values, leading to larger resolution errors. However, the trend is clearly evident, and it further quantifies the end effect. This approach does not identify the different loss mechanisms, but does depict the dynamic end effect discussed elsewhere [14].

It was pointed out earlier that the magnetizing reactance of the 5-pole L configuration is lower than that of the 10-pole configuration due to the large net effect of the entry edge. For a given V/Hz/pole, the current is therefore higher at low values of slip for the 5-pole configuration.

When data is normalized to a constant current condition, large discrepancies occur between the two configurations for the measured parameters (on a per-pole basis) because of the different proportions of magnetizing current in the normalizing current. This is especially true of vertical forces, which reach maximum values at low slips. At high slips, dynamic end effect becomes unnoticeable when comparing current, voltage, and efficiency characteristics of the 5- and 10-pole configurations. Corresponding vertical force data at high slips agree more closely in terms of prorated vertical forces between the two configurations, as noted in Table 8-5.

TABLE 8-5

VERTICAL FORCES

Configuration	Vertical Force per Pole at 0.0 Slip, kN (I = 1400 A)	Vertical Force per Pole at 1.0 Slip, kN (I = 1400 A)	Slip at Zero Force
10-pole	-1.9	+0.88	0.175
5-pole T	-0.7	+0.70	0.2

Figures 8-24 and 8-25 show the pitching moment* associated with the vertical force characteristics just discussed. Pitching moment is a result of redistribution of flux toward the rear end of the motor.

* +ve pitching moment indicates front end up, tail end down for energized portion of primary.

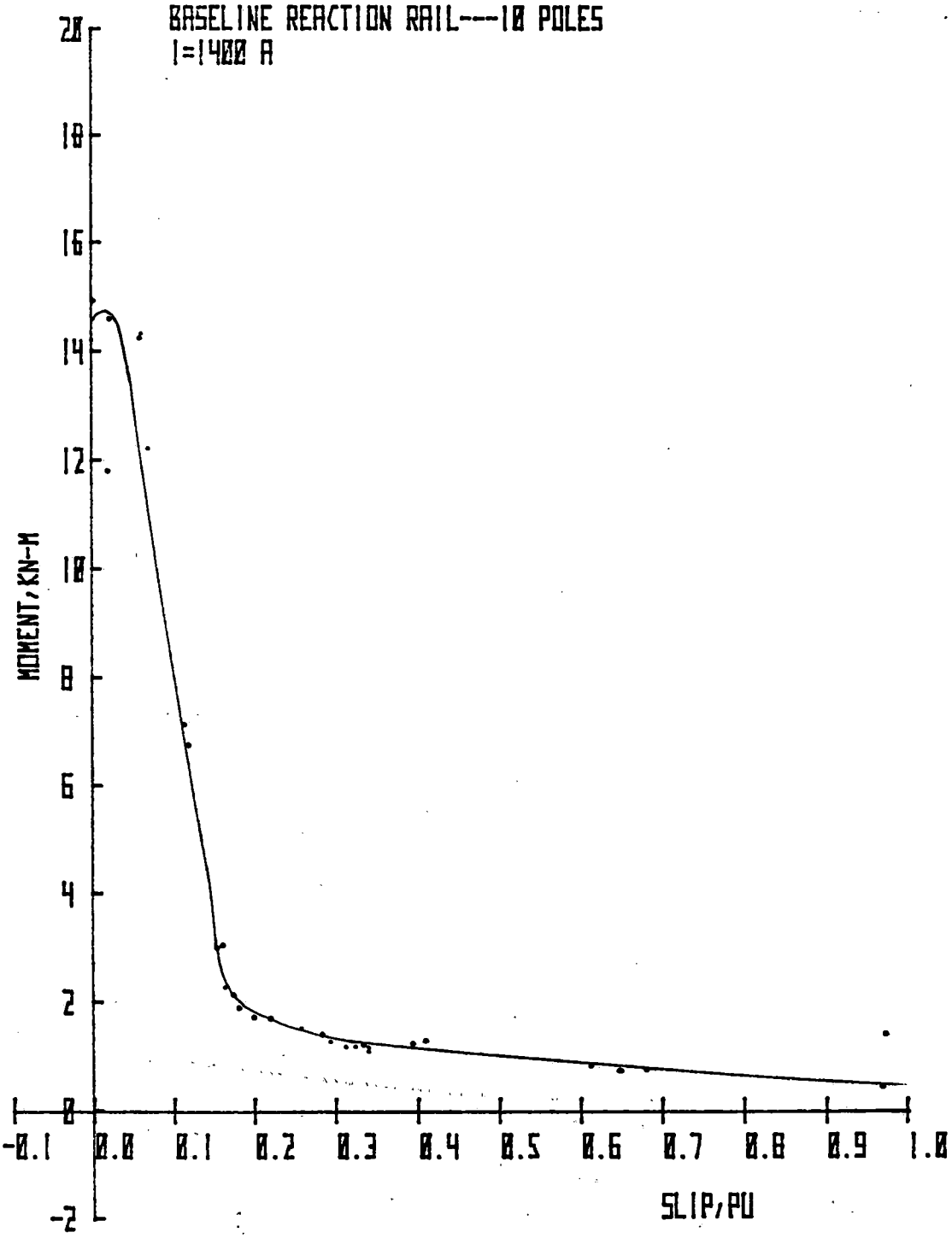

Figure 8-24. Pitching Moment vs Slip, 10-Pole SLIM

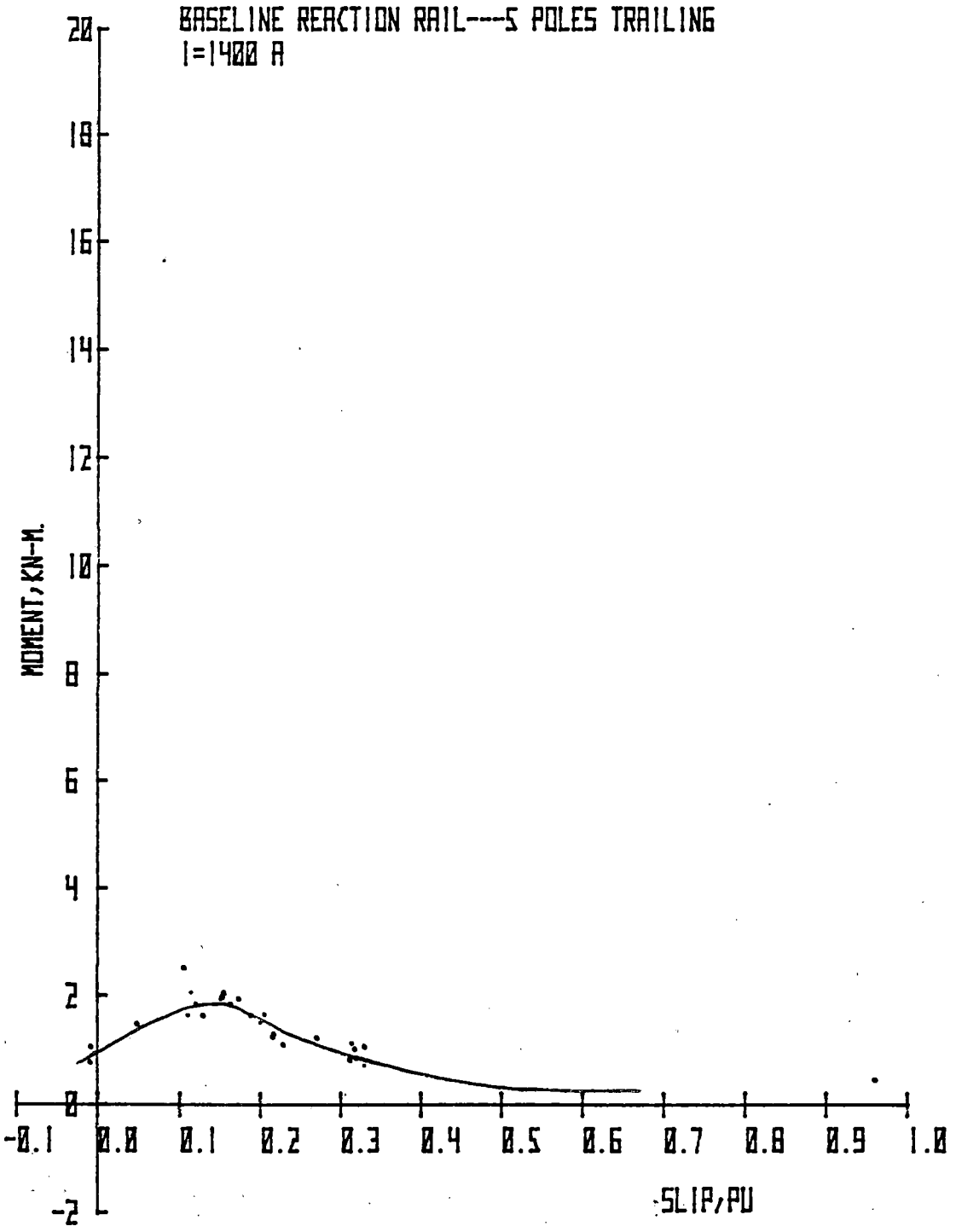

Figure 8-25. Pitching Moment vs Slip, 5-Pole (Trailing) SLIM

As expected,the 10-pole configuration shows a high +ve pitching moment at very low values of electrical slip, due to redistribution of the essentially attractive component force to the rear of the primary.

The 5-pole T configuration produces a rather surprising result: the pitching moment decreases at low slip values. This cannot be satisfactorily explained, and measurement error at slip below 0.1 is suspected.

COMPARISON OF 5-POLE L AND T CONFIGURATIONS

Tests completed on the two 5-pole configurations produced sufficient data for a detailed comparison. Generally, the differences in measured parameters were either insignificant or small. Only the measurably different parameters are discussed in this section. Complete acquired data on these two configurations is, however, shown in Volume II.

Efficiency

Figure 8-26 shows a small increase in the 5-pole L efficiency due to the presence of extended iron at the rear of the machine.

Figures 8-27 and 8-28 again reveal a slight difference (approximately 2 percent) between 5-pole L and 5-pole T efficiency.

Power Loss

Figures 8-29 and 8-30 show a significant difference in the measured power loss at low slips. However, this parameter has previously been pinpointed as subject to significant measurement error.

COMPARISON OF VERTICAL FORCE CHARACTERISTICS

A significant difference exists in the vertical force characteristics due to the presence of flux in the unenergized portion of the 5-pole L motor primary. This leads to an increase in attraction force at low slips where flux redistribution occurs, and flux is drawn into the unenergized portion of the winding (see Figures 8-31 and 8-32). In addition, a large increase in pitching moment occurs, as this measurement is sensitive to forces operating at a large effective lever arm from the center of the energized portion of the primary (shown in Figures 8-33 and 8-34). This characteristic is further explained by reference to the section dealing with distributed parameters, in particular the effect of extended primary iron on pole fluxes.

DISTRIBUTED PARAMETERS

The 10-pole SLIM primary, modified to permit connections of different numbers of poles, together with individual phase-belt voltage, current, power, and flux measurements, represents an excellent opportunity to examine the variation of these parameters as a function of electrical slip, and explore the implications of the redistribution of flux that occurs in a linear motor.

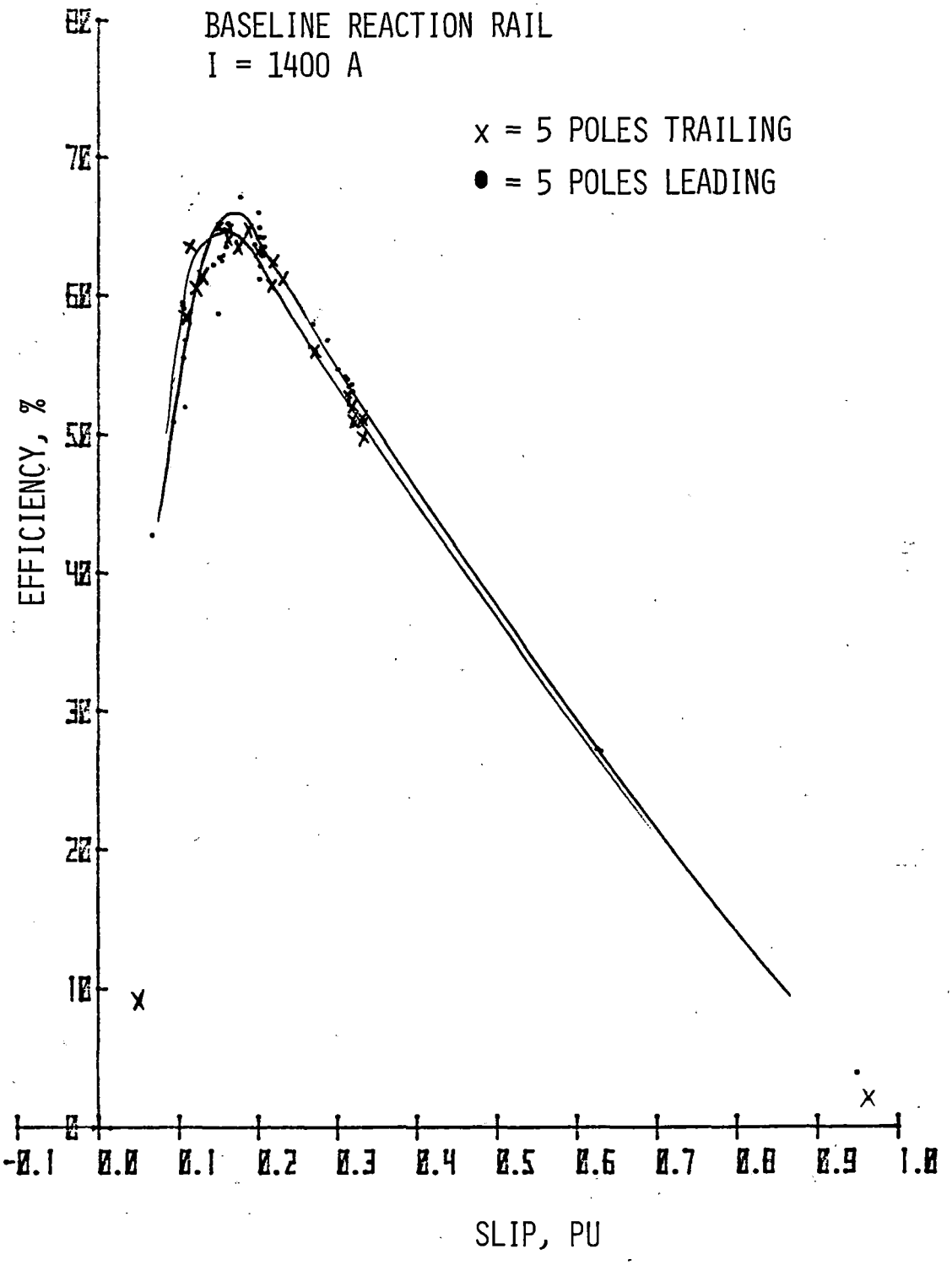

Figure 8-26. Efficiency vs Slip, 5-Pole (Trailing) and 5-Pole (Leading SLIM

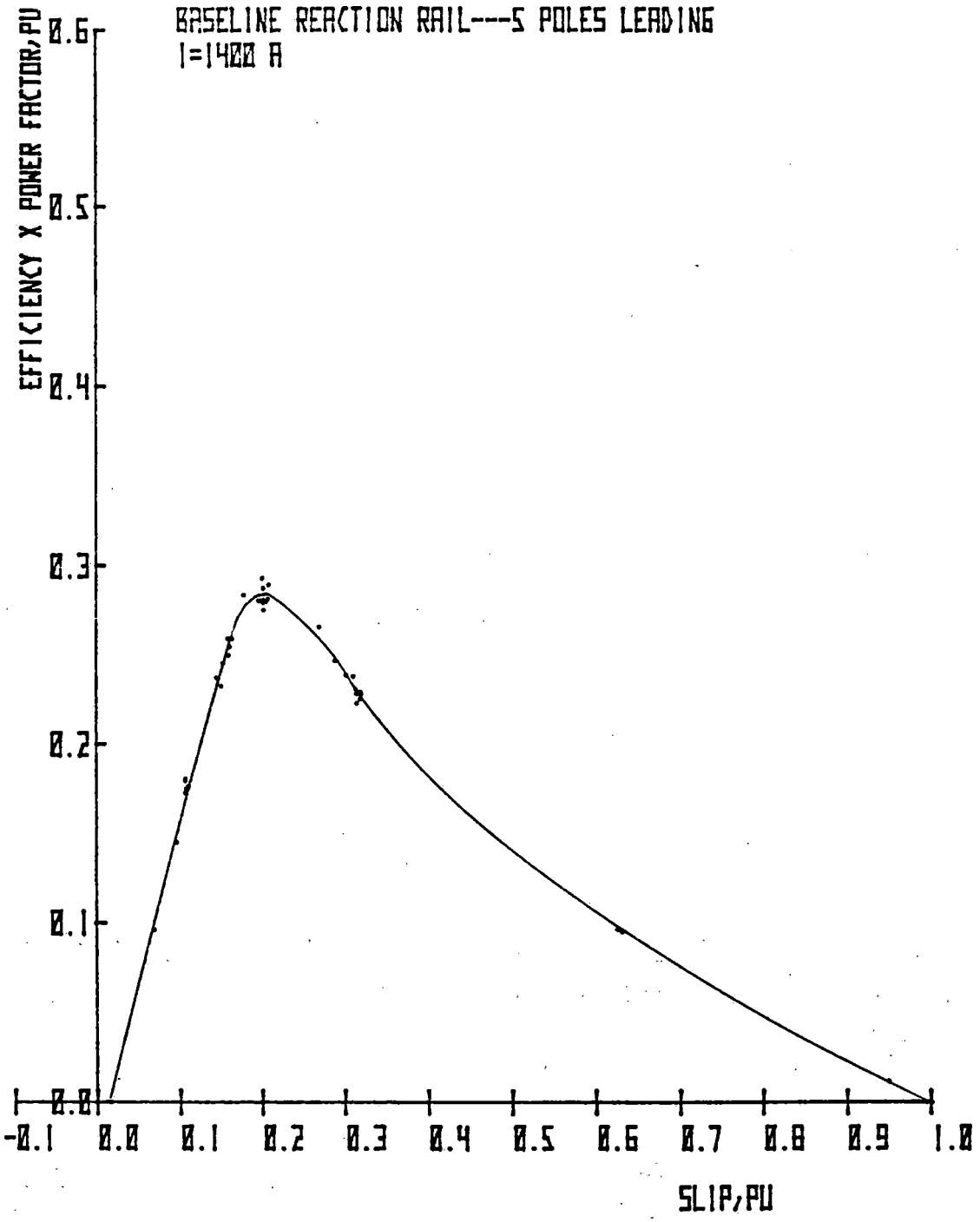

Figure 8-27. Efficiency x Power Factor vs Slip, 5 Poles Leading

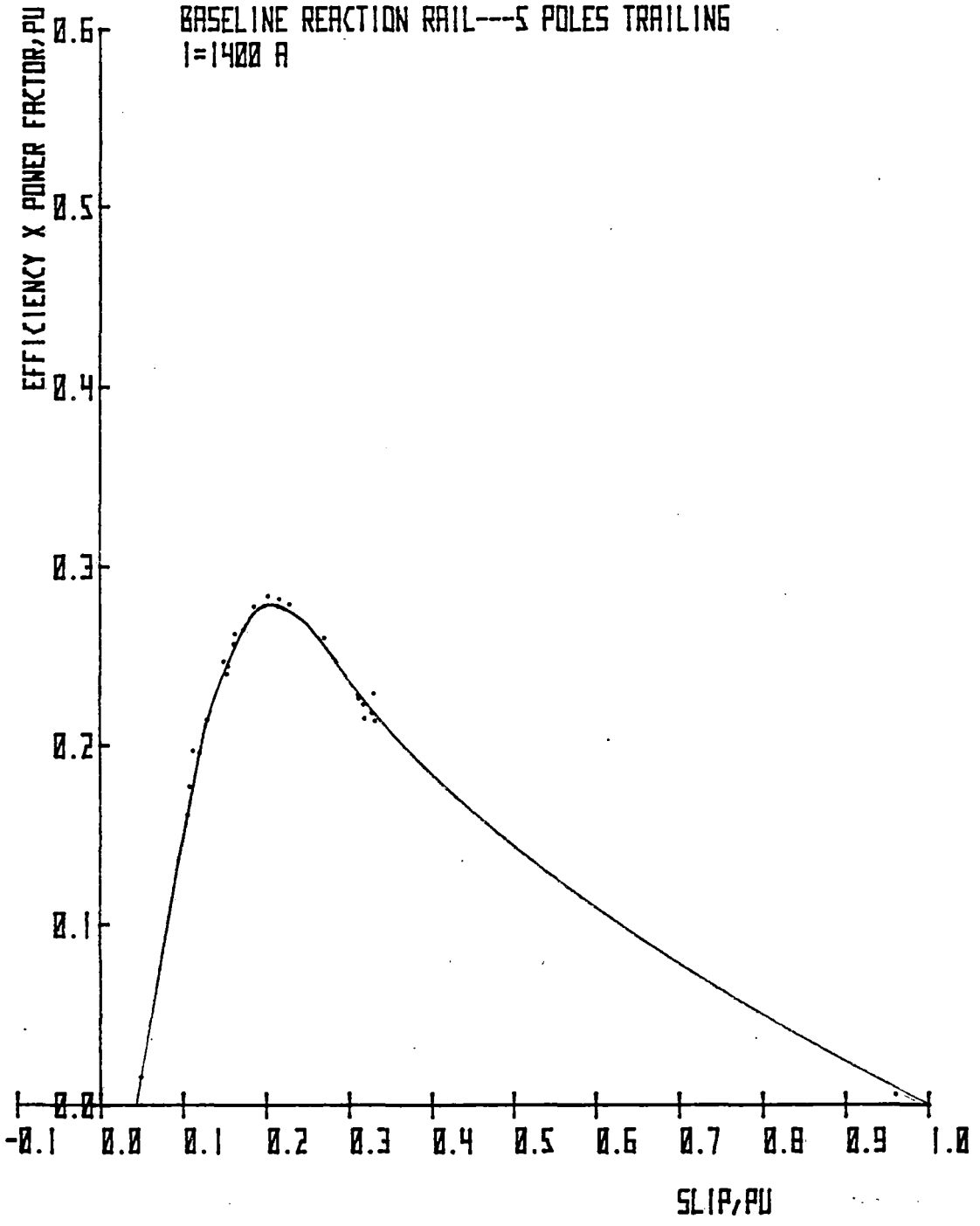

Figure 8-28. Efficiency x Power Factor vs Slip, 5 Poles Trailing

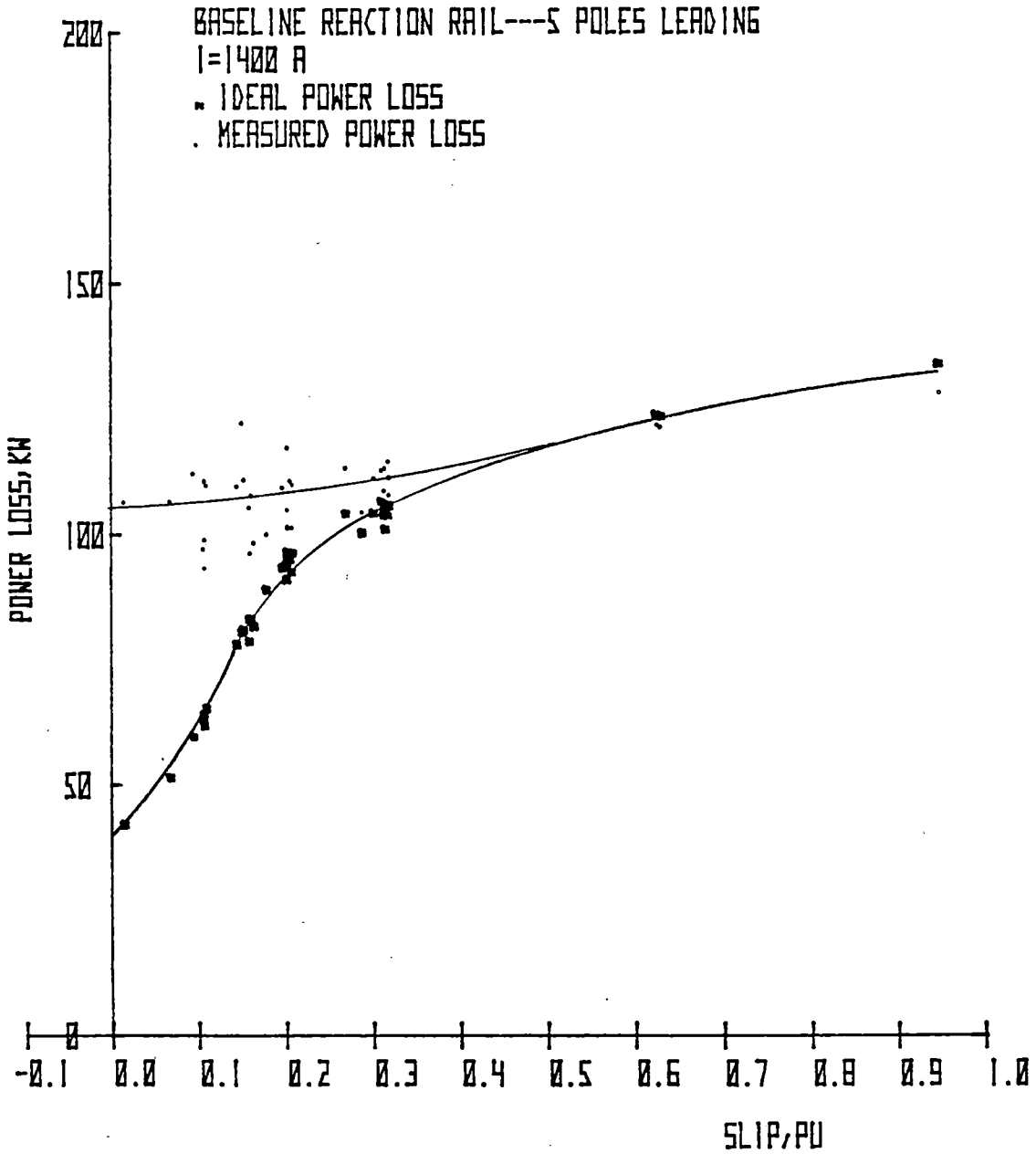

Figure 8-29. Ideal and Measured Power Loss vs Slip, 5 Poles Leading

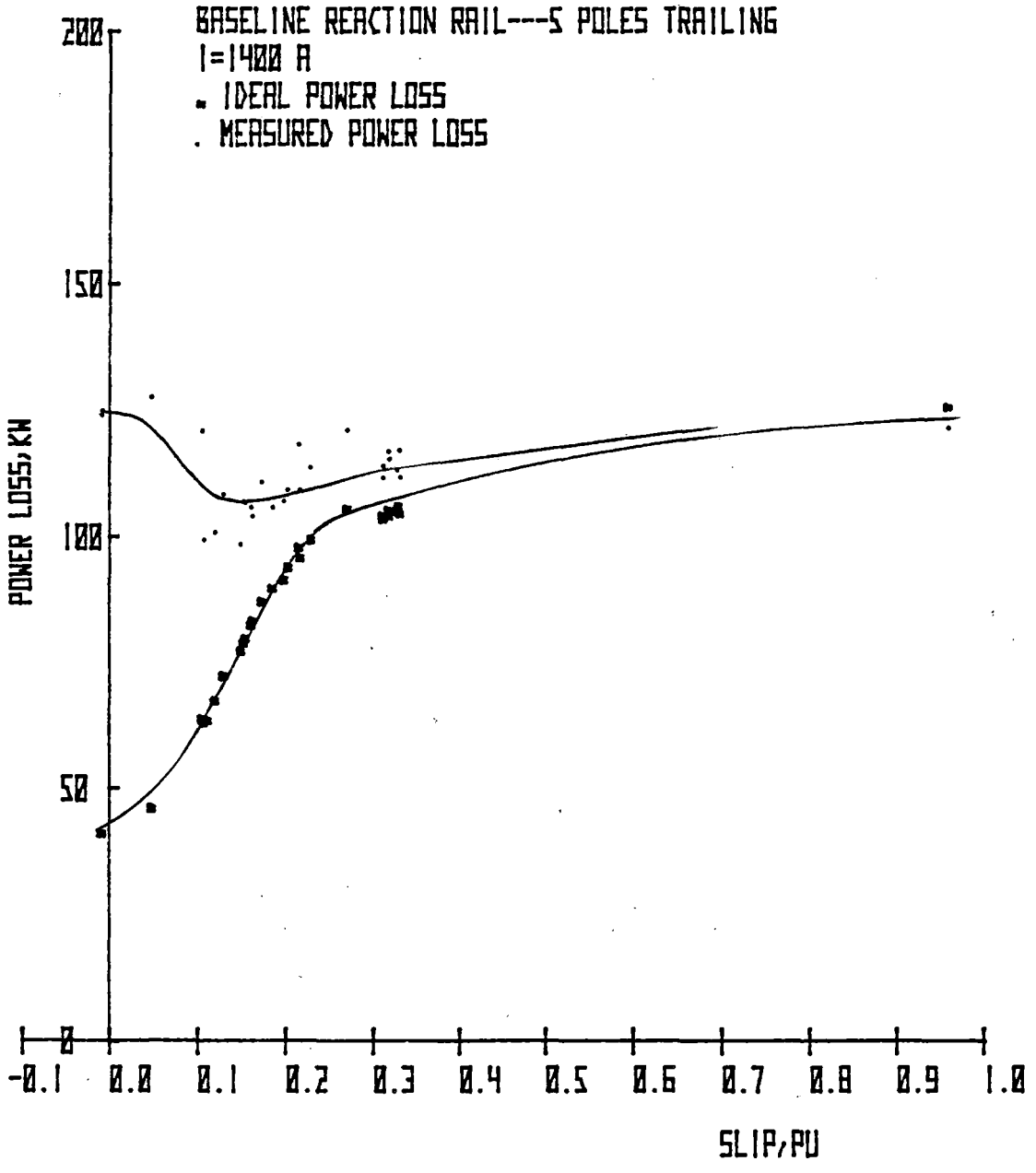

Figure 8-30. Ideal and Measured Power Loss vs Slip, 5 Poles Trailing

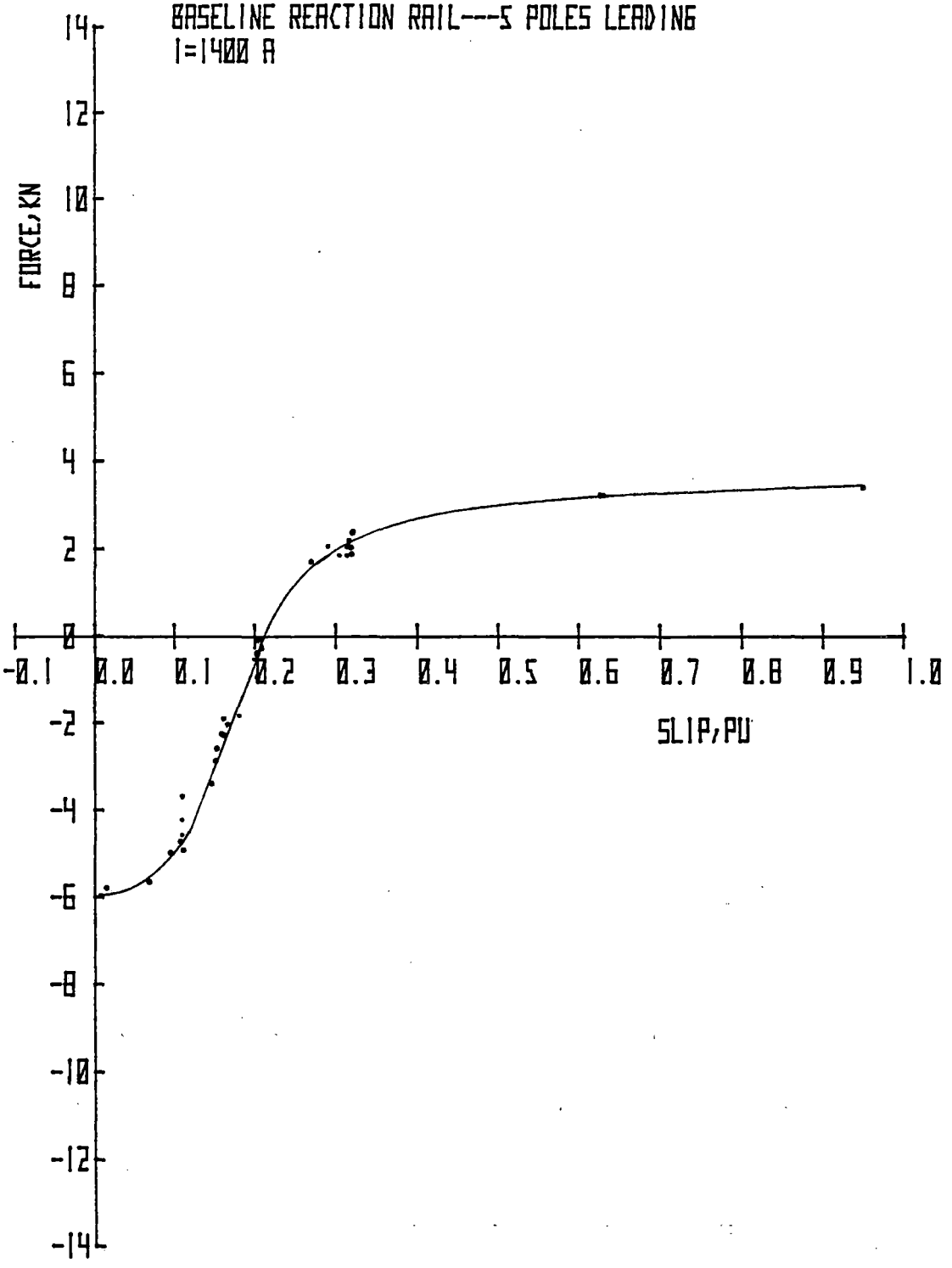

Figure 8-31. Total Vertical Force vs Slip, 5 Poles Leading

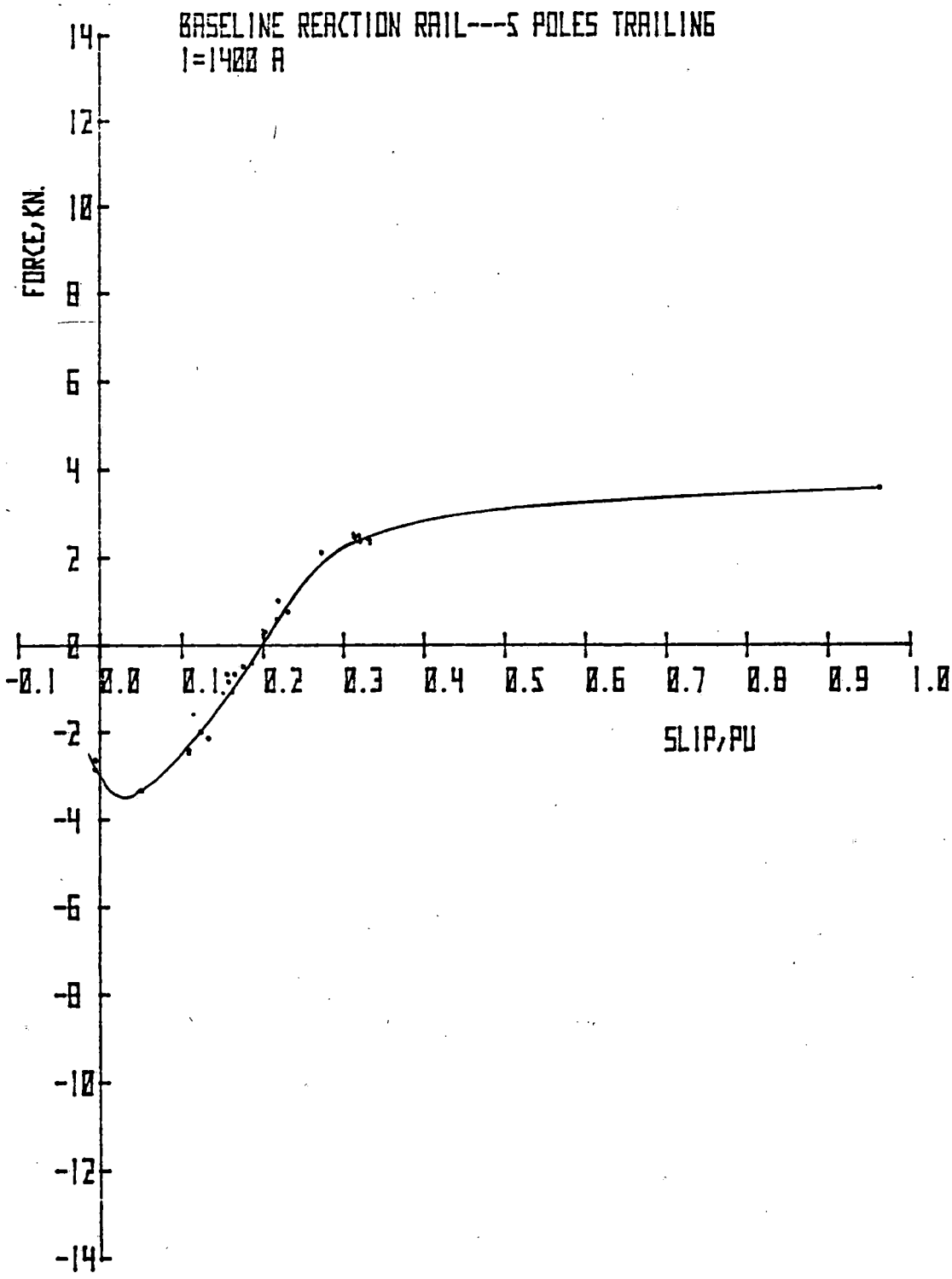

Figure 8-32. Total Vertical Force vs Slip, 5 Poles Trailing

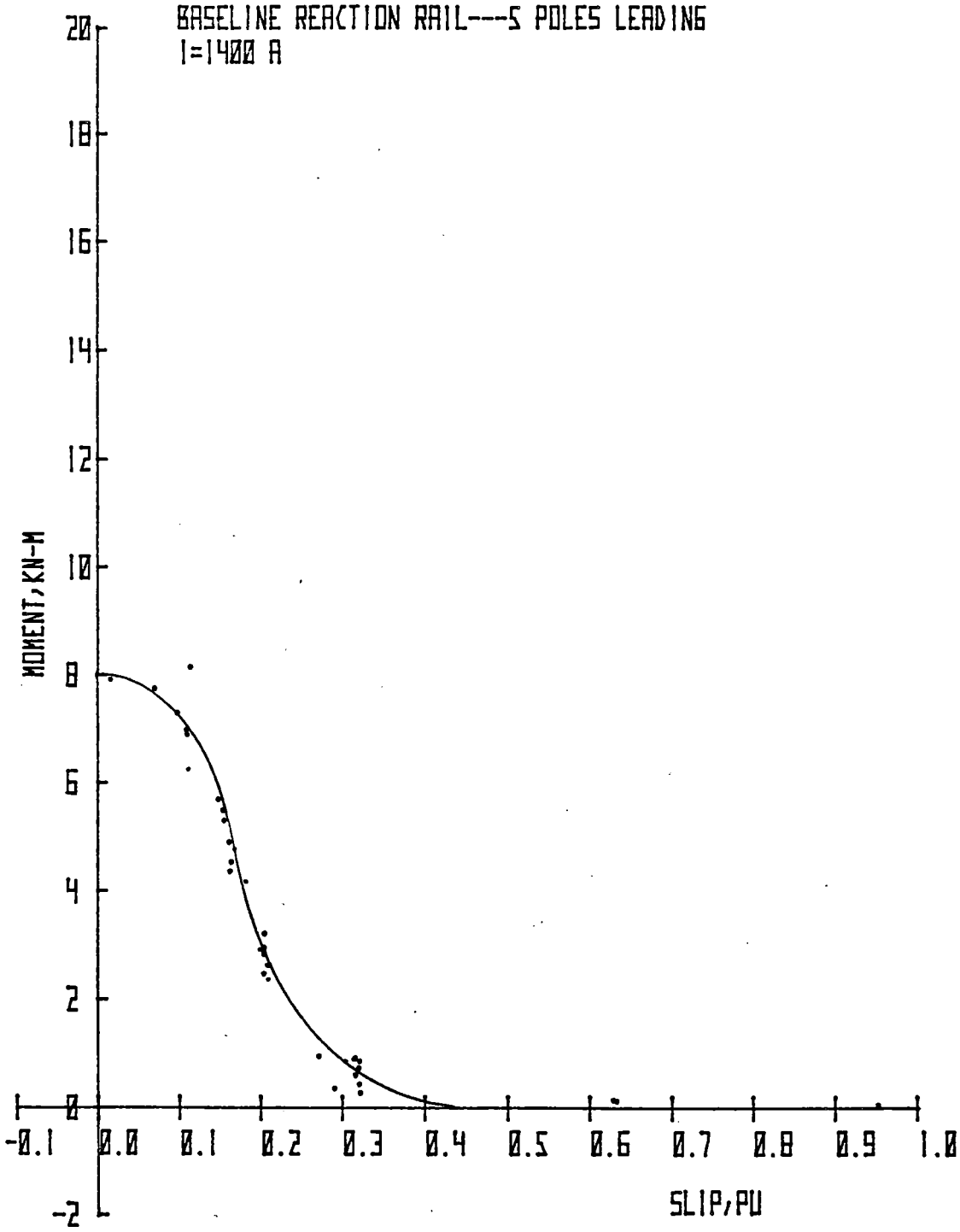

Figure 8-33. Pitching Moment vs Slip, 5 Poles Leading

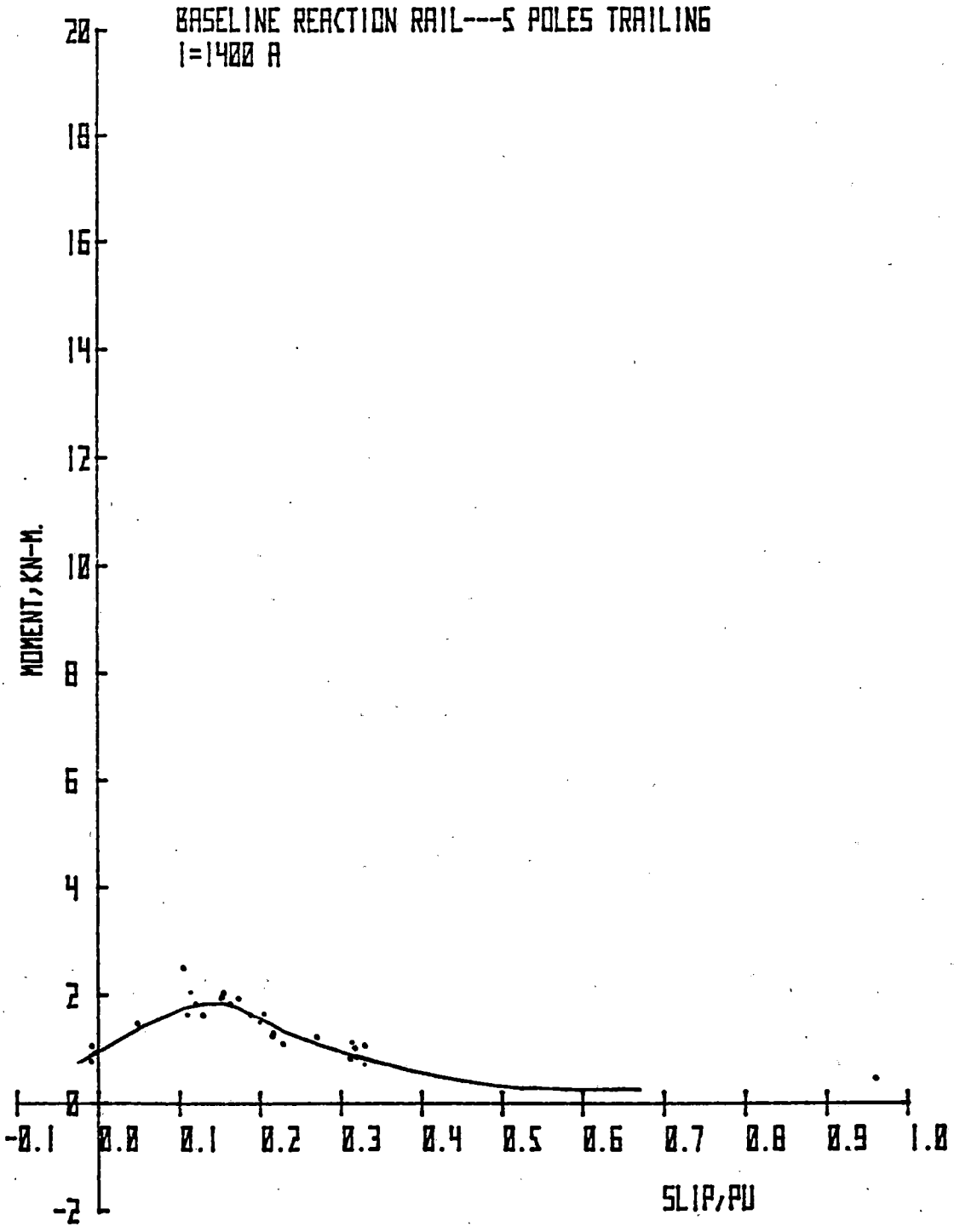

Figure 8-34. Pitching Moment vs Slip, 5 Poles Trailing

Ten-Pole Tests

Figures 8-35 and 8-36 show the variation of pole flux, power per pole, kVAR per pole, and voltage magnitude per pole along the machine for different phase belts and values of electrical slip. To facilitate comparison, power, kVAR and voltage are expressed in per unit quantities, i.e., the phase-belt quantity divided by the total quantity for that phase. The pole flux is normalized to 0.346 V/Hz/pole and therefore tends to reflect a per-unit quantity, as a constant V/Hz tends to imply a constant mutual flux condition.

Figure 8-35 shows distributed parameters for phase A at an electrical slip of 0.678. At this value of slip, no end effects are detectable on electrical performance characteristics. Very little redistribution of phase-belt parameters is seen. The pole flux distribution shows a low value at either end of the machine due to half-filled slots, and a magnetic discontinuity at the end of the windings. Figure 8-36 shows a substantial periodicity in power per pole and kVAR per pole. This is due to interaction of a forward traveling mmf wave (corresponding to a regular traveling field in a rotary machine) with an end effect traveling wave, magnetized by the secondary member. The end effect traveling wave is stationary with respect to the secondary member, and produces a retarding force when it reacts with the secondary current. In practice, the end effect traveling wave decays as a result of energy dissipation in the secondary. The periodicity of the resultant traveling wave is shown in an earlier report [1] and is given by the expression:

$$\text{Periodicity} = 2\left(\frac{1+\sigma}{\sigma}\right)\tau p$$

where σ is the slip (per unit) and τp is pole pitch.

Referring to figure 8-36, a test run at slip = 0.178 would be expected to show a corresponding power distribution of 5.8 τp. The test data gives a value of 6.0. The net output force of the motor is related to the magnitude of the resultant power distribution curve.

Qualitatively, it can be seen that the real power progressively transfers to the rear of the machine with decreasing slip.

It can also be seen from these curves that other distributed parameters follow this law. Figures 8-37 and 8-38 reflect progressively decreasing values of slip, and continuing shift of flux to the rear of the machine. Figures 8-39 and 8-40 show data corresponding to Figure 8-38, affording a comparison of the distribution on all three phases for three test runs with essentially similar slip values.

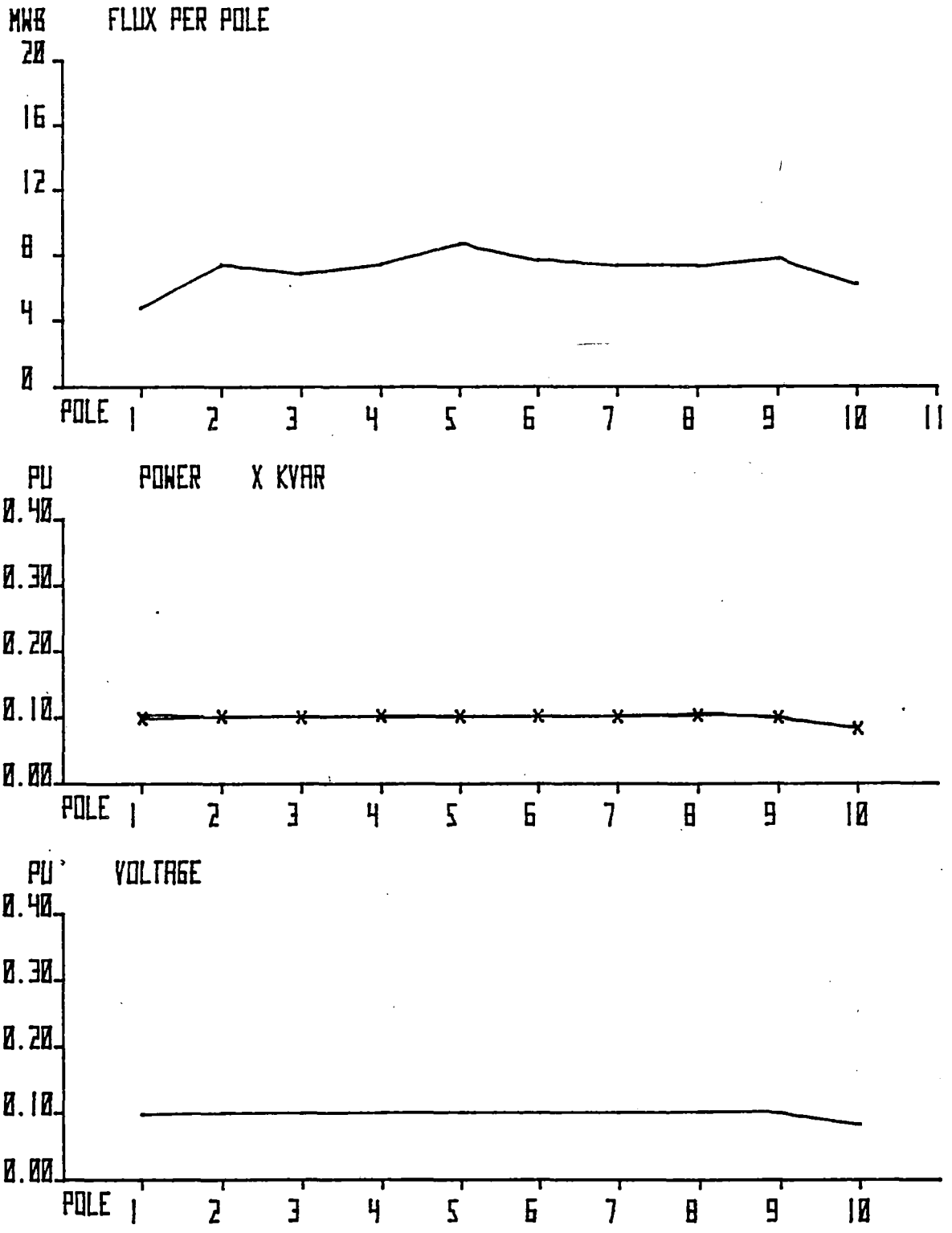

Figure 8-35. Distributed Parameters, Phase A at 0.678 Slip

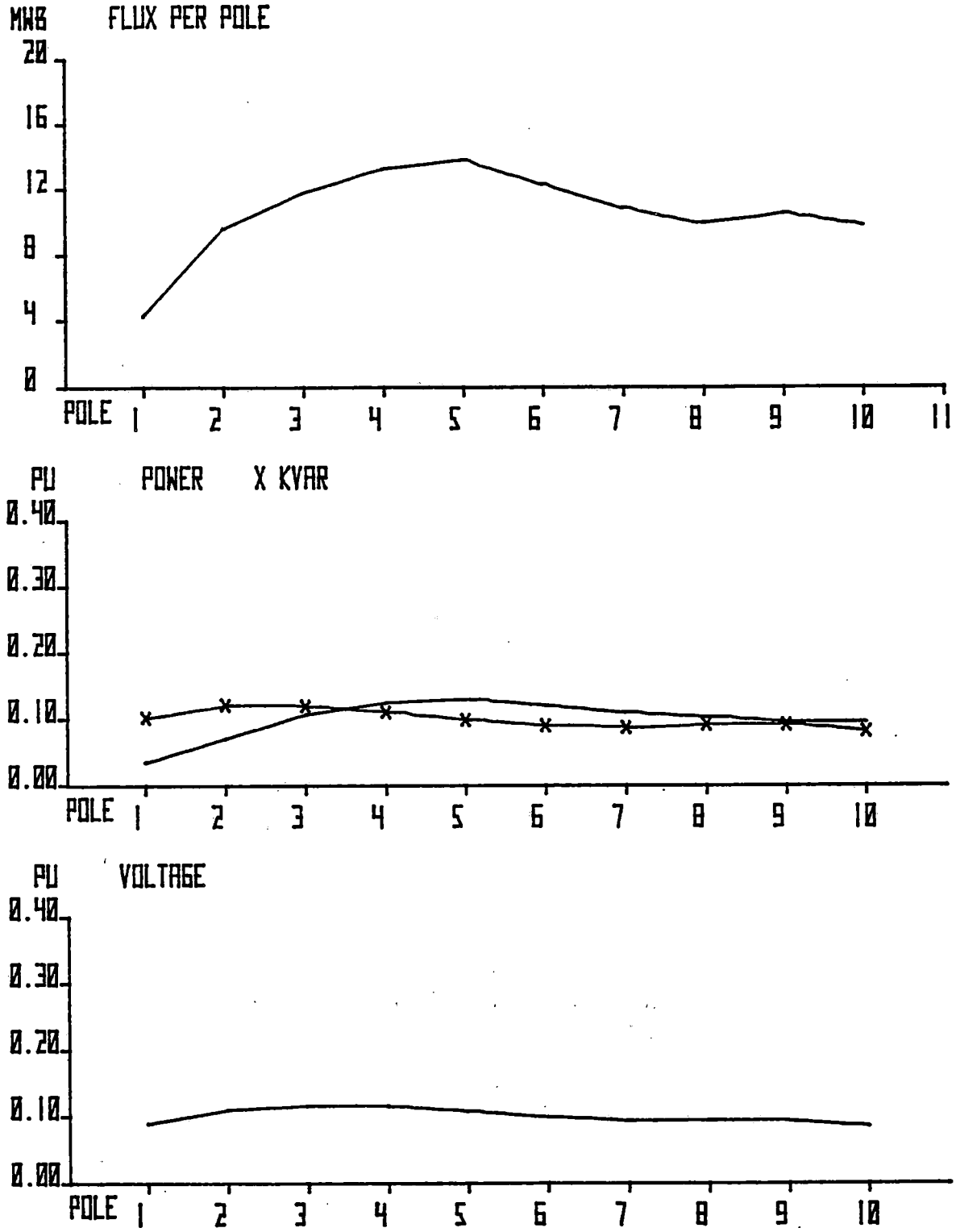

Figure 8-36. Distributed Parameters, Phase A at 0.178 Slip

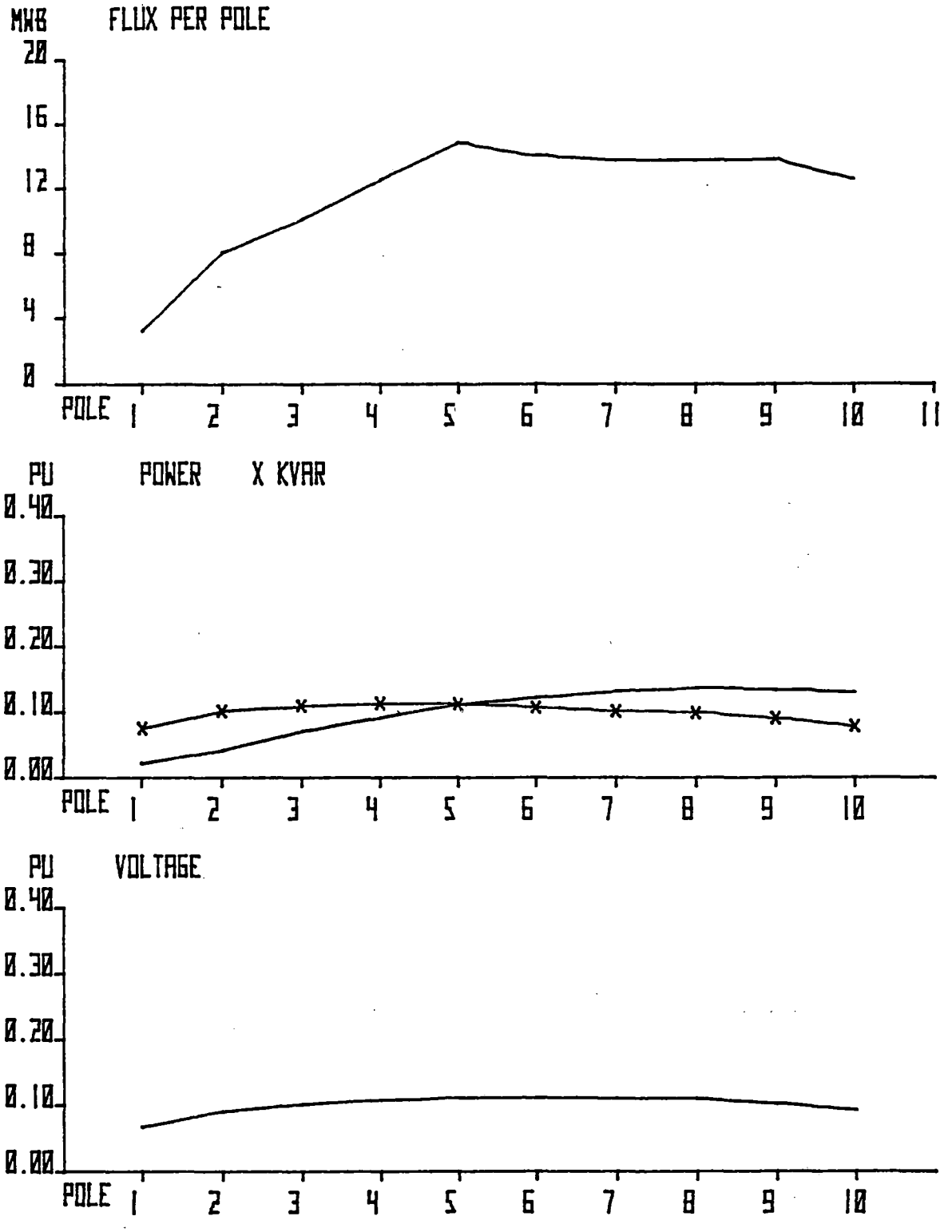

Figure 8-37. Distributed Parameters, Phase A at 0.110 Slip

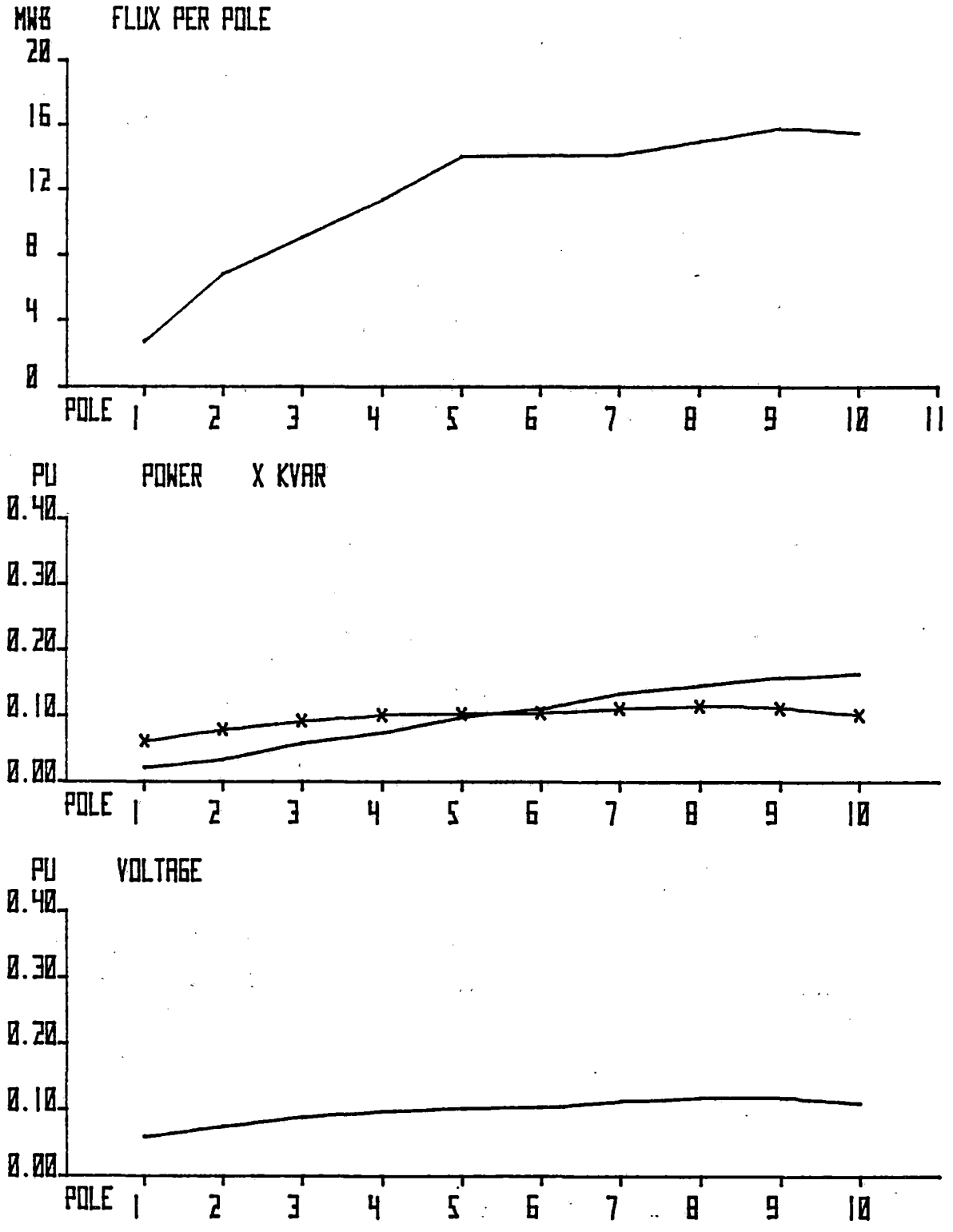

Figure 8-38. Distributed Parameters, Phase A at 0.055 Slip

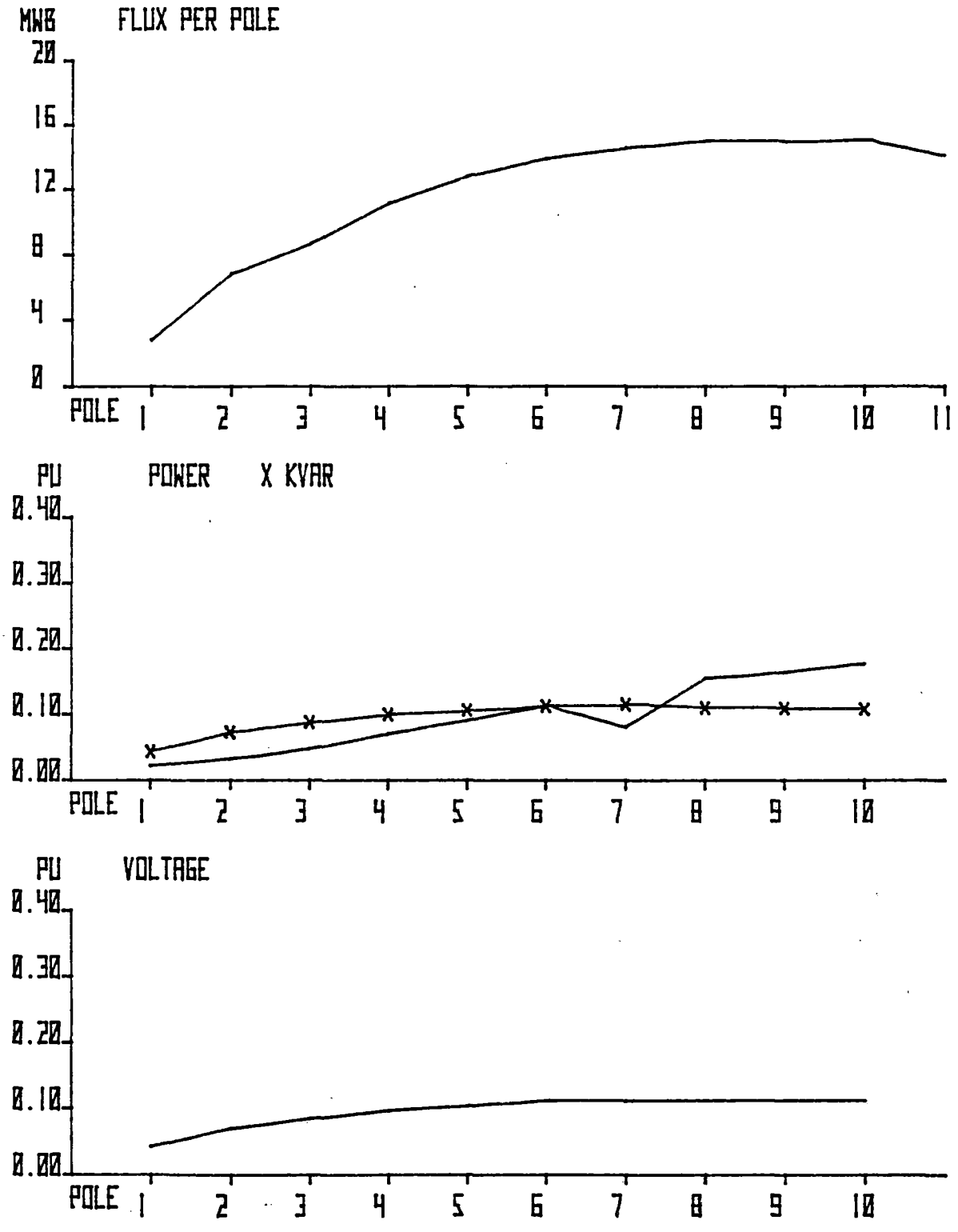

Figure 8-39. Distributed Parameters, Phase C at 0.057 Slip

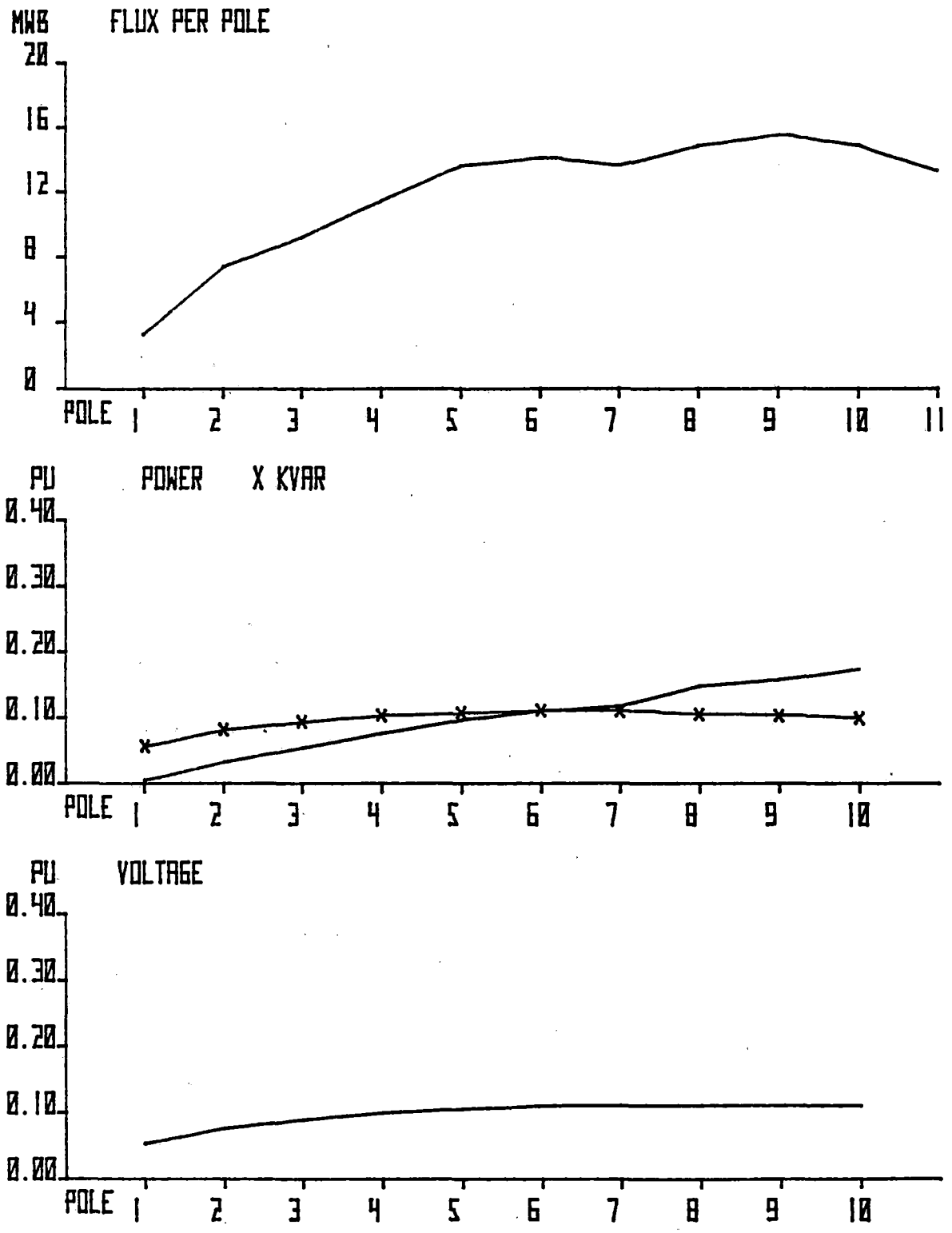

Figure 8-40. Distributed Parameters, Phase B at 0.068 Slip (10 Poles)

Five-Pole Leading Configuration Tests

Figures 8-41, 8-42, and 8-43 depict distributed parameters for the 5-pole L configuration, with all three phases monitored during three similar test runs. The flux traces should be identical for all three curves, differences being due only to measurment error. However, the differences in the other parameters give rise to unbalanced conditions in the machine, which in turn vary for each pole of the machine, and are dependent on slip.

Table 8-6 specifies the phase arrangement in slots at the front and rear of the machine, which partially cause the phase imbalances.

Five-Pole Leading and Trailing Configuration Tests

Figures 8-44, 8-45, and 8-46 show the variation in distributed parameters for the 5-pole L configuration as a function of slip. Figures 8-47, 8-48, and 8-49 show similar data for the 5-pole T configuration. While the two sets of data are essentially similar on a per-pole basis, the following differences do exist:

- Although the flux at the rear of the 5-pole T exit edge was not measured, it is likely that the flux decays more rapidly in the 5-pole T exit region than in the 5-pole L exit region, because of the absence of primary iron in the flux wake region. This is seen to cause the difference in performance between the two configurations.

- Distribution of phase-belt voltages is similar to that of pole fluxes. Some degree of averaging occurs in the phase-belt voltage distributions due to the distributed nature of the primary windings, including primary leakage and mutual flux (see Figures 8-44 and 8-47).

- The kVAR-per-pole distribution indicates that the magnetizing component of each pole is approximately constant. However, the power per pole is successively redistributed to the rear of the machine.

EFFECT OF SATURATION ON NORMALIZED PARAMETERS

Test Rationale

To fully explore the effects of saturation in the motor, the SLIM was tested at excitation levels exceeding 0.5 V/Hz/pole. LIMRV powerplant limitations are discussed fully elsewhere [11], but for reader convenience, a brief description of alternator excitation limitations is given in Appendix E.

It can be seen from Figure E-1 that the motor may be excited at a maximum of 4.7 V/Hz in the 10-pole configuration, and at a maximum of 3.0 V/Hz in the 5-pole configuration. The latter condition entails a mean excitation of 0.6 V/Hz/pole. Accordingly, investigation of saturation effects was accomplished with the motor configured for 5-pole connection.

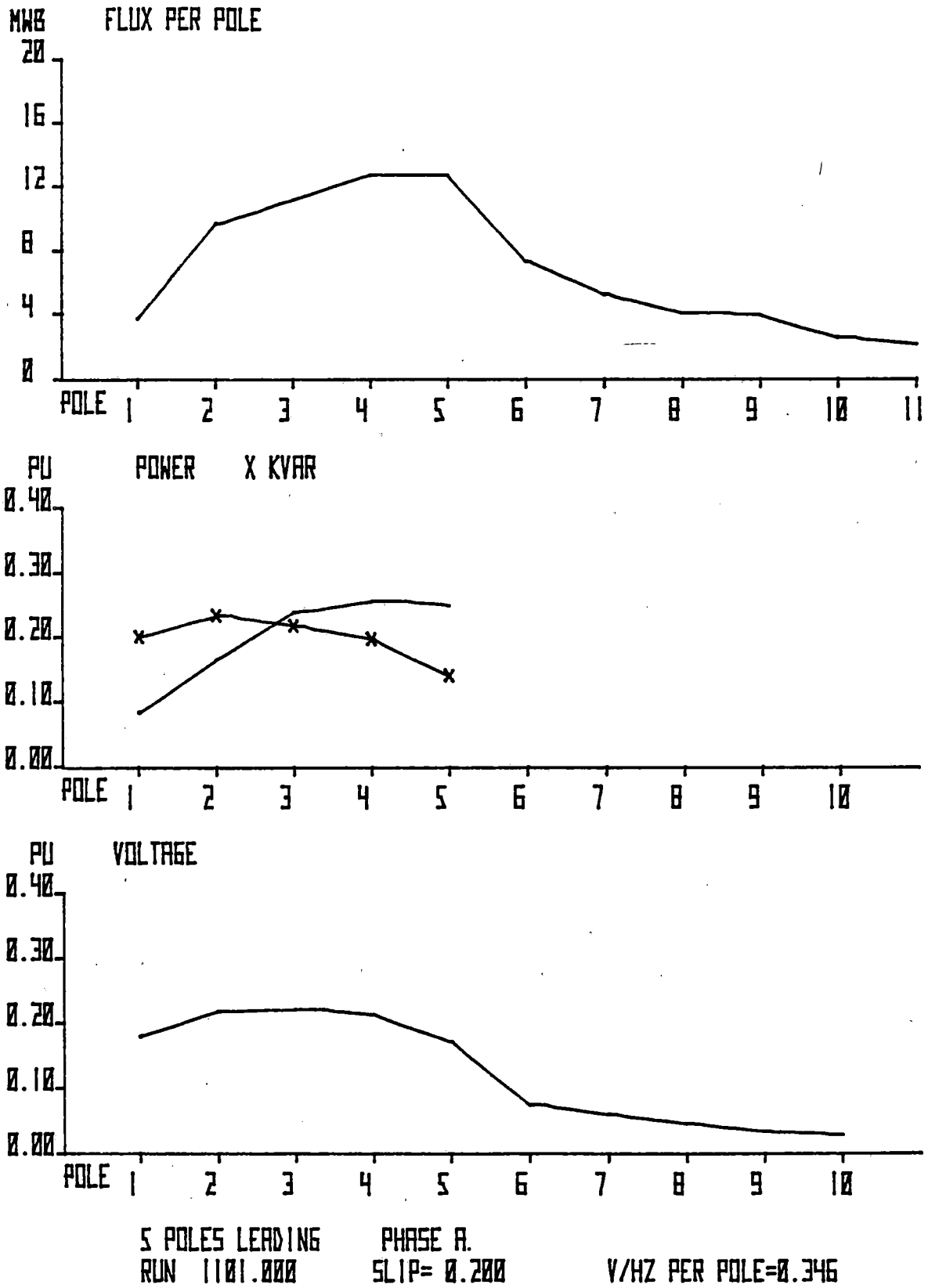

Figure 8-41. Distributed Parameters, Phase A at 0.200 Slip

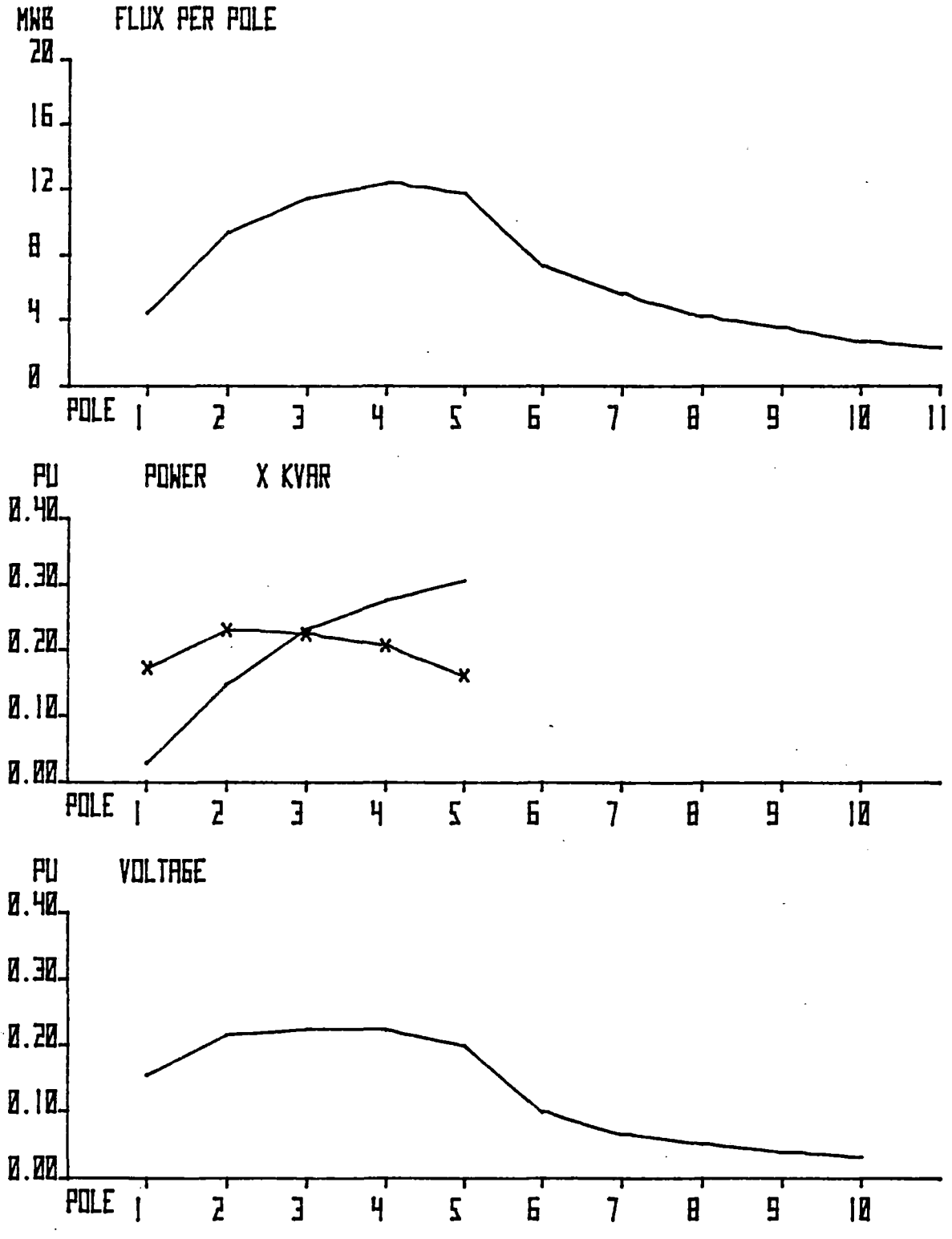

Figure 8-42. Distributed Parameters, Phase B at 0.201 Slip

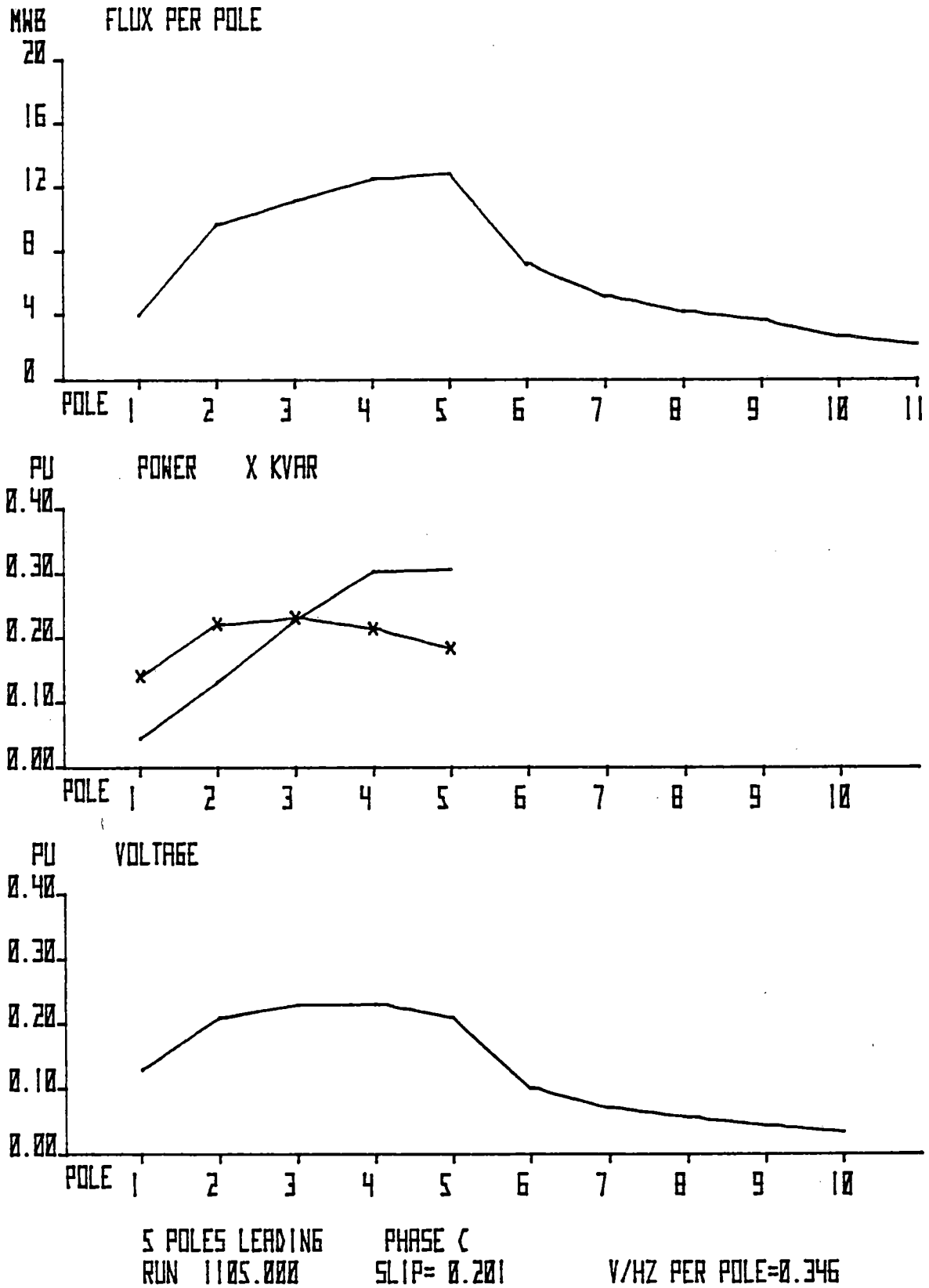

Figure 8-43. Distributed Parameters, Phase C at 0.201 Slip

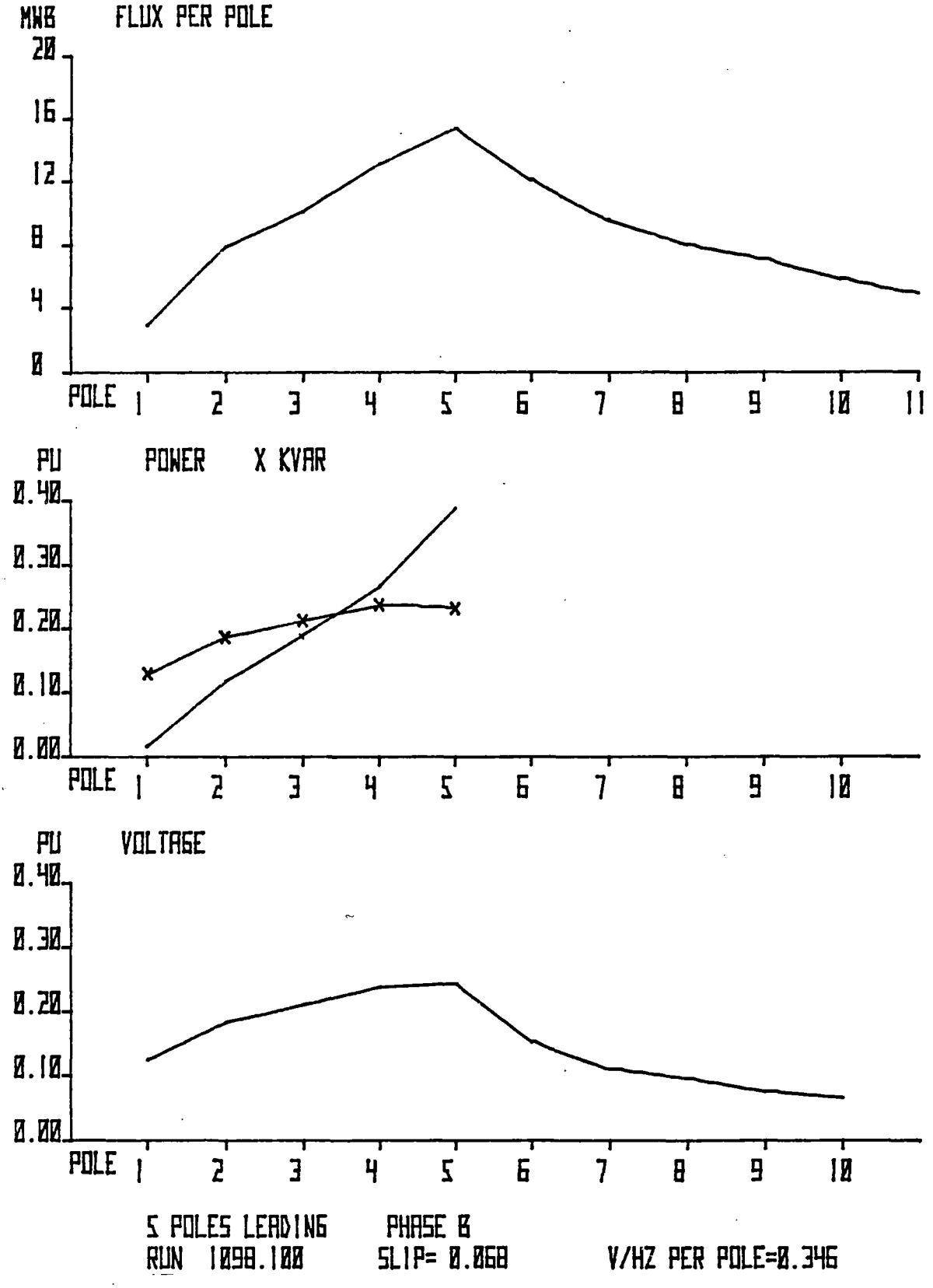

Figure 8-44. Distributed Parameters, Phase B at 0.068 Slip (5 Poles)

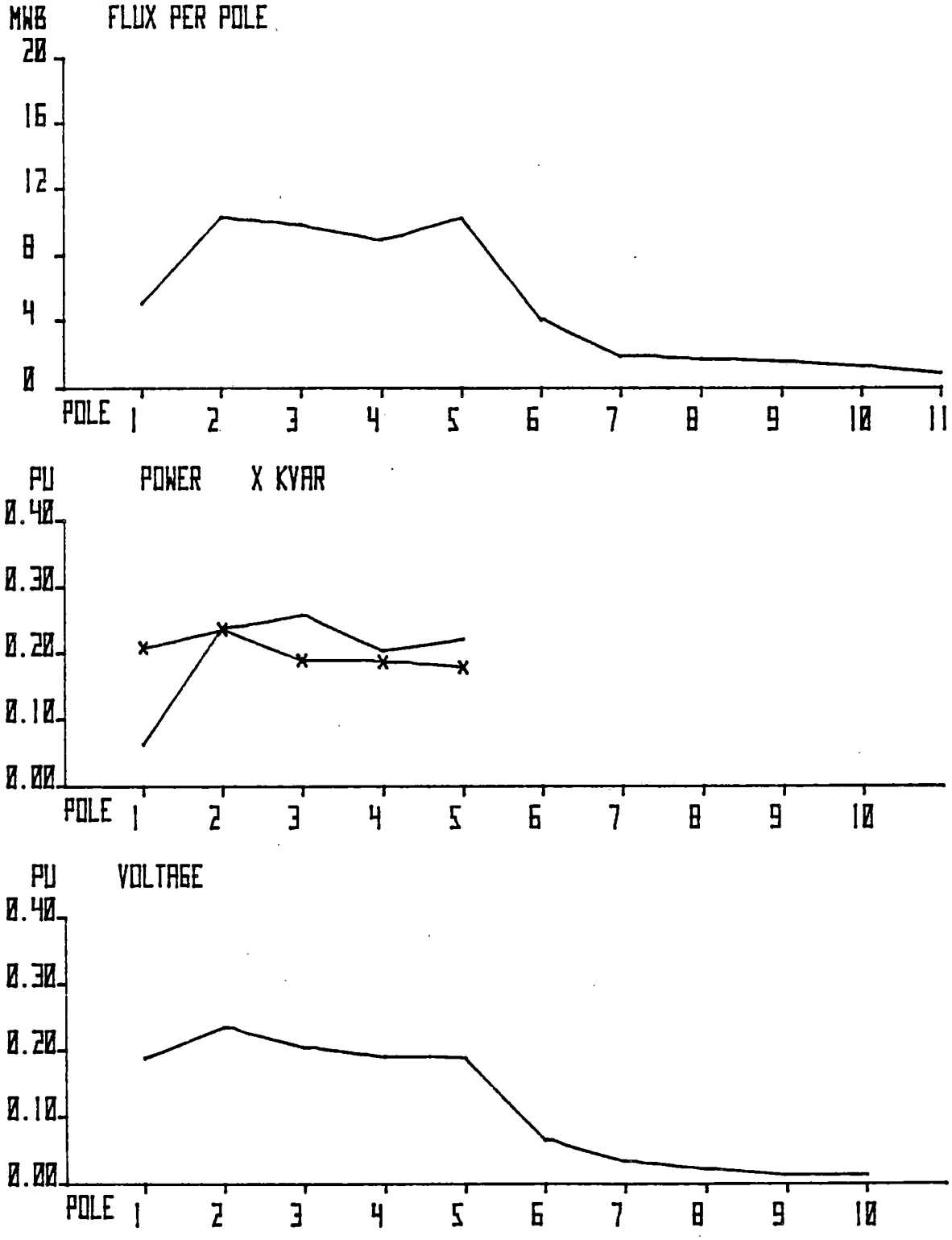

Figure 8-45. Distributed Parameters, Phase B at 0.316 Slip

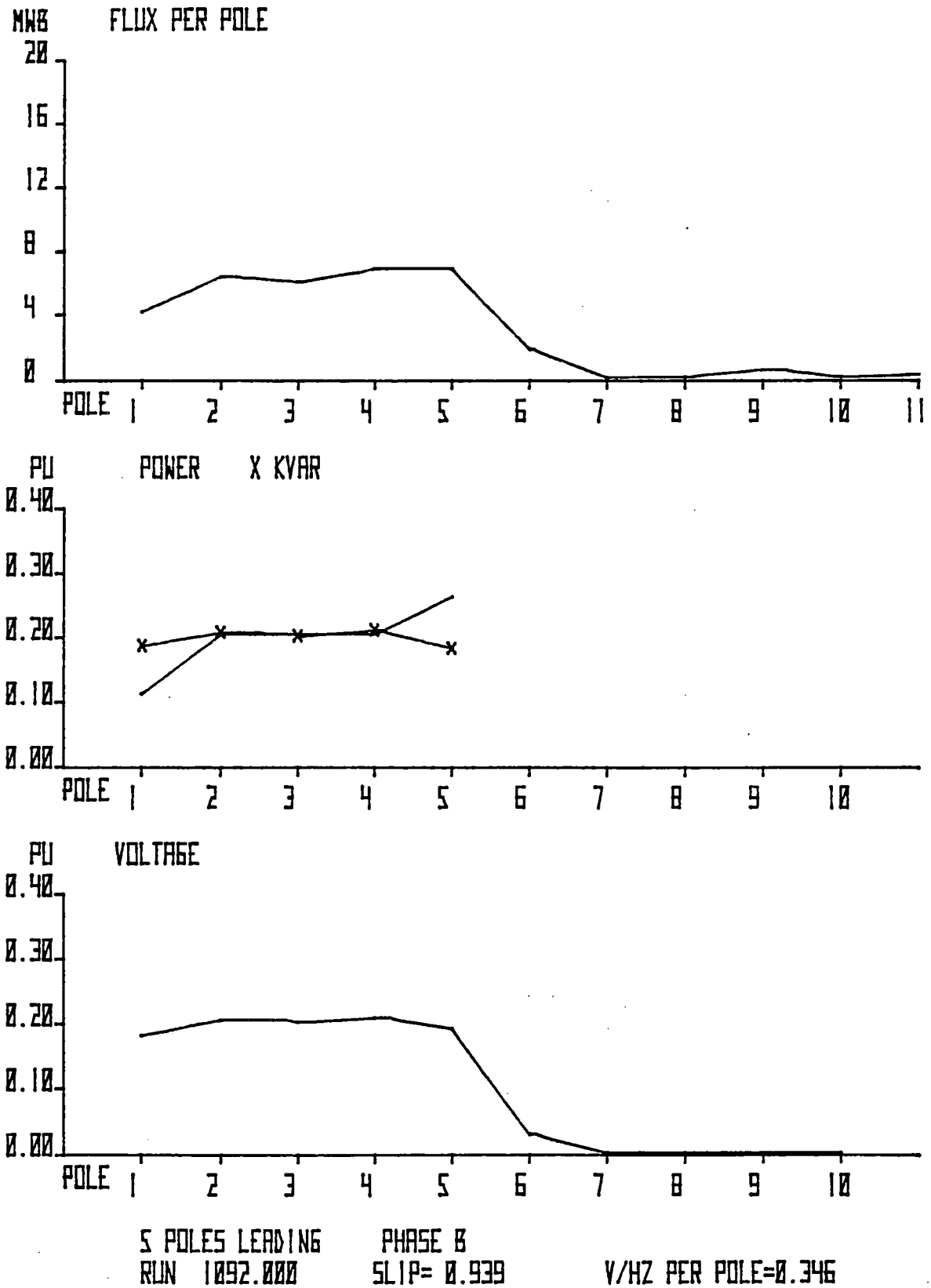

Figure 8-46. Distributed Parameters, Phase B at 0.939 Slip

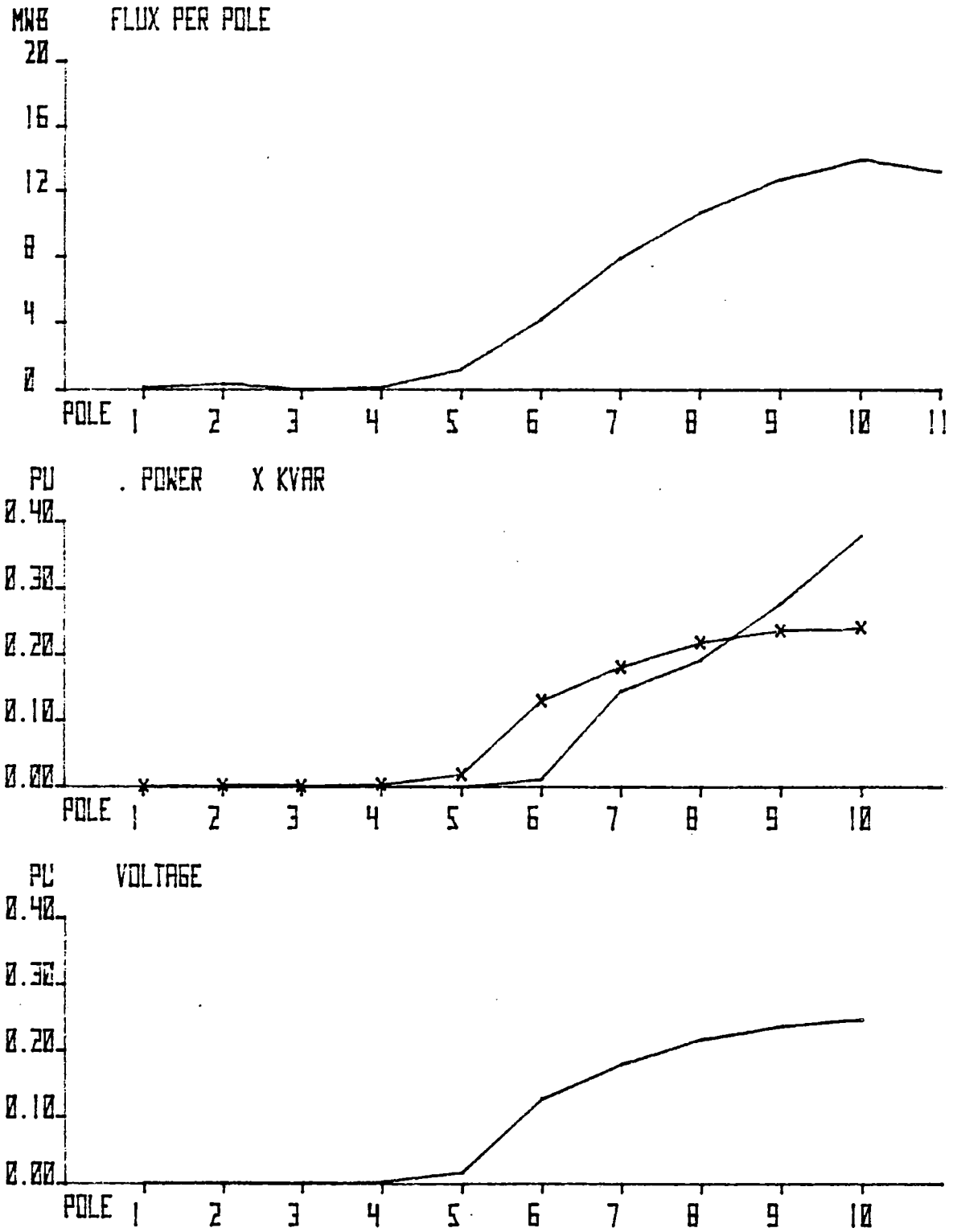

Figure 8-47. Distributed Parameters, Phase B at 0.048 Slip

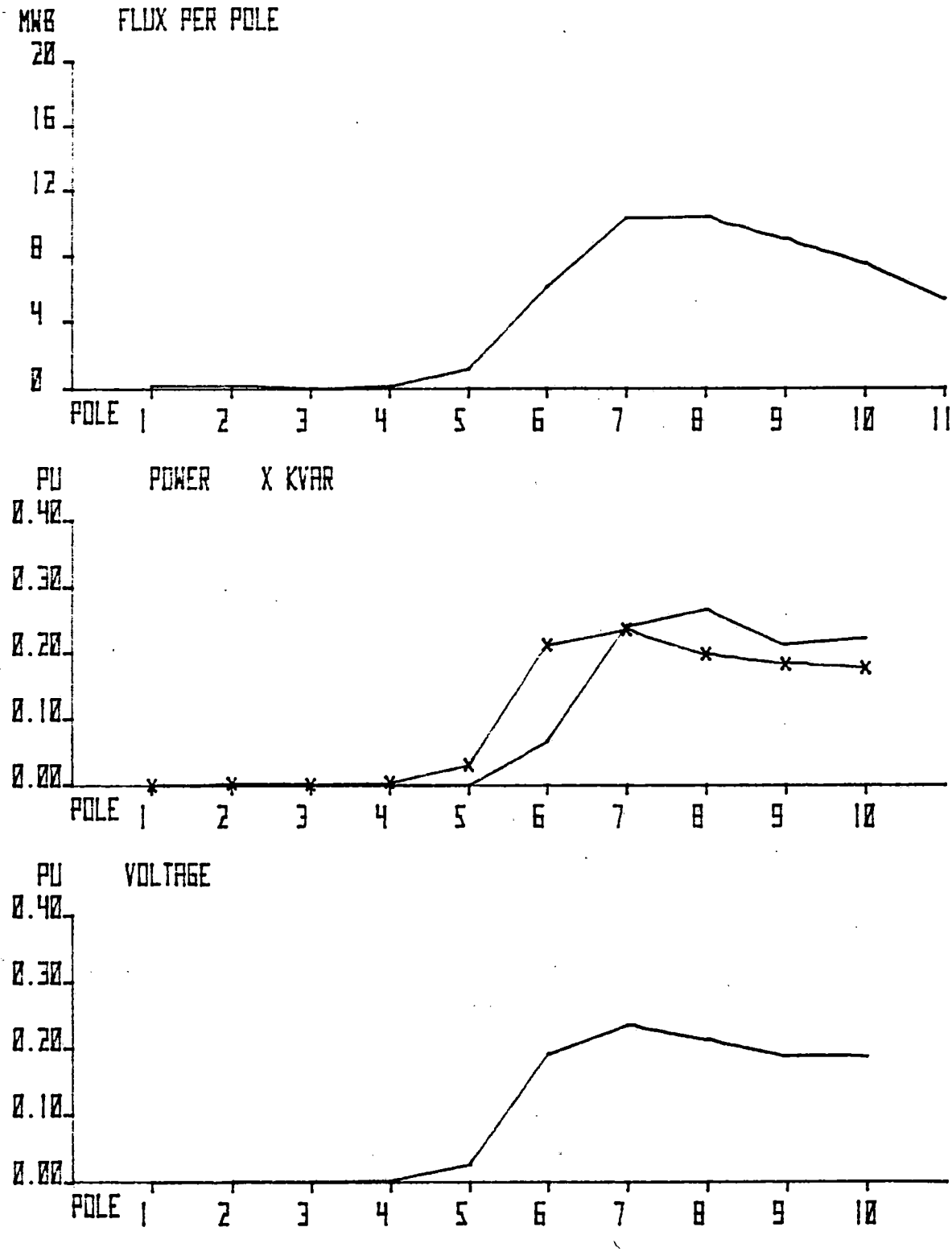

Figure 8-48. Distributed Parameters, Phase B at 0.318 Slip

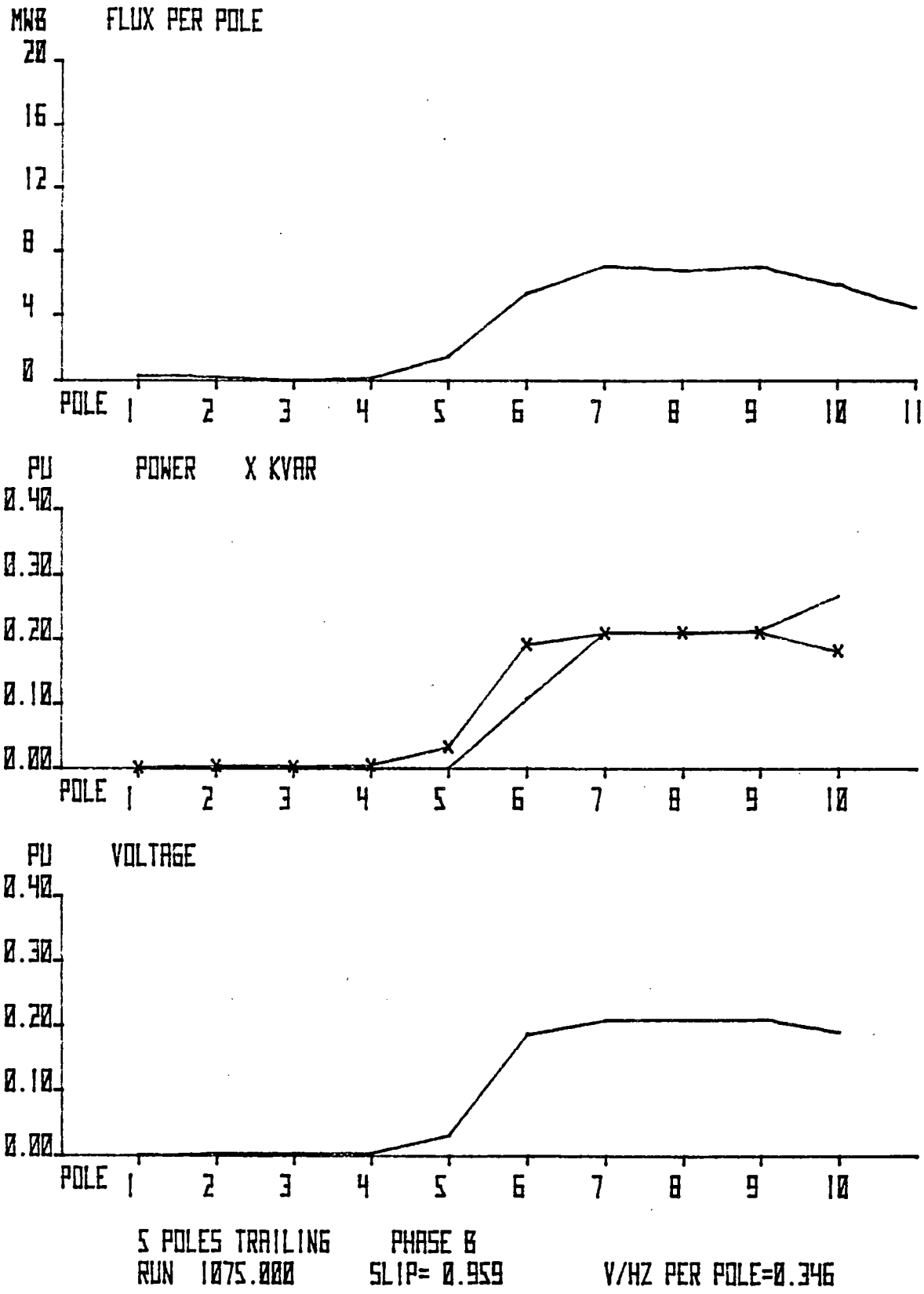

Figure 8-49. Distributed Parameters, Phase B at 0.959 Slip

TABLE 8-6

SLIM PHASE ARRANGEMENT

	Slots										
	1-5	6-10	11-15	16-20	21-25	---	136-140	141-145	146-150	151-155	156-160
Phase (slot root)	C	B	-A	C	B	---	C	B	A	-	-
Phase (slot tip)	-	-	-C	-B	A	---	B	A	-C	-B	A

Test Results

Figure 8-50 and 8-51 show distributed parameters data for two test runs at similar slips with test excitation levels of 0.51 and 0.33 V/Hz/pole, respectively. Both sets of data were normalized to 0.346 V/Hz/pole and plotted. A comparison of these two curves shows:

- A slight reduction in peak pole flux of the #5 pole at the higher excitation level.
- No detectable difference in other distributed parameters.

Figures 8-52 and 8-53 graphically depict two electrical performance characteristics obtained at different levels of test excitation. Figure 8-52 shows mean line current variation with slip for the 5-pole L configuration at three excitation levels. Figure 8-53 shows thrust variation with slip for the 5-pole L configuration at the same three excitation levels. A measurable difference in normalized parameters occurs at the high excitation level, 0.51 V/Hz/pole. There is no detectable difference at the two lower excitation levels, 0.34 and 0.43 V/Hz/pole.

General Conclusions

- Testing at excitation levels up to 0.43 V/Hz/pole reveals that the effects of saturation are within experimental error.
- At an excitation level of 0.51 V/Hz/pole, thrust degradation occurs (0.17 kN at the peak thrust of 3.65 kN). In addition, an increased normalized mean line current of approximately 0.05 kA (3.8 percent at 0.2 slip) is drawn from the supply.
- Over the stated range of excitation, no detectable change occurs in power, kVAR, and voltage distribution. However, pole flux peaks are apparently reduced.

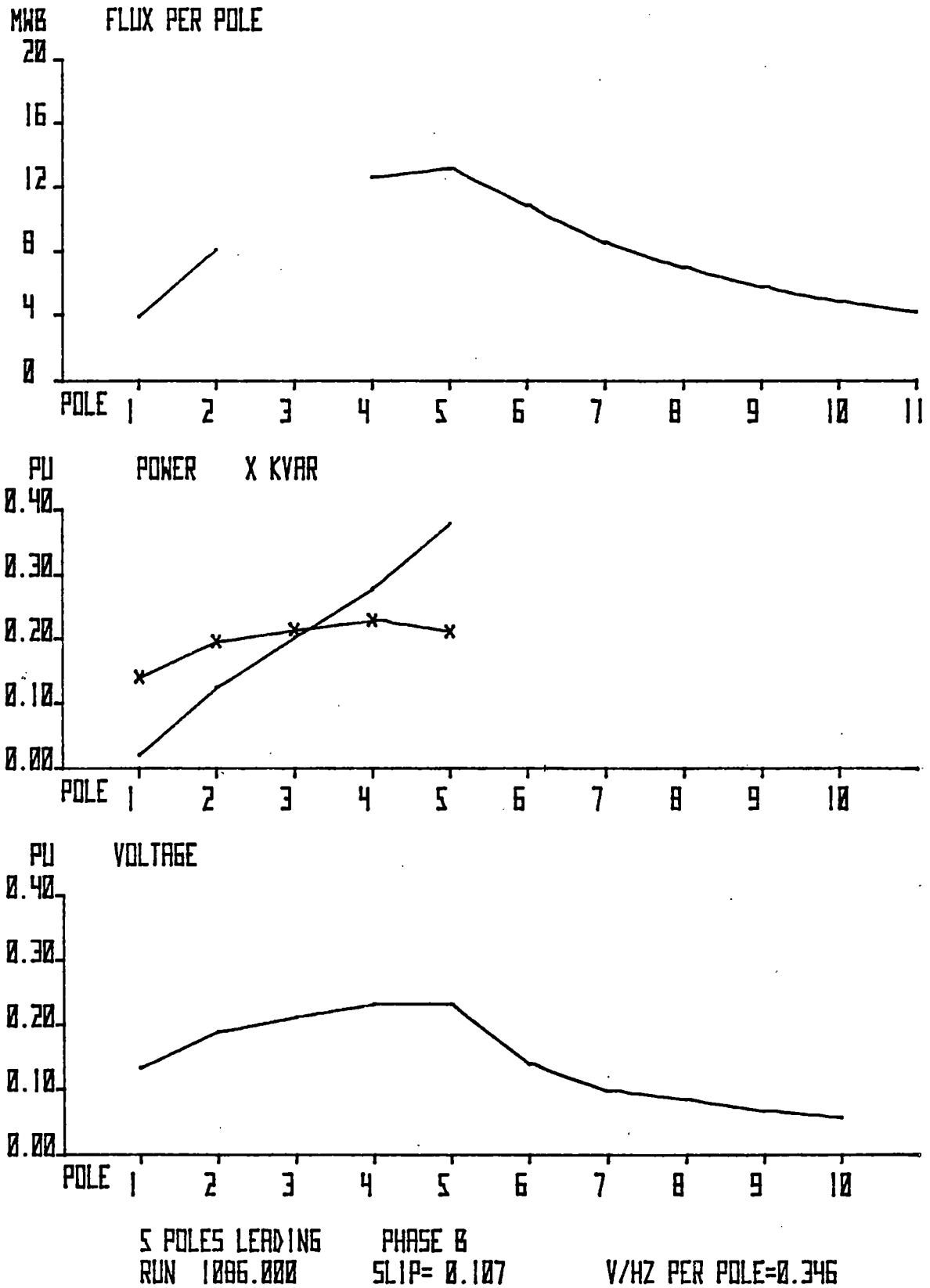

Figure 8-50. Distributed Parameters, Phase B at 0.107 Slip, High Excitation

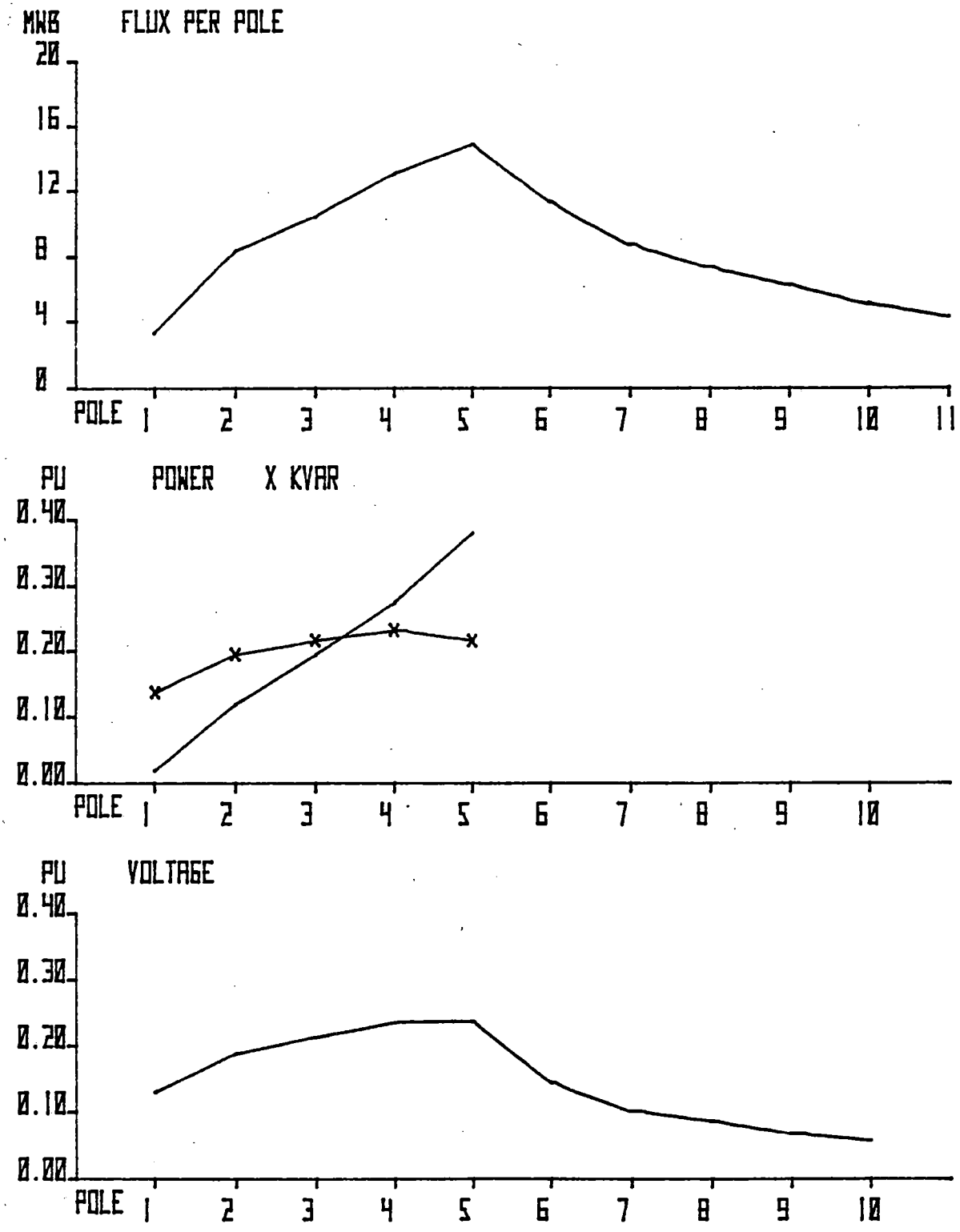

Figure 8-51. Distributed Parameters, Phase B at 0.346 Slip, Low Excitation

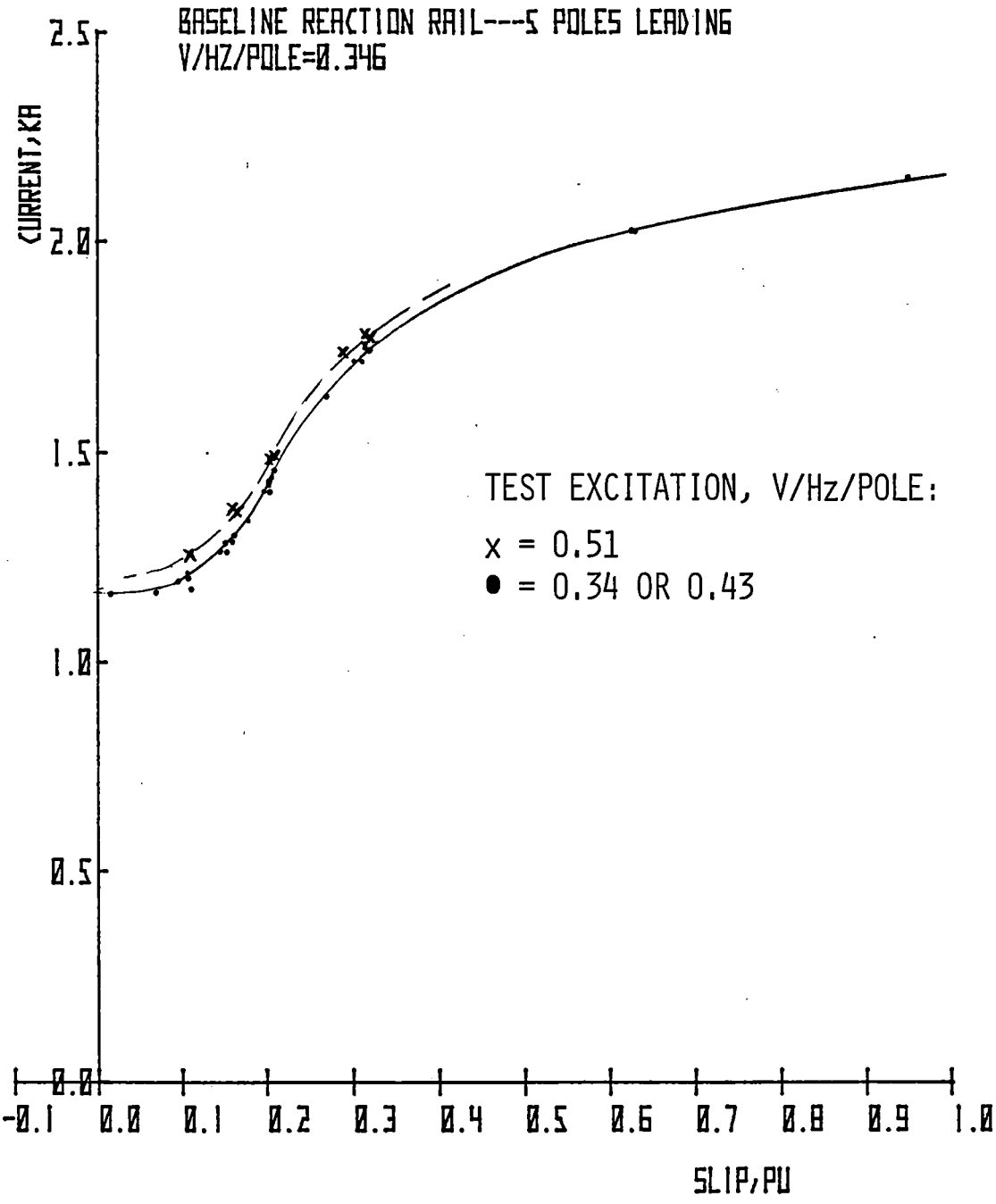

Figure 8-52. Mean Line Current vs Slip, 5 Poles Leading

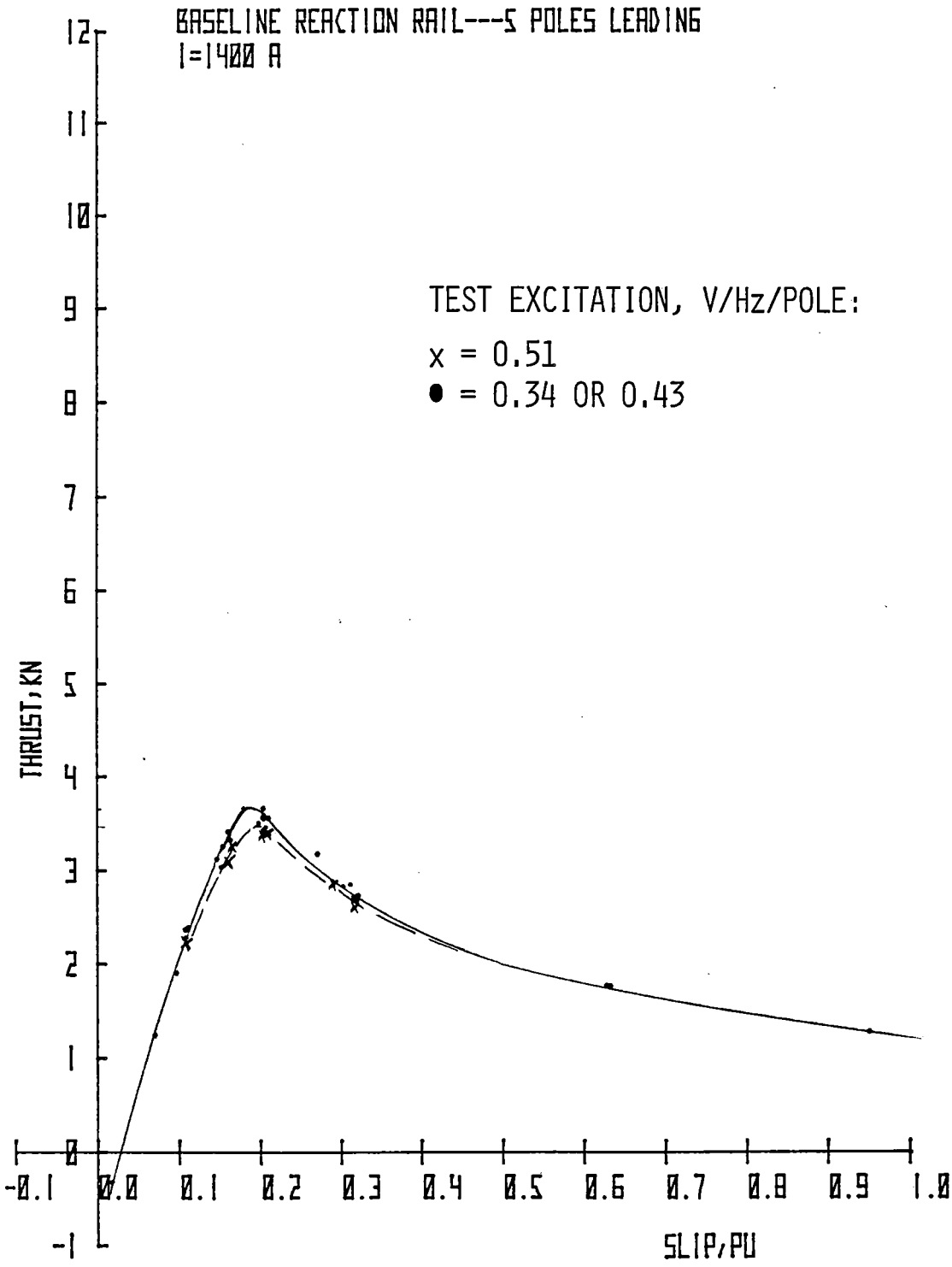

Figure 8-53. Thrust vs Slip, 5 Poles Leading

- Changes in other parameters were found to be small. Complete data is shown in Volume II.

- Testing at an excitation level of 0.43 V/Hz/pole or below will cause no appreciable error due to normalizing.

EFFECT OF SECONDARY DISCONTINUITIES

In Appendix B, Figure B-3 shows details of the aluminum jumper strap that was fitted to the rail to reduce the effect of current discontinuities at the junction of adjacent aluminum cover sections. Performance of such devices is difficult to predict for a practical installation. Therefore, tests were performed to evaluate strap effectiveness.

Test Description

The vehicle was operated with dc excitation at low speed, to minimize unrelated mechanical disturbances. Eddy currents, however, caused high motor forces, both braking and attraction forces. Current discontinuities cause transient variations in vertical forces, and it was the purpose of this test to examine these transient forces with the aluminum jumper strap installed, and again with the strap removed.

Test Results

Run 1118 was conducted at low speed (0 to 5 m/s) with dc excitation over a section of the reaction rail fitted with jumper straps, and a section without the straps. No differences in electrical performance or vertical force characteristics were detectable, either on a steady-state or a transient basis.

Discussion

With the benefit of the ever-elusive hindsight, it appears from subsequent testing that a low-speed ac excitation test would have enabled pole flux monitoring while the motor traversed reaction rail discontinuities. Other tests reported herein revealed distinct perturbations in pole flux as the vehicle traversed over discontinuities. It would have been instructive to repeat run 1118 with ac excitation to acquire microscopic information on the effect of current jumpers. On the other hand, the actual testing performed disclosed no significant force variations at the discontinuity interface not equipped with jumpers. Thus, efficiency of the current jumpers was not proved. It would, however, appear that a reaction rail constructed without current jumpers would fail to provide significant force transients through the primary due to the secondary discontinuities.

SECTION 9

SOLID IRON REACTION RAIL TESTS

INTRODUCTION

Tests of the SLIM with the solid iron reaction rail were performed in the 10-pole configuration only. Two nominal airgaps were used:

- Gap = 26 mm nominal. This is the same primary/secondary setting used for the baseline reaction rail tests except that the aluminum cover has been removed. Therefore, the entrefer is identical with that in the baseline reaction rail tests.

- Gap = 18 mm nominal. This represents the minimum safety operating gap for the LIMRV in the SLIM configuration when testing at speeds up to 67 m/s.

DC BRAKING TESTS

Data was acquired from runs 1119 and 1120 for the purpose of:

- Ascertaining the eddy current braking characteristic

- Evaluating the effect of saturation

Table 9-1 lists excitation levels for the two runs.

TABLE 9-1

EXCITATION LEVELS OF DC BRAKING TESTS, 26-MM AIRGAP

Run	I Test, kA	I Norm, kA	RATI
1119	0.97	1.36	0.71
1120	1.36	1.36	1.00

Figures 9-1 and 9-2 show the braking characteristic of the 10-pole SLIM for runs 1119 and 1120, respectively.

Figures 9-3 and 9-4 show the variation of vertical force with speed (constant excitation). The effects of saturation are summarized in Table 9-2.

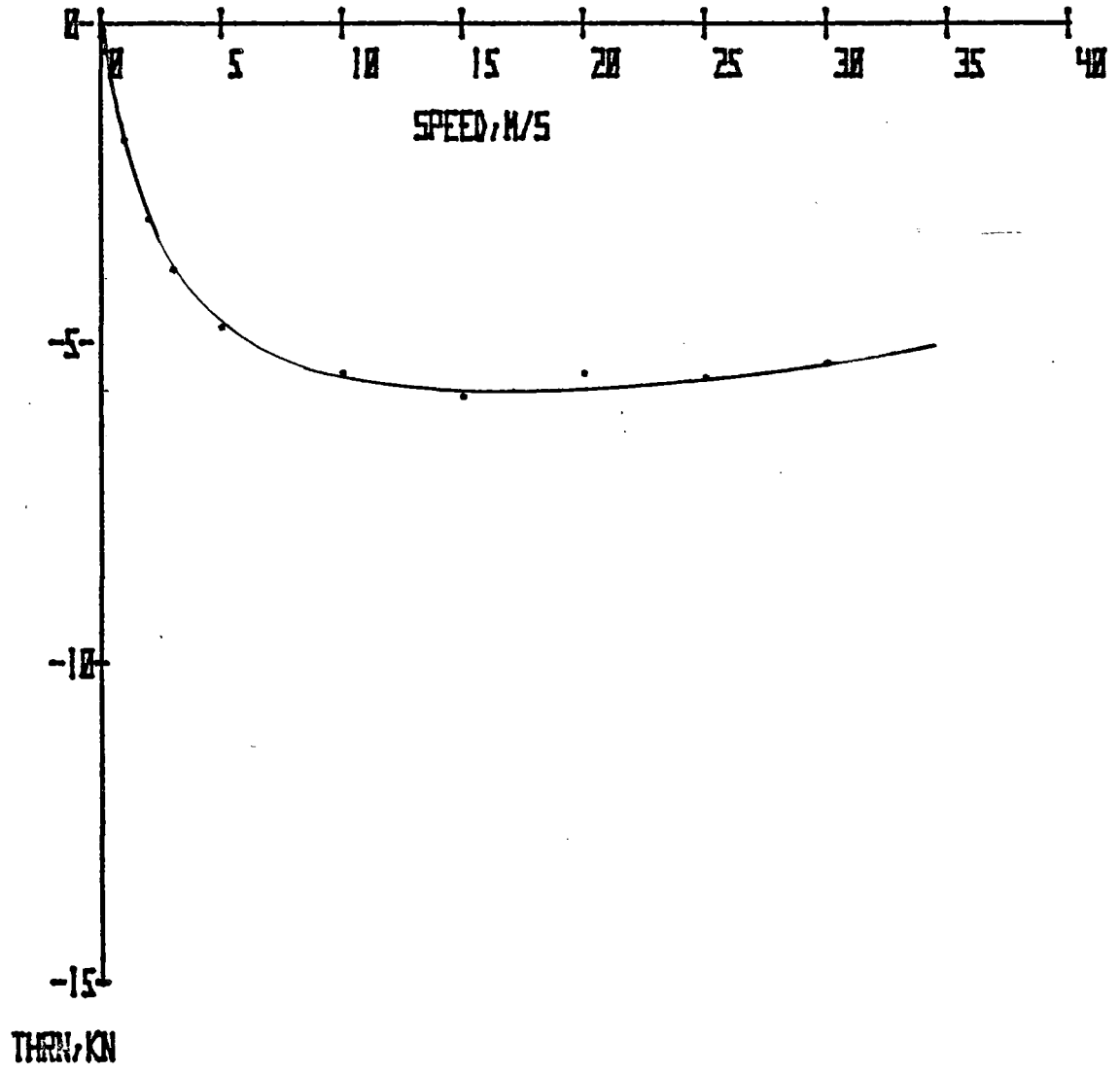

Figure 9-1. Braking Force vs Speed, 10-Pole SLIM, Run 1119

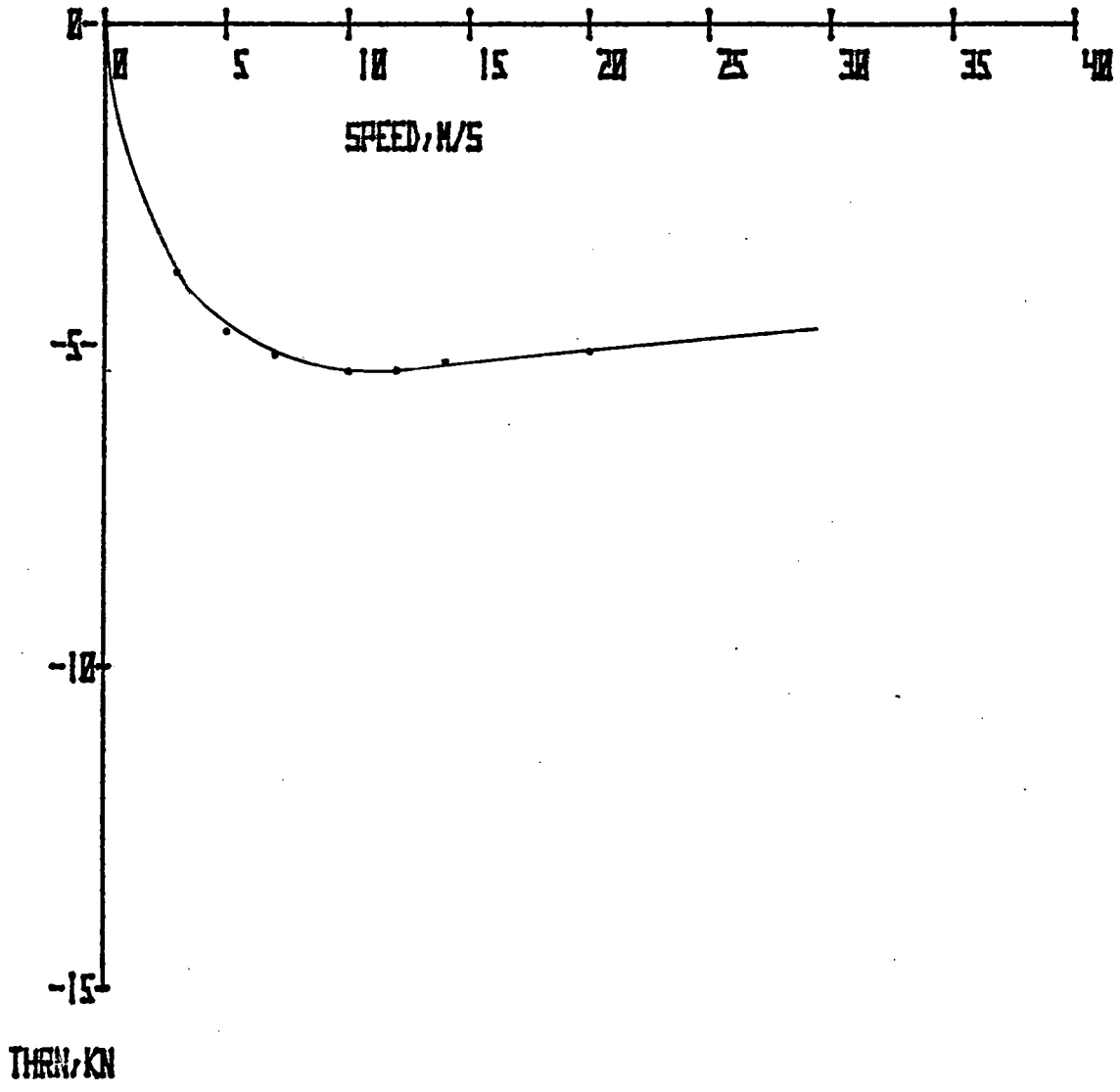

Figure 9-2. Braking Force vs Speed, 10-Pole SLIM, Run 1120

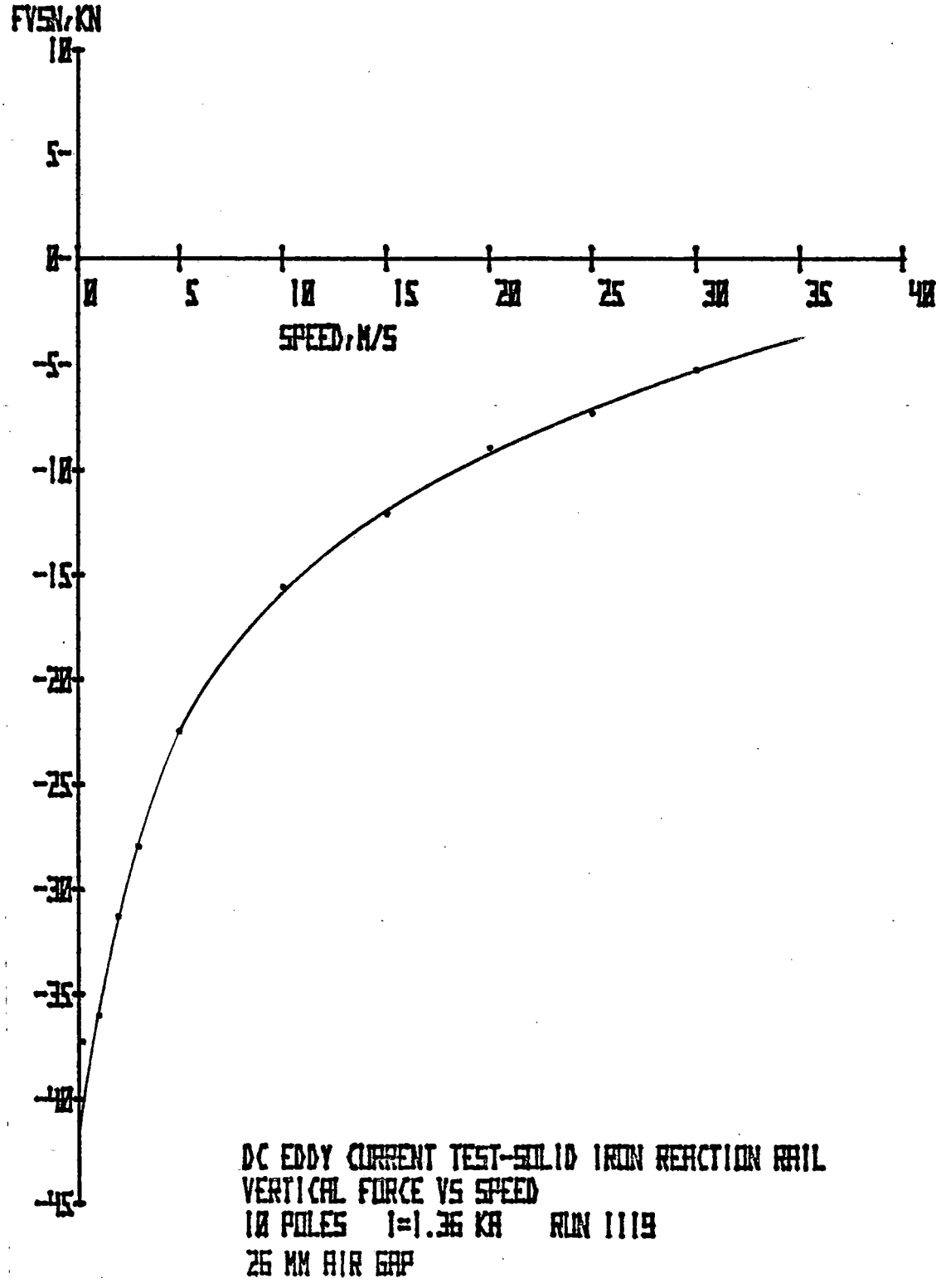

Figure 9-3. Vertical Force vs Speed, 10-Pole SLIM, Run 1119

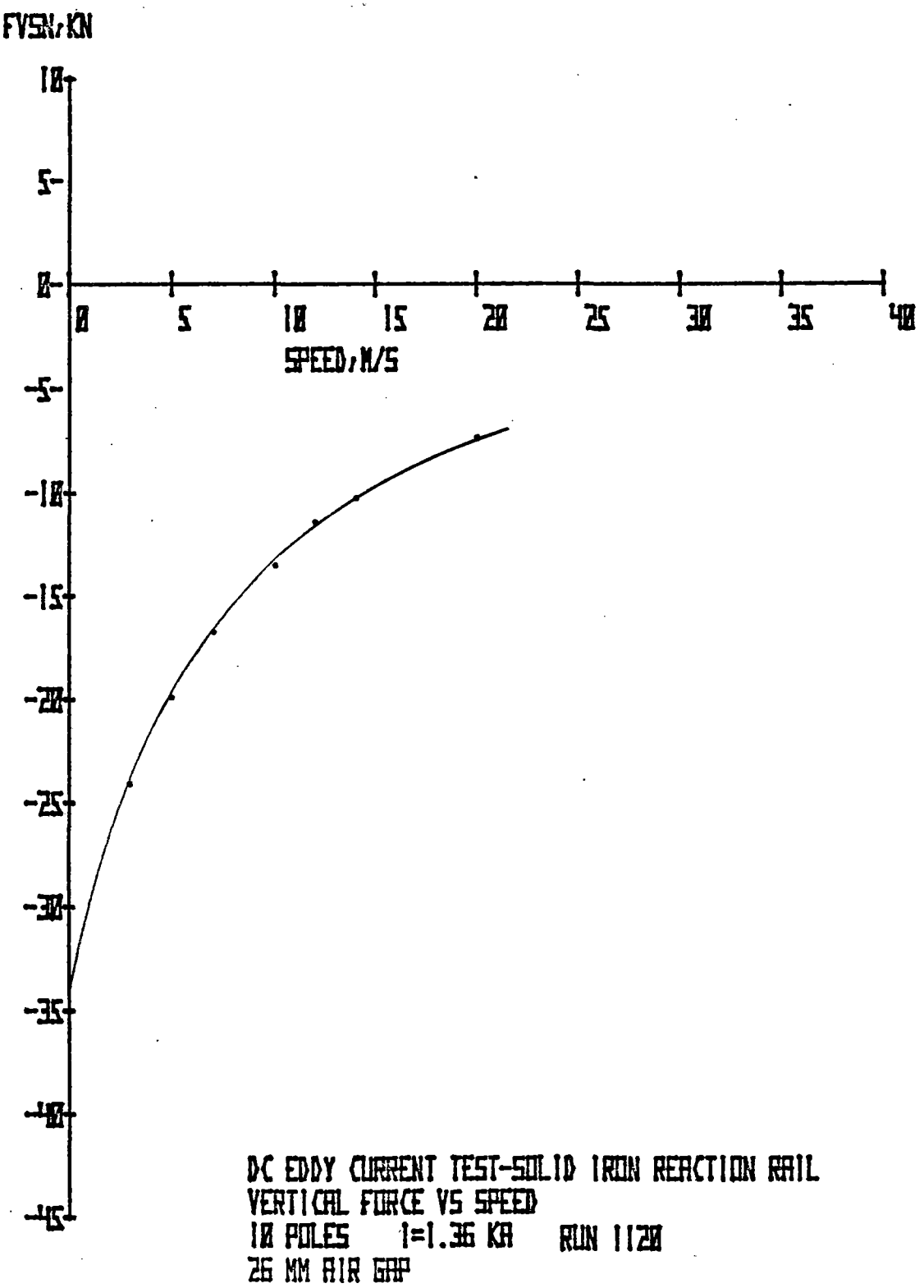

Figure 9-4. Vertical Force vs Speed, 10-Pole SLIM, Run 1120

TABLE 9-2

EFFECT OF SATURATION ON BRAKING FORCE AND VERTICAL FORCE

Run	RATI	Peak Braking Force (Normalized to 1.36 kA), kN, at Given Speed	FVSN at Speed = 0, kN	FVSN at Speed = 20 m/s, kN
1119	0.71	-5.7 at 17.0 m/s	-41.8	-9.1
1120	1.00	5.35 at 12.9 m/s	-34.0	-7.5

The following observations are derived from Table 9-2:

- Peak braking force is dependent on the saturation level, although the peak value is not clearly defined.
- The effect of saturation on vertical force at the higher current (1.36 kA) is manifested by a significant loss of force (17 to 18 percent).
- The effect of saturation on the braking force at speeds above 15 m/s is significant due to flux penetration effects in the reaction rail.

AIRGAP VARIATION

Figures 9-5 and 9-6 show the braking and vertical force characteristics for constant current excitation at a reduced airgap of 18 mm.

Figure 9-7 shows the variation of vertical force vs (excitation current)^2 for the motor at zero speed.

Figures 9-5, 9-6, and 9-7 lead to the following observations:

- The onset of nonlinear behavior occurs at a current level of approximately 0.55 kA.
- At an excitation current level of 0.77 kA, the departure of the vertical force from linearity is approximately 8.3 percent (Figure 9-7).
- The braking force has a flat characteristic above 5 m/s at the reduced airgap of 18 mm. Because of the high saturation effects at the 1.36-kA current level, the flat characteristic appears to be due to low penetration depth.

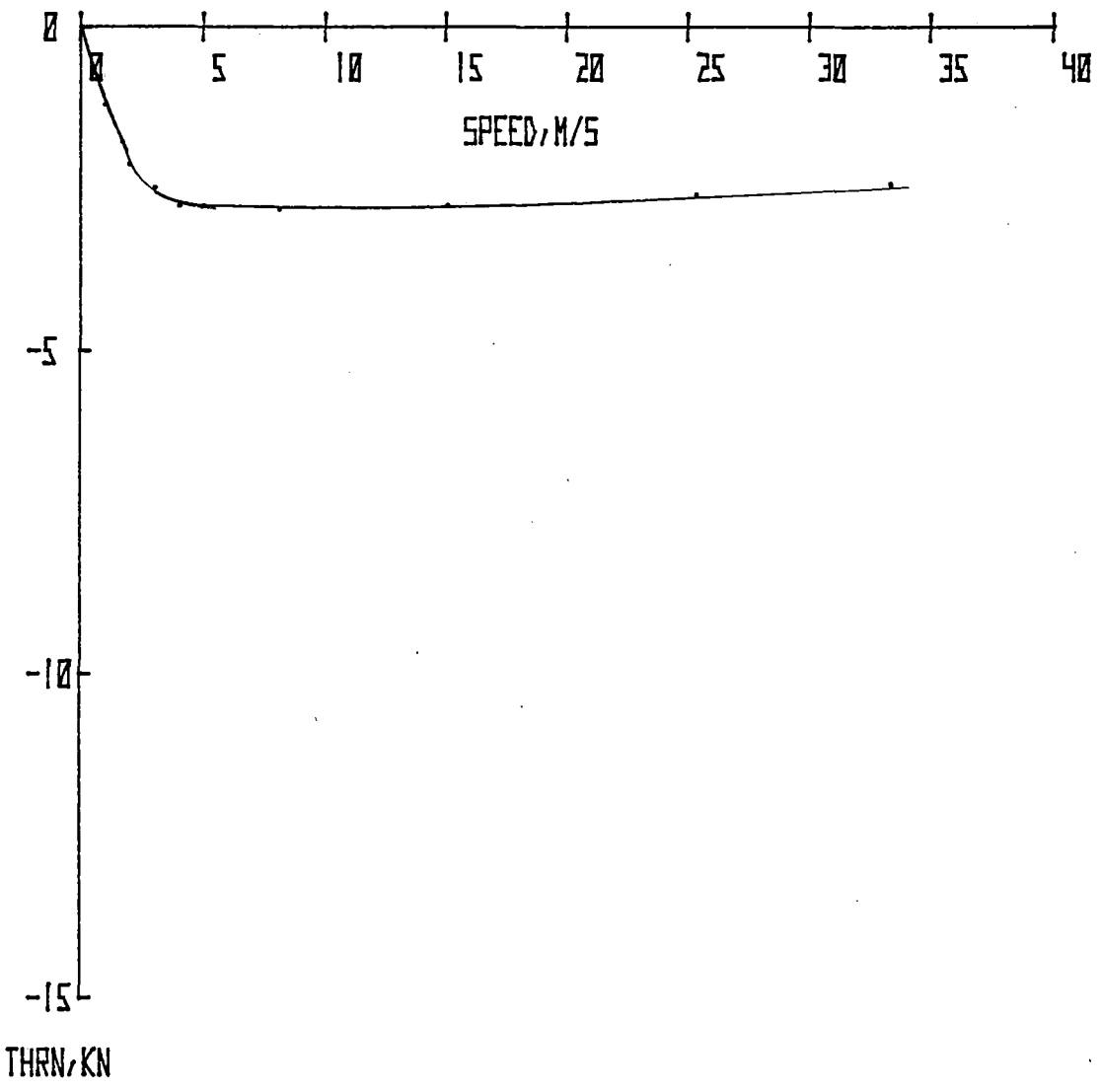

Figure 9-5. Braking Force vs Speed, 10-Pole SLIM, Run 1081

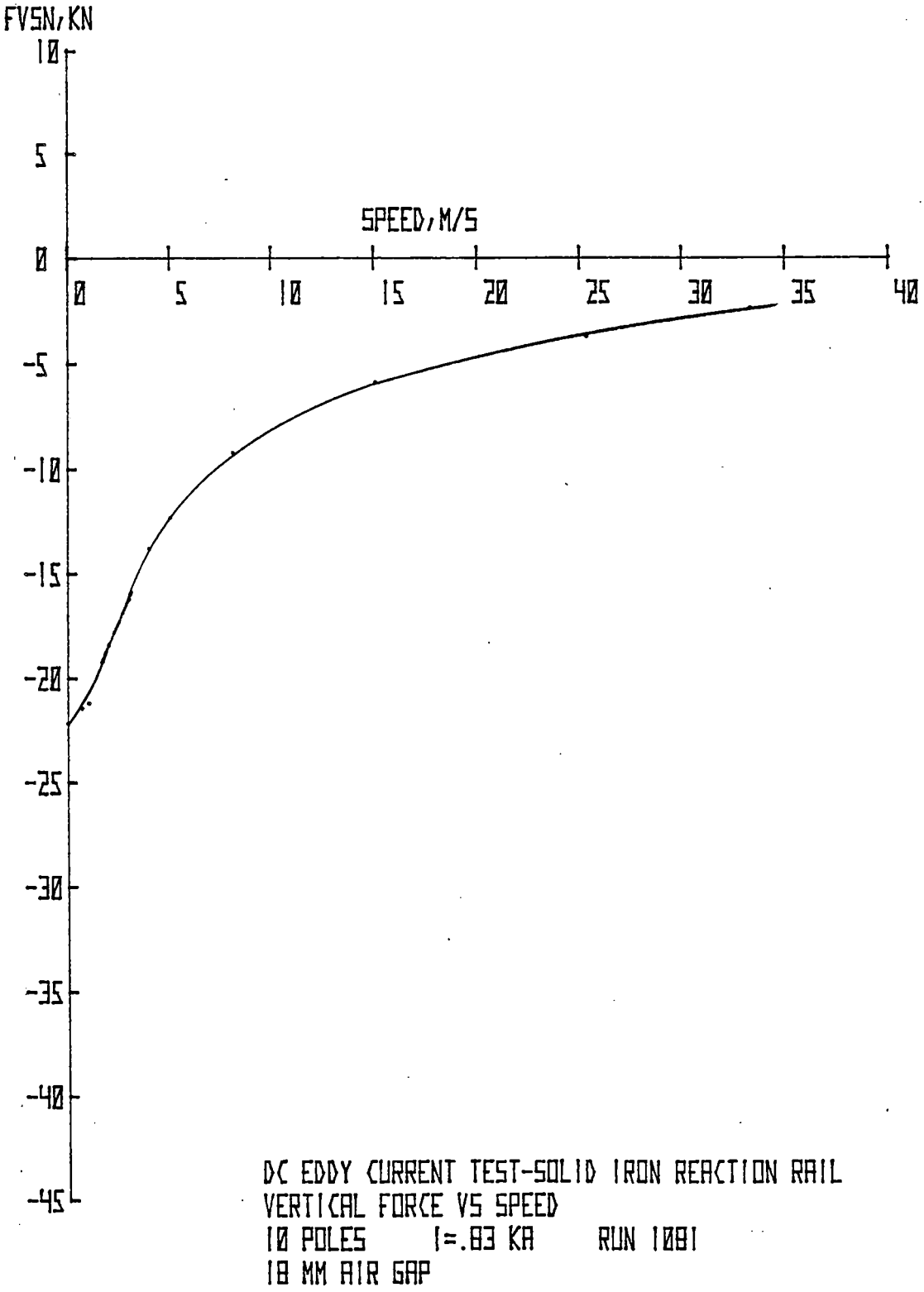

Figure 9-6. Vertical Force vs Speed, 10-Pole SLIM, Run 1081

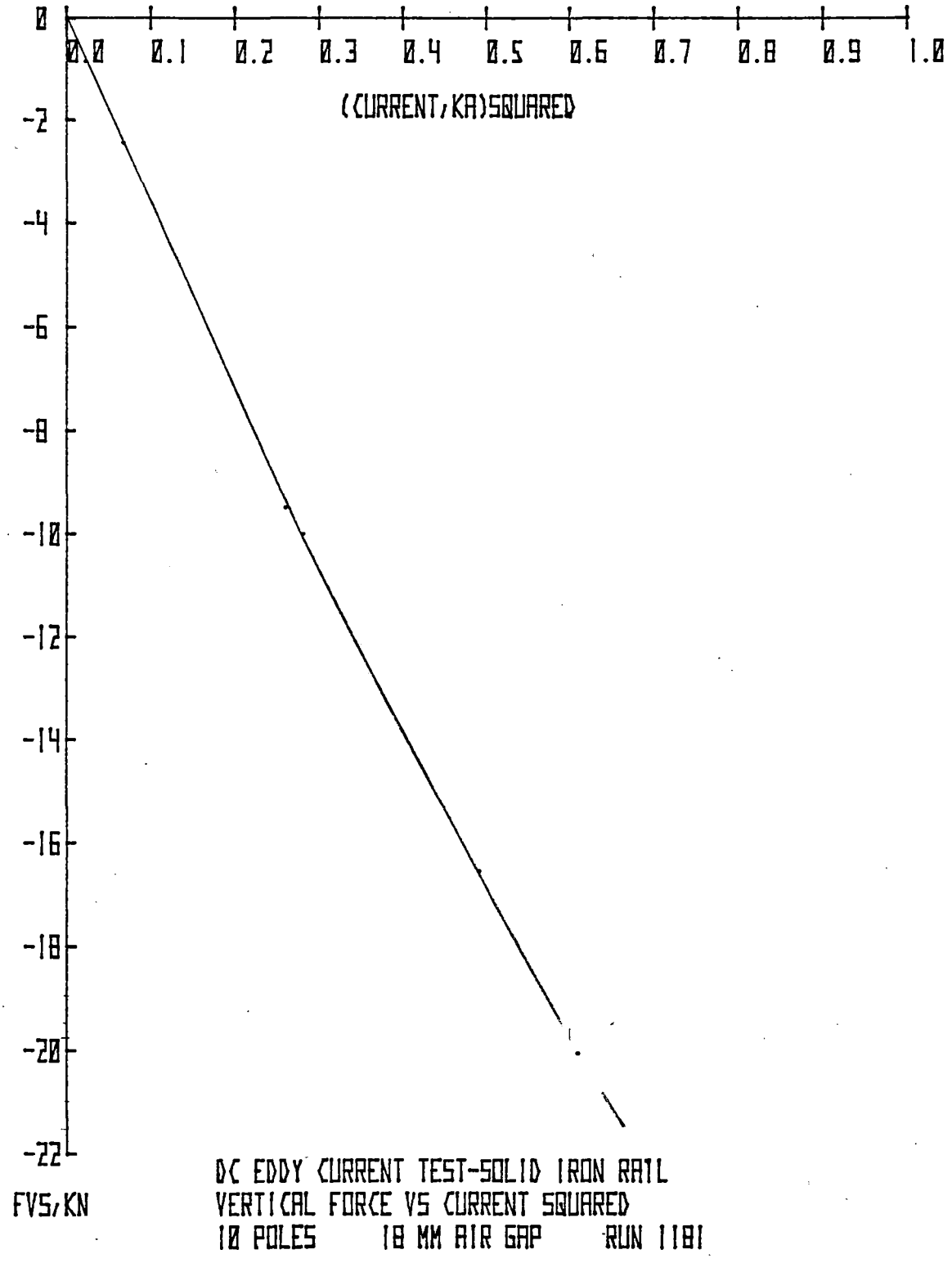

Figure 9-7. Vertical Force vs Current Squared, 10-Pole SLIM, Run 1181

ELECTRICAL PERFORMANCE TESTS

Introduction

All solid iron reaction rail tests were performed at an excitation level of approximately 0.416 V/Hz/pole, resulting in a predictably higher saturation effect. Data were later normalized to the 0.346 V/Hz/pole condition for comparison with the baseline reaction rail test results.

Thrust vs Slip

Figures 9-8 and 9-9 show the thrust vs slip characteristic normalized to 1400 A for 18- and 26-mm airgaps, respectively.

Figures 9-10 and 9-11 show the same data normalized to 0.346 V/Hz/pole. The curves in the above figures elicit the following observations:

- The interception of the thrust and slip axes is approximately at the zero-speed point. Thus, one of the manifestations of end effect, i.e., loss of force, is less significant for the solid iron reaction rail than for the baseline reaction rail.

- At low slips, the difference in thrust between the two airgaps is greater when the data is normalized to the constant current condition rather than to the constant V/Hz/pole condition. This illustrates the difficulty of normalizing such data; but the apparently favorable thrust characteristic at a 26-mm airgap (data normalized to constant V/Hz/pole is achieved at the expense of higher primary input power. (See Power Loss vs Slip in this section).

Current vs Slip

Figures 9-12 and 9-13 show the variation of mean primary current with slip for airgaps of 18 and 26 mm.

Figures 9-14 and 9-15 show the corresponding current loci for the current vs slip characteristics. These curves support the following observation:

- Even though the current magnitudes for the 18- and 26-mm airgaps are almost identical, the real component of the LIM primary current is clearly higher for the 18-mm airgap. This explains the significant difference between the thrust curves when the normalizing constant does not take into account the phase angle.

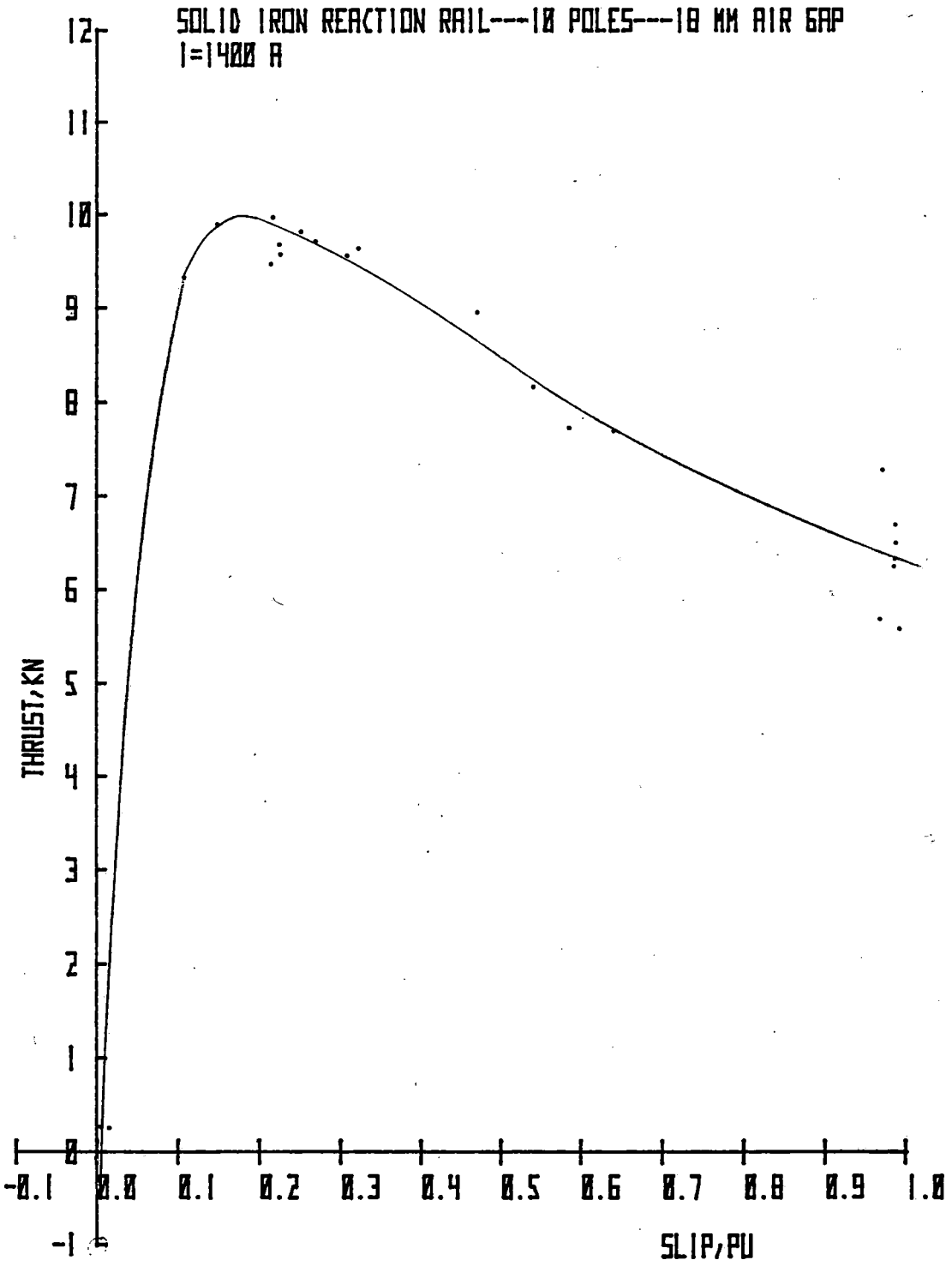

Figure 9-8. Thrust vs Slip, 10-Pole SLIM, 18-mm Airgap, I = 1400 A

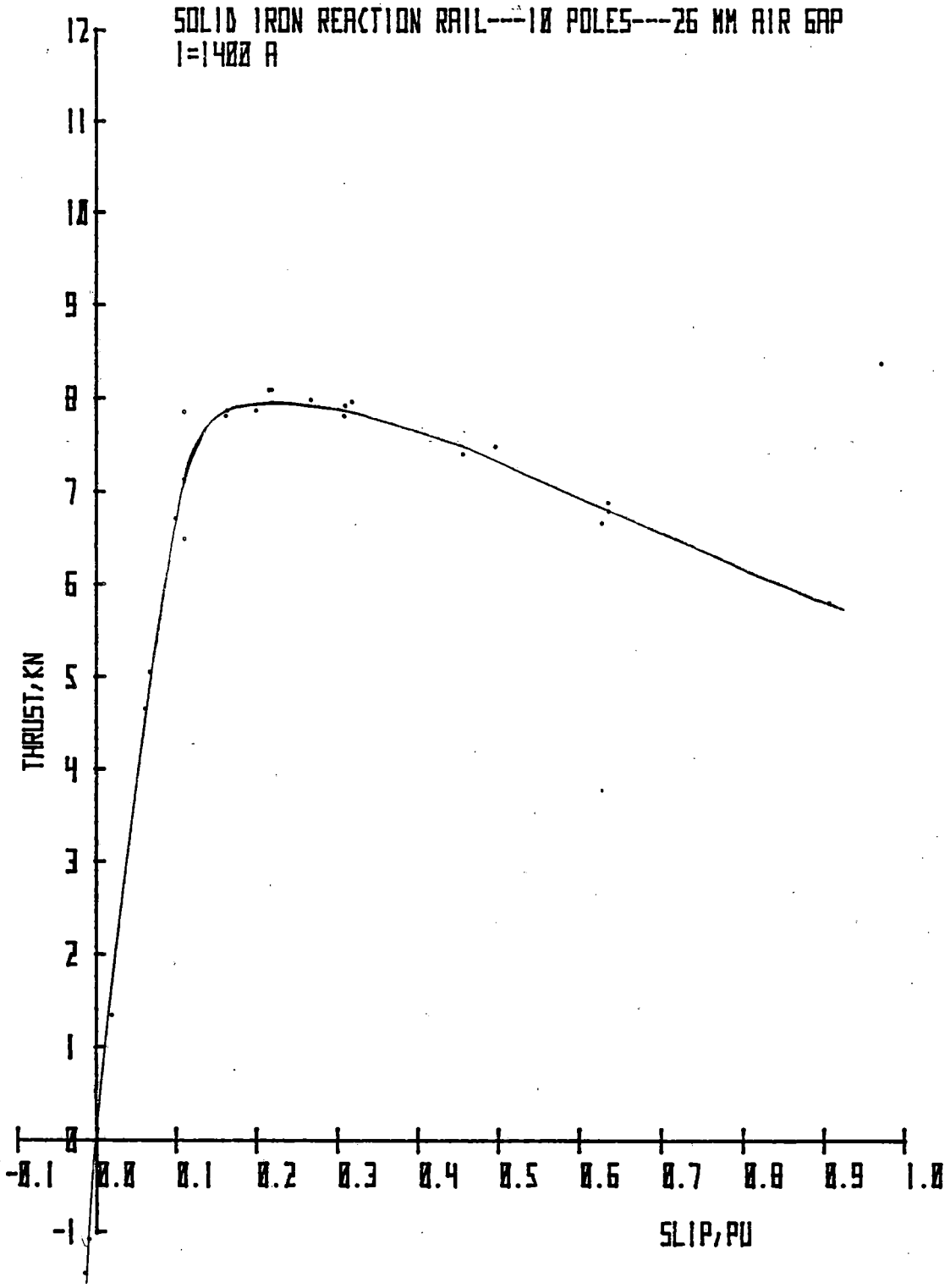

Figure 9-9. Thrust vs Slip, 10-Pole SLIM, 26-mm Airgap, I = 1400 A

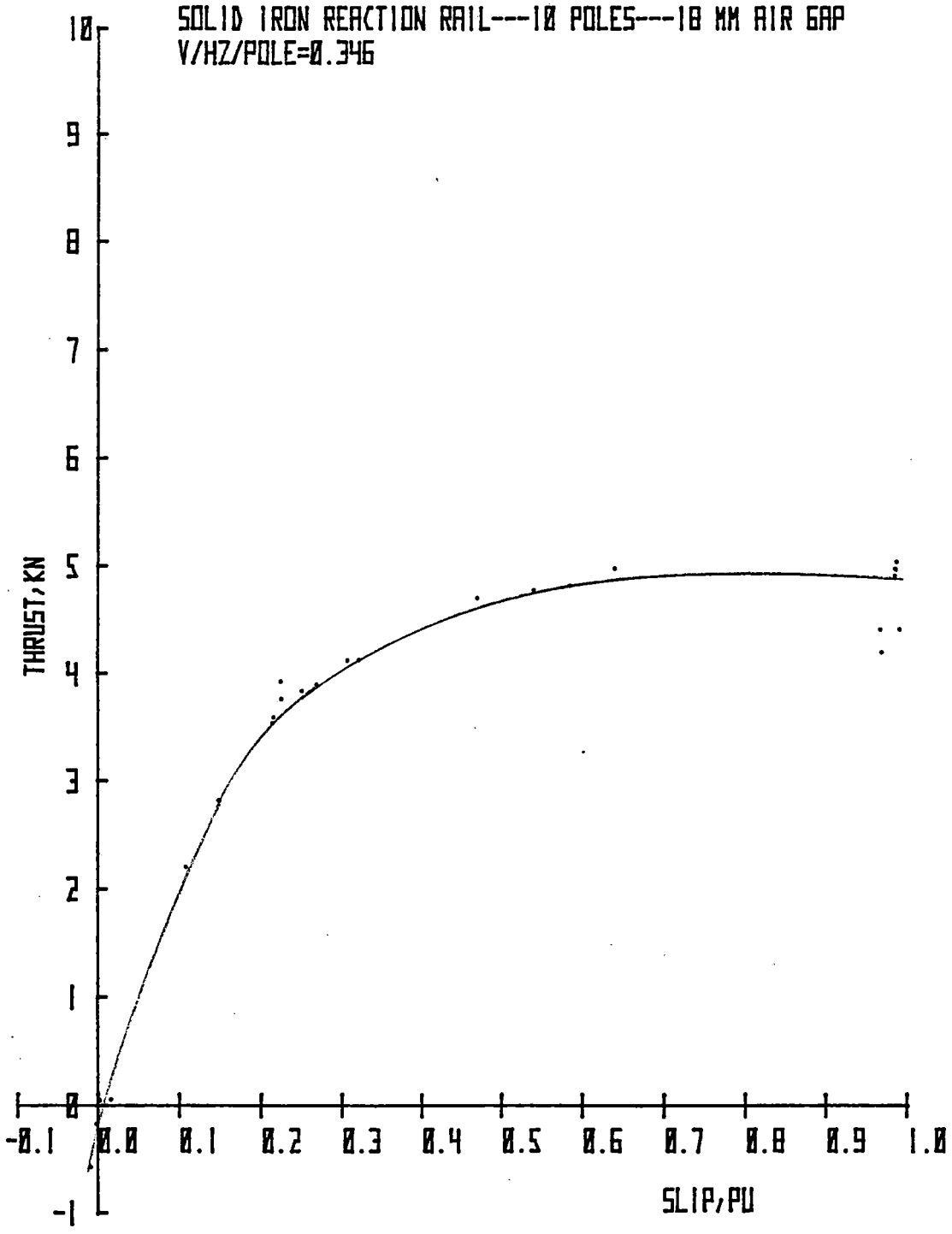

Figure 9-10. Thrust vs Slip, 18-mm Airgap, V/Hz/Pole = 0.346

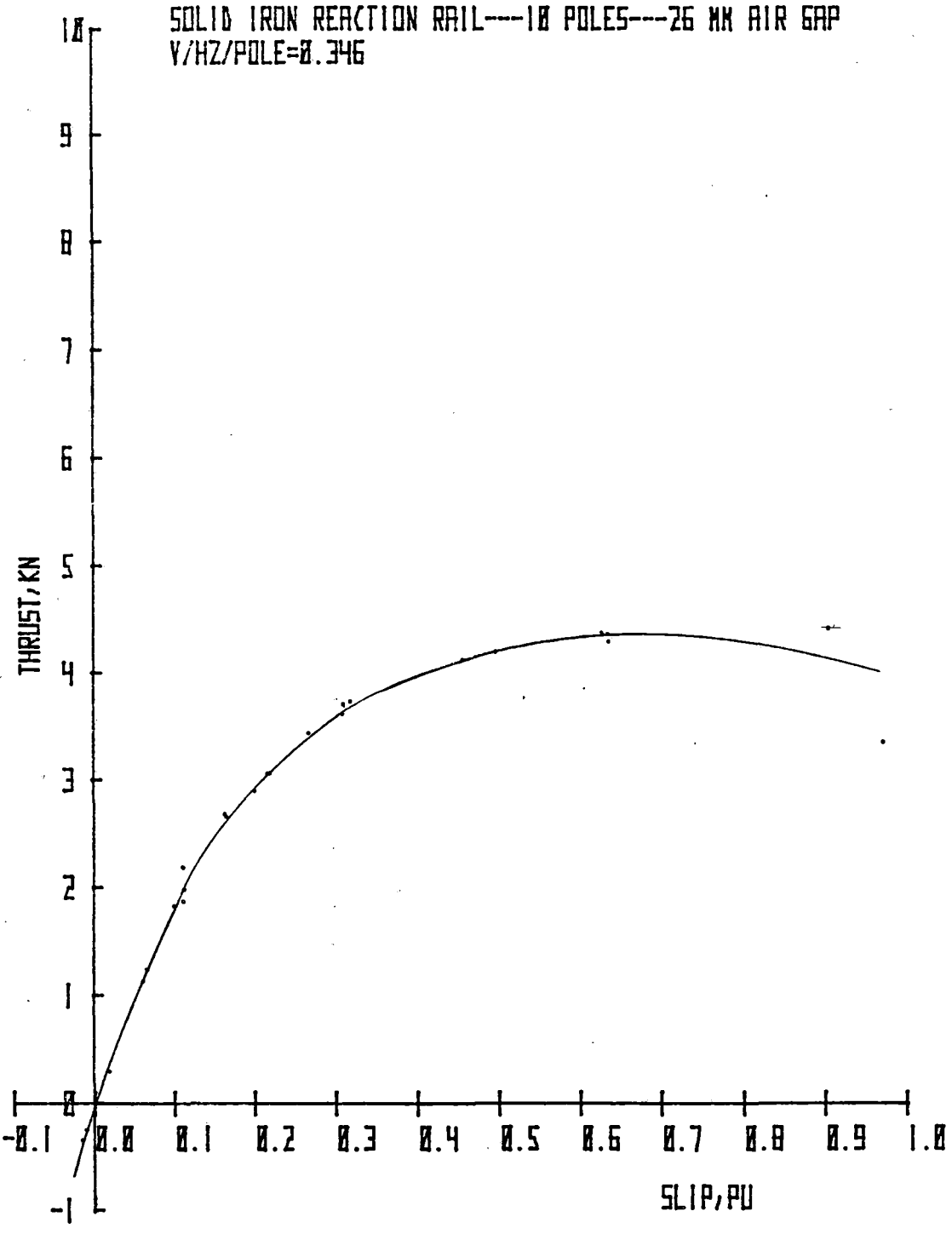

Figure 9-11. Thrust vs Slip, 26-mm Airgap, V/Hz/Pole = 0.346

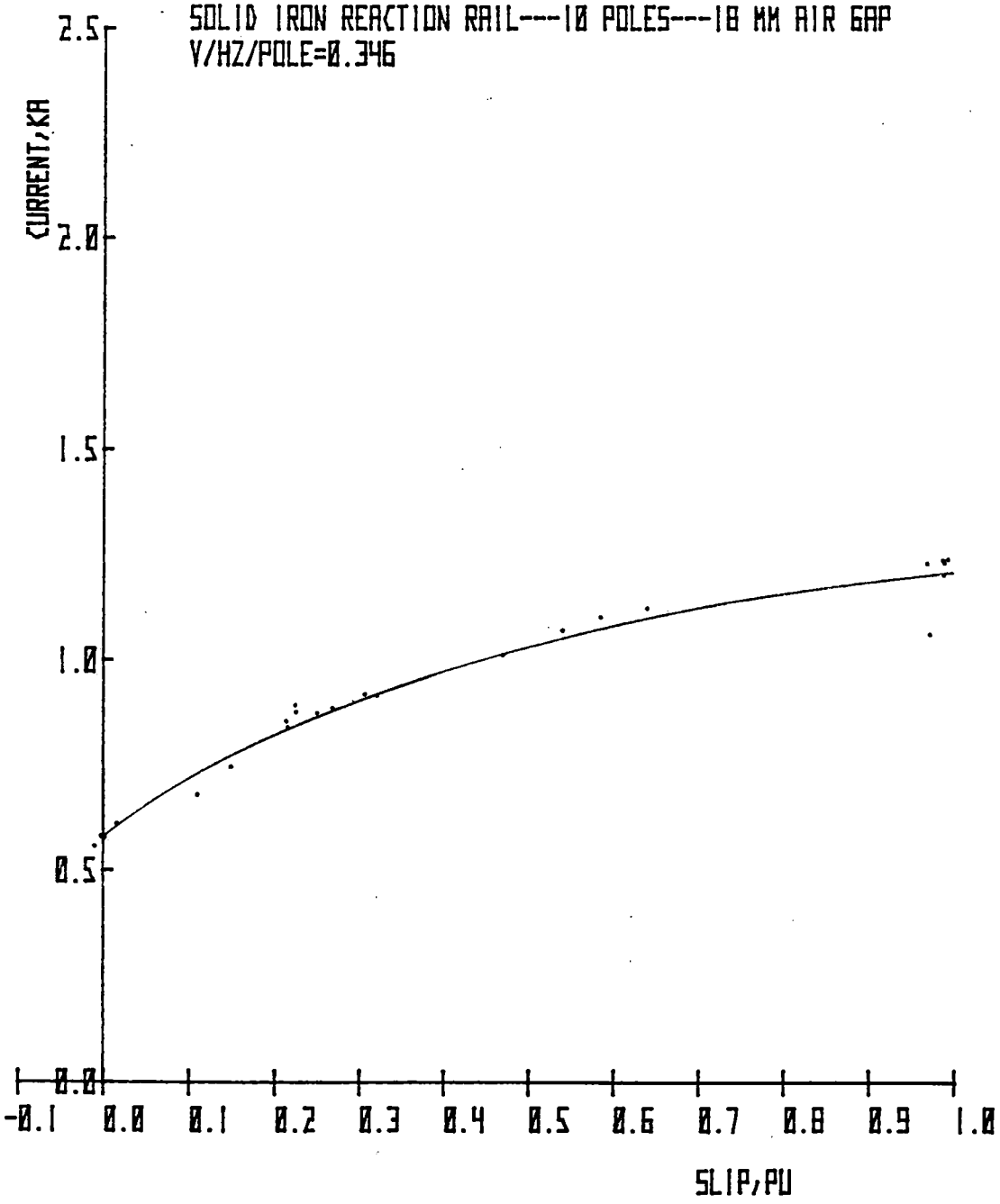

Figure 9-12. Mean Line Current vs Slip, 18-mm Airgap

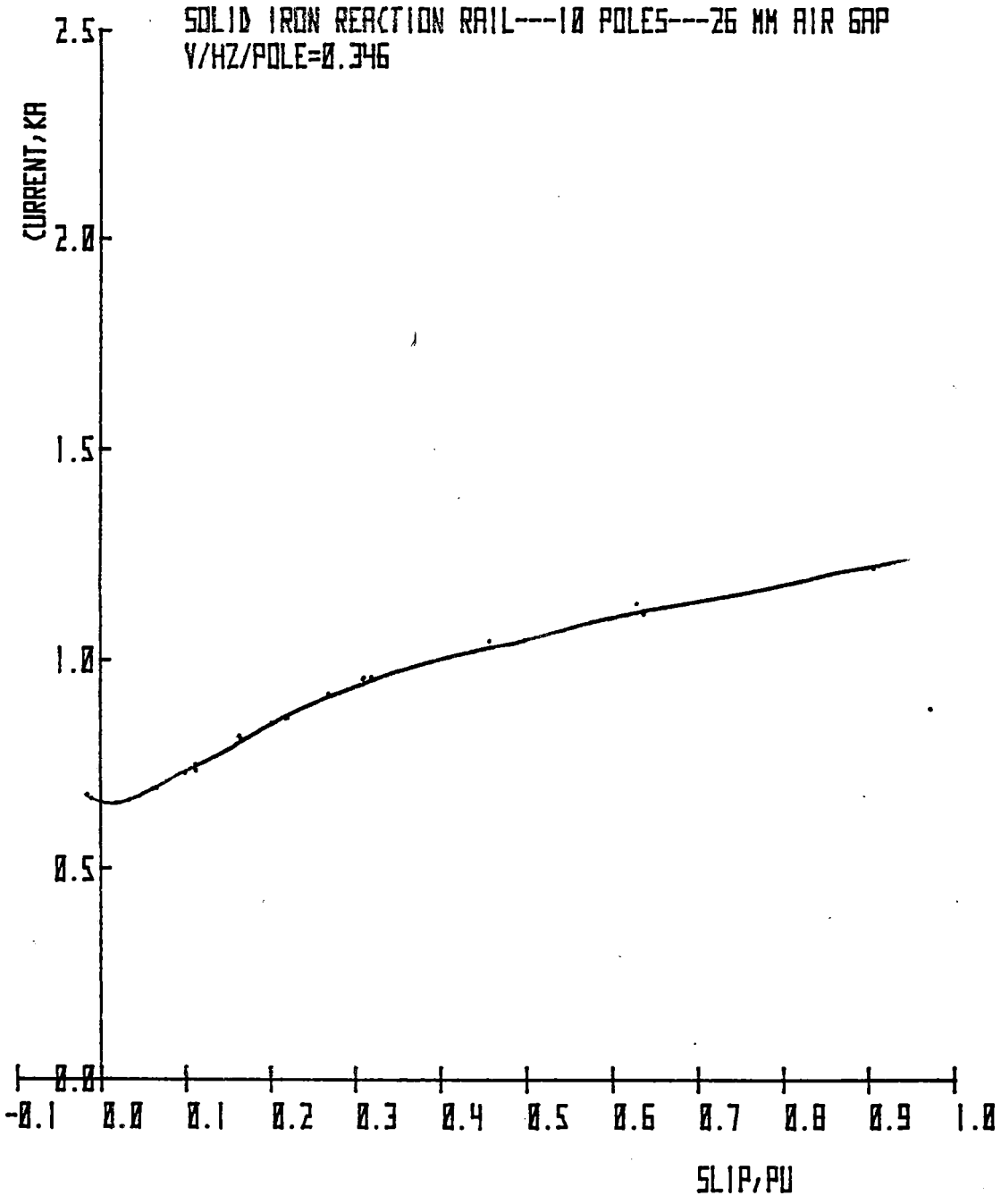

Figure 9-13. Mean Line Current vs Slip, 26-mm Airgap

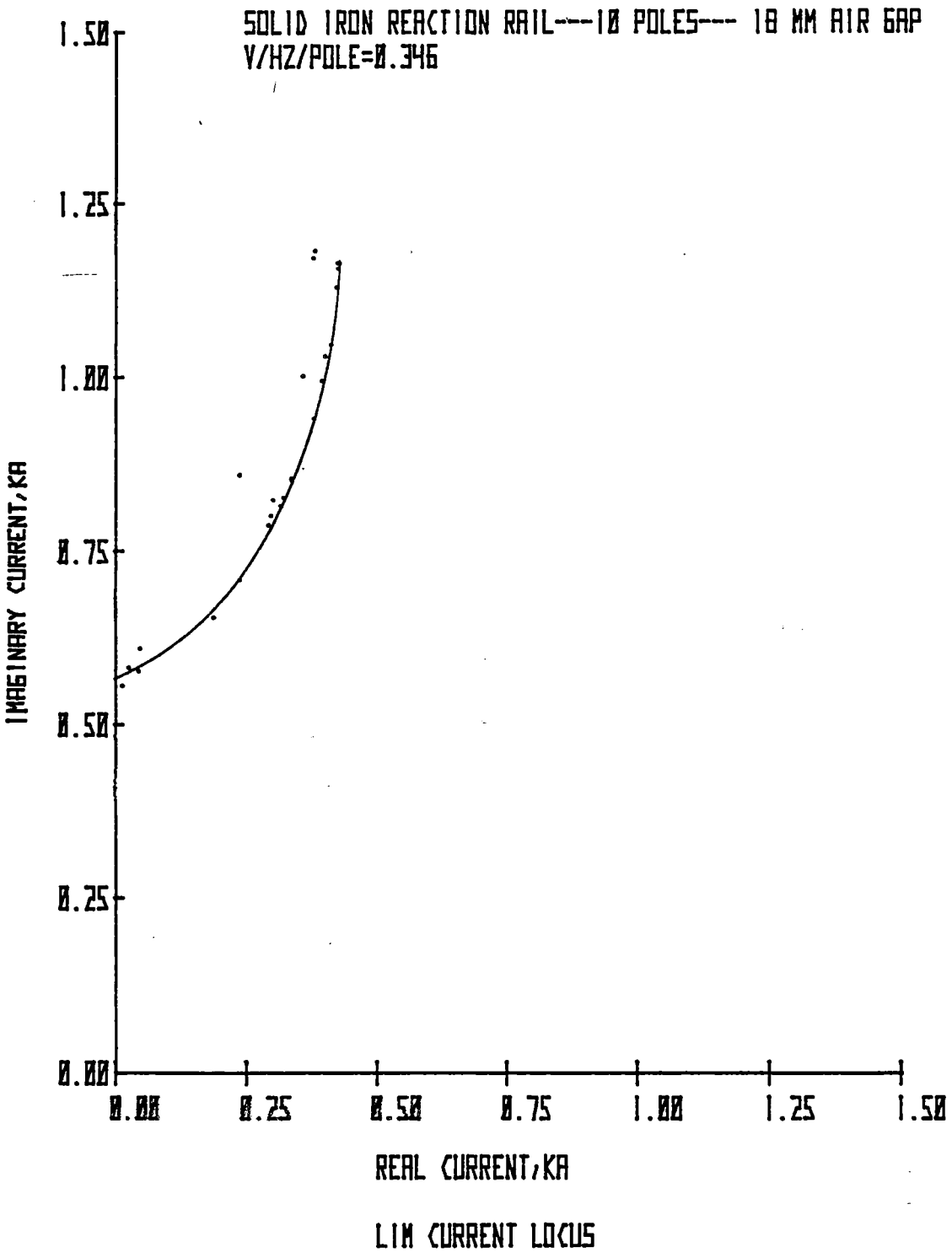

Figure 9-14. Imaginary Current vs Real Current, 18-mm Airgap

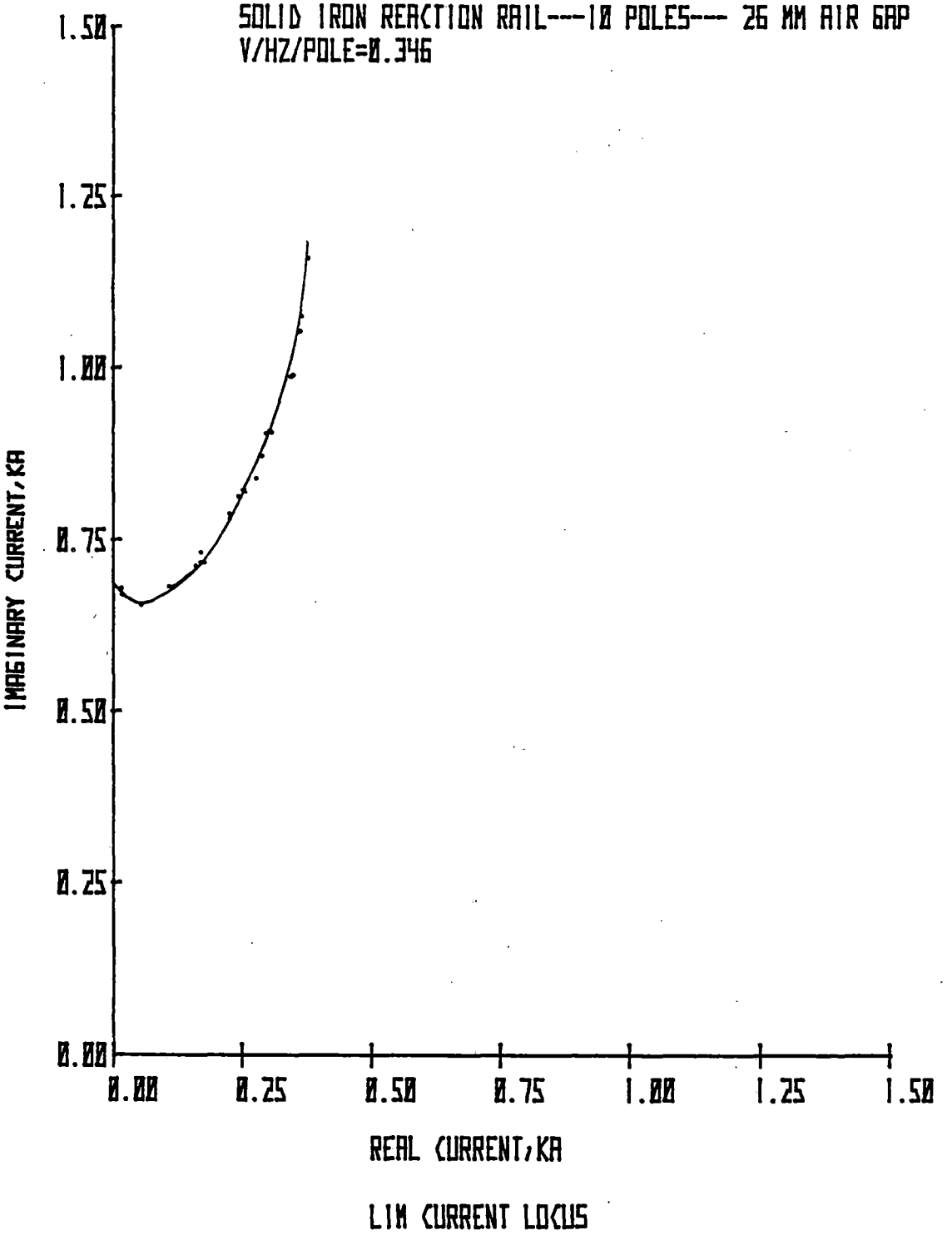

Figure 9-15. Imaginary Current vs Real Current, 26-mm Airgap

Mean Voltage Variation vs Slip

Figures 9-16 and 9-17 show the variation of mean phase voltage with slip for 18- and 26-mm airgaps, respectively. With data normalized to a constant current of 1400 A, the mean voltage per pole for the two airgaps is listed in Table 9-3.

TABLE 9-3

MEAN VOLTAGE VARIATION

Slip	Voltage per Pole, 18-mm Airgap, V	Voltage per Pole, 26-mm Airgap, V	$\frac{V_{18}}{V_{26}}$
0.0	79.6	68.3	1.17
0.2	55.8	53.8	1.04
0.4	46.4	45.9	1.01
1.0	37.2	36.5	1.02

At high values of slip, the motor's kVA is apparently unaffected by airgap and may be considered to be a direct function of the secondary impedance.

Efficiency and Power Factor vs Slip

Figures 9-18 and 9-19 show the variation of efficiency with slip at the two airgaps.

Figures 9-20 and 9-21 show the variation of power factor with slip at these same two airgaps. Note the approximately constant power factor above slip = 0.3.

This consistency also suggests consistency in the secondary impedance load angle over the same slip range. This feature is discussed in a theoretical treatment of induction motors with solid rotors [23]. In the 26-mm airgap test, the power factor is lower in the 0.3-to-1.0 slip range due to the lower magnetizing reactance of the larger airgap.

Figures 9-22 and 9-23 show the product of efficiency and power vs slip for both airgaps. The curves reflect a drop in performance acceptability when:

- Utilizing the solid iron reaction rail instead of the composite baseline reaction rail (compare with Figure 8-14)
- Utilizing a larger airgap

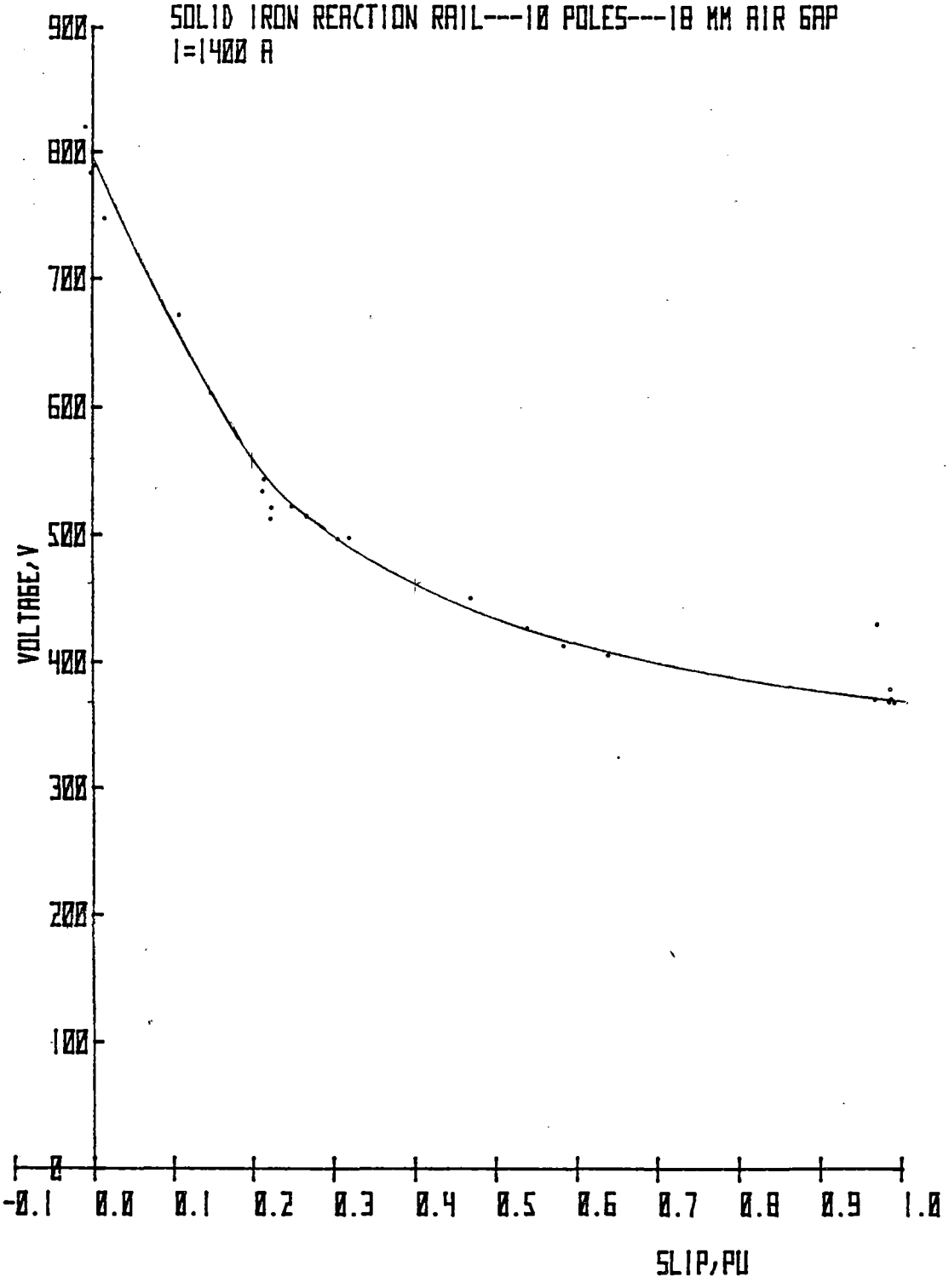

Figure 9-16. Mean Phase Voltage vs Slip, 18-mm Airgap

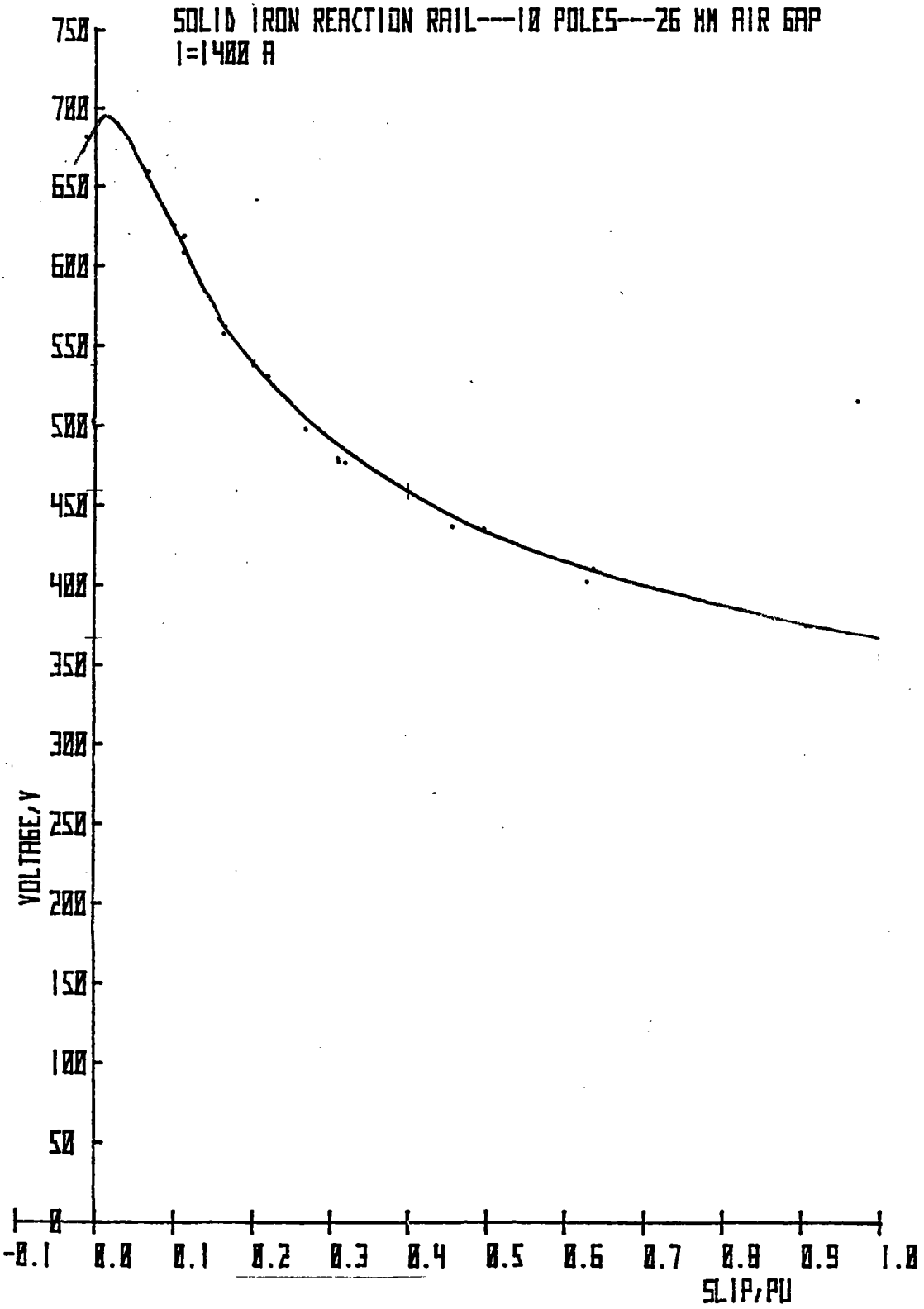

Figure 9-17. Mean Phase Voltage vs Slip, 26-mm Airgap

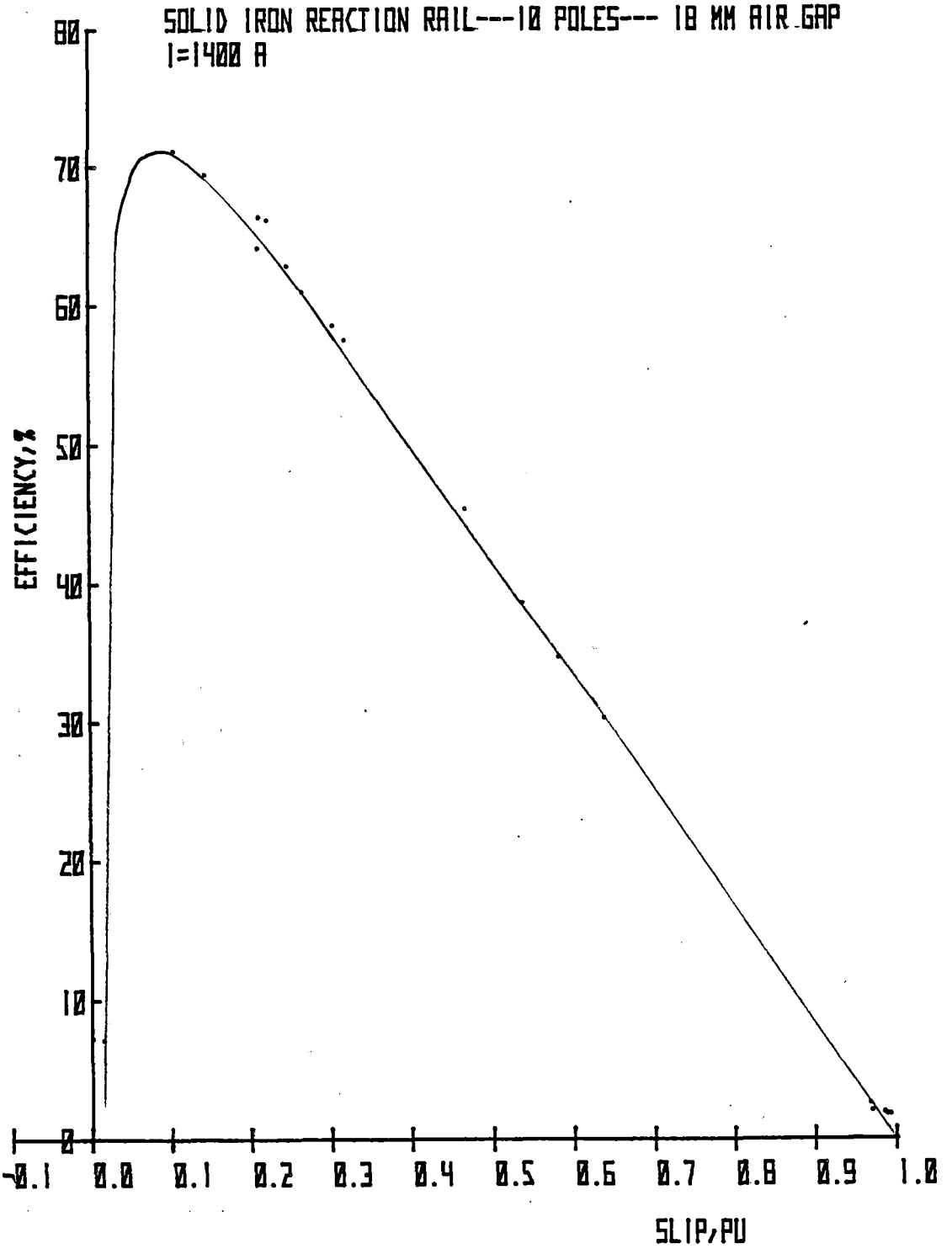

Figure 9-18. Efficiency vs Slip, 18-mm Airgap

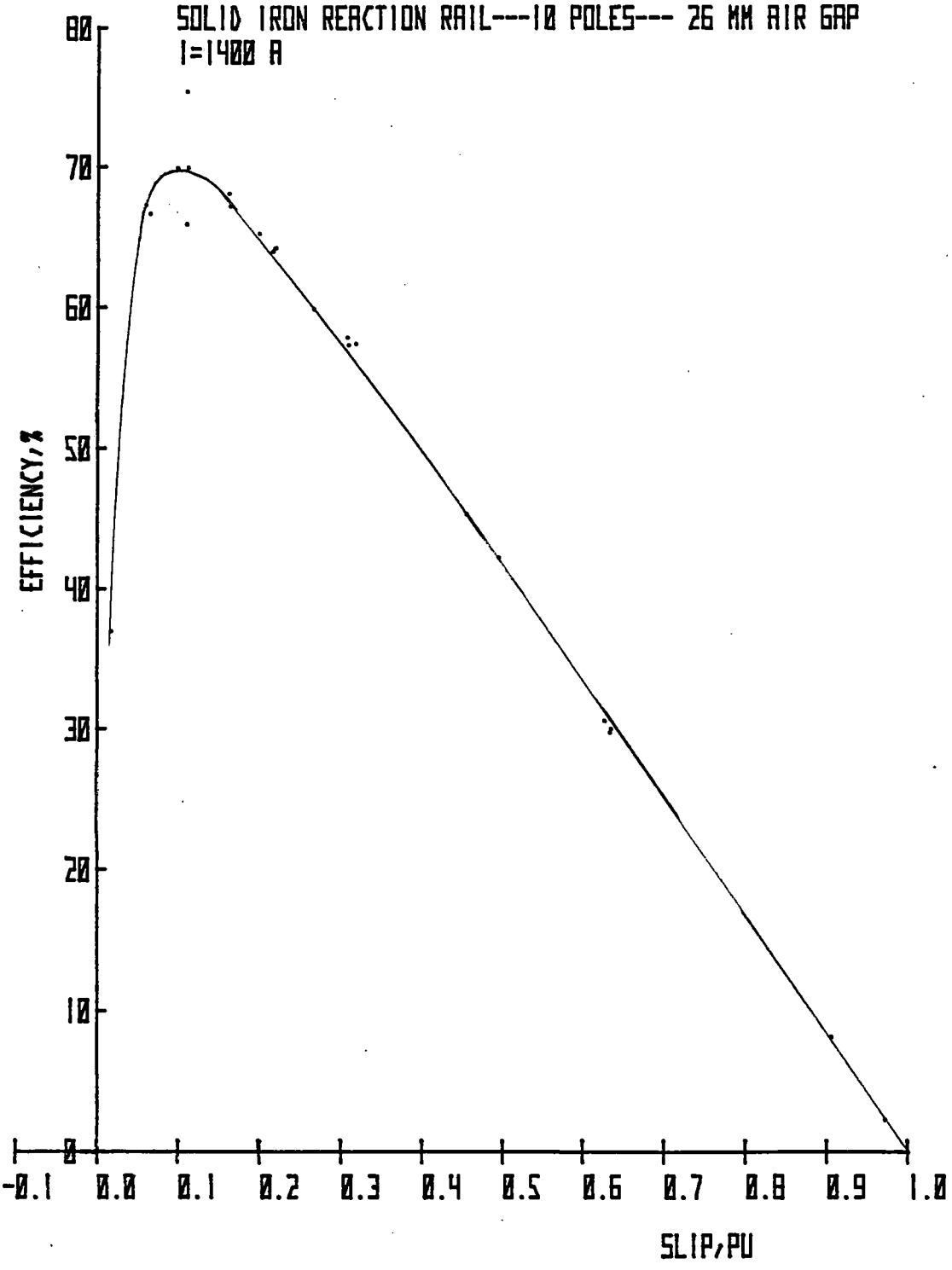

Figure 9-19. Efficiency vs Slip, 26-mm Airgap

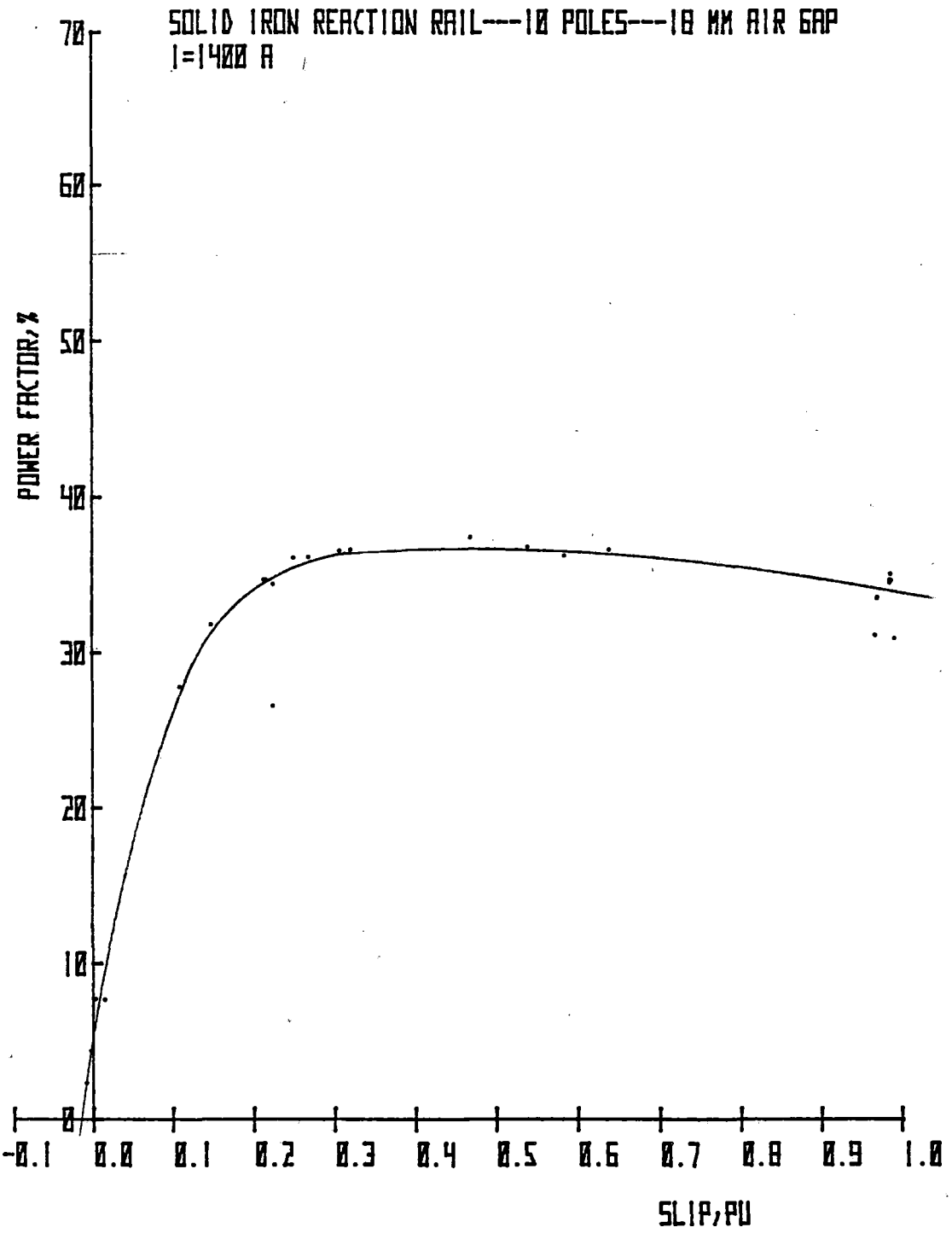

Figure 9-20. Power Factor vs Slip, 18-mm Airgap

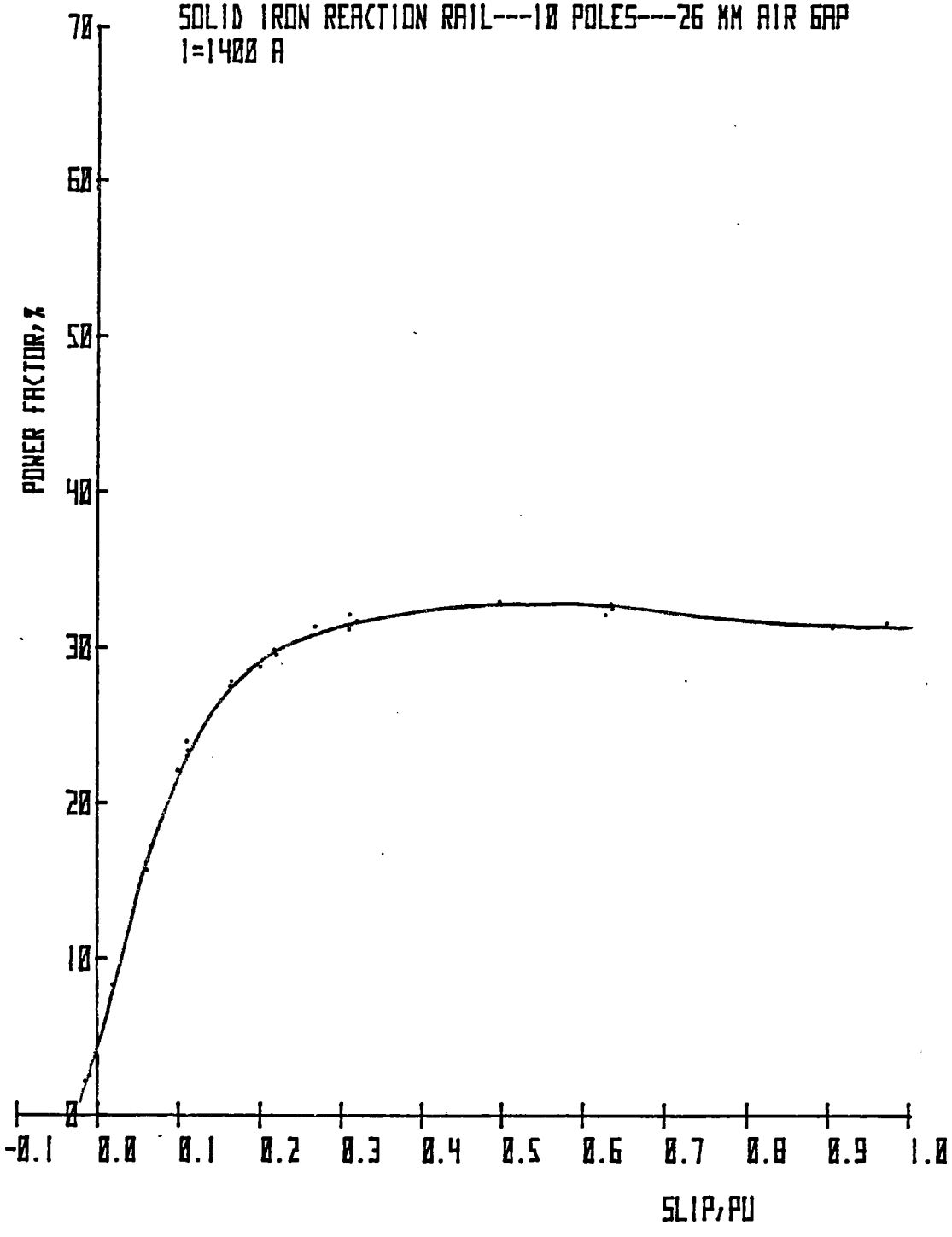

Figure 9-21. Power Factor vs Slip, 26-mm Airgap

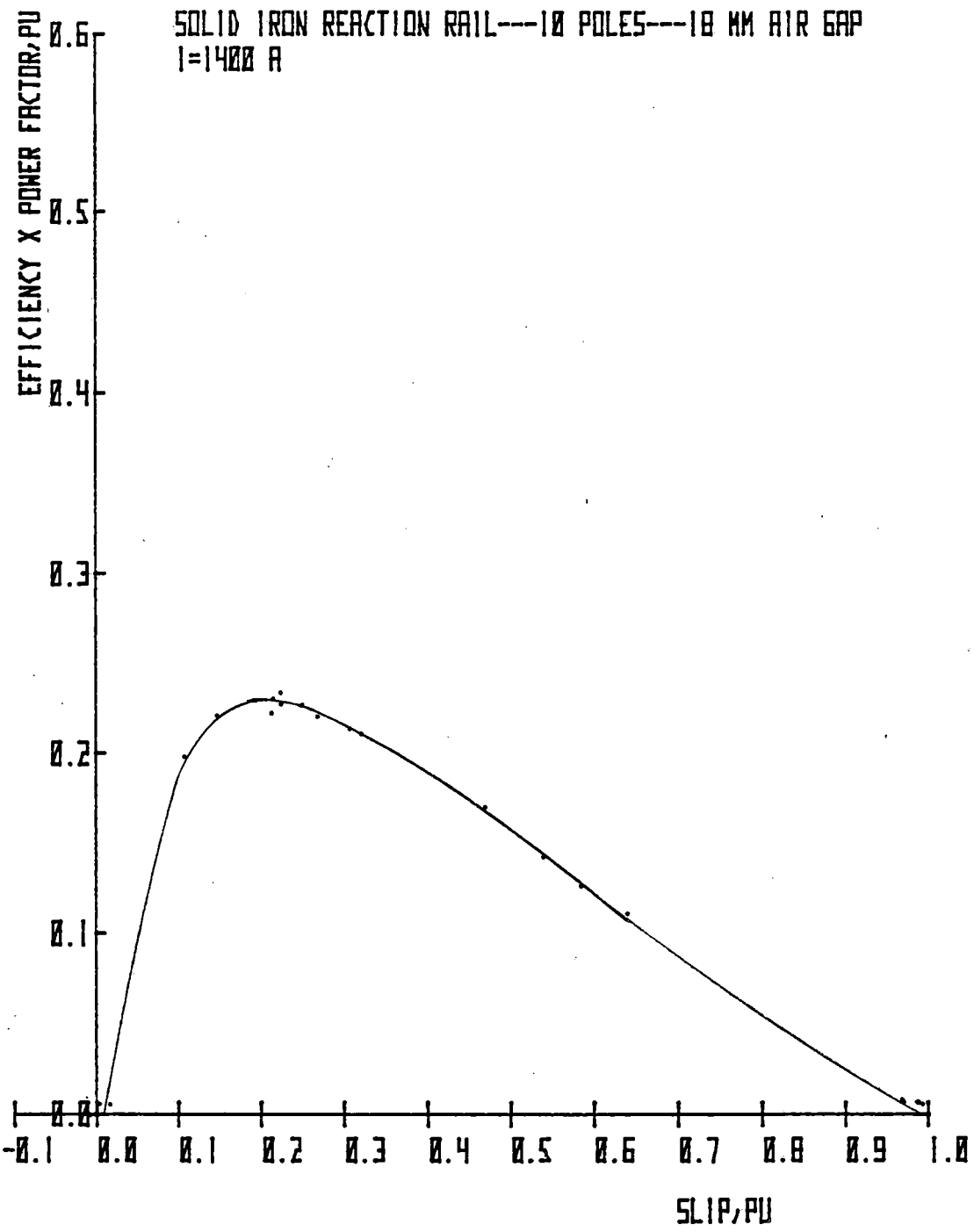

Figure 9-22. Efficiency X Power Factor vs Slip, 18-mm Airgap

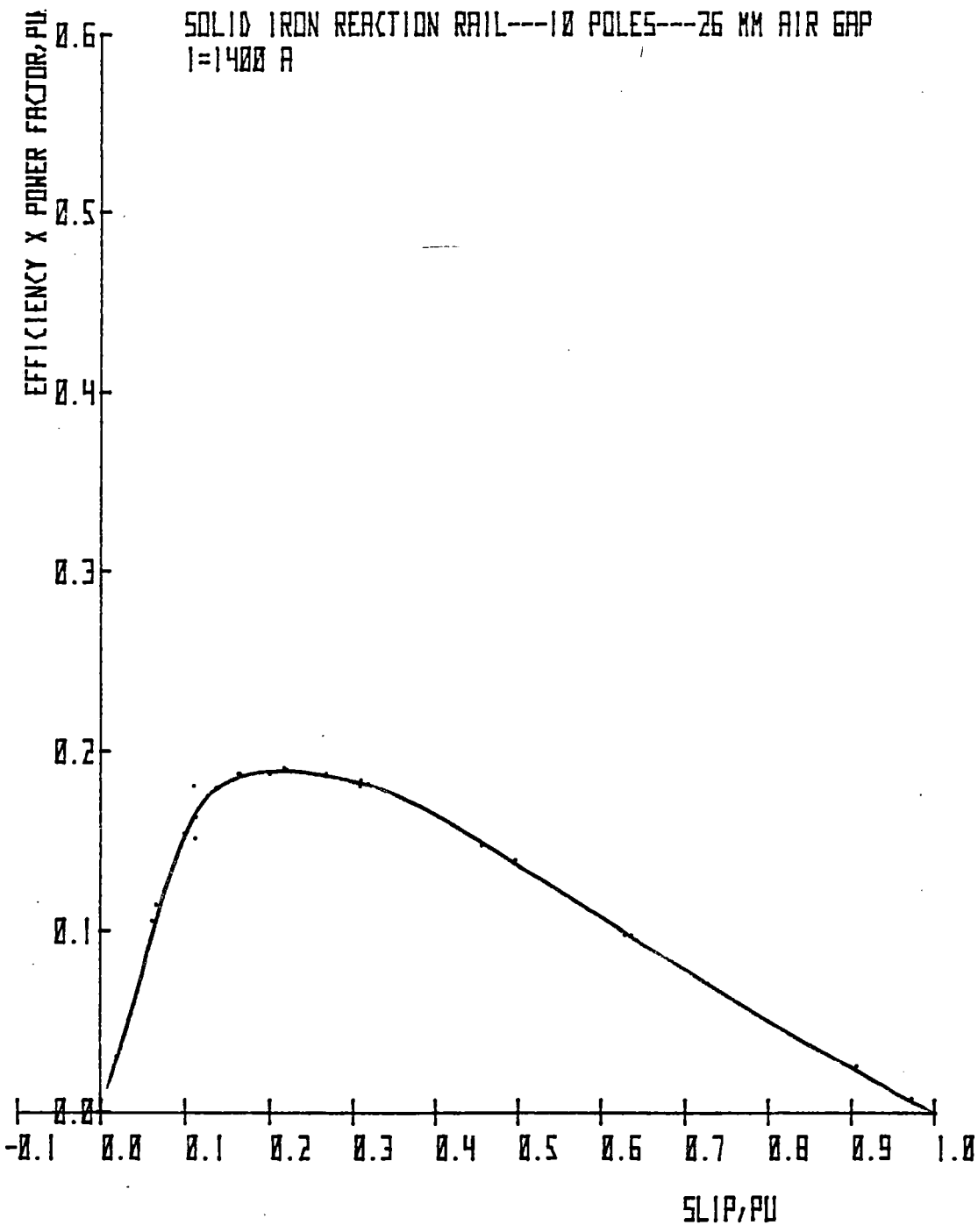

Figure 9-23. Efficiency X Power Factor vs Slip, 26-mm Airgap

Power Loss vs Slip

Computation of ideal and measured power losses was discussed in Section 8.

Figures 9-24 and 9-25 show the ideal and measured power losses as a function of slip for data normalized to a constant current of 1400 A.

To illustrate the difficulty of comparing different motor configurations, Tables 9-4 and 9-5 contrast measured power loss at three values of slip for 18- and 26-mm airgap widths. The data is presented for two excitation conditions:

- 0.346 V/Hz/pole (constant flux)
- 1400 A (constant current)

TABLE 9-4

MEASURED POWER LOSS KW AT 0.346 V/HZ/POLE

Motor Gap	Slip = 0.1	Slip = 0.3	Slip = 0.4
18 mm	115	212	318
26 mm	97	222	308

TABLE 9-5

MEASURED POWER LOSS KW AT 1400 A

Motor Gap	Slip = 0.1	Slip = 0.3	Slip = 0.4
18 mm	235	308	360
26 mm	172	268	308

It can be seen that the difference between the two airgaps is smaller when the data is normalized to a constant V/Hz/pole, rather than to a constant current.

With a 26-mm airgap, larger stator losses are incurred to set up a given primary flux condition. In addition, the constant primary flux condition tends to produce constant reaction rail power loss, modified only by increased leakage losses.

Because measured power loss is derived from thrust, thrust levels for the two airgaps are approximately equal for the constant flux condition; the difference is attributable to increased leakage. (See Thrust vs Slip in this section).

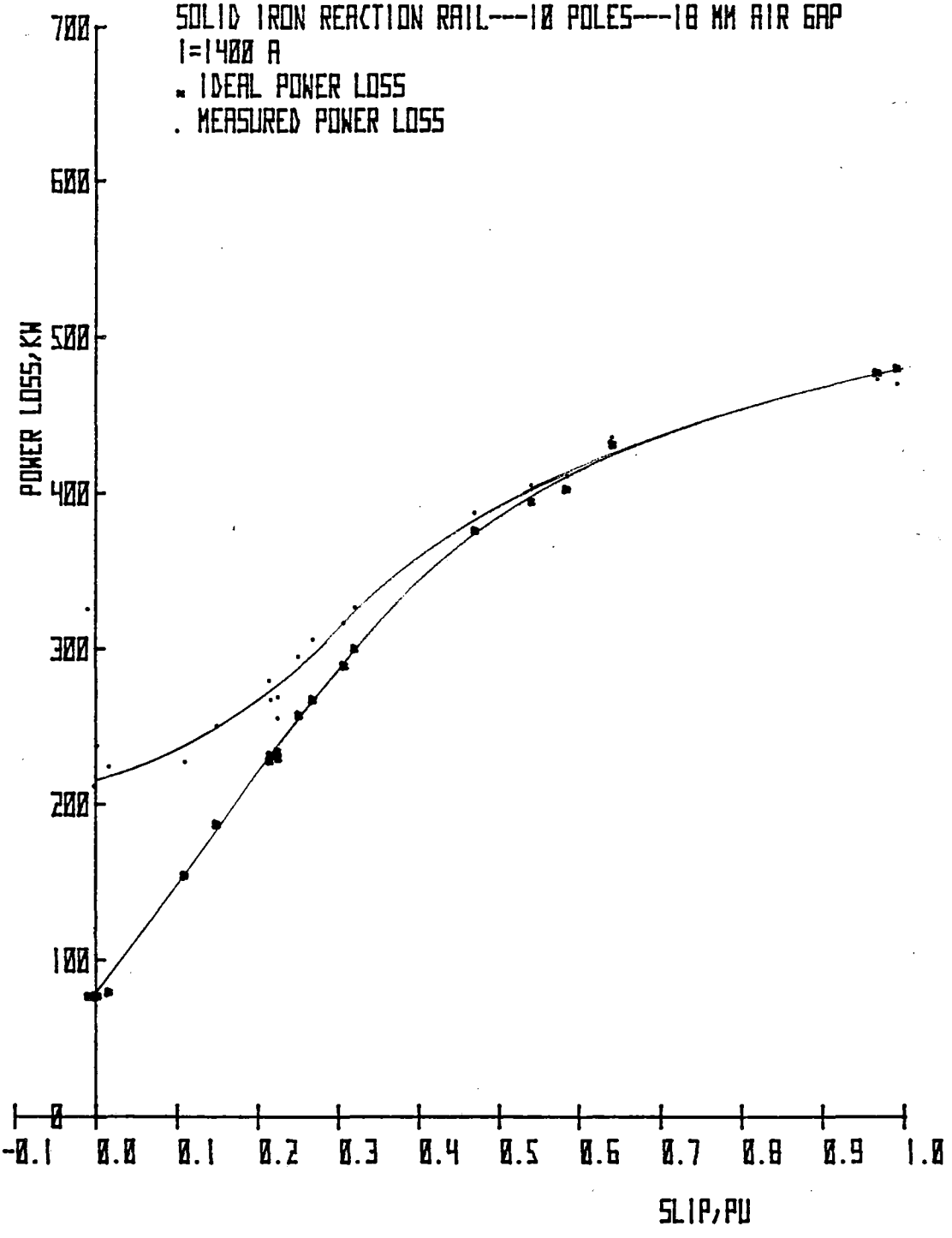

Figure 9-24. Ideal and Measured Power Loss vs Slip, 18-mm Airgap

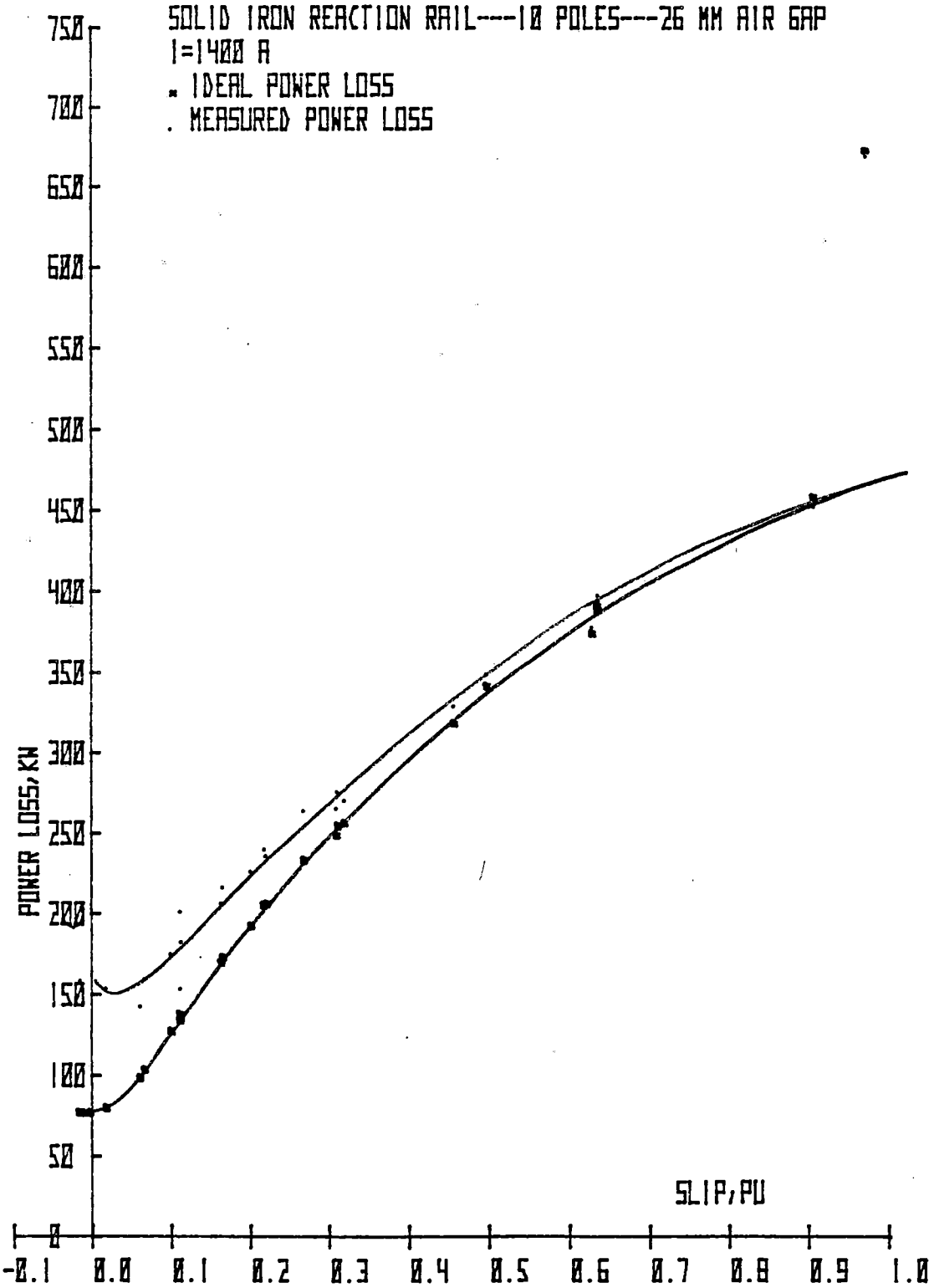

Figure 9-25. Ideal and Measured Power Loss vs Slip, 26-mm Airgap

Vertical Force Characteristics

Figures 9-26 and 9-27 show the total vertical force normalized to 1400 A as a function of slip. Although there is a marked similarity in the curves above 0.4 slip, the total attractive force, kN, at zero slip is substantially greater, i.e., more negative, for the 18-mm airgap than the 26-mm airgap.

With no saturation effects, it might be expected that the ratio of $\frac{(FVSN)\ 18\ mm}{(FVSN)\ 26\ mm}$ at zero slip will approximate the squared ratio of the two airgaps.

In this case:

$$\frac{FVSN\ 18\ mm}{FVSN\ 26\ mm} = \frac{-59.5}{-44.5} = 1.34$$

But, $$\left(\frac{\frac{1}{18\ mm}}{\frac{1}{26\ mm}}\right)^2 = 2.08$$

In this condition, the occurrence of substantial nonlinearities is indicated.

Note that in the motoring mode, the vertical force is always in attraction with the solid iron reaction rail, but clearly exhibits a crossover slip with the baseline reaction rail.

Figures 9-28 and 9-29 show pitching moment as a function of slip. Both curves show small differences of flux in the 0.2-to-0.3 slip range. A large redistribution of flux occurs in the 0.0-to-0.2 slip range. This increase in flux, combined with the test's high excitation levels, emphasizes the unpredictability of vertical forces from airgap ratios.

DISTRIBUTED PARAMETERS

Figures 9-30, 9-31, and 9-32 show distributed parameters for the motor with the 18-mm airgap at decreasing values of slip.

Figures 9-33, 9-34, and 9-35 show the same parameters for the 26-mm airgap. In comparison to data from the baseline reaction rail tests, these curves show that the variation along the machine is greater for the solid iron reaction rail than for the baseline reaction rail, and the pole flux is also significantly greater.

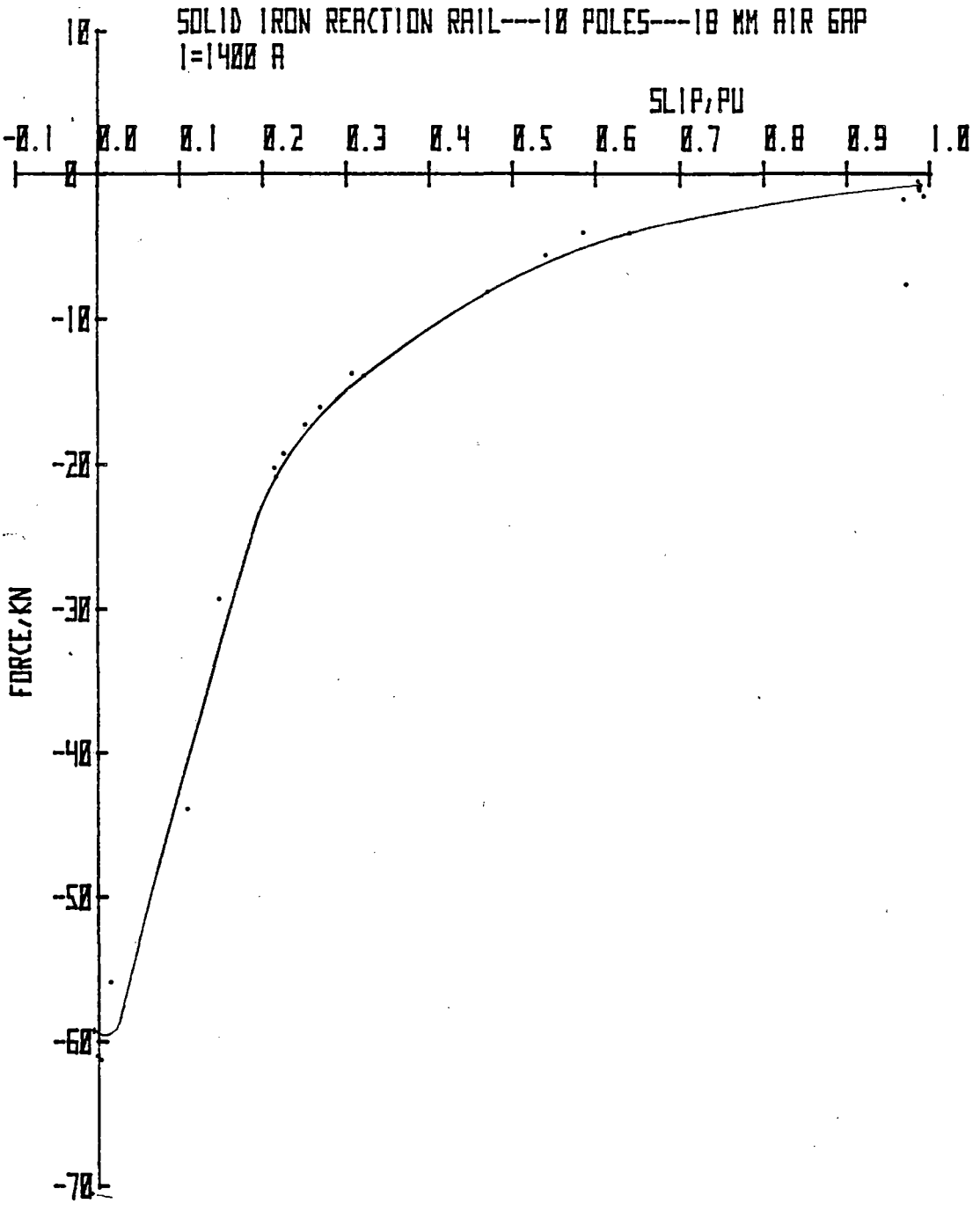

Figure 9-26. Total Vertical Force vs Slip, 18-mm Airgap

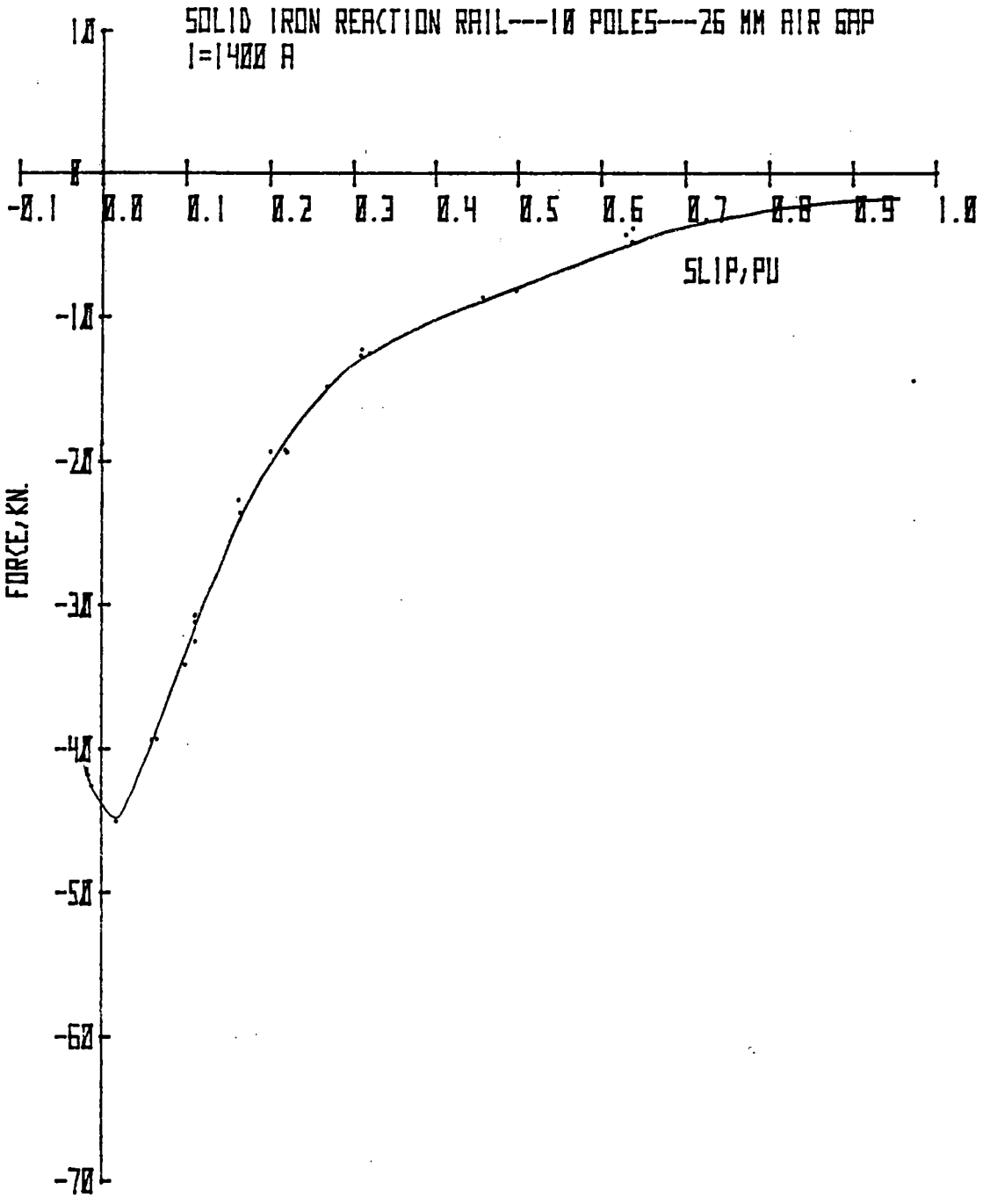

Figure 9-27. Total Vertical Force vs Slip, 26-mm Airgap

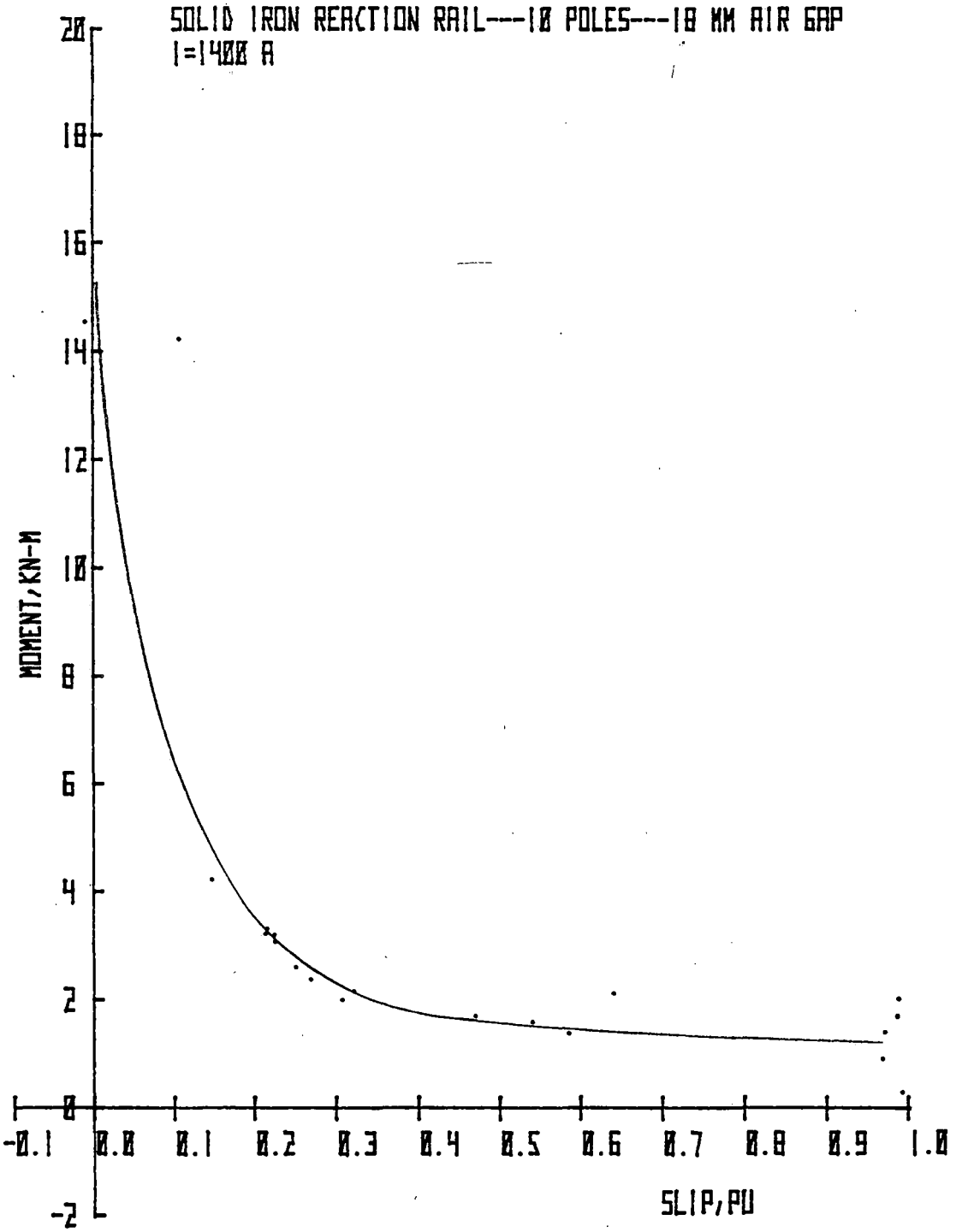

Figure 9-28. Pitching Monent vs Slip, 18-mm Airgap

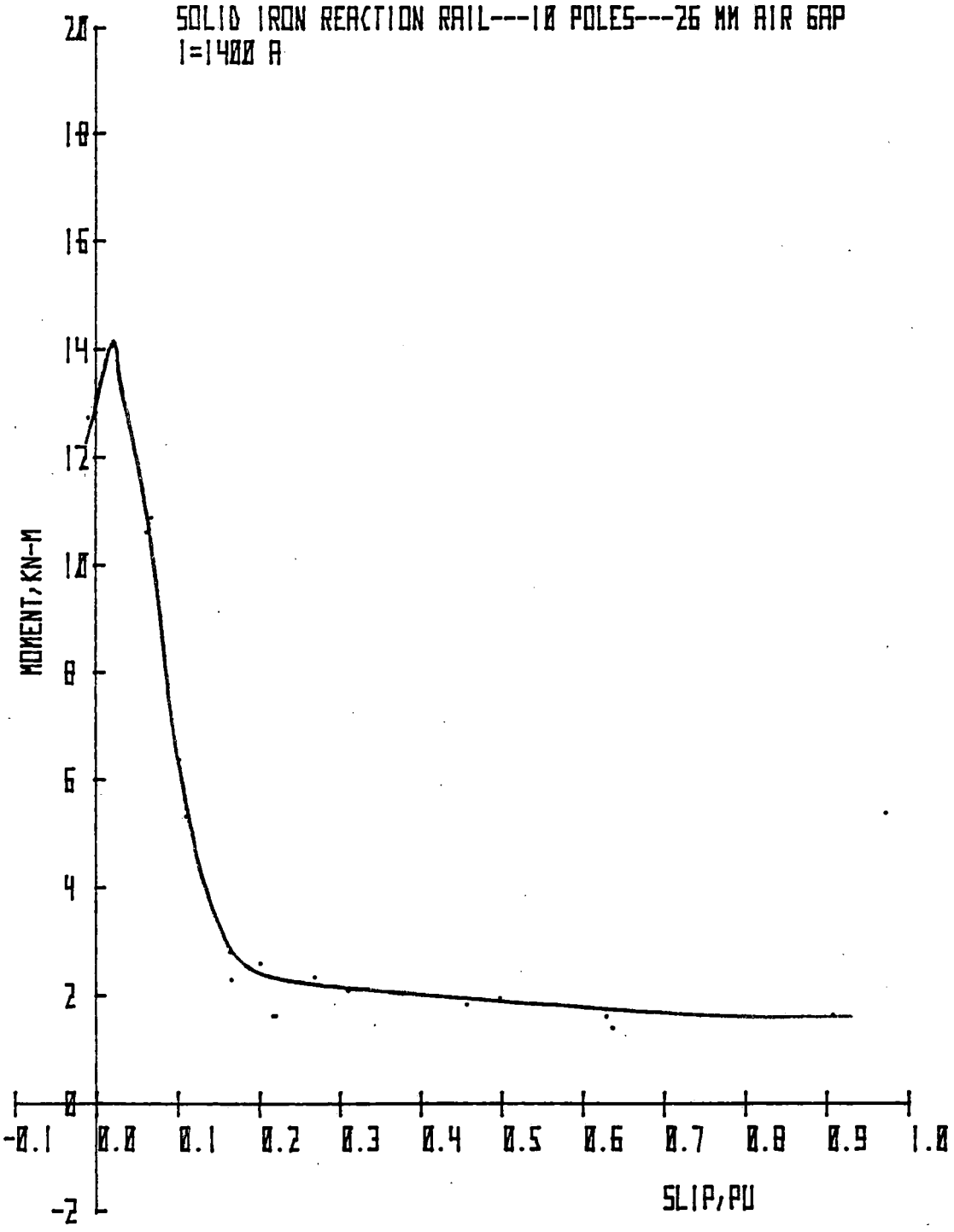

Figure 9-29. Pitching Moment vs Slip, 26-mm Airgap

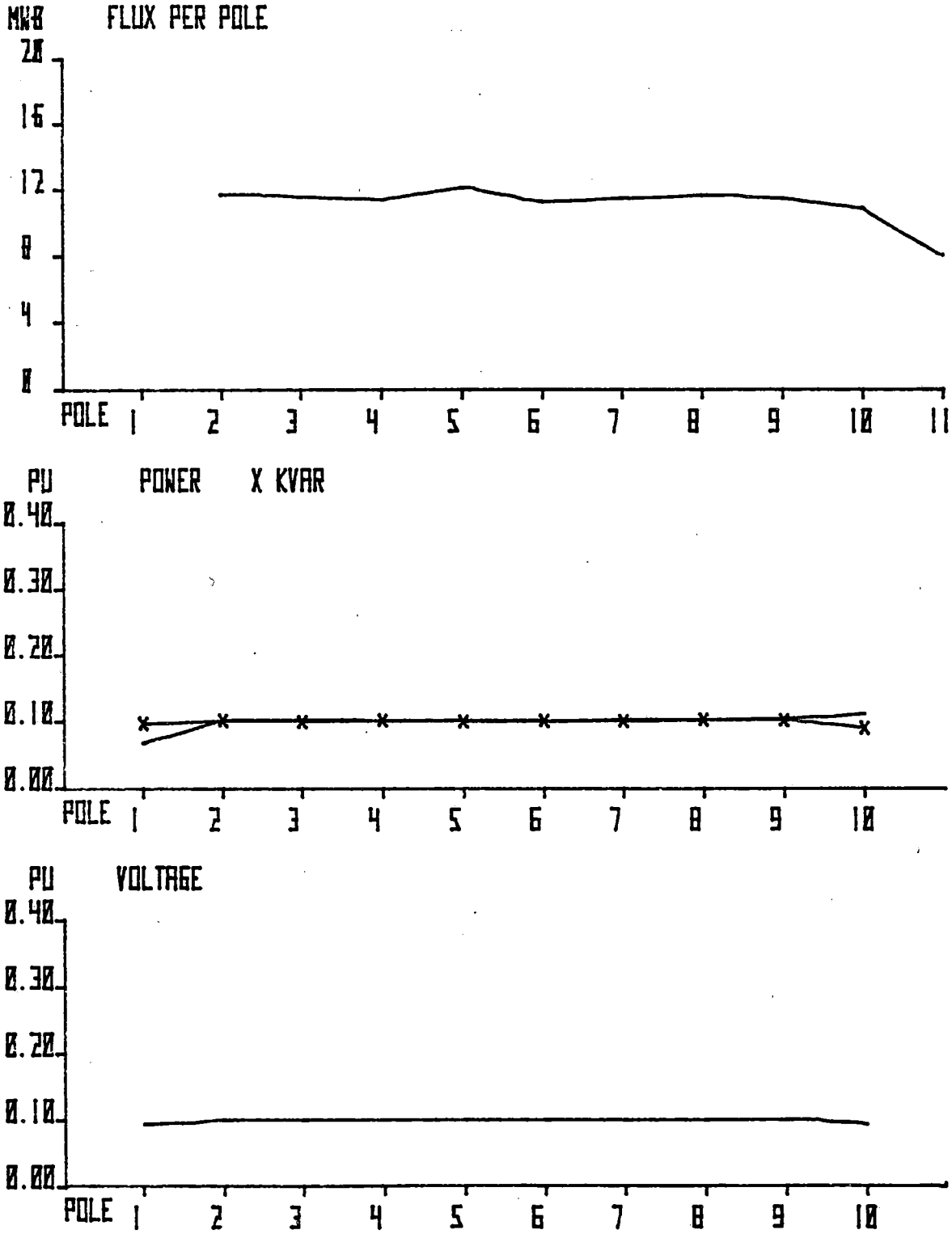

Figure 9-30. Distributed Parameters, Run 1157

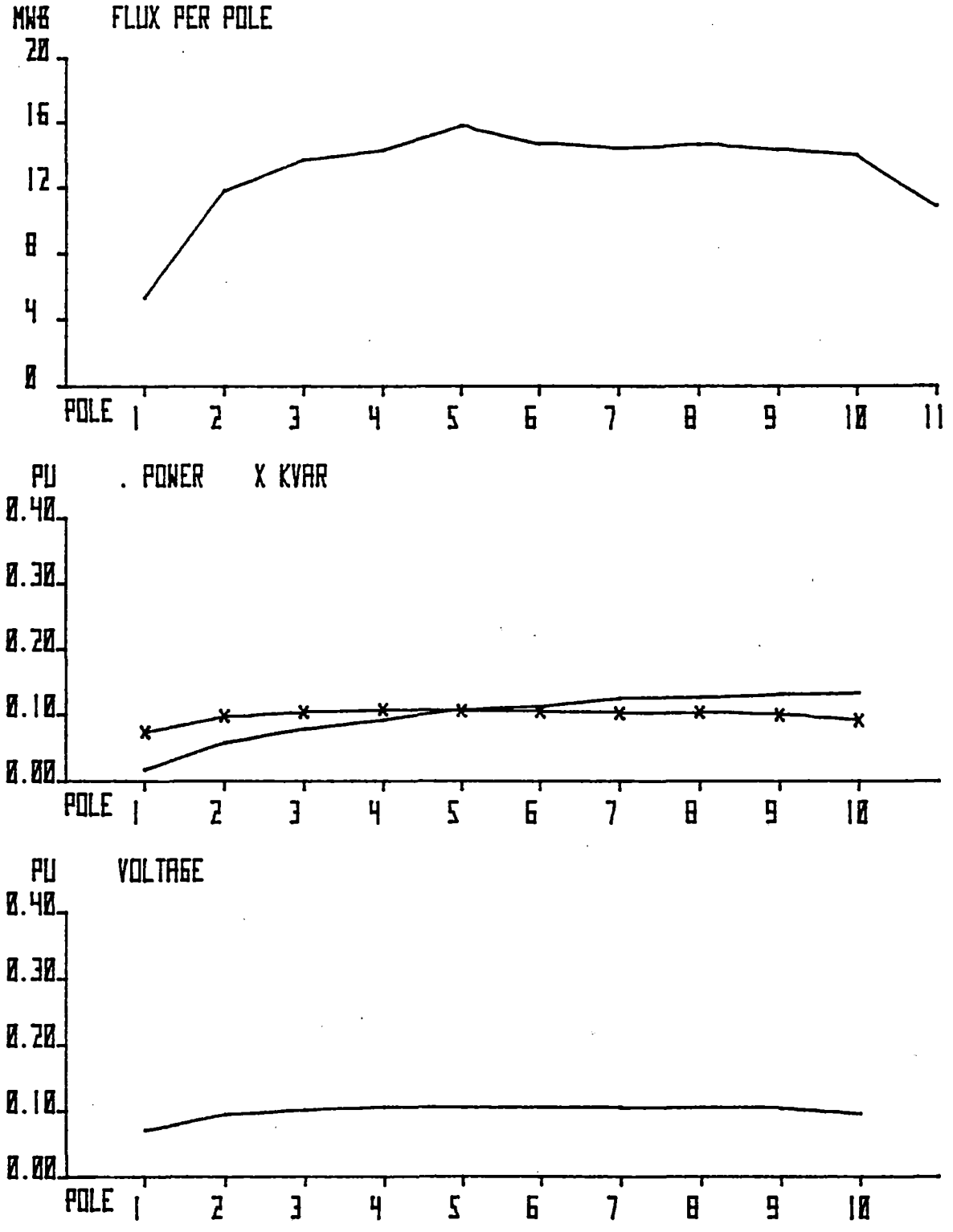

Figure 9-31. Distributed Parameters, Run 1176

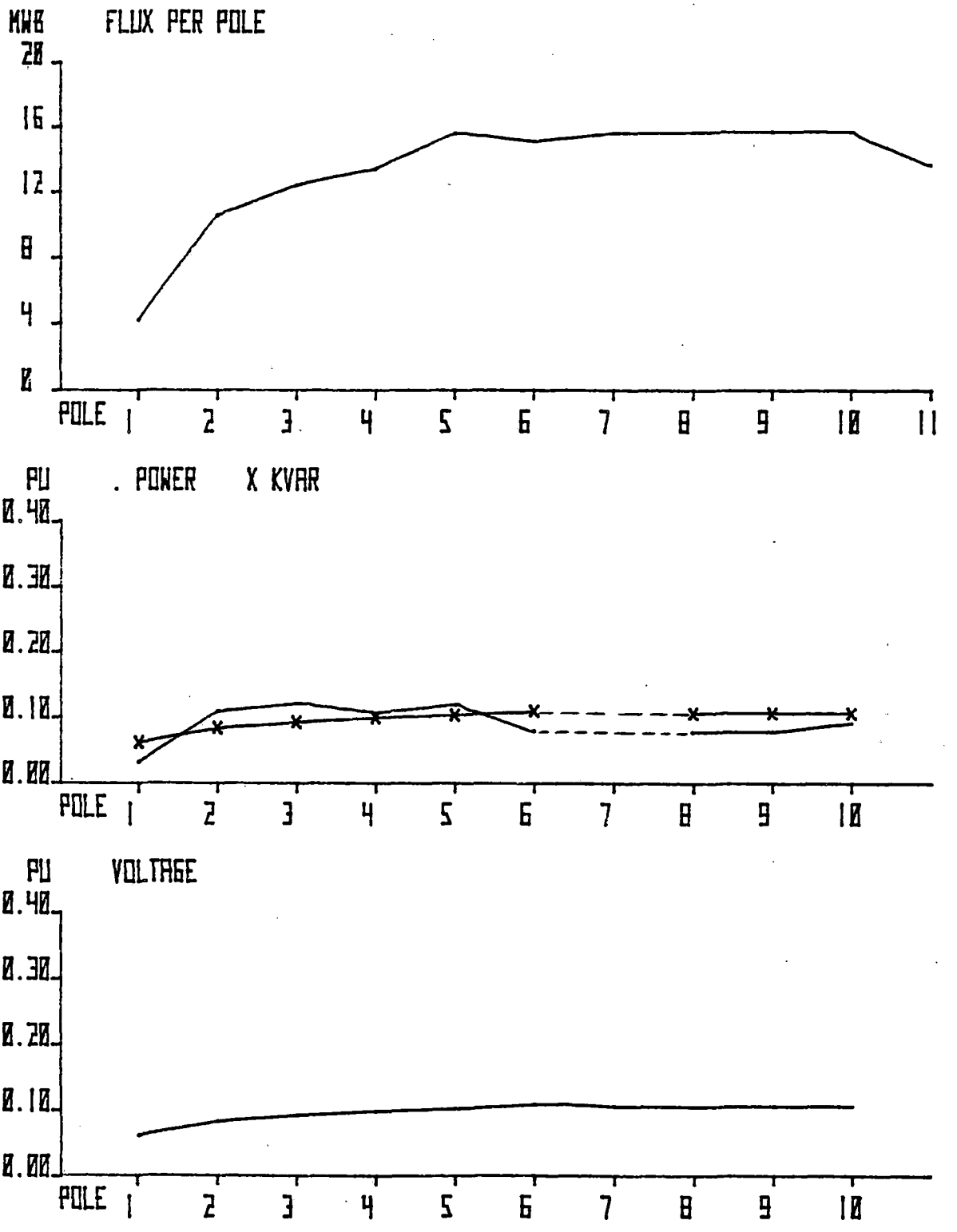

Figure 9-32. Distributed Parameters, Run 1167

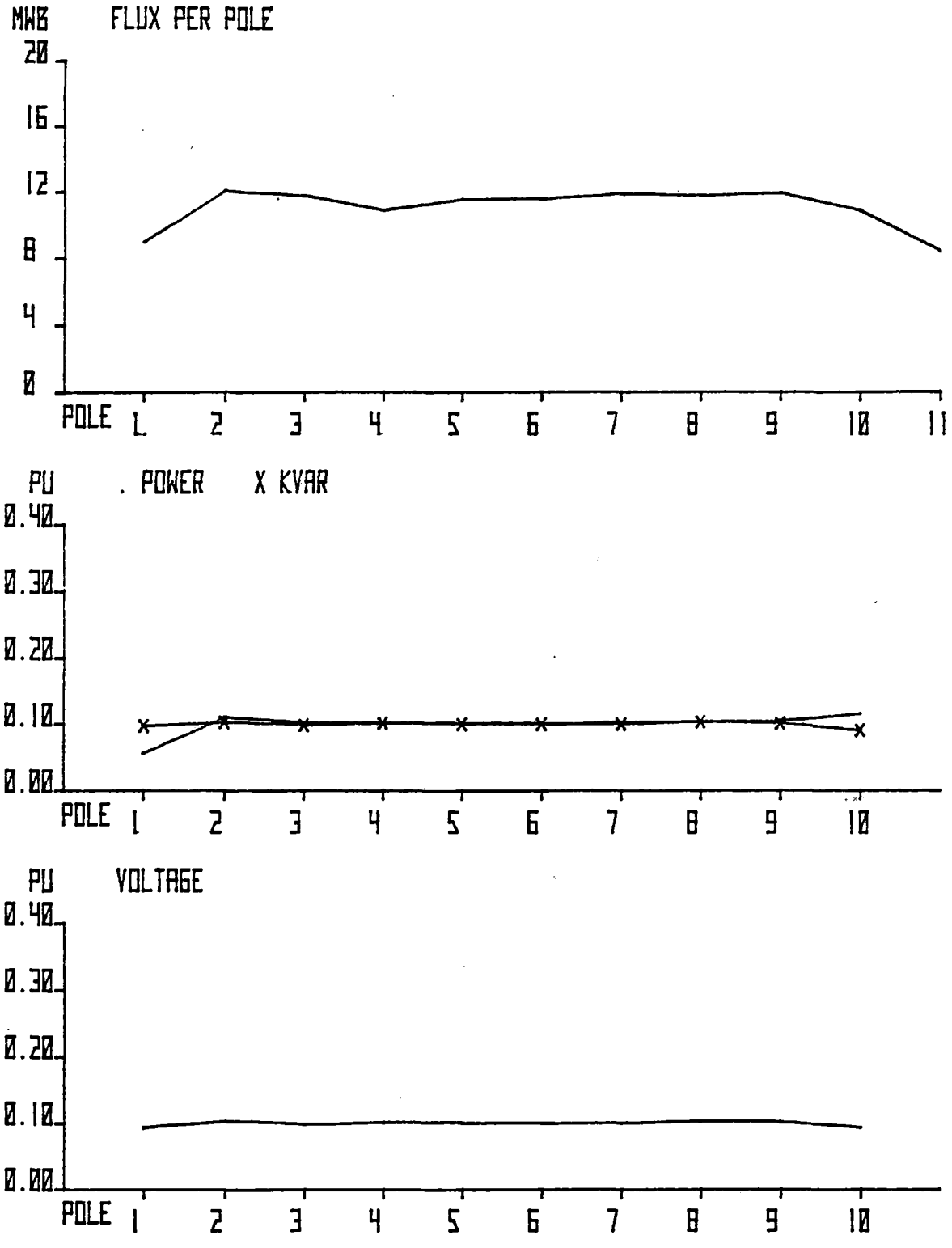

Figure 9-33. Distributed Parameters, Run 1123.3

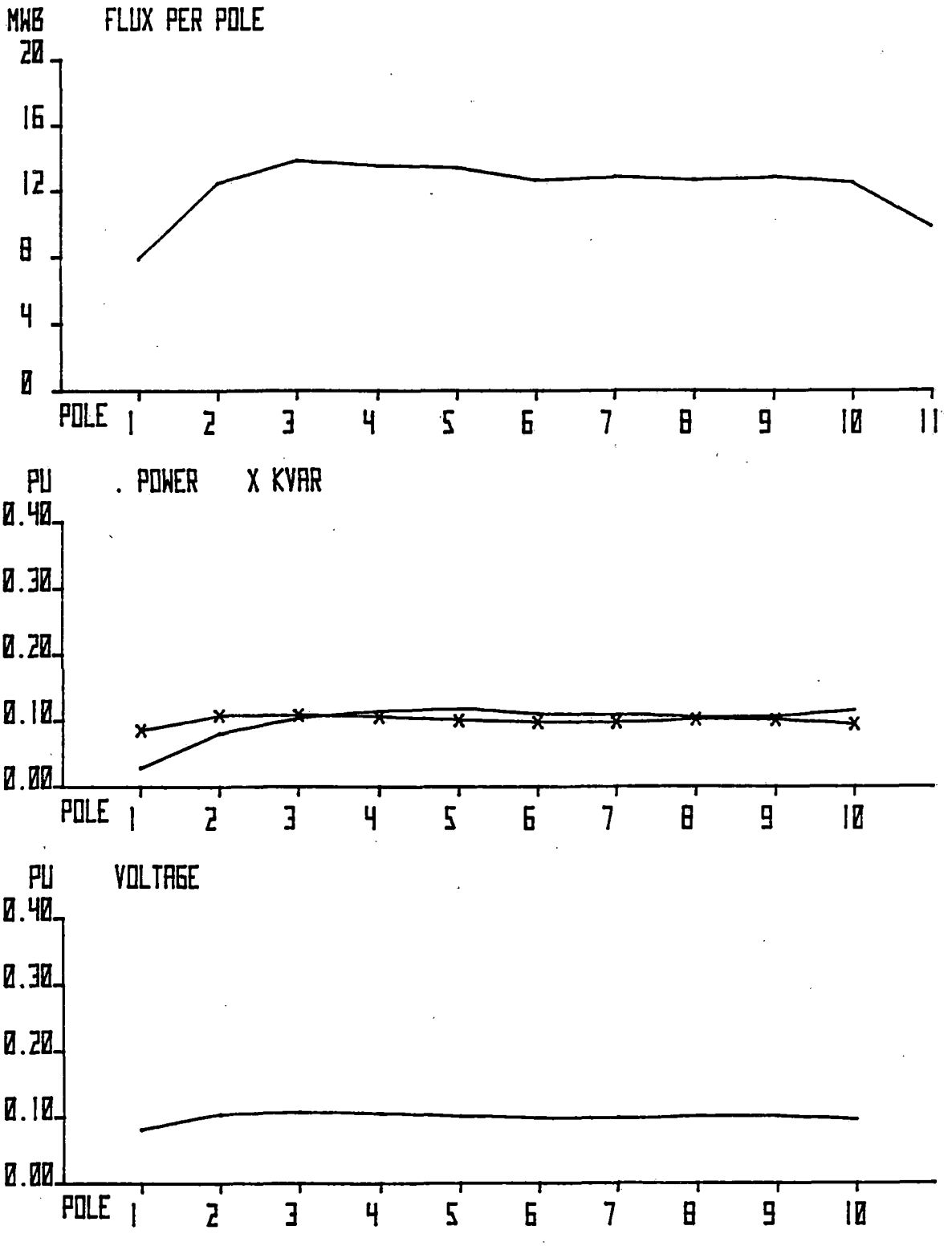

Figure 9-34. Distributed Parameters, Run 1126

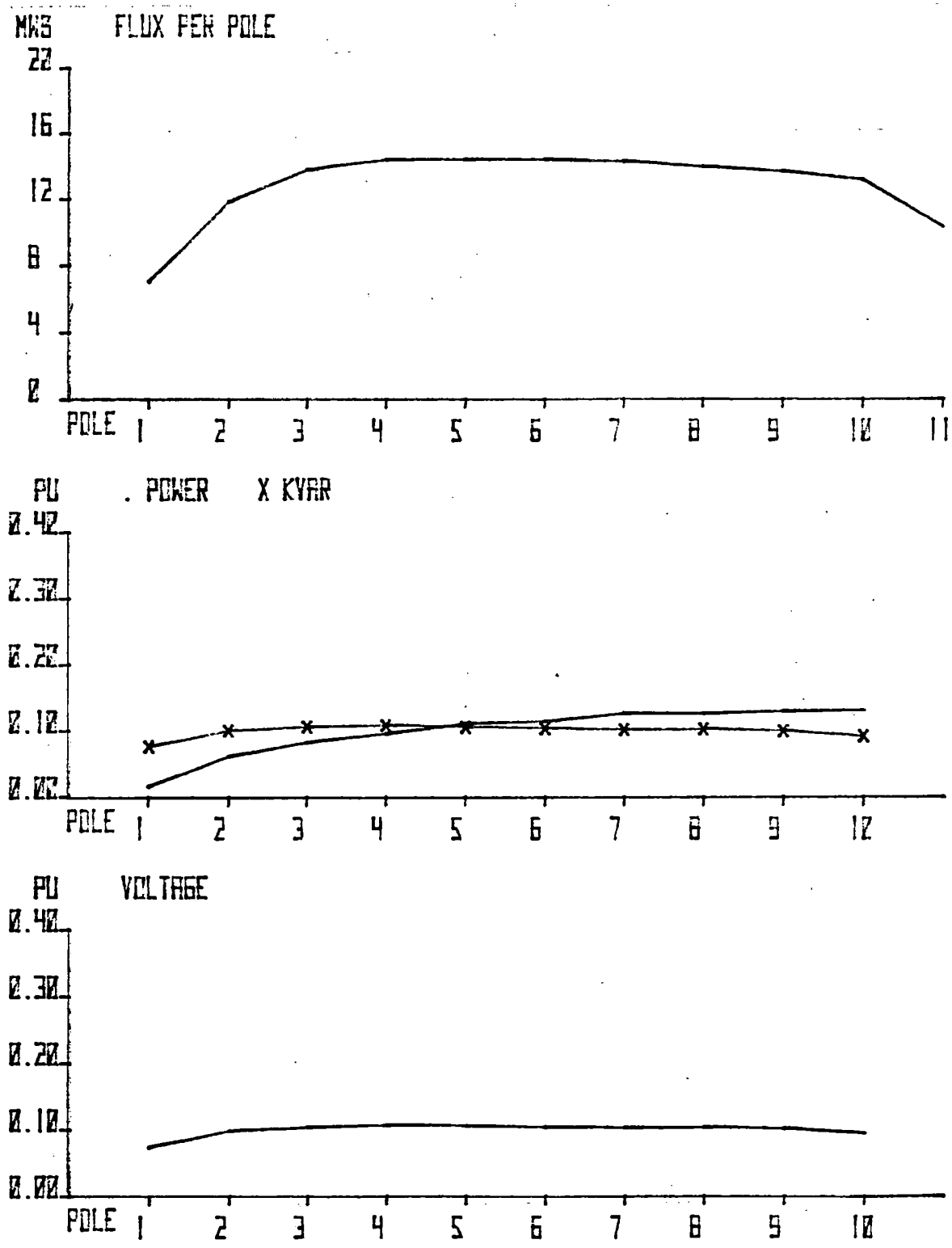

Figure 9-35. Distributed Parameters, Run 1128

SECTION 10

FLUX MEASUREMENT OVER LAMINATED TRACK SECTION

INTRODUCTION

This section discusses measurement of primary and secondary fluxes in the region of station number 1715.8 (laminated track section). The purpose of this exercise is to examine the efficacy of fabricating backiron in three horizontal coarse laminations (see Figure 10-1) in an attempt to measure flux penetration in solid iron.

Supporting analytical studies on track flux modeling are detailed in Appendix I.

POLE FLUX MEASUREMENT

Baseline Reaction Rail

Figure 10-2 shows details of the SLIM primary, and the location and designation of each pole face search coil.

Figures 10-3 and 10-4 show pole flux variation as a function of arbitrary time units for low-speed runs 1022 and 1023, details of which are given in Table 10-1.

The effect of current discontinuities at the edge of each 6.1-m aluminum section can be clearly seen. The effect is to locally decrease eddy currents in the region of discontinuity, thereby causing loss of thrust and decrease in the repulsive component of vertical force (alternatively seen as an increase in the pole flux, thereby causing an increased attractive force component in the vertical force).

It can also be seen that the laminated backiron has negligible effect on the pole fluxes, and therefore negligible effect on motor forces.

Solid Iron Reaction Rail (Large Airgap)

Figures 10-5 and 10-6 show pole flux variation as a function of arbitrary time units for runs 1122 and 1123, details of which are given in Table 10-1.

Unlike the baseline reaction rail, the laminated section shows a significant increase (up to 15%) in pole flux compared with the solid iron pole flux data.

In addition, the discontinuities between adjacent steel sections can be detected by noting the transient increase in pole flux as the respective pole traverses the gap (e.g., runs 1122, 1123, 1156).

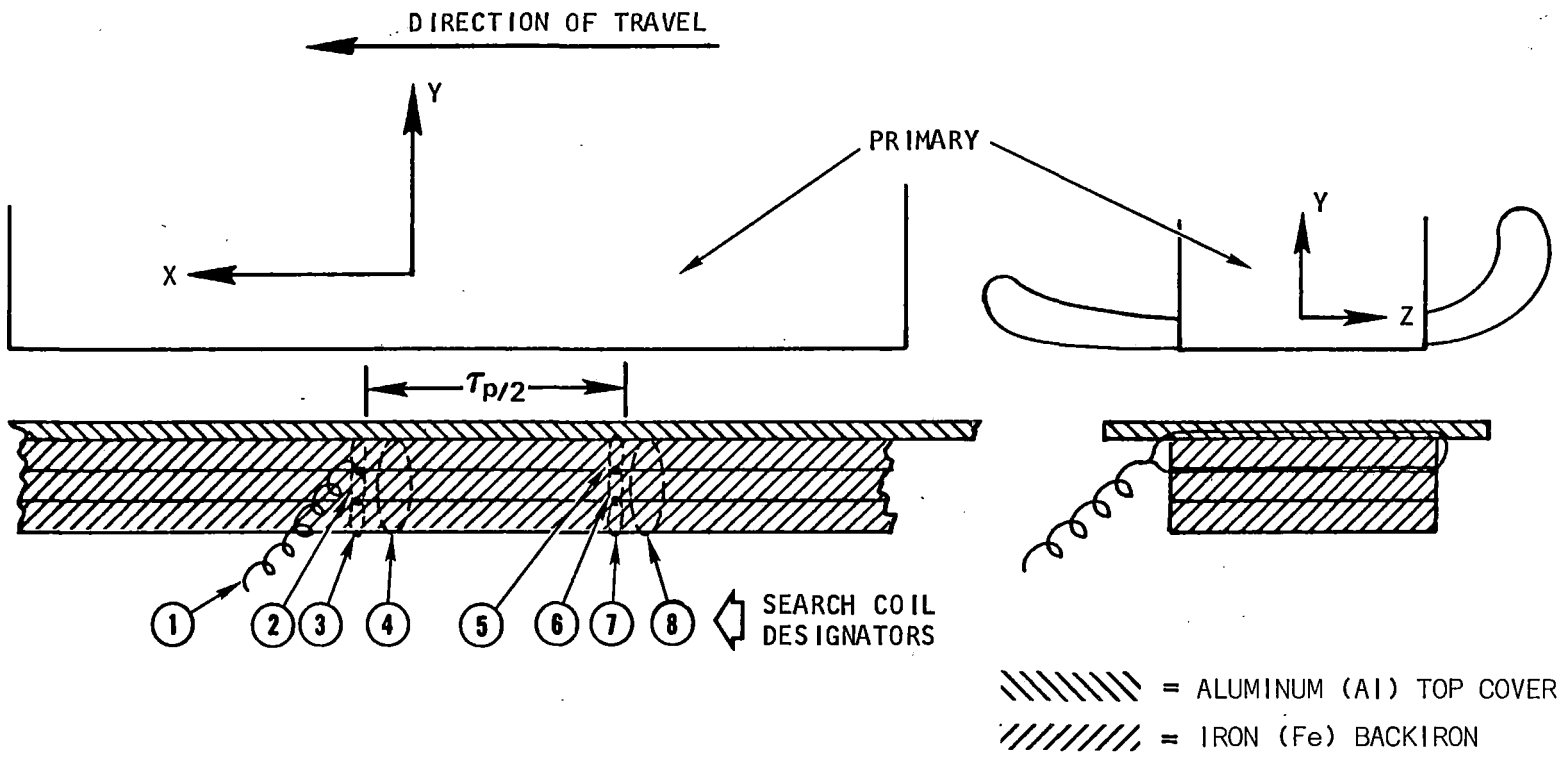

Figure 10-1. Backiron Fabrication for Track Flux Measurement

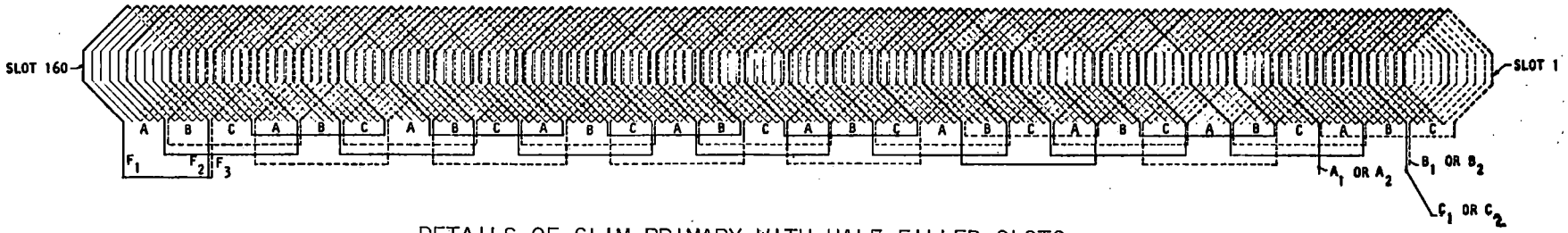

DETAILS OF SLIM PRIMARY WITH HALF-FILLED SLOTS

COIL DESIGNATION	SLOT LOCATION
F1	1, 16
F2	16, 31
F3	31, 46
F4	46, 61
F5	61, 76
F6	76, 91
F7	91, 106
F8	106, 121
F9	121, 136
F10	136, 151
F11	145, 160

TOTAL COILS: 11

Figure 10-2. Location of Primary Pole Search Coils

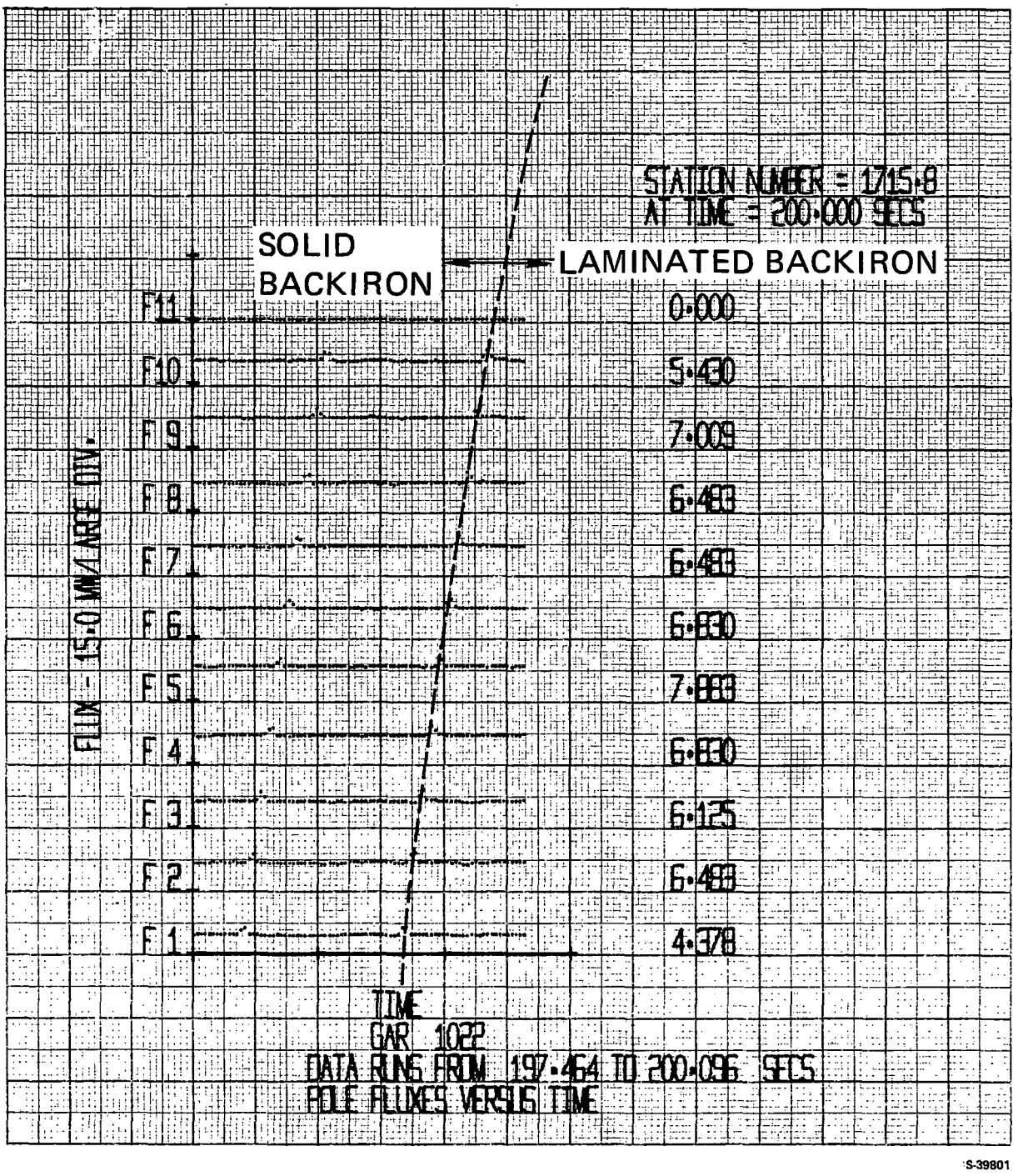

Figure 10-3. Pole Flux Variations, Run 1022

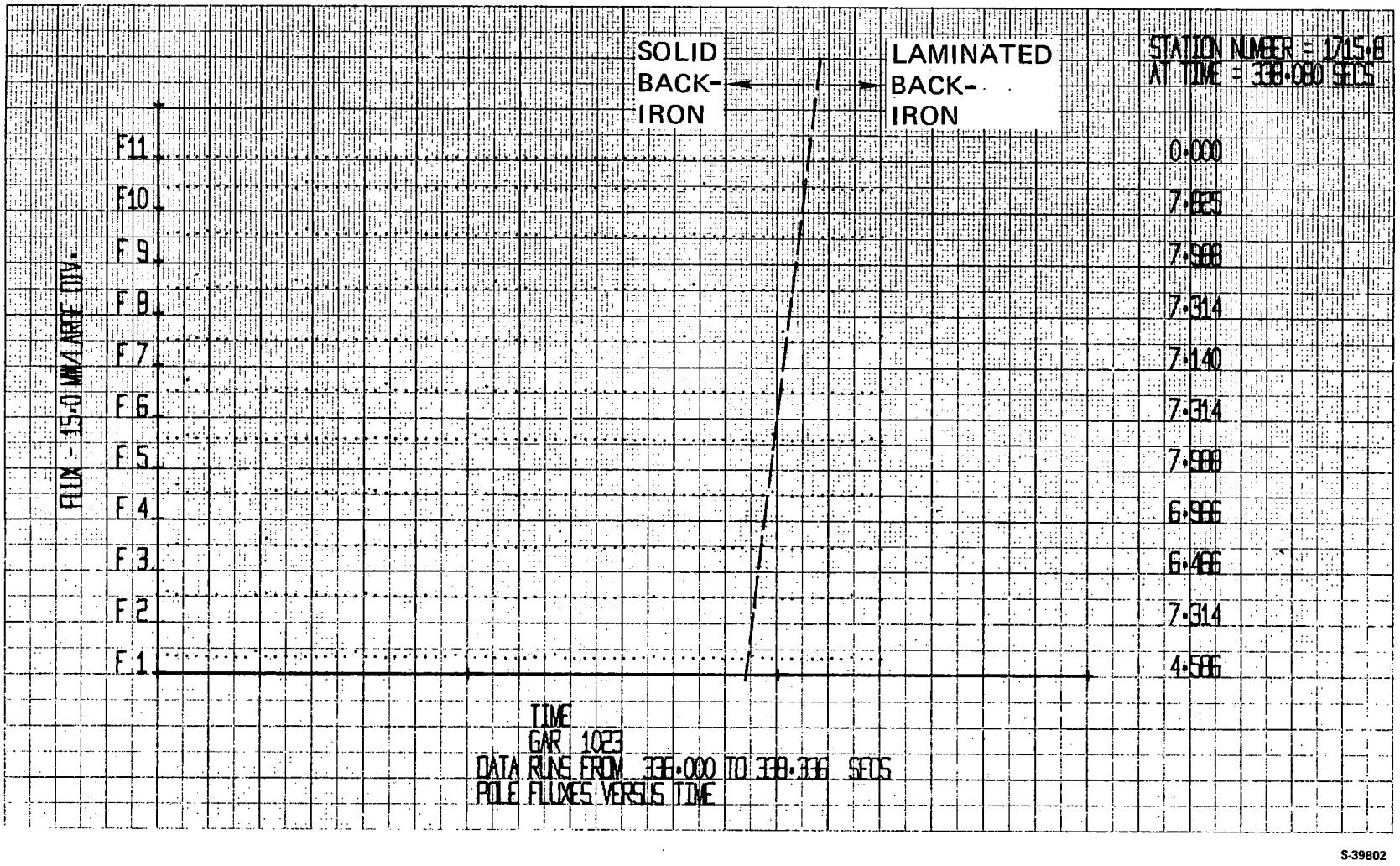

Figure 10-4. Pole Flux Variations, Run 1023

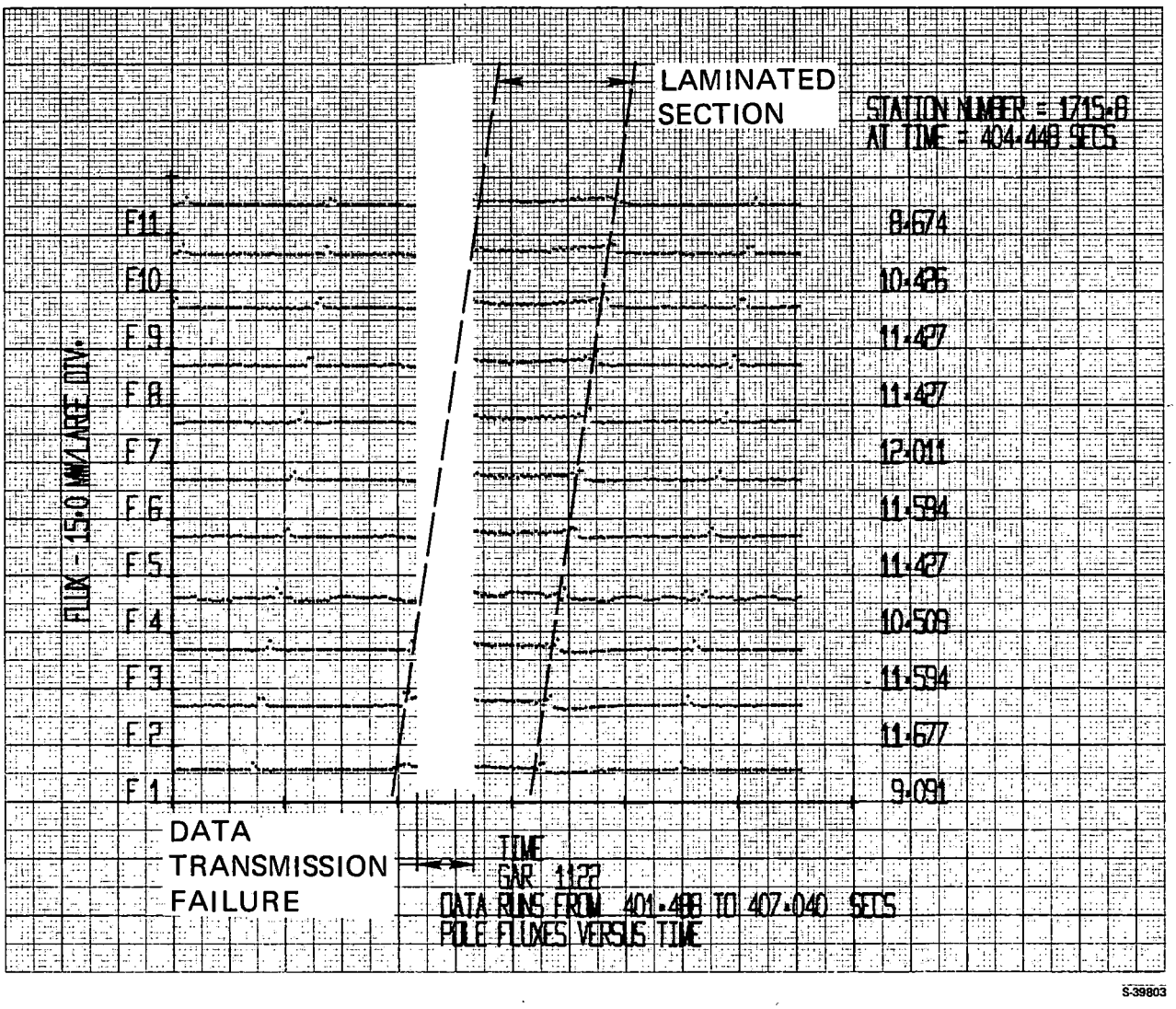

Figure 10-5. Pole Flux Variations, Run 1122

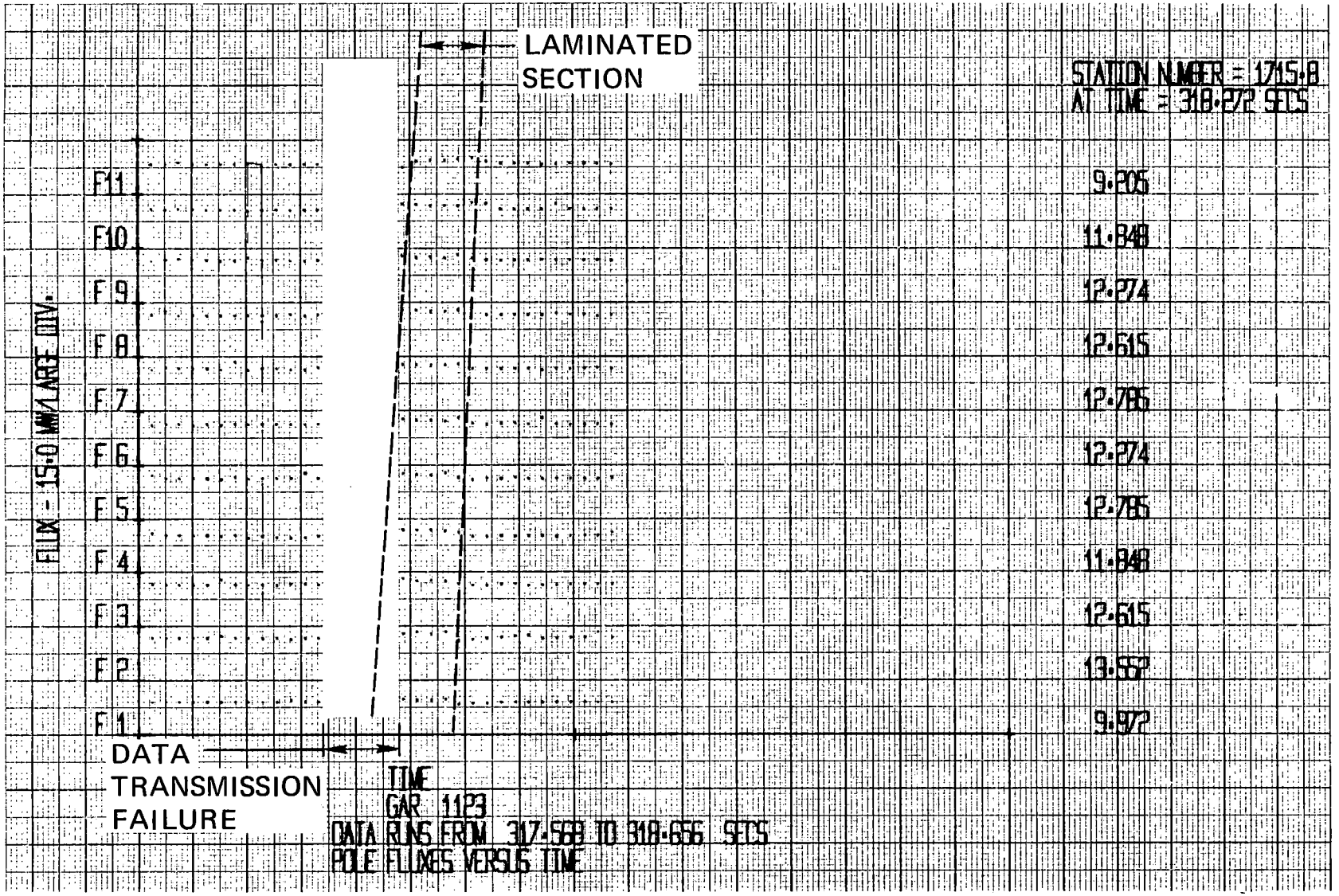

IS-39804

Figure 10-6. Pole Flux Variations, Run 1123

TABLE 10-1

INSTANTANEOUS VALUES OF SLIM PARAMETERS AT STATION 1715.8

Run	IA, A	V/Hz	Frequency, Hz	Velocity, m/s
1022	1899	3.08	94.2	4.8
1023	1829	3.18	61.8	19.2
1122	1249	4.14	88.8	4.86
1123	1109	4.05	46.0	34.8
1156	1279	4.32	90.5	1.48
1157	1249	4.29	62.5	23.0

NB: A data dropout occurs during various runs at the instant the vehicle passes under the bridge. Under normal circumstances this has no effect, unless a selected data point is being acquired at the instant of the radio link loss. During the pole flux low-speed tests, the effect is more dominant. Data transmission returns to normal after a short time (approximately 0.5 s). This brief loss of data has negligible effect on data continuity. That is, dc levels of flux can be obtained for all flux channels for all sections.

Solid Iron Reaction Rail (Small Airgap)

Figures 10-7 and 10-8 show similar pole flux data for the reduced airgap tests.

The same increase in pole flux is noted over the laminated reaction rail, but in addition, a superimposed ripple is noted on each pole flux. This may be caused by the reflected effect on the machine of each pole in turn traversing the discontinuity. Upon traversing the discontinuity, an EMF is induced in each phase belt, which causes a modulation in other phase belts due to the close coupling of the magnetic circuit. This does not occur at the interfaces of the solid portions of the reaction rail because of the high losses associated with this ripple.

Some care must be taken in the interpretation of solid and laminated back-iron data. The current and voltage levels change when the motor passes over the special section. However, an examination of the data at an instant when the motor straddles two different types of reaction rail clearly confirms that the differential of flux levels still exists for poles linked with different types of reaction rails.

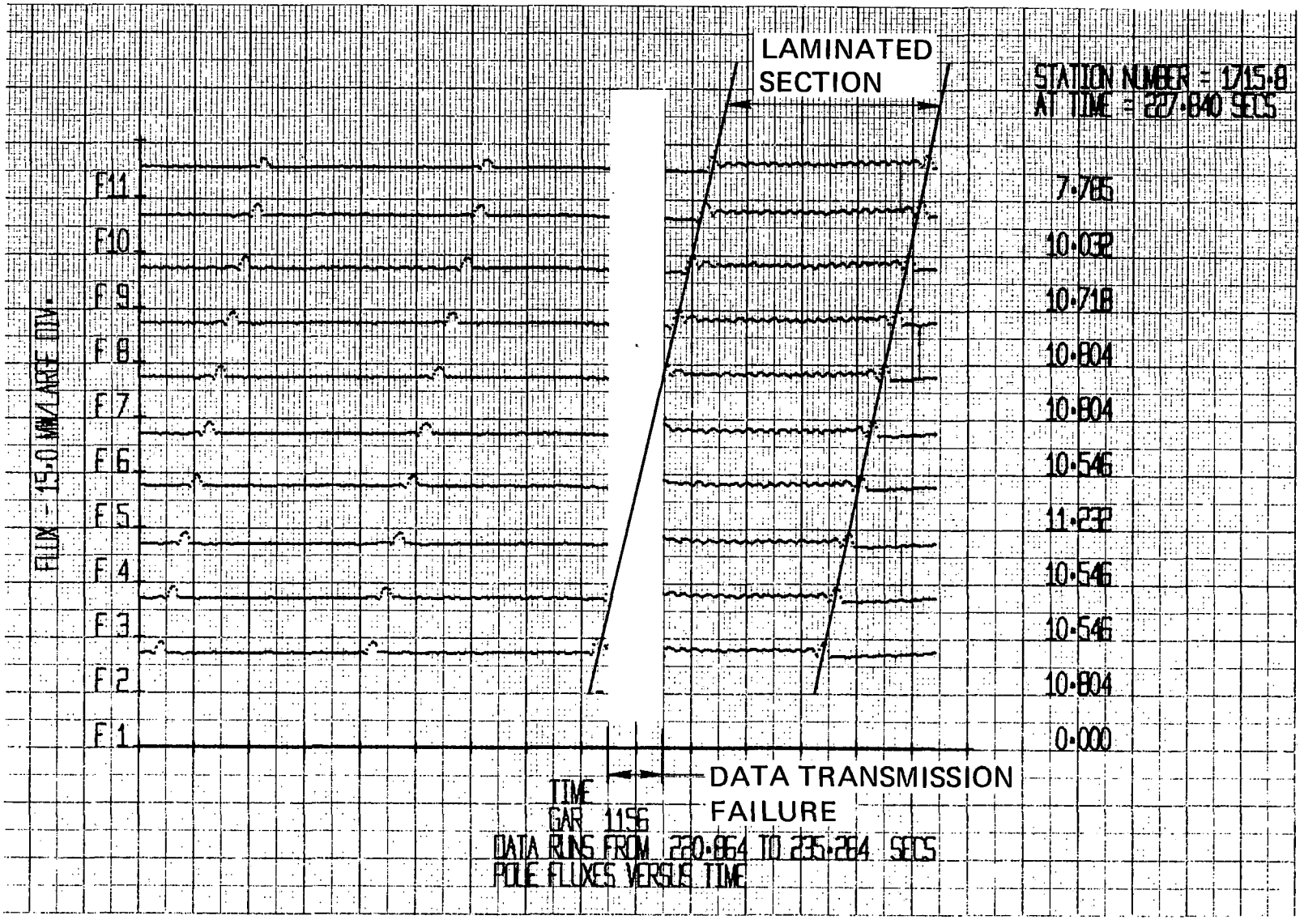

S-39805

Figure 10-7. Pole Flux Variations, Run 1156

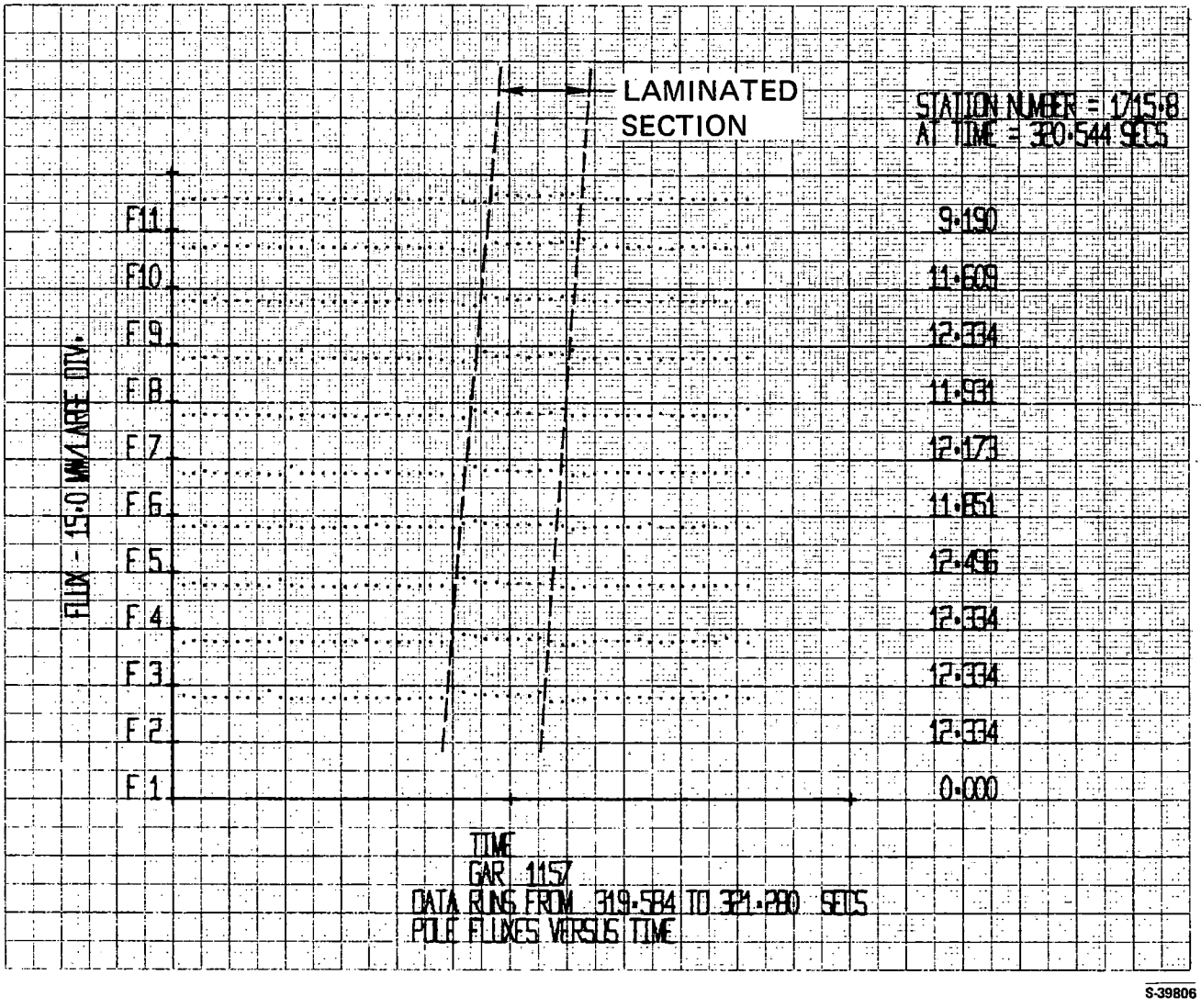

Figure 10-8. Pole Flux Variations, Run 1157

A summary of pertinent instantaneous data illustrating this point is shown in Table 10-2. However, in order to assess the effect of the laminated section, F5 data (pole flux #5) was normalized (Table 10-3) to two excitation conditions, and its magnitude compared over the two different types of reaction rail. These excitation conditions were: I = 1400 A (indicated by F5N mnemonic), and V/Hz = 3.46 (indicated by F5V mnemonic)

Test Validity

It appears that the method of laminating the track backiron to facilitate flux pentration measurements has, at best, limited validity for measurement without the aluminum cover. Table 10-3 shows that the ratio of pole flux for the two types of reaction rail backiron departs significantly from unity when the data is normalized to constant current (test runs without the aluminum cover). The same data normalized to constant V/Hz reveals a smaller departure from unity for the larger airgap case, and a negligible difference between fluxes for the smaller airgap case.

One explanation of this behavior is that constant V/Hz excitation specifies approximately constant airgap flux, assuming the primary impedance is small. At the large airgap, the magnetizing reactance is low, and the consequent voltage drop across the primary impedance is significant. Magnetizing reactance is approximately inversely proportional to gap, and at smaller gaps, therefore, the voltage drop due to primary impedance is less. The ratio of airgap voltage E and supply voltage V tends to unity as gap width decreases to zero. Changes in secondary impedance due to the laminated and solid backiron configurations will thus have less effect at smaller airgaps. The difference between the solid and laminated backiron performance may be due to:

- Finite airgaps between adjacent horizontal laminations causing discrete changes of permeability within the backiron.
- High resistance paths between adjacent horizontal laminations causing large current flow in the top laminations.

However, Table 10-3 also shows that for the baseline reaction rail there is negligible difference in pole flux between laminated and solid sections. This indicates that the flux penetration in a coarsely laminated section of backiron is affected by the provision of a highly conducting plate on top of the backiron section. It also indicates that the departure of the coarsely laminated backiron behavior from that of the solid backiron may be caused by current flowing in the top lamination only.

TRACK FLUXES

Additional Instrumentation

Appendix F provides details of the initial track flux installation. After completion of the baseline reaction rail tests, the aluminum cover was removed, and tests were begun on the solid iron reaction rail. During the course of this tests, certain differences in motor characteristics were noted between

TABLE 10-2

INSTANTANEOUS DATA FROM FLUX VARIATION TESTS

Run 1022	Solid Iron	Laminated Iron
Time, s	198.720	200.0
IA, A	1899	1899
V/Freq, V/Hz	3.09	3.08
F5, mWb	7.863	7.883
Run 1023		
Time, s	337.632	338.08
IA, A	1829	1829
V/Freq, V/Hz	3.19	3.18
F5, mWb	8.137	7.988
Run 1122		
Time, s	403.008	404.448
IA, A	1469	1249
V/Freq, V/Hz	4.09	4.14
F5, mWb	9.465	11.427
Run 1123		
Time, s	317.824	318.272
IA, A	1289	1109
V/Freq, V/Hz	4.12	4.05
F5, mWb	11.252	12.785
Run 1156		
Time, s	227.840	232.0
IA, A	1449	1279
V/Freq, V/Hz	4.03	4.32
F5, mWb	11.232	11.596
Run 1157		
Time, s	320.128	320.544
IA, A	1389	1249
V/Freq, V/Hz	4.13	4.29
F5, mWb	11.868	12.496

TABLE 10-3

NORMALIZED FLUX VARIATION TEST DATA

Data Source	Type Rail	Mech Airgap, mm	Solid Iron	Laminated	Solid/ Laminated
Run 1022					
F5V, mWb	Baseline	24	8.30	8.34	0.995
F5N, mWb			5.80	5.81	0.998
Run 1023					
F5V, mWb	Baseline	24	8.32	8.19	1.02
F5N, mWb			6.23	6.11	1.02
Run 1122					
F5V, mWb	Solid Iron	27.5	7.54	9.00	0.84
F5N, mWb			9.02	12.81	0.70
Run 1123					
F5V, mWb	Solid Iron	27.5	8.90	10.30	0.86
F5N, mWb			12.22	16.14	0.76
Run 1156					
F5V, mWb	Solid Iron	18	9.09	8.75	1.04
F5N, mWb			10.85	12.70	0.85
Run 1157					
F5V, mWb	Solid Iron	18	9.37	9.49	0.98
F5N, mWb			11.96	14.01	0.85

the special laminated section, and the remainder of the reaction rail. Accordingly, two additional search coils were installed in the special laminated section, one-half pole pitch apart, to effect comparison of the true solid iron track flux with the total flux in the laminated section. Details of this installation are also given in Appendix F.

Baseline Reaction Rail

Table 10-4 shows pertinent supporting data for track flux data obtained from runs 1022 through 1036. It can be seen that the excitation frequency varies significantly from the selected data criterion of 94.3 ±1 Hz. Two nominal levels of excitation were investigated to detect possible effects of saturation.

TABLE 10-4

SUPPORTING DATA FOR TRACK FLUXES, BASELINE REACTION RAIL

Ref. Figure	Run	IA, A	V/Hz	DF, Hz	Freq, Hz	Velocity m/s	Time
10-9	1022	1889	3.08	94.2	101.1	4.8	200.0
10-10	1023	1829	3.18	61.8	88.0	19.2	338.08
10-11	1024	1760	3.48	35.8	98.1	44.6	162.304
10-12	1025	1360	3.52	16.8	93.7	54.8	151.744
10-13	1026	1430	3.52	19.4	92.0	51.8	160.960
10-14	1027	1070	3.68	9.9	95.2	60.7	148.928
10-15	1028	951	3.60	6.7	95.2	62.8	142.240
10-16	1030	860	3.55	-0.2	94.4	67.3	156.064
10-17	1031	1910	4.16	27.8	94.1	47.0	163.008
10-18	1033	1500	4.24	15.2	90.6	53.8	161.048
10-19	1035	1250	4.36	10.1	93.7	59.2	146.880
10-20	1036	1120	4.40	5.1	93.6	63.3	144.960

Figures 10-9 through 10-20 show track flux data for runs 1022 through 1036 (cross-referenced in Table 10-4).

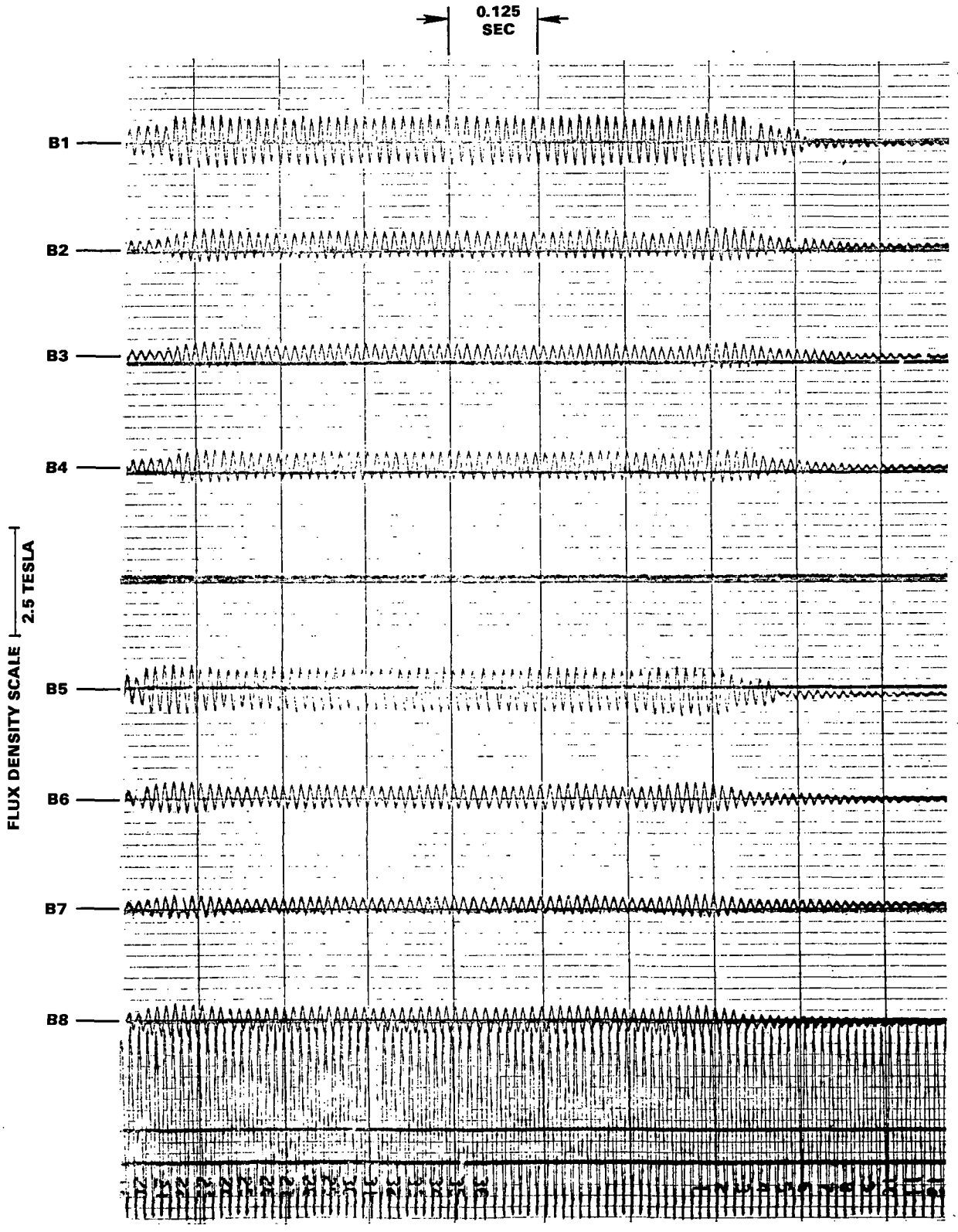

Figure 10-9. Track Flux Densities, Run 1022

S-39781

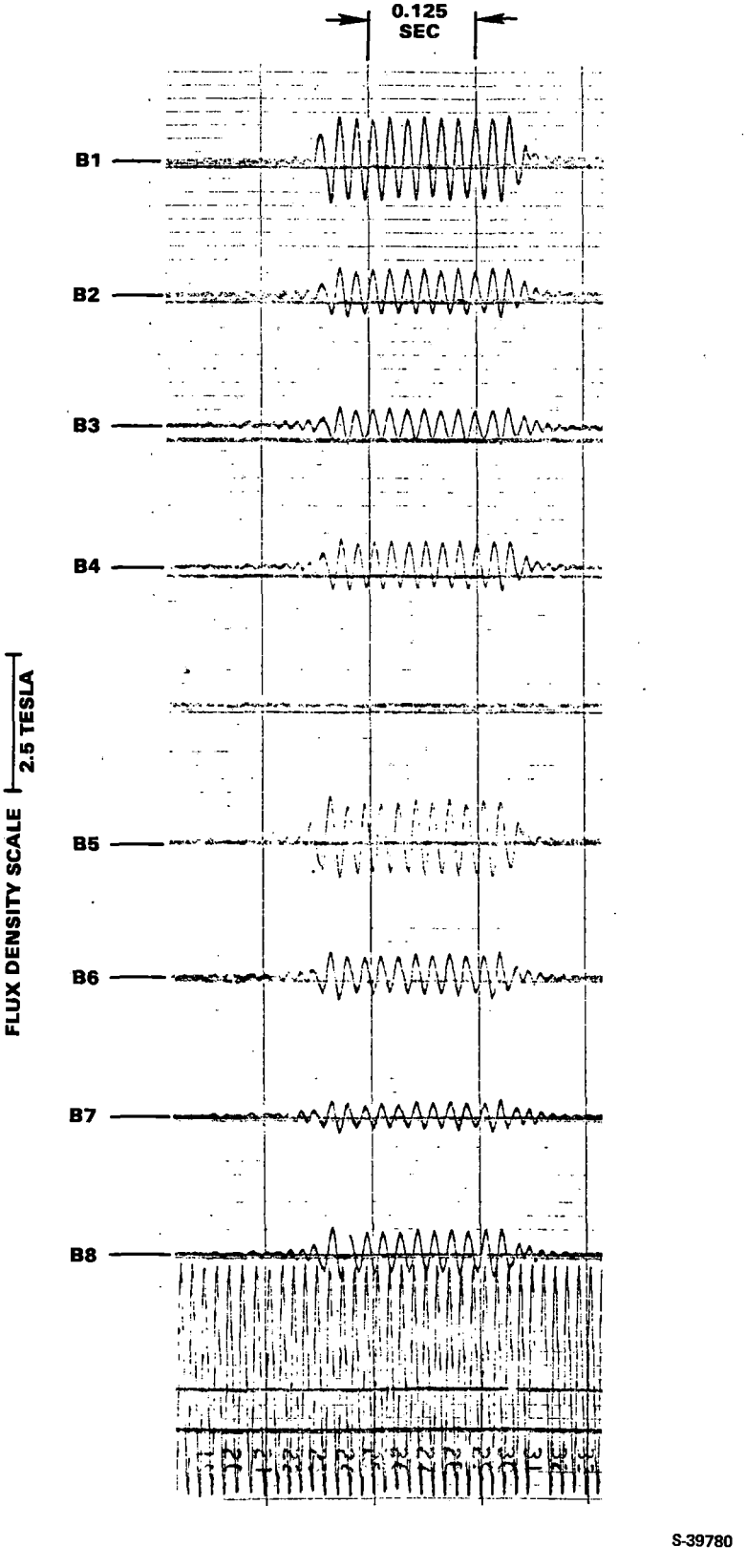

Figure 10-10. Track Flux Densities, Run 1023

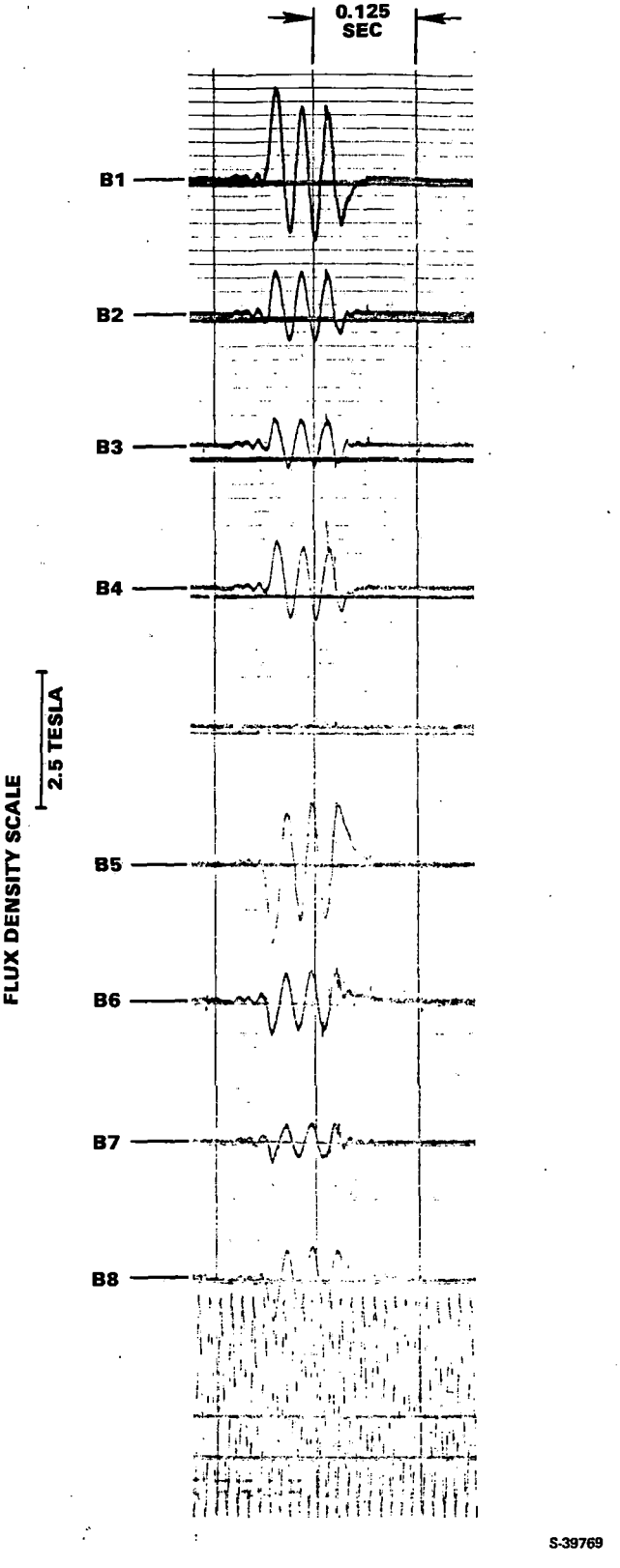

Figure 10-11. Track Flux Densities, Run 1024

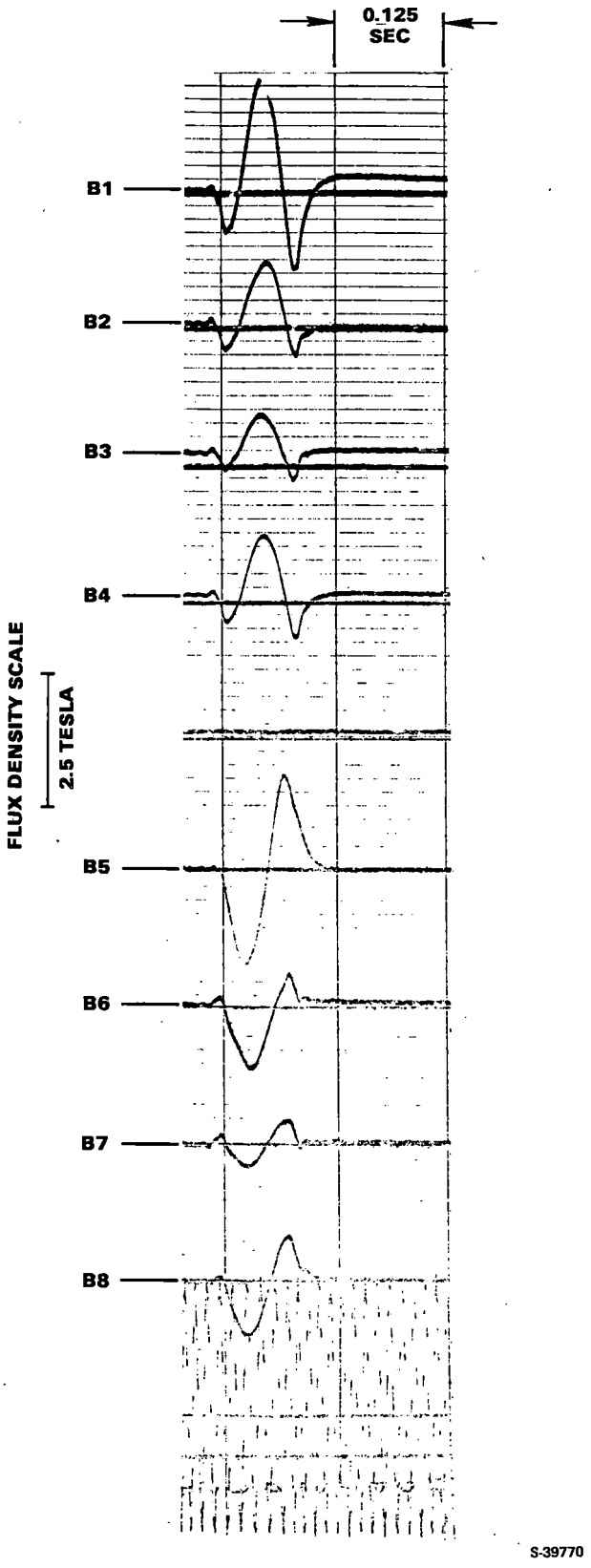

Figure 10-12. Track Flux Densities, Run 1025

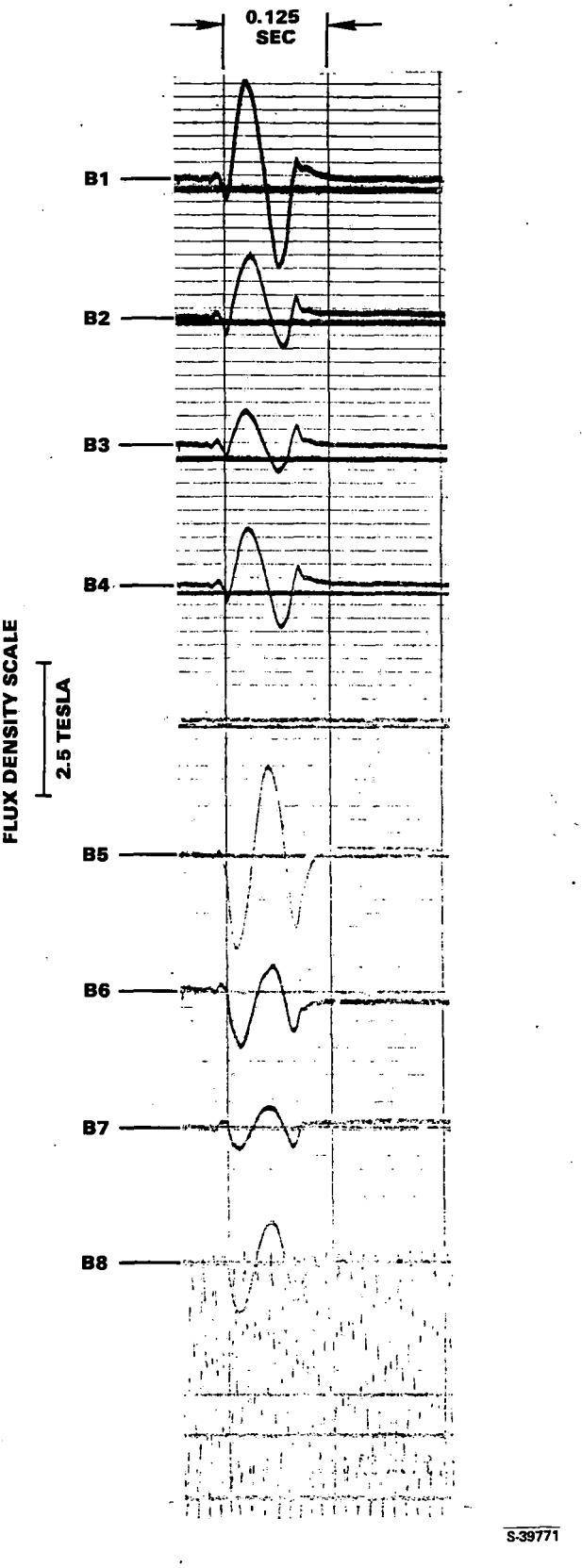

Figure 10-13. Track Flux Densities, Run 1026

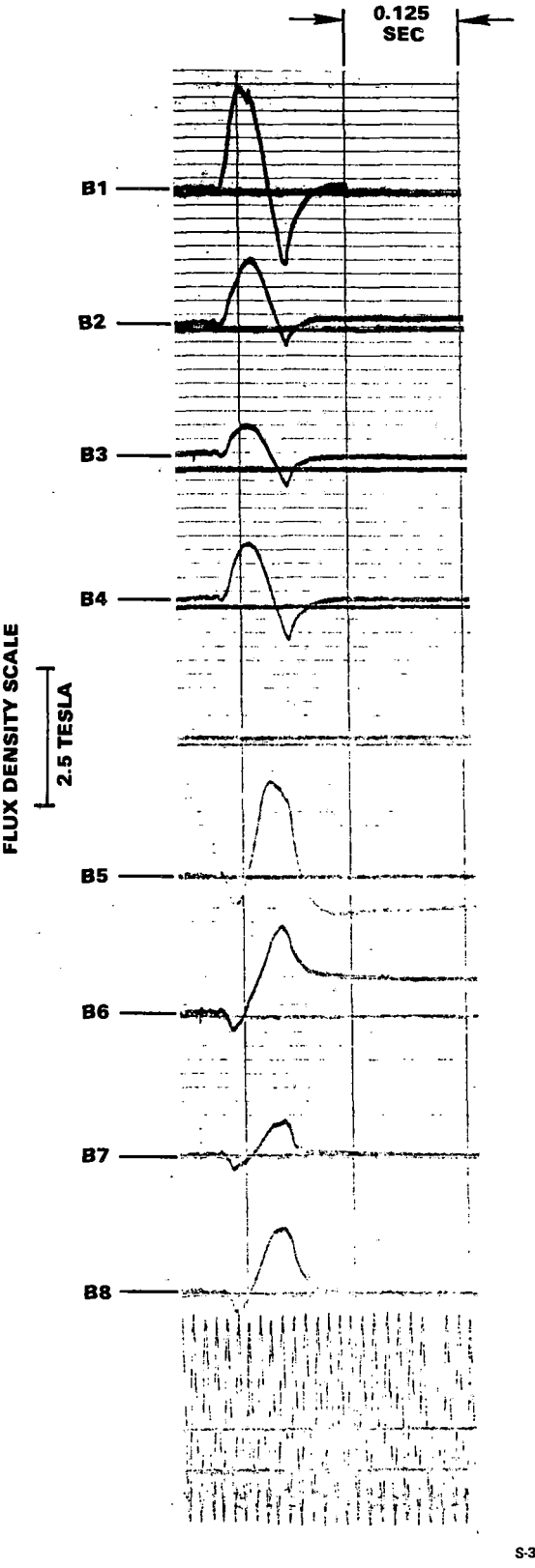

Figure 10-14. Track Flux Densities, Run 1027

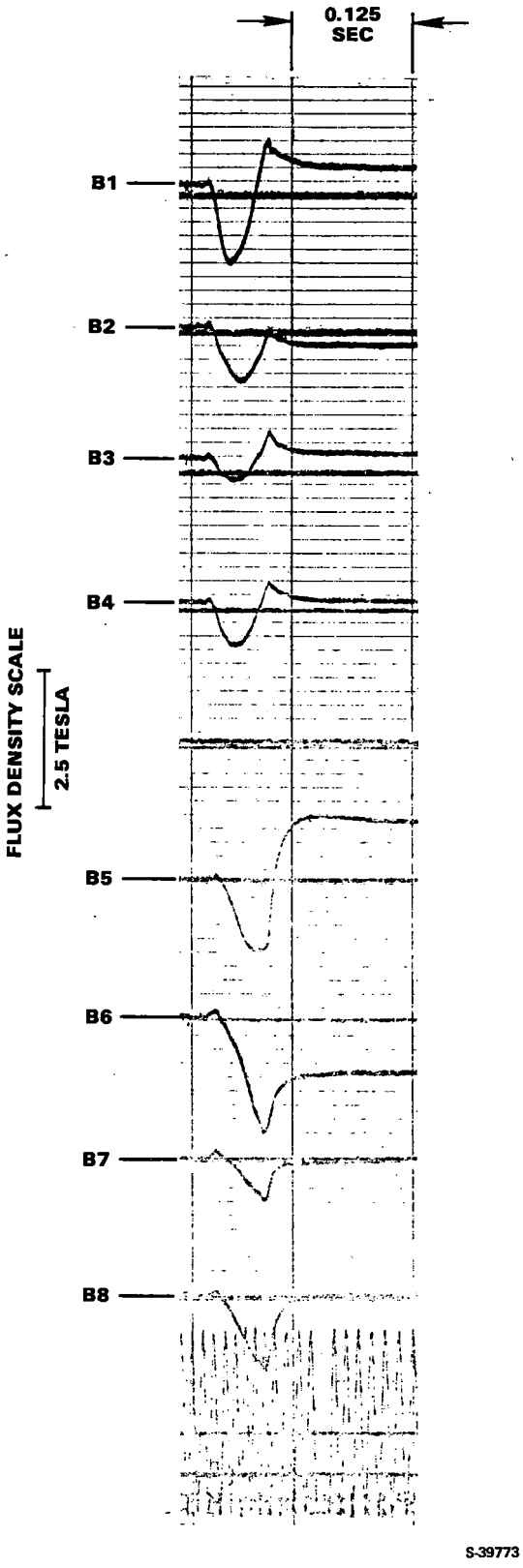

Figure 10-15. Track Flux Densities, Run 1028

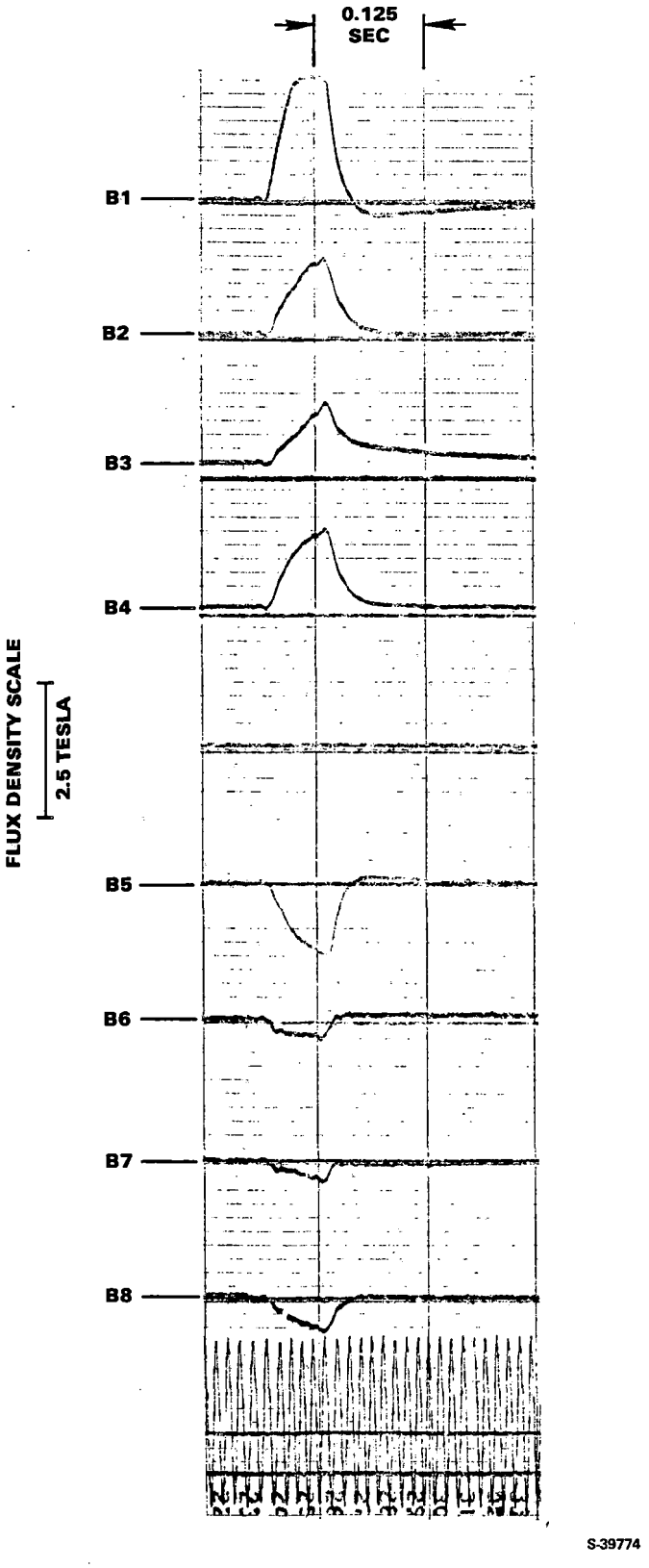

Figure 10-16. Track Flux Densities, Run 1030

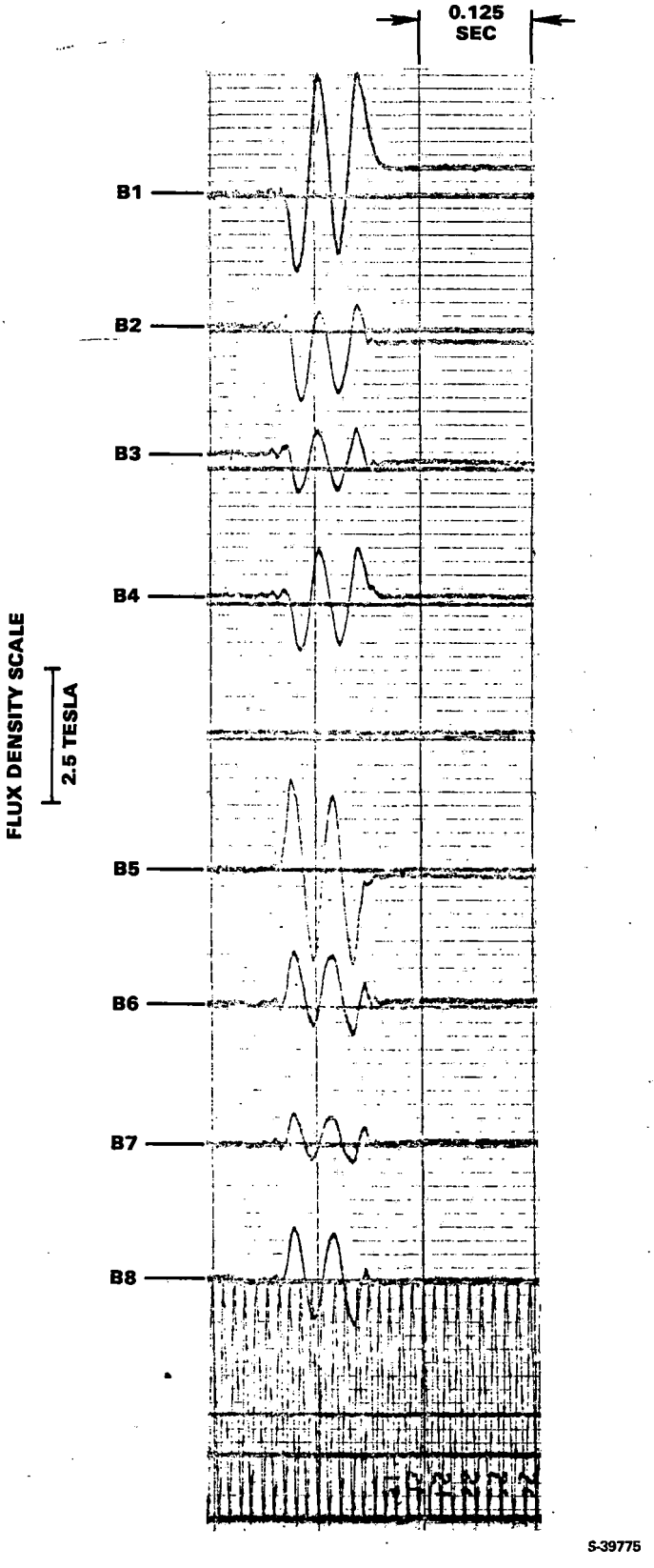

Figure 10-17. Track Flux Densities, Run 1031

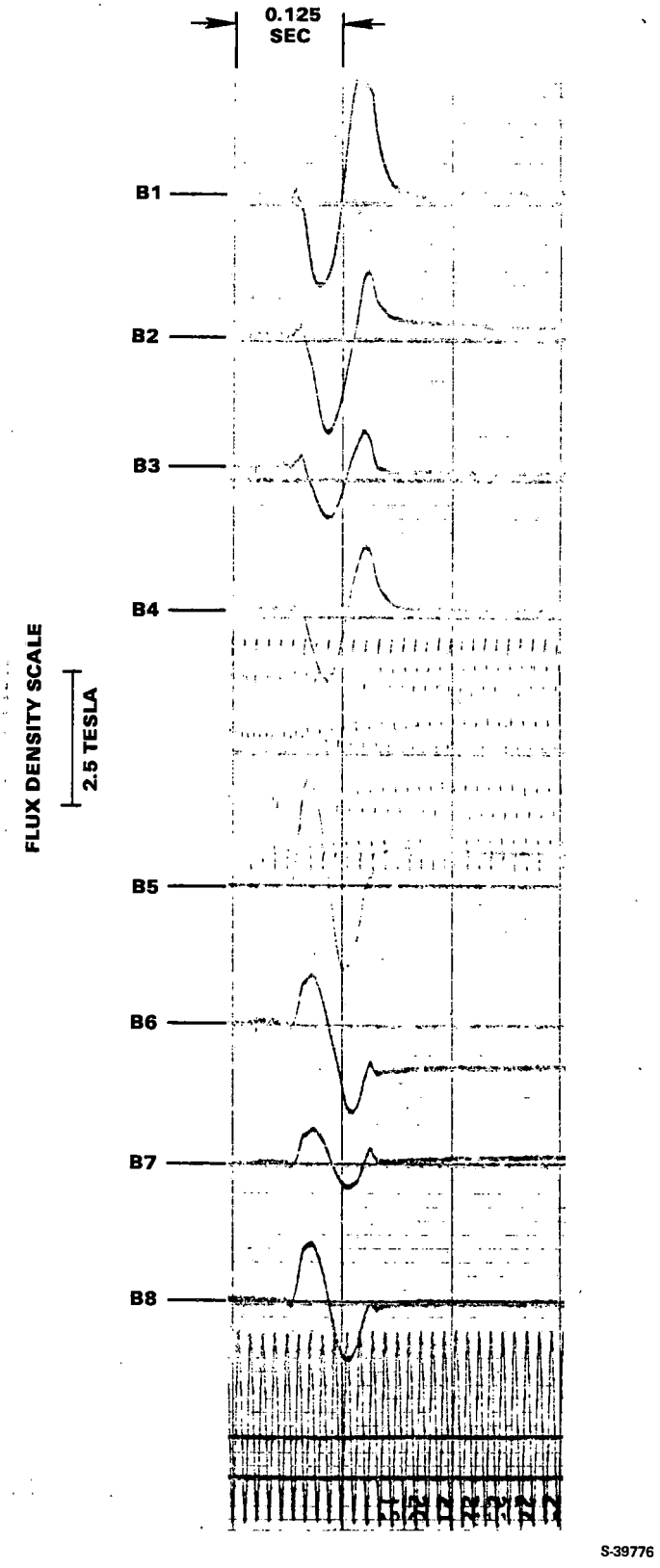

Figure 10-18. Track Flux Densities, Run 1033

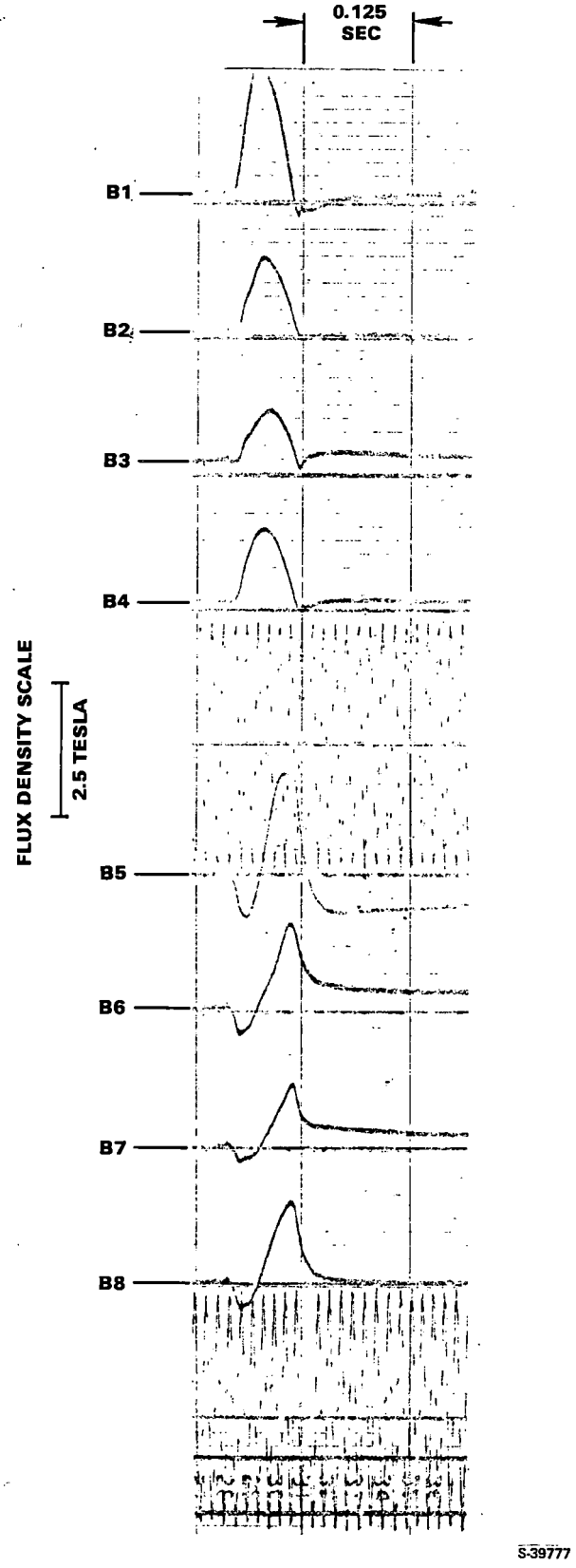

Figure 10-19. Track Flux Densities, Run 1035

The following observations were made about these flux traces.

- Remanent Flux

  Significant remanent magnetism is evident in the separate layers (see Figures 10-12 through 10-20) for the higher speed runs, although this remanence is not apparent in the search coils linking the total backiron. This degree of remanence is a function of the longitudinal position along the backiron and the vertical penetration depth. However, this is difficult to quantify, as no datum flux level is shown on these curves, and the integrators processing the search coil EMF's are reset prior to each run.

- Effect of Saturation on Flux Distribution

  To compare similar runs at different excitation levels for the purpose of assessing the effect of backiron saturation, it is convenient to examine low-speed runs, where several cycles of track flux are observed. By so doing, the relative position of the traveling flux wave with respect to the fixed-track flux coils becomes unimportant. High-speed runs are difficult to analyze, as pointed out earlier in this section, in that different portions of a fraction of a flux cycle occur for two runs at identical frequencies and slips.

  Unfortunately, only two such runs at high slip were available for comparison, and the slips differ as summarized in Table 10-5. Flux distribution is also compared in Table 10-5. From this tabulated data, one may conclude that the flux distribution is unaffected by these changes of excitation within the accuracy of measurement. This poses a major problem in interpreting these waveforms, as absolute flux densities cannot be determined. However, it appears that the total flux waveforms do not undergo a zero excitation level change. These readings may therefore be compared with pole flux data for an estimate of leakage flux.

TABLE 10-5

FLUX DISTRIBUTION AS A FUNCTION OF SATURATION LEVEL

Run	1024	1031
Slip	0.36	0.30
Frequency, Hz	98.1	94.1
V/Hz	3.48	4.16

Percentage of total flux measured by search coil:				
*①	49	= 100%	52	= 100%
②	25		23	
③	26		25	
⑤	52	= 100%	57	= 100%
⑥	24		22	
⑦	24		21	

*See Figure 10-1 for locations of search coils.

- Flux Traces by Search Coils

The number of cycles (or that fraction of a cycle) shown by the search coil voltage depends on the per unit slip and number of motor poles. The relationship can be derived as follows:

Number of flux wave cycles shown by search coil voltage = slip frequency x time duration of the search coil facing the motor primary.

The time duration is determined by the length of the primary divided by the motor speed.

Since: motor speed = $(1-s)f \cdot 2\tau_p$

motor length = $P\tau_p$

where s = slip, per unit

f = line frequency

τ_p = pole pitch

P = number of motor poles

the time duration T for the search coil to face the primary number is, therefore:

$$P = \frac{P\tau_p}{2(1-s)f\tau_p} = \frac{P}{2(1-s)f}$$

The number of cycles shown in the search coil voltage trace will be:

$$n = SfT = \frac{SP}{2(1-s)} \qquad \text{Eq. (10-1)}$$

for the LIMRV, P = 10, therefore, $n = \frac{5s}{1-s}$ Eq. (10-2)

To verify Eq. (2):

For run 1031, $S = \frac{27.8}{94.1} = 0.295$

Substitute in Eq. (2)

$$n = \frac{5 \times 0.295}{0.705} = 2.1 \text{ cycles}$$

For run 1033, $s = \frac{15.2}{90.6} = 0.168$

$$n = \frac{5 \times 0.168}{0.832} = 1.01 \text{ cycles}$$

For run 1035, $s = \frac{10.1}{93.7} = 0.108$

$$n = \frac{5 \times 0.108}{0.892} = 0.603 \text{ cycle}$$

The traces for these three runs do indeed confirm the validity of Eq. (2).

When the trace is a small fraction of a cycle, the rise and decay (after the primary left the search coil) of core flux may show a false impression of the flux wave. For example, where the primary faces the search coils for time t_e, as shown in Figure 10-21(a). The ideal trace is represented by the heavy line for 25 percent of a cycle. However, the actual trace is shown in Figure 10-21(b), where the rise and decay of the flux modify the shape of the trace. In Figure 10-21(c), the motor primary passes the search coil so quickly that the flux trace does not exhibit the magnitude of the ideal flux.

When the flux trace persists for more than one or two cycles, the flux rise and decay times become negligible.

- Relationship of South and North Search Coils

South search coils are located one-half pole pitch from the north search coils. The vehicle moves from north to south. The flux trace by the south search coils should be 90 electrical degrees lagging behind those by the north search coils. However, in some of the oscillographic tracings, the south coils seem to be connected to the oscillograph in reversed polarity. Therefore, the south coil traces are apparently 90 electrical degrees ahead of the north coil traces for runs 1024, 1025, 1026, and others.

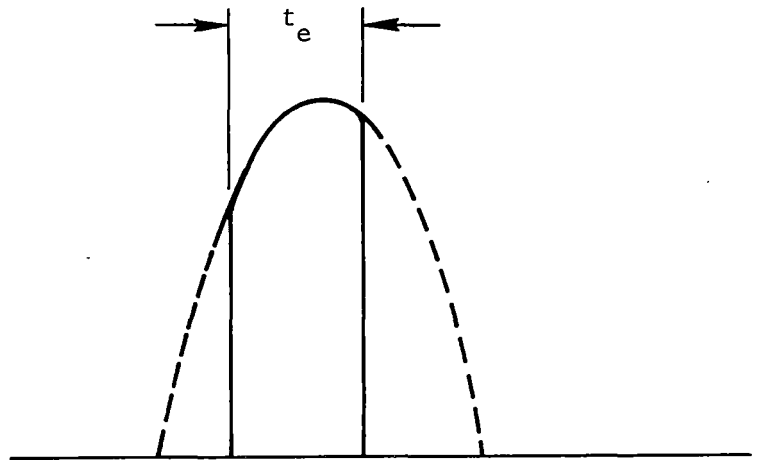

a. IDEAL FLUX TRACE

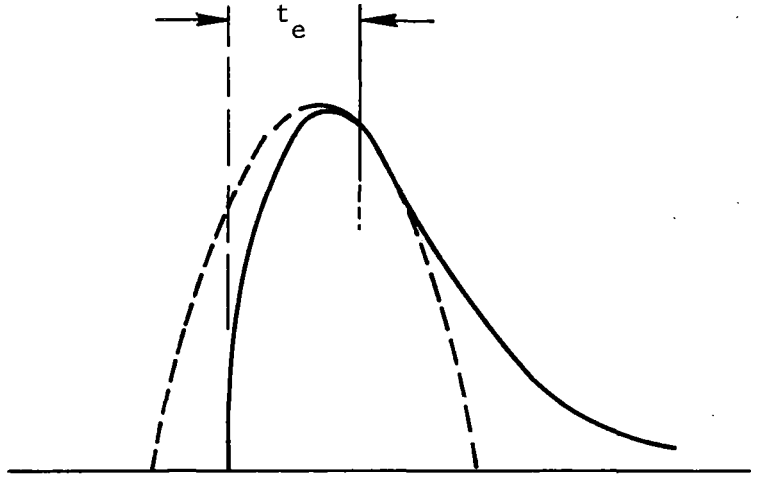

b. ACTUAL FLUX TRACE, MEDIUM VELOCITY

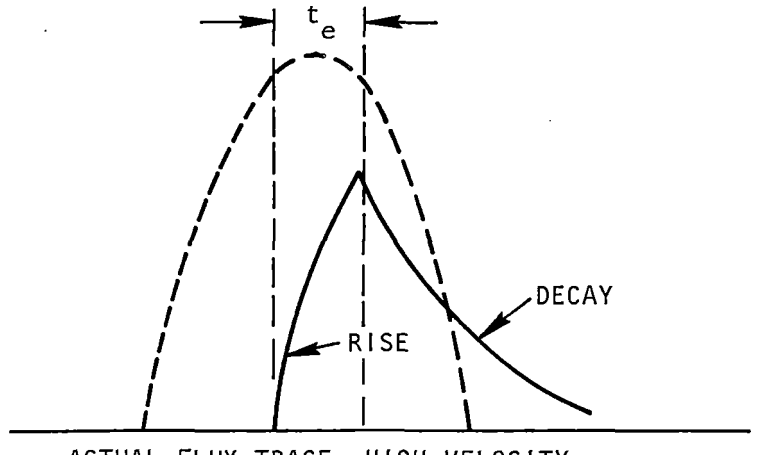

c. ACTUAL FLUX TRACE, HIGH VELOCITY

S-39740

Figure 10-21. Flux Traces for Fractional Cycle

When the flux trace covers only a fraction of a cycle, the traces of the north and south coils reflect different portions of a cycle. For example, in run 1035, the north coils traced the portion of a cycle from A to B in Figure 10-22(a). The south coils traced the portion C to D in Figure 10-22(b), where C is 90 degrees behind A. Because of the flux rise and decay, the actual traces are A'B' and C'D'.

- Component and Total Fluxes

The fluxes in the top, middle, and bottom are essentially in phase. They can be added arithmetically to compare with the flux reading of the search coil enclosing all three layers.

For example, examine the run 1031 data (north search coils) as listed in Table 10-7.

TABLE 10-7

COMPONENT AND TOTAL FLUXES, RUN 1031

Layer	Flex Density, Tesla	Coil Cross-Sectional Area, cm^2	Flux, mWb
Top, search coil ①	1.55	17.8	2.76
Middle, search coil ②	0.70	17.8	1.24
Bottom, search coil ③	0.35	26.7	0.93
Total, search coil ④	0.75	62.3	4.67

Top, middle, and bottom layer flux is 4.93 mWb, which is within 5 percent of the measured total flux, 4.67 mWb.

Solid Iron Reaction Rail

Table 10-8 lists pertinent supporting data for track flux tests on a 10-pole SLIM with a solid iron reaction rail. All tests were performed at a nomi-al excitation level of 4.3 V/Hz and an excitation frequency of 94.3 Hz.

The track flux traces are shown in Figures 10-23 through 10-31. The traces in Figures 10-23, 10-24, and 10-25 were generated by eight laminated flux search coils, those in Figures 10-26 through 10-30 by eight laminated search coils and two additional solid iron search coils as described earlier. Observations concerning these traces follow:

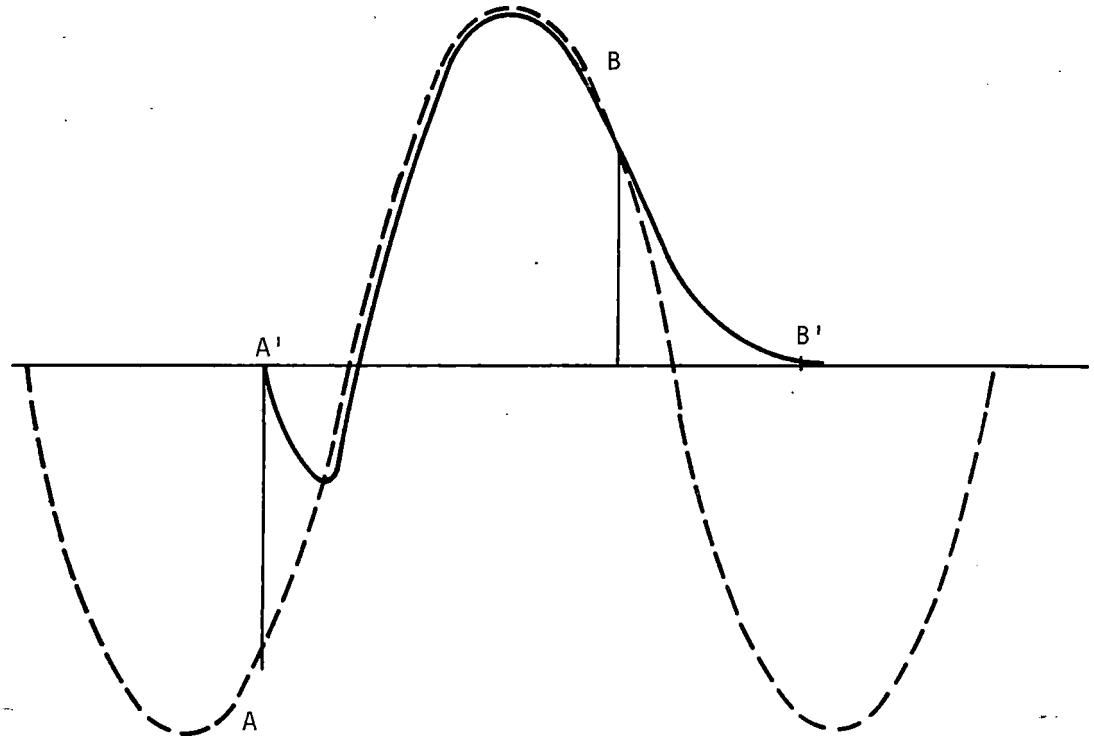

a. NORTH COIL

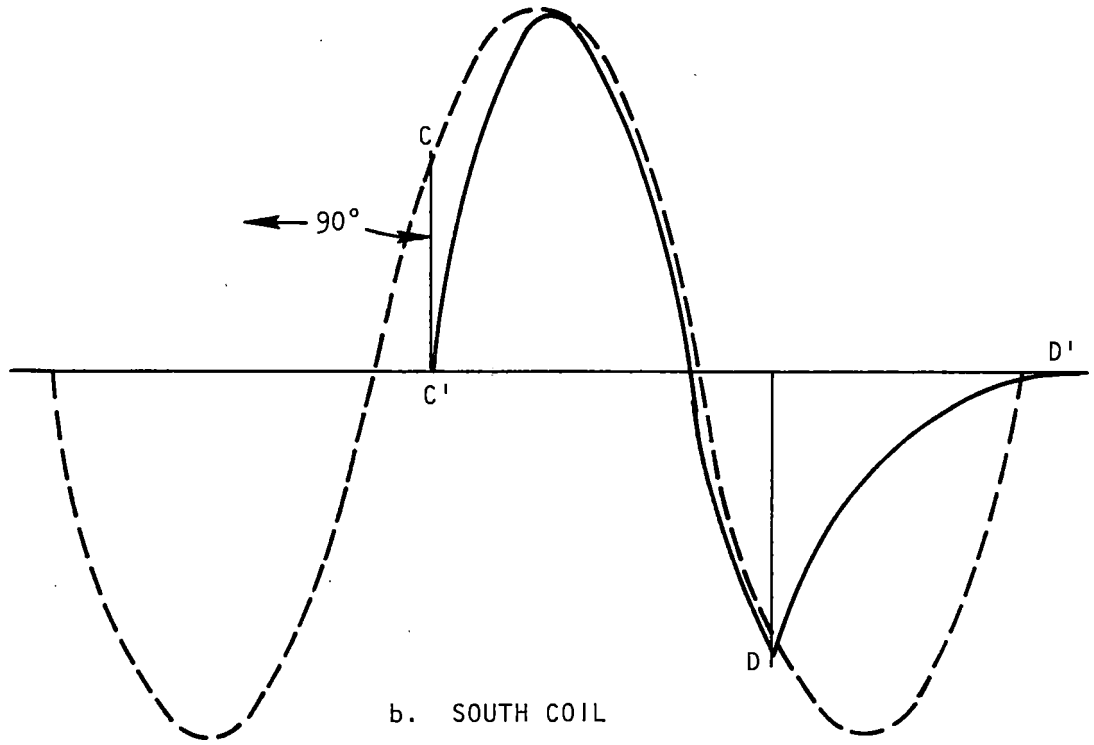

b. SOUTH COIL

S-39741

Figure 10-22. Search Coil Waveforms

- Very high apparent flux densities were recorded. For example, run 1172 involves a synchronous speed run, where the north search coils reflect negligible flux levels. This implies that the south search coils record peak flux levels along the motor. The unknown remanence factor makes quantification of this flux difficult. However, the single-amplitude flux density swing of the top lamination varies from 2.28 tesla at the front end (initial flux change) of the motor, and as much as 3.3 tesla at the trailing end (final flux change) of the motor.

TABLE 10-8

TOTAL TRACK FLUXES, SOLID SECTION

Run	Trace B9, peak-to-peak, T	Trace B10 peak-to-peak, T
1156	1.25	1.25
1157	1.41	2.19
1162	1.72	0.78

- A significant difference in phase angle occurs between the flux change in the top lamination and the corresponding changes in the middle lamination (see run 1170, Figure 10-29). A smaller difference in phase angle occurs between the middle and lower laminations. The phase shift may be identified with transverse currents enclosed in the upper laminations.

- A consistent difference exists between traces B4 and B9 (laminated and solid sections, respectively, south polarity) and B9 and B10 (laminated and solid sections, respectively, north polarity). This indicates that the use of coarsely laminated sections to investigate solid iron behavior has, at best, limited validity for magnitude measurement. This contention was supported earlier in the discussion of pole flux measurement.

- The relationship between traces B9 and B10 (total flux density, solid iron search coils) for runs 1156, 1157, and 1162 is shown in Table 10-9. No satisfactory explanation can be given for the different magnitudes noted between the two traces for low-speed runs 1157 and 1162.

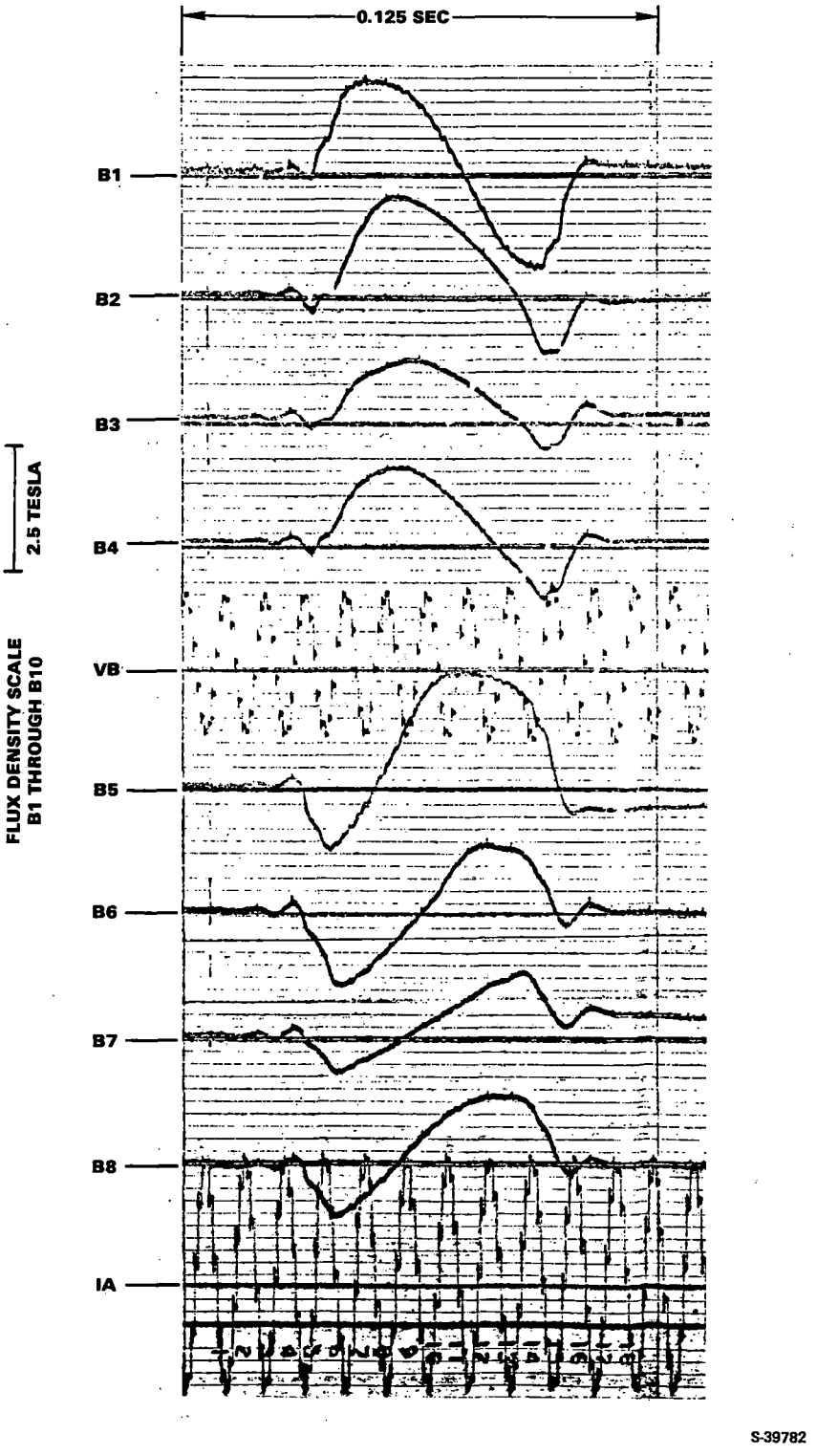

Figure 10-23. Track Flux Densities, Run 1133

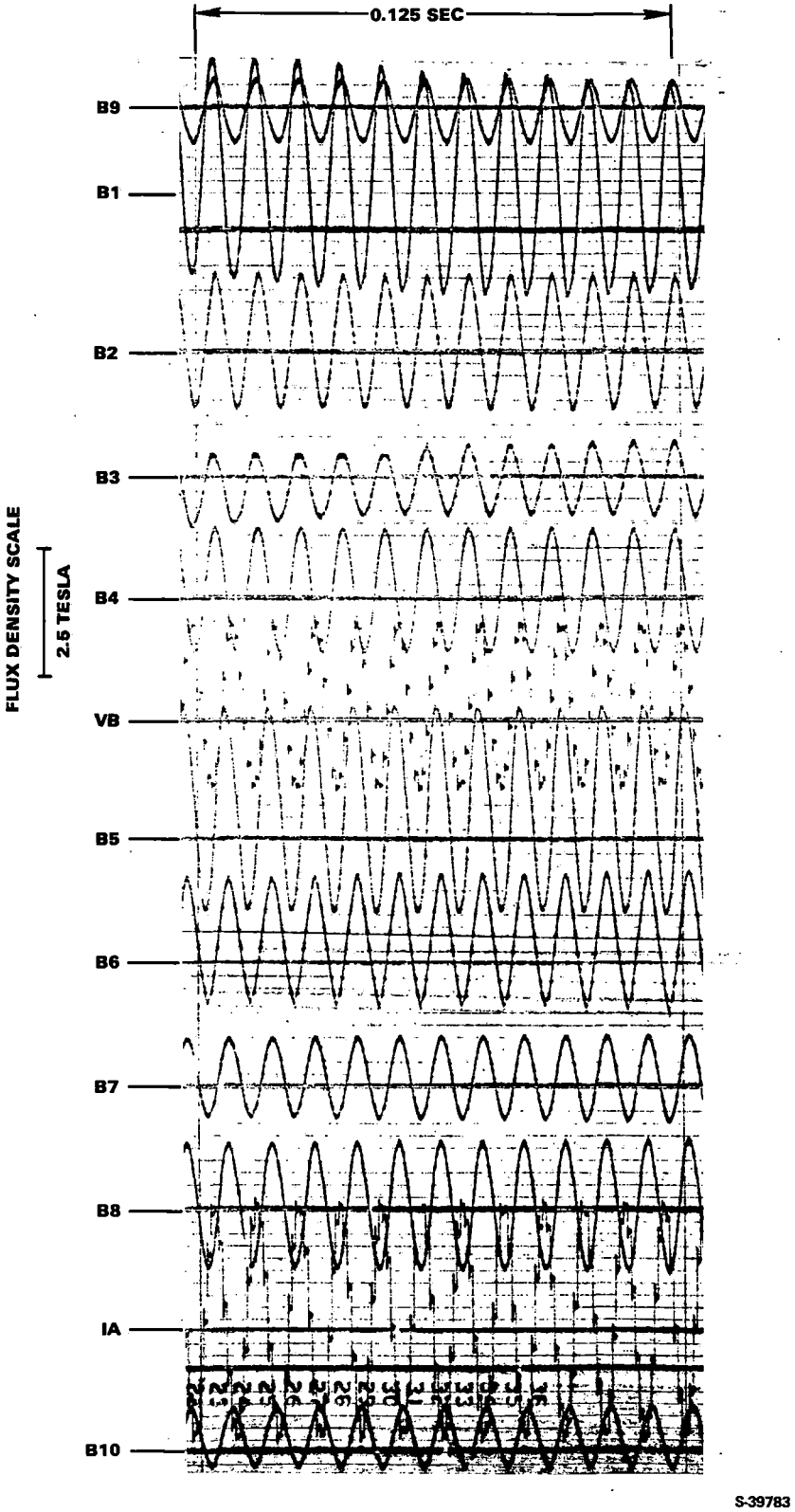

Figure 10-24. Track Flux Densities, Run 1156

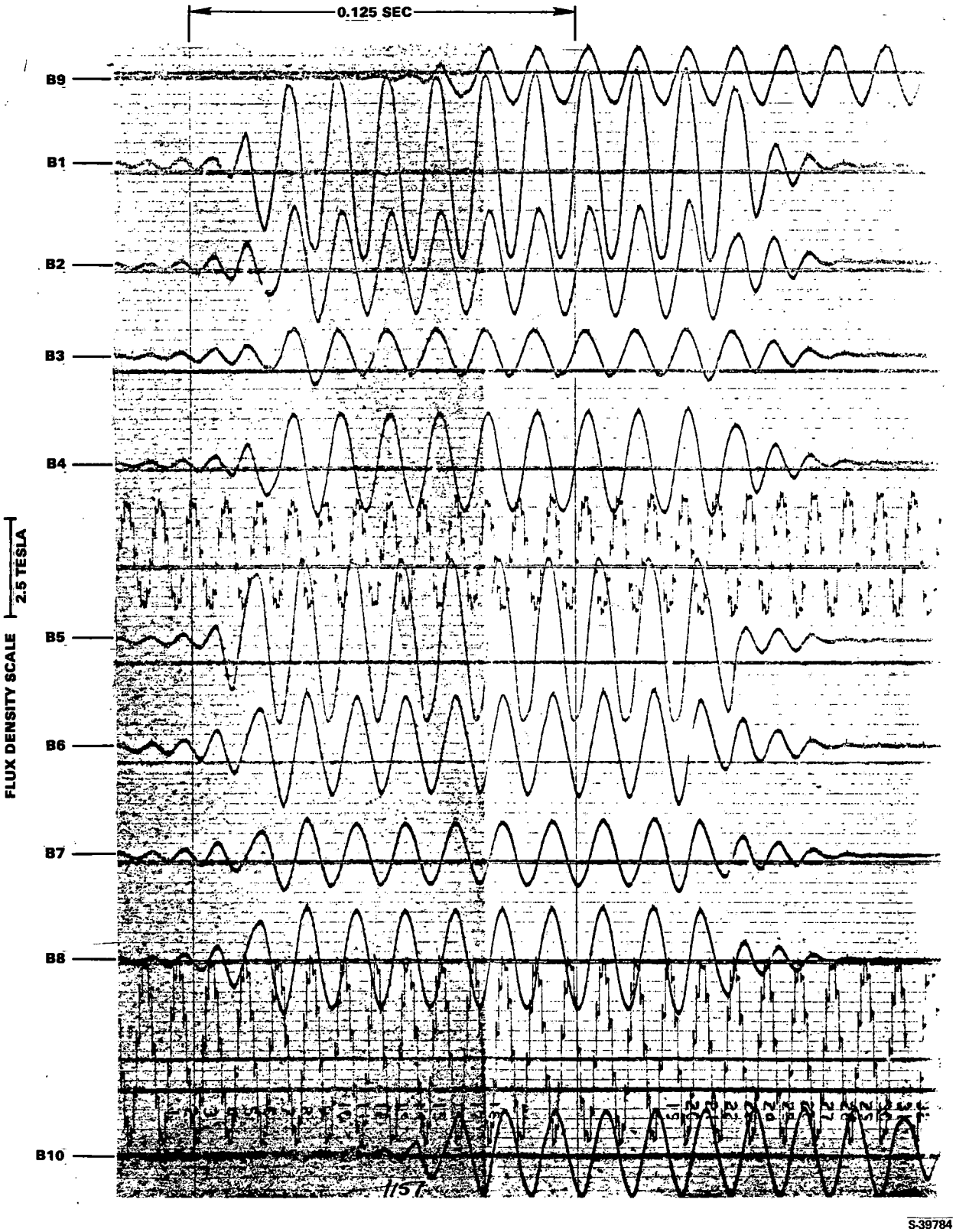

Figure 10-25. Track Flux Densities, Run 1157

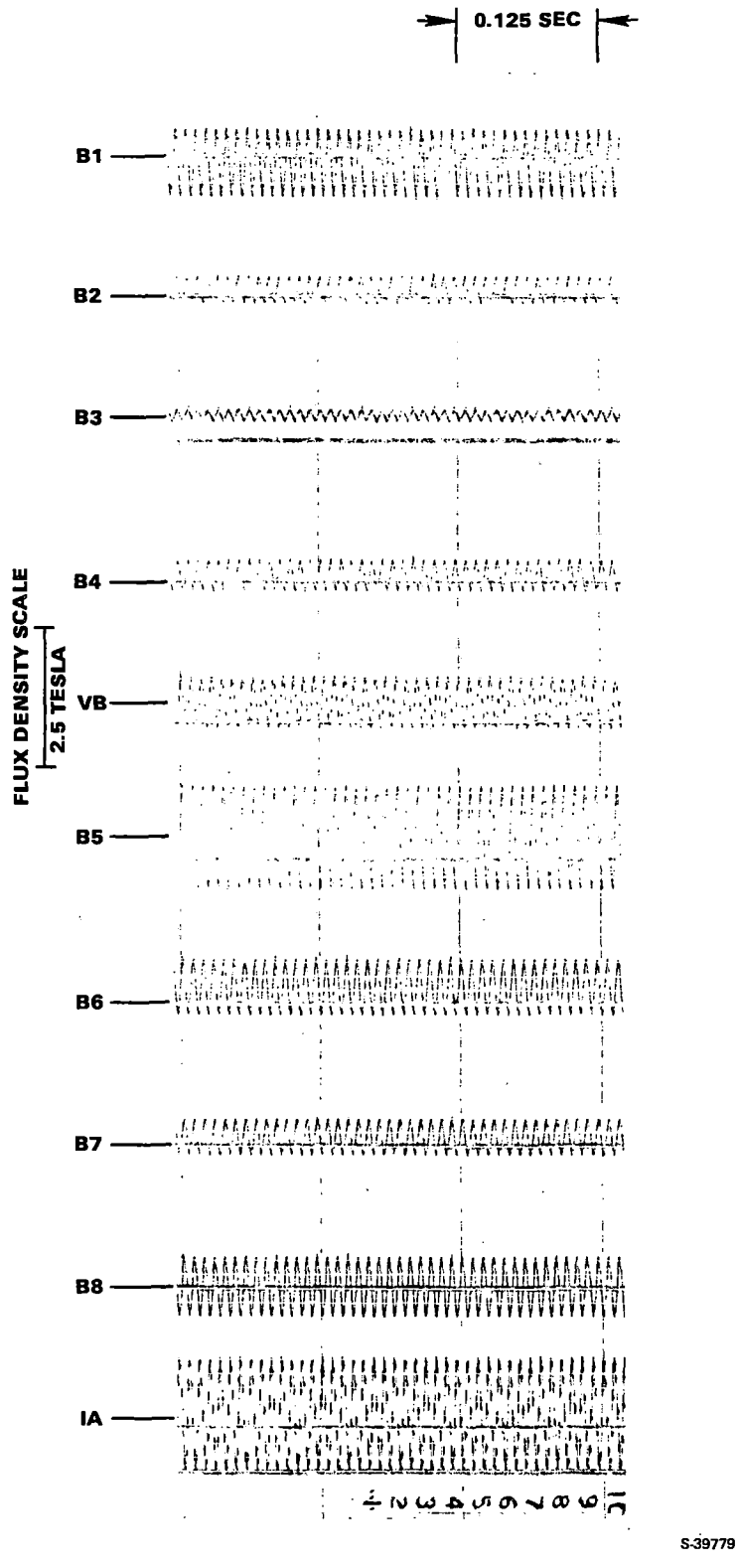

Figure 10-26. Track Flux Densities, Run 1158

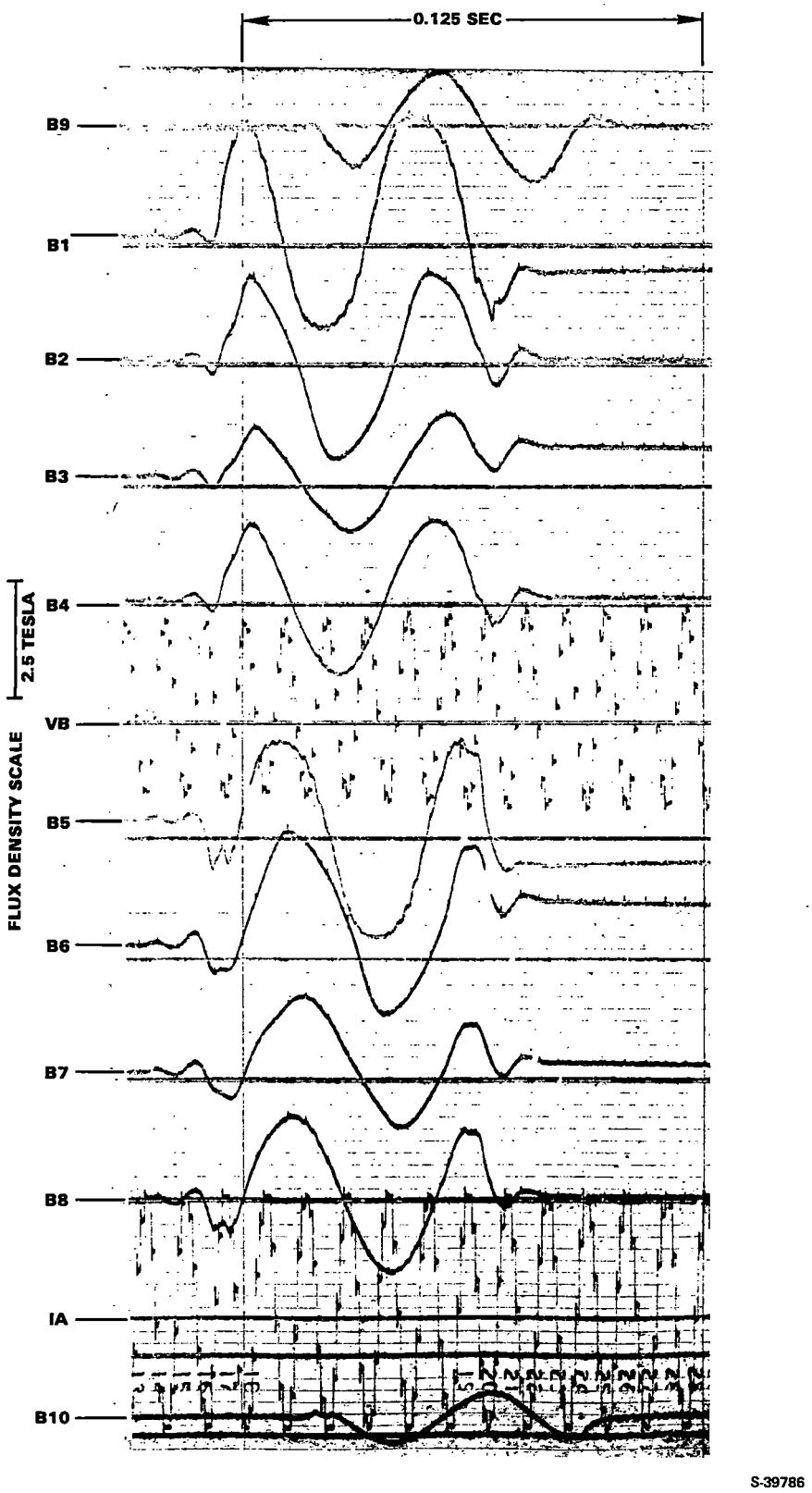

Figure 10-28. Track Flux Densities, Run 1164

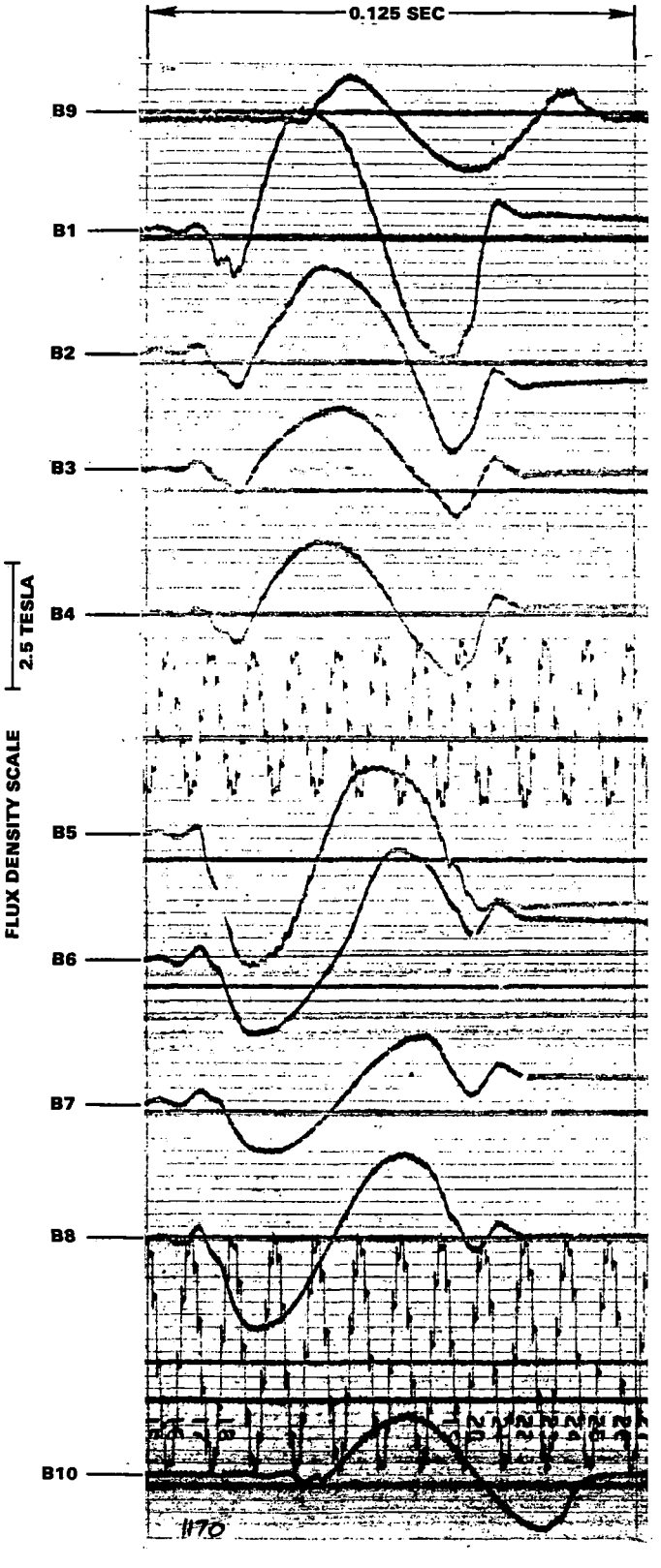

Figure 10-29. Track Flux Densities, Run 1170

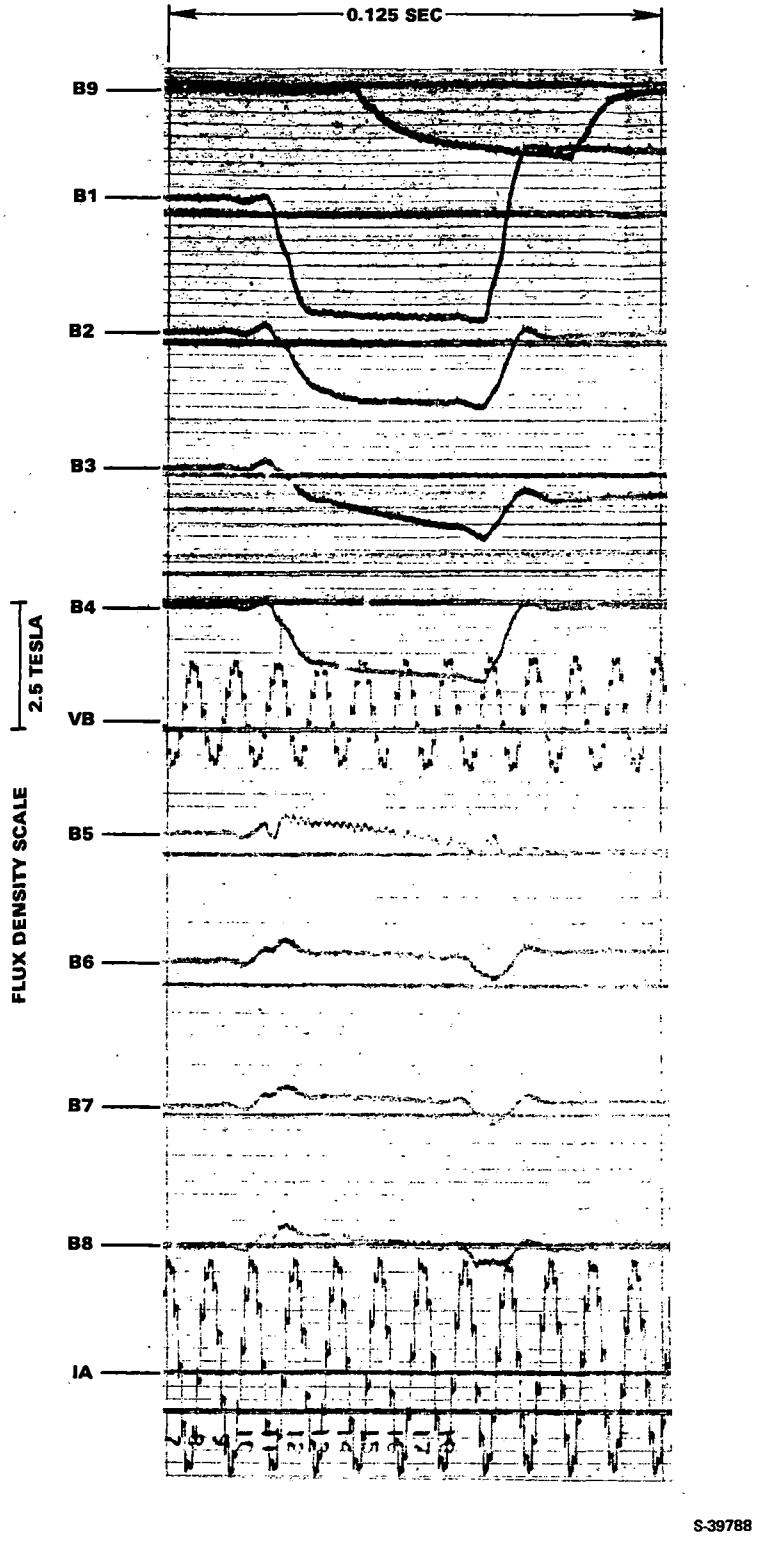

Figure 10-30. Track Flux Densities, Run 1172

SECTION 11

REFERENCES

(1) Study of Linear Induction Motor and Its Feasibility for High-Speed Ground Transportation, report to DOT study contract C-145-66/NEG, June 1967.

(2) Kalman, G. P., Irani, D., and Simpson, A., "Electrical Propulsion System for Linear Induction Motor Test Vehicle," Proceedings of 4th Intersociety Energy Conversion Engineering Conference, Washington, DC, September 1969.

(3) Linear Induction Motor Research, U.S. Department of Commerce, NTIS document FRA-RT-73-2-5, October 1971.

(4) "Analysis of LIM Electrical Performance Data," AiResearch document 73-9014, 1973.

(5) Chi, C. C., and Chen, R. P., "Linear Induction Motor Research Vehicle Wheel/Rail Adhesion Test," NTIS document FRA-OR&D 76-261, April 1976.

(6) Young, A. R., "Thrust Augmentation System Description for the LIM Research Vehicle Program," AiResearch document 74-10154, 1974.

(7) Powell, R. B., "Linear Induction Motor Electrical Braking Test," NTIS document FRA-OR&D 76-264, April 1976.

(8) Chi, C. C., "Linear Induction Motor Research Vehicle Speed Upgrading Tests (190 to 250 mph): Final Report," NTIS document FRA-OR&D 76-268, 1976.

(9) Powell, R. B., and McConville, J. H., "LIMRV Reaction Rail and Airgap Flux Distribution Test," AiResearch document 75-11965, January 1976.

(10) Bevan, R. J. A., "Effect of Machine Length on the Performance of Linear Induction Motors: An Experimental Investigation," NTIS document FRA-OR&D 79-07, December 1978.

(11) Bevan, R. J. A., "Linear Induction Motor Research Vehicle Systems Analysis (SLIM Configuration)," AiResearch document 78-15261, November 1978.

(12) LIMRV Reaction Rail Edge Effect Investigation: Effectiveness of Rail Slotting, NTIS document PB-261811/4GI, April 1976.

(13) LIM Electrical Performance Test, NTIS document PB-261856/9GI, June 1976.

(14) Boldea, I., and Nasar, S. A., "Quasi-1-Dimensional Theory of Linear Induction Motors with Half-Filled Primary End Slots," Proceedings of IEE, Vol. 122, No. 1, January 1975.

(15) Matrix Analysis of Linear Induction Motors, NTIS document PB-254574/7GI, September 1975.

(16) Elliott, D. G., "Comparison of Experimental and Theoretical Reaction Rail Currents, Rail Voltages, and Airgap Fields for the LIMRV," NTIS document FRA-ORD-77-33, June 1977.

(17) Method of Analysis of Linear Induction Motors, NTIS document N74-12914, 1973.

(18) Boldea, I., and Nasar, S. A., "Dc Braking Characteristics of Double-Sided Linear Induction Motors," International Quarterly Review, Electric Machines and Electromechanics, Vol. 3, No. 3, April 1979.

(19) Bolton, H., "Forces on Linear Induction Motor Secondaries with Lateral Asymmetry," Proceedings of IEE, Vol. 117, No. 12, December 1970.

(20) Bevan, R. J. A., "Test Plan, Linear Induction Motor Research Vehicle Electrical Performance Tests, SLIM Configuration," AiResearch document 78-14892, February 1978.

(21) Dobbs, D. J., et al., "Magnetically Levitated and Wheeled Minitram Comparison Study," British Rail report TREDYN2 to U. K. Transport and Road Research Laboratory, December 1974.

(22) Tracked Hovercraft Limited, U. K., "Linear Induction Motor Guidance System for Air Cushion Vehicles," December 1971.

(23) Chalmers, B. J., and Woolley, T., "General Theory of Solid Rotor Induction Machines," Proceedings of IEE, Vol. 119, No. 9, September 1972.

APPENDIX A

TEST FACILITY

This appendix contains additional input data for SLIM mathematical models, as well as general information about the test facility.

Table A-1 lists pertinent dimensions and provides other design data on the SLIM primary and secondary (reaction rail). Figure A-1 specifies the dimensions of the primary stack lamination. Figure A-2 shows physical details of the primary stack lamination. Figures A-3 and A-4 show the LIM primary winding coil assembly and winding connections, respectively. Table A-2 lists leading particulars of the LIMRV.

Design highlights of the SLIM primary suspension and reaction rail will be found in Appendix B. Appendix F describes the special 6.1-m track section used for measuring backiron track flux.

TABLE A-I

SLIM LEADING CHARACTERISTICS

Peak Thrust Point	
Thrust	8.8 kN
Slip, per unit	0.265
Excitation	0.346 V/Hz/pole
Current	1400 A, RMS
Frequency	94.3 Hz
Airgap (primary to secondary)	25.4 mm
LIM Primary Stack	
Material	AISI M-19C-4
Width	254 mm
Length	3810 mm
LIM Primary Winding	
Poles	10
Pole pitch	355.6 mm
Slots	160
Slot pitch	23.698 mm
Slot width	16 mm
Conductors per slot	2 (10 slots at each end are half-filled)
Slots per pole	15
Coil pitch	2/3
Conductors	4 lengths of 33.6 mm^2 (nominal) square magnet wire per coil (MIL-W-593C)
Coils	Double-layer, diamond, lower end bent 90 degrees
Series conductors per phase	100
LIM Secondary (Reaction Rail)	
Cover	
Material	Aluminum alloy, 6061-T6
Conductivity	47.5 percent I.A.C.S. (20°C)
Overall width	457.2 mm
Thickness	4.06 mm (typ)
Backiron	
Material	AISI 1010
Overall width	279.4 mm
Thickness	22.23 mm (typ)

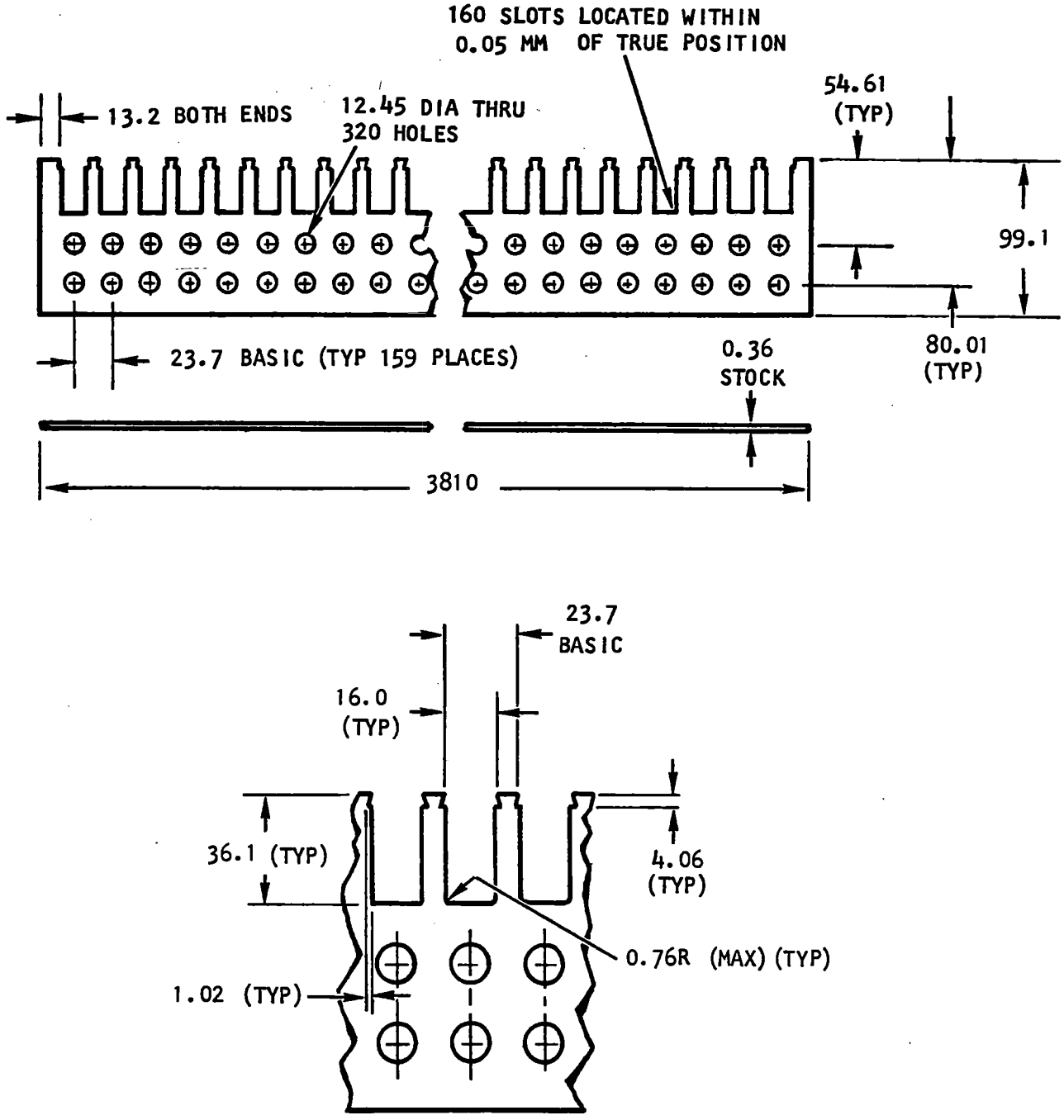

NOTES:

1. ALL DIMENSIONS ARE IN MILLIMETERS.
2. MATERIAL CONFORMS TO AISI M-19C-4.

S-99506-A

Figure A-1. LIM Primary Stack Lamination

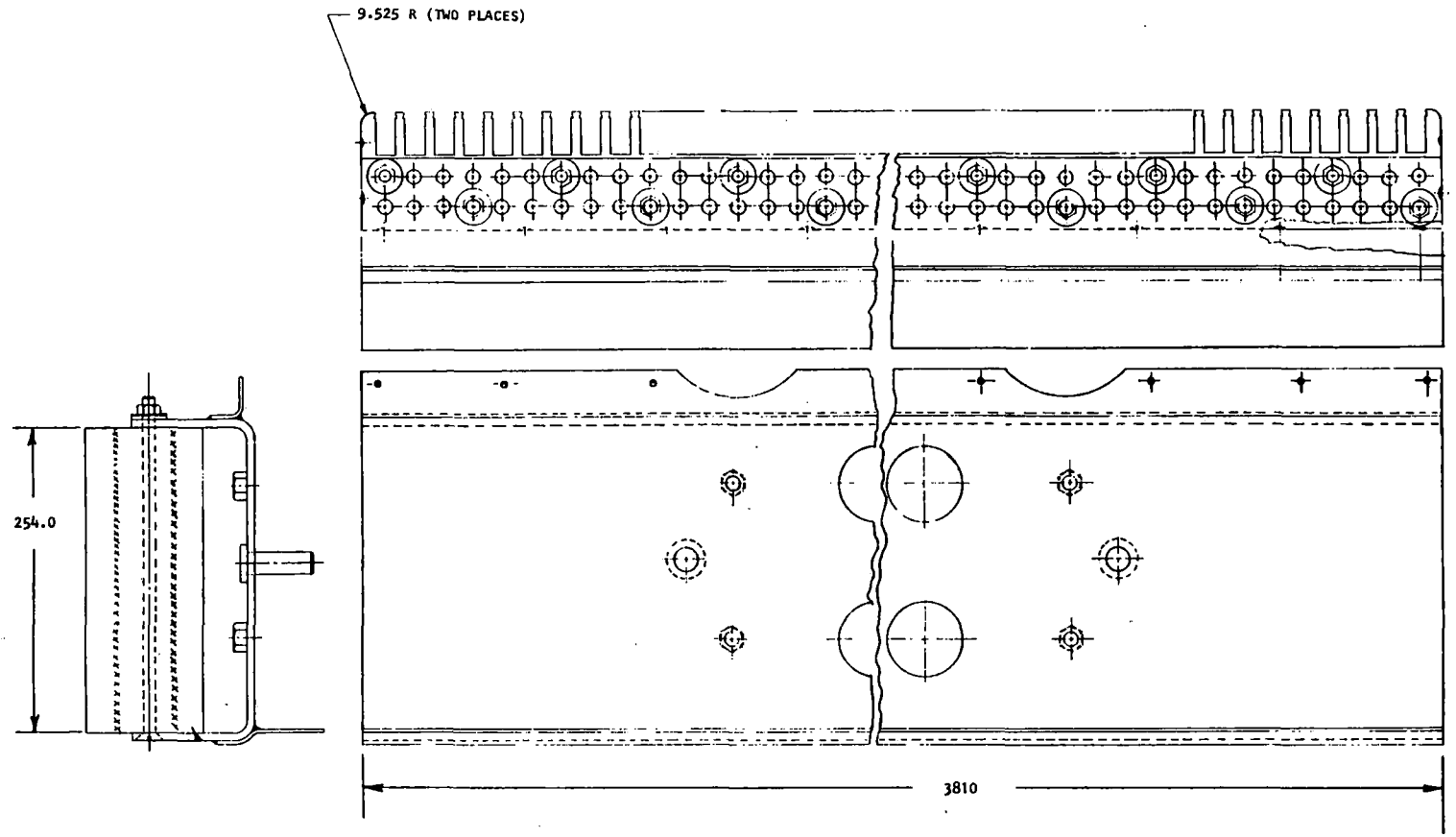

Figure A-2. LIM Primary Stack Assembly

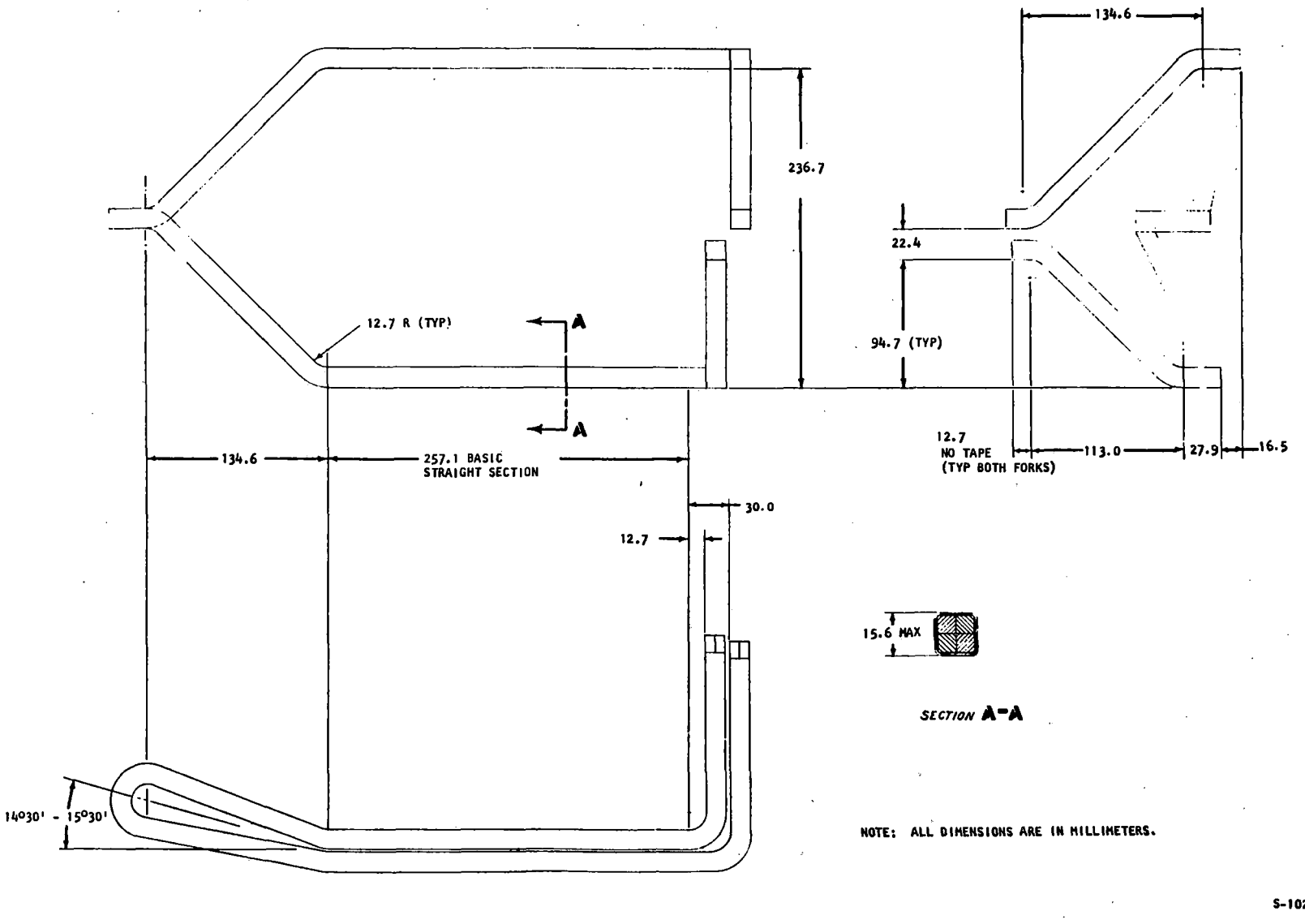

Figure A-3. LIM Primary Winding Coil Assembly

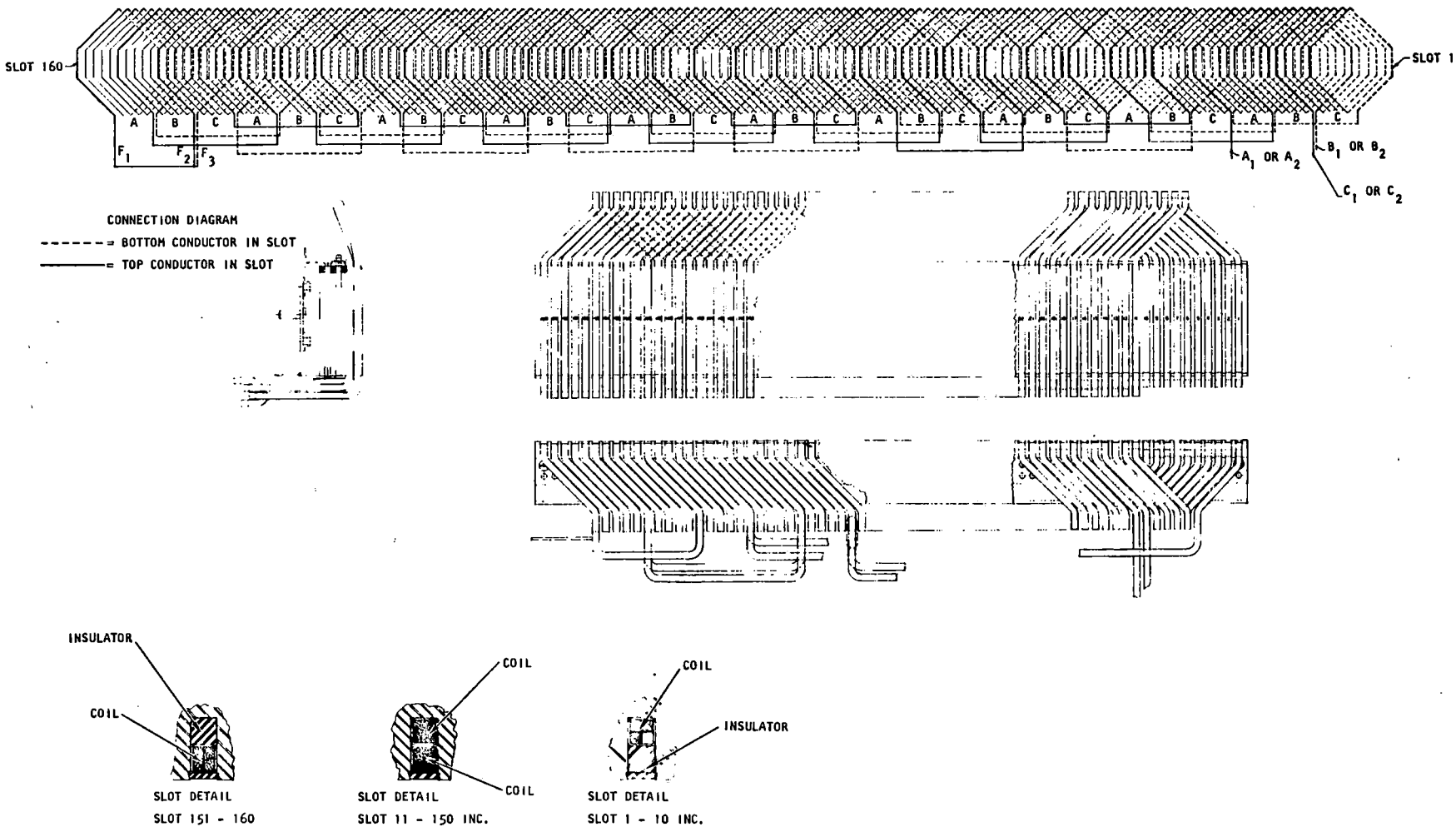

Figure A-4. LIM Primary Winding Connections

TABLE A-2

LIMRV LEADING PARTICULARS

Dimensions	
Length	16.6 m
Width	2.1 m
Weight (dry)	26,000 kg
Primary Power Source	Gas turbine driving 3-ph alternator through reduction gearbox
Gas Turbine	
Type	General Electric T64-10, twin-spool
Rating	2.23 MW at 13,600 rpm
Gearbox	
Ratio	81:31 stepdown
Torque limit	1.83 kN-m
Alternator	
Type	AiResearch 4-pole synchronous, 3-ph
Rating	1040 V, L-L, 173 Hz, 300 kVA at 5200 rpm
Linear Induction Motor	
Type	AiResearch 10-pole, double-sided
Rating	See Table A-1
Auxiliary Power Source	Gas turbine/alternators/compressor
Outputs	1. Compressed air for starting main turbine 2. 120/208 V, 3-ph, 400-Hz, 125 kVA 3. 120/240 V, 1-ph, 60-Hz, 12.5 kVA 4. 28 Vdc
Trucks (2 required)	
Type	Budd-Pioneer III
Axles per truck	Two
Gauge	Standard
Wheelbase	2.6 m
Wheel diameter	0.965 m
Spring rates	Adjustable (substitution)
Damping coefficients	Adjustable (air pressure)

TABLE A-2 (Continued)

Braking Systems	
Mechanical	Disk brakes, two per wheelset (8 total), electropneumatically operated
Dynamic	DLIM plus 2000-kW onboard resistor bank
Aerodynamic	Spoiler type, actuated with compressed air
Instrumentation	
Onboard	1. Transduce, signal condition, and: a. digitize and transmit via telemetry link at 256 kilobits/sec b. display on meters (real time) in vehicle cab 2. Control and monitor LIMRV operation from cab
Remote (Data Site)	Receive binary data via telemetry link and: a. record in gapped format on magnetic tape b. display via oscillographic means, or display on meters (real time)
Thrust Boosters (2 required)	
Type	Pratt & Whitney J52-P3 jet engine
Mounting	Rear, outboard

APPENDIX B

SLIM DESIGN HIGHLIGHTS

This appendix summarizes the major features of SLIM.

PRIMARY

Suspended from front truck.

Adjustable airgap (0 to 25 mm nominal mechanical gap with respect to baseline reaction rail (secondary).

Passive primary guidance system.

Five temperature-compensated load transducers for measurement of vertical force and pitching moment, including a center hanger support bracket instrumented to measure vertical and lateral forces.

Four additional lateral load transducers.

Motor primary held captive in the event of primary support failure.

Dynamic modeling confirms vehicle stability above maximum test speed of 67 m/sec.

Force measuring system calibrated by hydraulically operated fixture capable of applying thrust forces, vertical forces, and pitching moments, and measuring cross coupling components thereto (see Figure B-1).

Motor modified from double-sided to single-sided configuration.

Motor layout permits connection of different numbers of electrically active poles.

Lateral adjustment of motor primary not provided.

BASELINE REACTION RAIL

Figures B-2 and B-3 show dimensions and construction details of baseline reaction rail. Constructed of 6.3-m lengths of aluminum cover with current jumpers at each cover discontinuity to ensure current continuity.

Track designed for facile installation.

Reaction rail amenable to theoretical analysis.

Solid backiron, construction grade.

Eight thousand feet of reaction rai.

Stainless steel angle provides basis for securing aluminum cover and achieving minimum interference with electrical and magnetic requirements.

Specially instrumented reaction rail section for wayside measurement of flux and temperature, to be synchronized with onboard electrical data.

SOLID IRON REACTION RAIL

Track amenable to testing without aluminum cover.

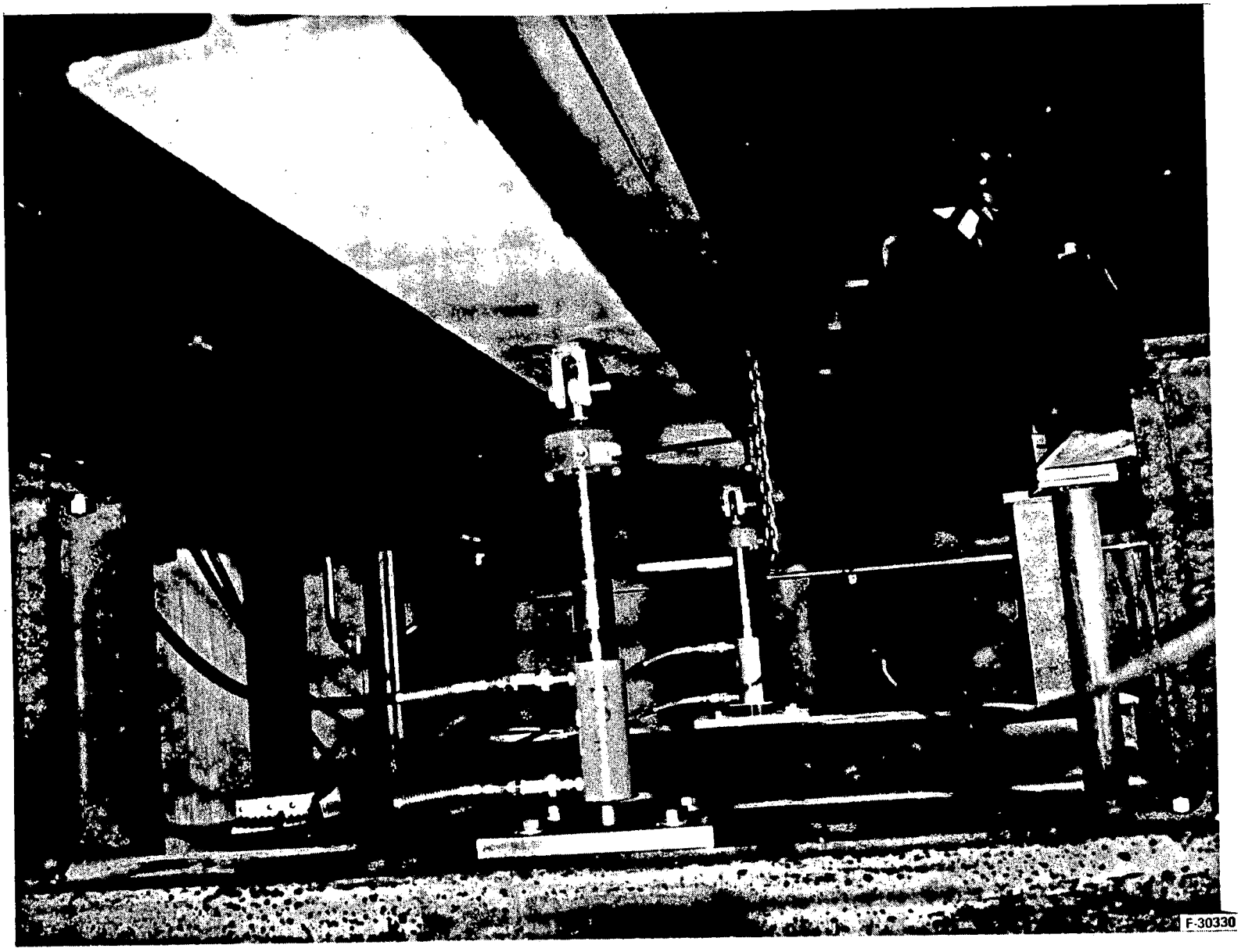

Figure B-1. Underside of SLIM Thrust Calibration Beam Showing Load Cells

(Photo courtesy of TTC, Pueblo, CO)

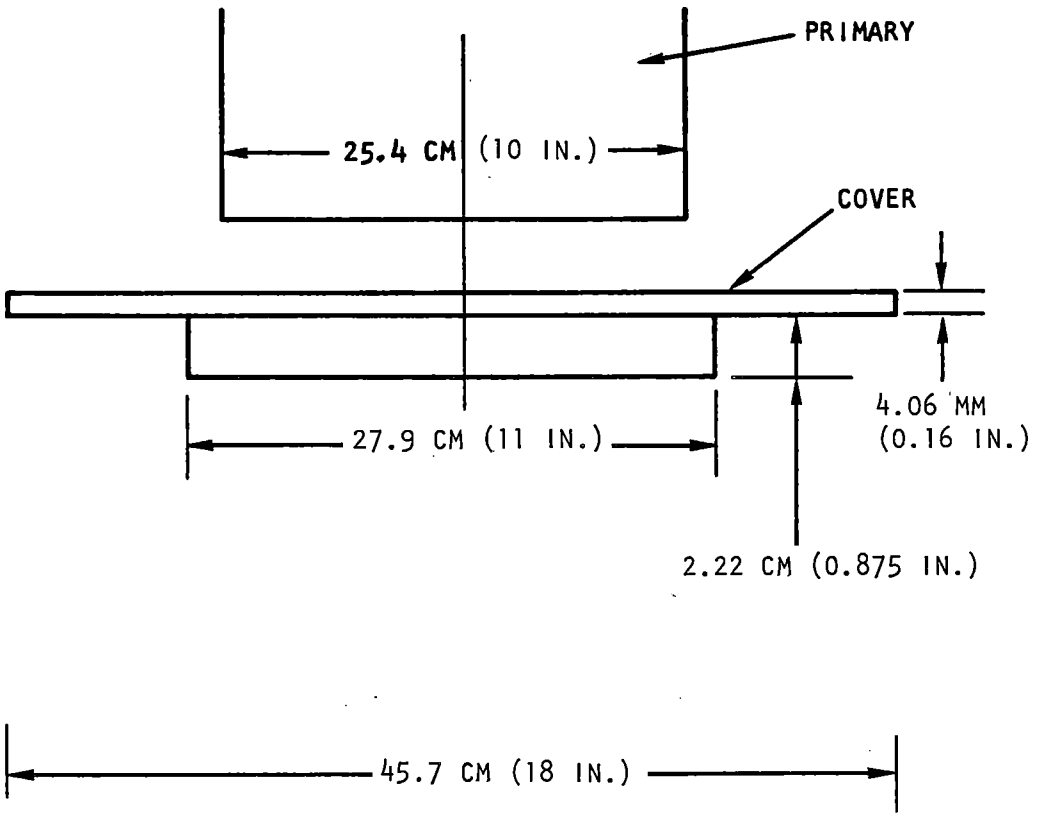

BASELINE REACTION RAIL LENGTH = 2438 M (8000 FT)
RAIL SECTION LENGTH = 6.1 M (20 FT)
COVER MATERIAL, 6061-T6 ALUMINUM ALLOY
BACKIRON MATERIAL, AISI 1010 STEEL

S-32325

Figure B-2. SLIM Cover and Backiron Dimensions

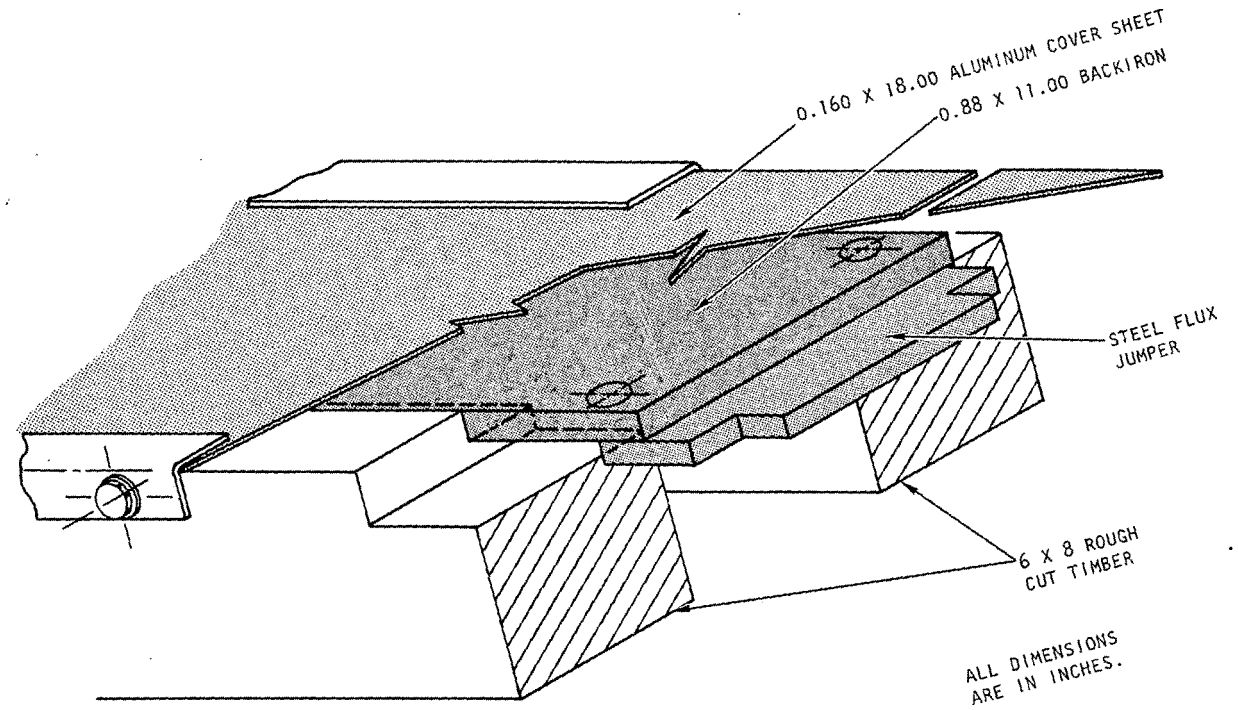

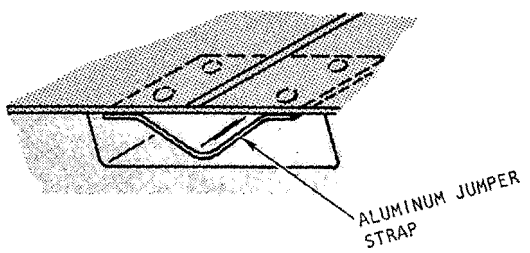

S-39297

Figure B-3. SLIM Reaction Rail

APPENDIX C

SLIM DATA ACQUISITION SYSTEM

1. INTRODUCTION

The SLIM data acquisition system was able to utilize much of the hardware and software used for previous LIMRV test programs. Some changes were necessitated by the differences between SLIM and DLIM suspension systems and airgap widths, and some upgrading of the system was accomplished.

2. DESCRIPTION OF DATA ACQUISITION SYSTEM

2.1 SUMMARY

The main function of the LIMRV data acquisition system is to record and analyze test data. In previous testing, it has also provided the vehicle operators with real-time data for remote vehicle operation.

Sensors onboard the LIMRV produce electrical signals in response to the status of a variety of electrical and mechanical parameters. These signals are conditioned, converted to a digital format, and transmitted over a radio link to a stationary control center, where the data is recorded and selected parameters are displayed for use by the remote operator.

The recorded data is combined with stored calibration data and re-recorded in a computer-compatible format. These recorded reels of tape are expressed to the AiResearch facility at Torrance, California, where various computations, plots, and printouts are produced. Data meeting certain predetermined criteria are automatically stored for later processing of "merged data" covering the entire test program.

Figure C-1 is a block diagram of the entire DAS.

2.2 LIMRV ONBOARD EQUIPMENT

2.2.1 General

Figure C-2 is a functional block diagram of the onboard data acquisition and remote control system.

Onboard sensors continuously measure a wide variety of electrical and mechanical parameters. These sensors and related parameters are described in Table C-1. Most sensor output is in analog format, although some parameters are output directly in digital format.

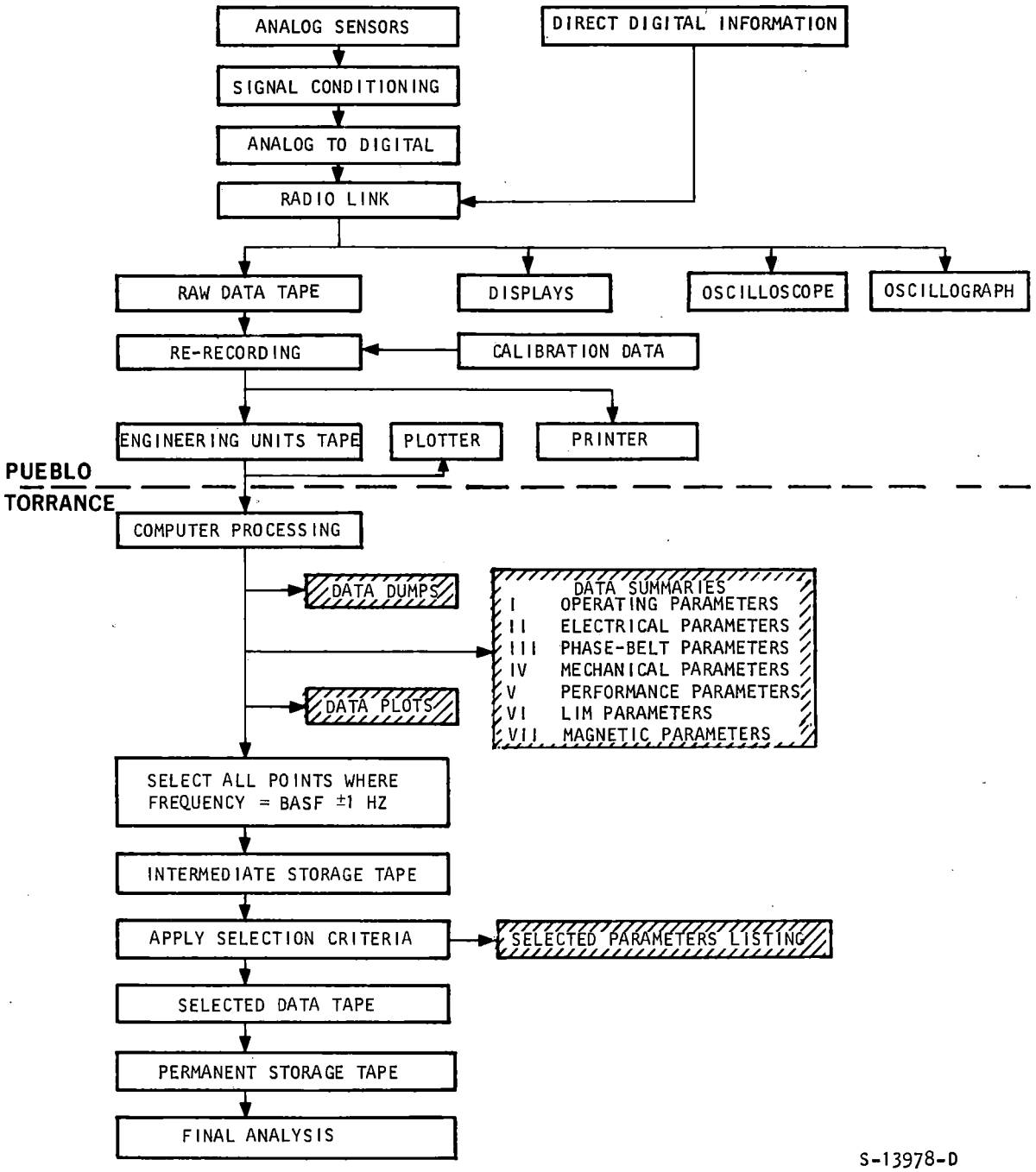

Figure C-1. Data Acquisition System Block Diagram

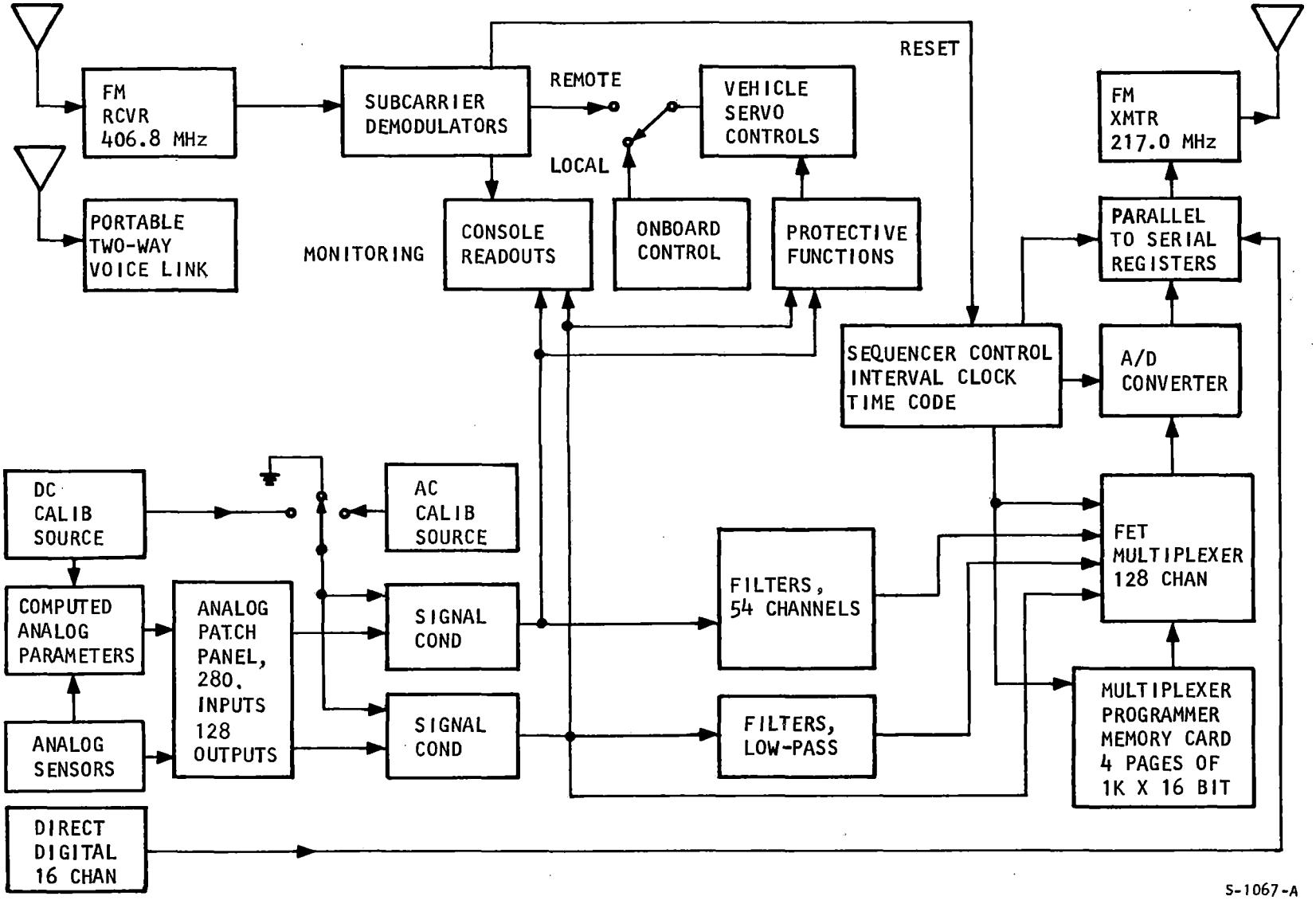

Figure C-2. Onboard Data Acquisition and Remote Control System Functional Block Diagram

TABLE C-I

ONBOARD SENSORS

Parameter		Sensor			
No.	Description	Type	Part No.	Mfr	Location
001	Bolster position, front, V, left	LVDT	SS609	Collins	Outboard end, front bolster
002	Bolster position, front, V, right	LVDT	SS609	Collins	Outboard end, front bolster
003	Bolster position, rear, V, left	LVDT	SS609	Collins	Outboard end, rear bolster
004	Bolster position, front, T, left	LVDT	SS609	Collins	Outboard end, front bolster
005	Bolster position, rear, T, left	LVDT	SS609	Collins	Outboard end, rear bolster
006	Truck accel, front, V	SA	4211A-10-A	Systron-Donner	Middle, front truck frame
007	Truck accel, front, T	SA	4211A-10-A	Systron-Donner	Middle, front truck frame
008	Truck accel, rear, T	SA	4211A-10-A	Systron-Donner	Middle, rear truck frame
009	Truck accel, rear, V	SA	303 B 16	Kistler	Middle, rear truck frame
010	Vehicle accel, T	SA	303 B 16	Kistler	Plate behind cab
011	Vehicle accel, V	SA	303 M 132.7	Kistler	Plate behind cab
012	Vehicle accel, L	SA	303 B 16	Kistler	Plate behind cab
013	Truck journal bearing 1 accel, L	SA	4211A-20-A	Systron-Donner	Right front journal bearing
014	Truck journal bearing 1 accel, V	SA	4211A-20-A	Systron-Donner	Right front journal bearing
015	Truck journal bearing 1 accel, T	SA	303 B 16	Kistler	Right front journal bearing
016	Truck axle 1 displacement, L, right	LVDT	SS 607	Collins	Journal bearing (measures elastomer deformation)
017	Truck axle 1 displacement, L, left	LVDT	SS 607	Collins	Journal bearing
018	LIM gap, front	PD	KD2300-12CU	Kaman	SLIM
019					
020					
021	LIM accel	SA	303 B 16	Kistler	SLIM, left side, middle (unfiltered)
022	Total transverse force	SG	None	AiResearch	SLIM
023	Analog frequency	Monopole	--	AiResearch	Alternator torque shaft
024	Vertical force	Load cell	631239	Celesco	SLIM, right front (unfiltered)
025	Vertical force	Load cell	631239	Celesco	SLIM, left front (unfiltered)
026	LIM thrust	Load cell	1210-AF	Interface	Rear of LIM
027	LIM accel	Same sensor as 021			
028	J52 throttle position, left	POT	--	PW	Part of engine

TABLE C-I (Continued)

Parameter		Sensor			
No.	Description	Type	Part No.	Mfr	Location
029	J52 throttle position, right	POT	--	PW	Part of engine
030	J52 speed, left	Tachometer	--	PW	Part of engine
031	J52 speed, right	Tachometer	--	PW	Part of engine
032	J52 temp, left, T5	TR	--	PW	Part of engine
033	J52 temp, right, T5	TR	--	PW	Part of engine
034	T64 temp, T5	TR	--	GE	Part of engine
035	T64 gas gen speed	Tachometer	--	GE	Part of engine
036	T64 throttle position	POT	--	AiResearch	On engine
037	T64 temp, T2	TR	--	GE	Part of engine
038	T64 torque	Monopole	--	GE	Part of gearbox
039	Brake pressure, front	SG	4-394-0001	CEC	Truck well
040	Brake pressure, rear	SG	4-394-0001	CEC	Truck well
041	Brake resistor bank temp	TC	MCA-150J	Hades	Resistor box
042	Fuel quantity	POT & float	--	AiResearch	Fuel tank
043	APU compt temp	RTD	5001-19	Thermal	APU compt
044	Alternator temp	RTD	5001-19	Thermal	Alternator
045	Alternator vibration	Piezoelec	6622MB	Endevco	Alternator
046	400-Hz voltage	Divider	--	AiResearch	PCI-2
047	Vertical force	Load cell	631239	Celesco	SLIM, center (unfiltered)
048	Analog slip freq				
049	LIM flux #1	Coil	None	AiResearch	A1P*
050	LIM flux #2	Coil	None	AiResearch	A2P*
051	LIM flux #3	Coil	None	AiResearch	A3P*
052	LIM flux #4	Coil	None	AiResearch	A4P*
053	LIM flux #5	Coil	None	AiResearch	A5P*
054	LIM flux #6	Coil	None	AiResearch	A6P*
055	LIM flux #7	Coil	None	AiResearch	A7P*
056	LIM flux #8	Coil	None	AiResearch	A8P*
057	LIM flux #9	Coil	None	AiResearch	A9P*
058	LIM flux #10	Coil	None	AiResearch	A10P*
059	LIM flux #11	Coil	None	AiResearch	A10PE*
060	Vertical force	Load cell	631239	Celesco	SLIM, right rear (unfiltered)

TABLE C-1 (Continued)

Parameter		Sensor			
No.	Description	Type	Part No.	Mfr	Location
061	Total A-ph current	CT	885AZ79G06	Westinghouse	Under T64
062	Total B-ph current	CT	885AZ79G06	Westinghouse	Under T64
063	Total C-ph current	CT	885AZ79G06	Westinghouse	Under T64
064	A-ph voltage	PT	EMP	Westinghouse	Right side of air conditioner
065	B-ph voltage	PT	EMP	Westinghouse	Right side of air conditioner
066	C-ph voltage	PT	EMP	Westinghouse	Right side of air conditioner
067	Phase-belt voltage 1	PT	EMP	Westinghouse	Right side of air conditioner
068	Phase-belt voltage 2	PT	EMP	Westinghouse	Right side of air conditioner
069	Phase-belt voltage 3	PT	EMP	Westinghouse	Right side of air conditioner
070	Phase-belt voltage 4	PT	EMP	Westinghouse	Right side of air conditioner
071	Phase-belt voltage 5	PT	EMP	Westinghouse	Right side of air conditioner
072	Phase-belt voltage 6	PT	EMP	Westinghouse	Right side of air conditioner
073	Phase-belt voltage 7	PT	EMP	Westinghouse	Right side of air conditioner
074	Phase-belt voltage 8	PT	EMP	Westinghouse	Right side of air conditioner
075	Phase-belt voltage 9	PT	EMP	Westinghouse	Right side of air conditioner
076	Phase-belt voltage 10	PT	EMP	Westinghouse	Right side of air conditioner
077					
078					
079	RMS total A-ph current	CT	885AZ79G06	Westinghouse	Under T64
080	RMS total B-ph current	CT	885AZ79G06	Westinghouse	Under T64
081	RMS total C-ph current	CT	885AZ79G06	Westinghouse	Under T64
082	Thrust (unfiltered)	Same sensor as 026			
083	Total vertical force	Sum of sensors (corrected for SLIM weight and filtered)			
084	Front vertical forces	024 + 025 (filtered)			
085	RMS A-ph voltage	Uses transducer for 064			
086	RMS B-ph voltage	Uses transducer for 065			
087	RMS C-ph voltage	Uses transducer for 066			
088	RMS phase-belt voltage 1	Uses transducer for 067			
089	RMS phase-belt voltage 2	Uses transducer for 068			
090	RMS phase-belt voltage 3	Uses transducer for 069			
091	RMS phase-belt voltage 4	Uses transducer for 070			
092	RMS phase-belt voltage 5	Uses transducer for 071			
093	RMS phase-belt voltage 6	Uses transducer for 072			
094	RMS phase-belt voltage 7	Uses transducer for 073			
095	RMS phase-belt voltage 8	Uses transducer for 074			
096	RMS phase-belt voltage 9	Uses transducer for 075			

TABLE C-1 (Continued)

Parameter		Sensor			
No.	Description	Type	Part No.	Mfr	Location
097	RMS phase-belt voltage 10	Uses transducer for 076			
098					
099					
100	Total A-ph avg power	Calculated onboard from voltage and current transducers			
101	Total B-ph avg power	Calculated onboard from voltage and current transducers			
102	Total C-ph avg power	Calculated onboard from voltage and current transducers			
103	Avg phase-belt power 1	Calculated onboard from voltage and current transducers			
104	Avg phase-belt power 2	Calculated onboard from voltage and current transducers			
105	Avg phase-belt power 3	Calculated onboard from voltage and current transducers			
106	Avg phase-belt power 4	Calculated onboard from voltage and current transducers			
107	Avg phase-belt power 5	Calculated onboard from voltage and current transducers			
108	Avg phase-belt power 6	Calculated onboard from voltage and current transducers			
109	Avg phase-belt power 7	Calculated onboard from voltage and current transducers			
110	Avg phase-belt power 8	Calculated onboard from voltage and current transducers			
111	Avg phase-belt power 9	Calculated onboard from voltage and current transducers			
112	Avg phase-belt power 10	Calculated onboard from voltage and current transducers			
113					
114					
115	Field current	Hall effect	--	AiResearch	Field PDR
116	Alpha command	Cont signal	--	AiResearch	PCI-2
117	Field PDR voltage	Divider	--	AiResearch	PCI-2
118	Voltage/freq ratio	Calculated onboard from B-C voltage			
119	Vertical force, center	Same as 047 (filtered)			
120	Dynamic brake current	CT	885AZ79G06	Westinghouse	Brake contactor
121	LIM temp 1	RTD	5001-19		AT3*
122	LIM temp 2	RTD	5001-19		AT6*
123	Vertical force	Load cell	631239	Celesco	SLIM, left rear (unfiltered)
124					
125					
126					

TABLE C-I (Continued)

Parameter		Sensor			
No.	Description	Type	Part No.	Mfr	Location
127	Avg axle speed	Avg of four tachometers			
128	Vertical forces, rear	060 + 123 (filtered)			
129	Speed MSH	See para 2.5.1			
130	Speed LSH	See para 2.5.1			
131	Station MSH	See para 2.5.17			
132	Station LSH	See para 2.5.17			
133	Station subdivision	See para 2.5.17			
134	Frequency MSH	See para 2.5.2			
135	Frequency LSH	See para 2.5.2			
136	Slip MSH	See para 2.5.3			
137	Slip LSH	See para 2.5.3			
138-1	Full service brakes	Command signal			
138-2	Turbine fault	Command signal			
138-3	Aero brakes	Command signal			
138-4	Drag chute	Command signal			
138-5					
138-6	Speed multiplier	See para 2.5.1			
138-7					
138-8					

LEGEND

CT	current transformer
L	longitudinal
LSH	least significant half
LVDT	linear variable differential transformer
MSH	most significant half
PCI-2	power control and instrumentation module
PD	proximity detector
POT	potentiometer
PT	potential transformer
RTD	resistance temperature detector
SA	servoaccelerometer
SG	strain gage
T	transverse
TC	thermocouple
TR	thermocouple ring
V	vertical
*	see Drawing 44308

Analog signals are routed from the sensor to a patchboard capable of accepting 280 three-wire inputs with 128 three-wire outputs. Different types of signal conditioning paths consisting of amplifier, filter, and preliminary computation combinations are selected to fit the desired response of the parameters. The input signals to the signal conditioning amplifiers are connected through field-effect transistor (FET) switches. Active filters with unity gain are provided on 54 channels.

A 128-channel multiplexer sequentially switches the input channels one at a time to the analog-to-digital (A/D) converter. The multiplexer consists of 128 FET switches with overvoltage protection in the form of zener diodes. Gating of the switches is sequenced with an 8-line address from logic controlled by a 4096-word, 16-bit core memory. The individual channels can be gated at one or more of the 1024 time slots that make up a complete data frame. Clock timing pulses to the memory card are generated within the sequencer control module.

Each time-sequential analog sample from the multiplexer is fed to an A/D converter. Two 8-bit converters (successive approximation types) are used in flip-flop parallel to digitize the signals to parallel binary. These are transferred to shift registers where the data is converted from parallel to serial form and fed to the FM transmitter. Direct digital channels, including sync words, time words, vehicle speed, frequency, slip, and vehicle position station numbers are transferred directly to the shift registers in parallel and then shifted to serial at the appropriate times into the data stream. The time

required for a complete 1024-word (8 bits per word) data frame is 0.032 sec. Thus, 32,000 8-bit data words are produced each second.

Digital clock frequencies and all timing signals and time words are obtained from a 1.024-MHz crystal oscillator and necessary countdown logic. Multiplexer operation in this synchronous manner ensures an accurate time relationship between the time words and each data slot in the frame format. The timing module provides sequencing clock signals to the multiplexer programmer, multiplexer, A/D converters, and shift registers, as well as intervalometer time words for each data frame. Three 8-bit binary words totalize the time in milliseconds from reset zero, resulting in a full-scale capability of about 4.66 hours.

Data is transmitted via PCM/FM on a frequency of 217.0 MHz with a power of 20 W.

The onboard console contains many displays and meters with pushbutton selector switches, enabling the operators to check out all systems before a test run. Safety and protective functions are onboard and automatic. Loss of the RF remote link results in an automatic, safe shutdown and braking of the vehicle to a stop.

2.2.2 SLIM Support and Force Measuring System

A completely new positioning and force measuring system was required by the conversion from DLIM to SLIM configuration. Figure C-3 shows the front half of the motor support system, comprising four pin-jointed, vertical support links LV1, LV2, LV4, and LV5, located at the front and rear ends of the motor, to measure vertical force. Lateral pin-jointed support links LT1, LT2, LT4, and LT5 are instrumented to measure SLIM lateral force.

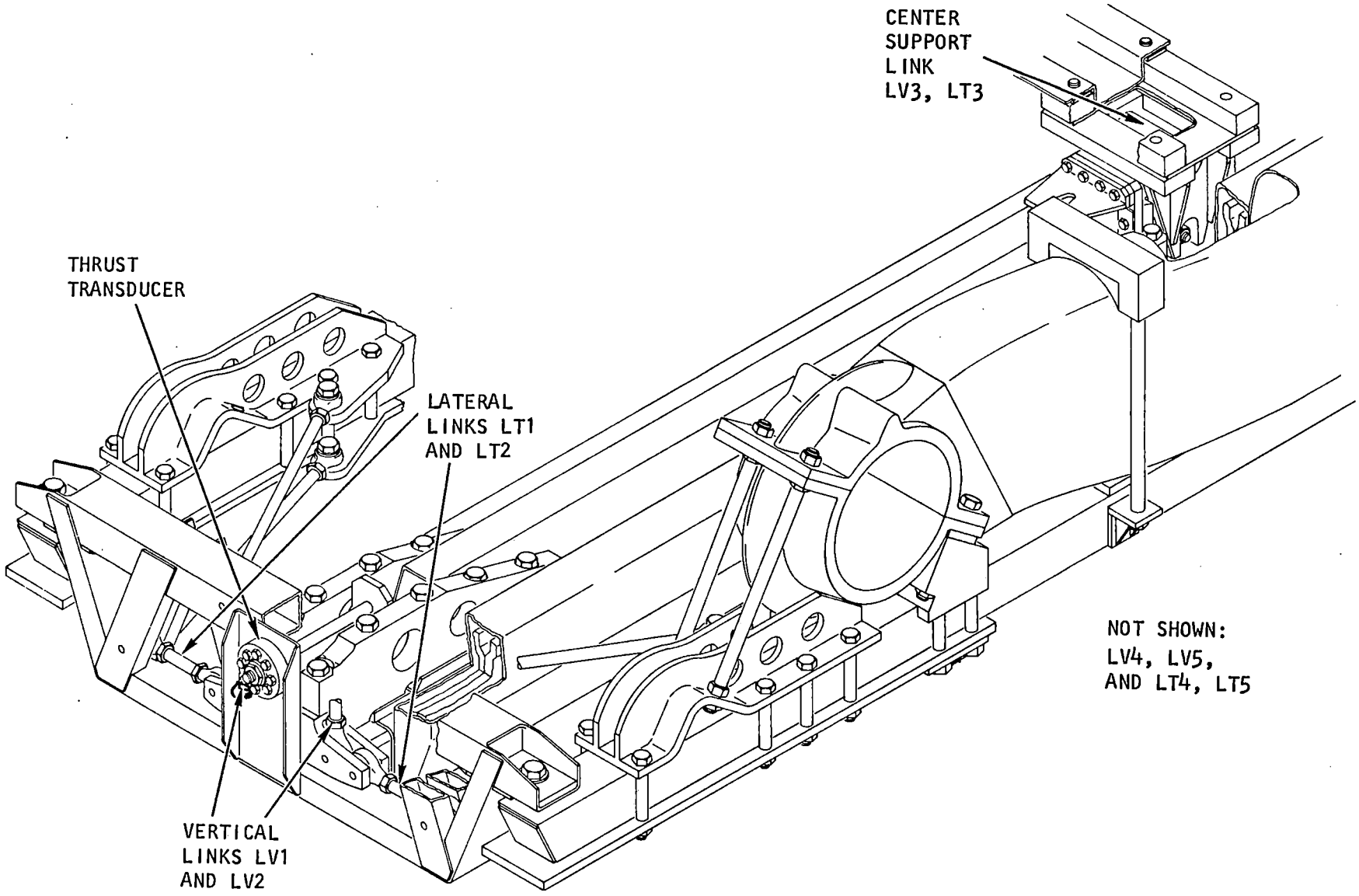

Figure C-3. Motor Support System, SLIM Configuration

The midpoint of the span between the four vertical load links is supported by a hanger that is instrumented in lateral (LT3) and vertical (LV3) forces. Load cells are installed at each of the five vertical and lateral restraint points to measure the local forces. An additional load cell at the front of the SLIM primary measures thrust.

Outputs of the 11 transducers identified above are conditioned onboard as shown in Figure C-4. The five lateral force signals are added and the filtered sum is incorporated in the data stream. The five vertical force signals are combined to yield the filtered sum of the two front cells (LV1 + LV2), the filtered center cell output (LV3), the filtered sum of the two rear cells (LV4 + LV5), and the filtered sum of all five cells (FV, FEV). The thrust signal is available with two levels of filtering options. The combined sum of all vertical force transducers is also available after computer summation at Torrance.

2.3 FIXED STATION EQUIPMENT

Figure C-5 is a functional block diagram of the fixed station (data van) data acquisition and remote control system.

Incoming data from the vehicle is received as PCM/FM in NRZS coding and is processed by a PCM decommutator that converts it from serial- to parallel-bit configuration. At the interface controller/channel selector, preselected time slots in the data stream are routed to the real-time monitoring circuits, but all the data continues on to the buffer controller and onsite minicomputer. D/A converters and direct digital registers feed the appropriate signals to meters, digital readouts, CRT displays, and a 36-channel light beam oscillograph.

A control console in the data van is similar in layout and operation to the onboard control arrangement. The console provides real-time monitoring of the vehicle control parameters, and 12 channels of analog commands for vehicle

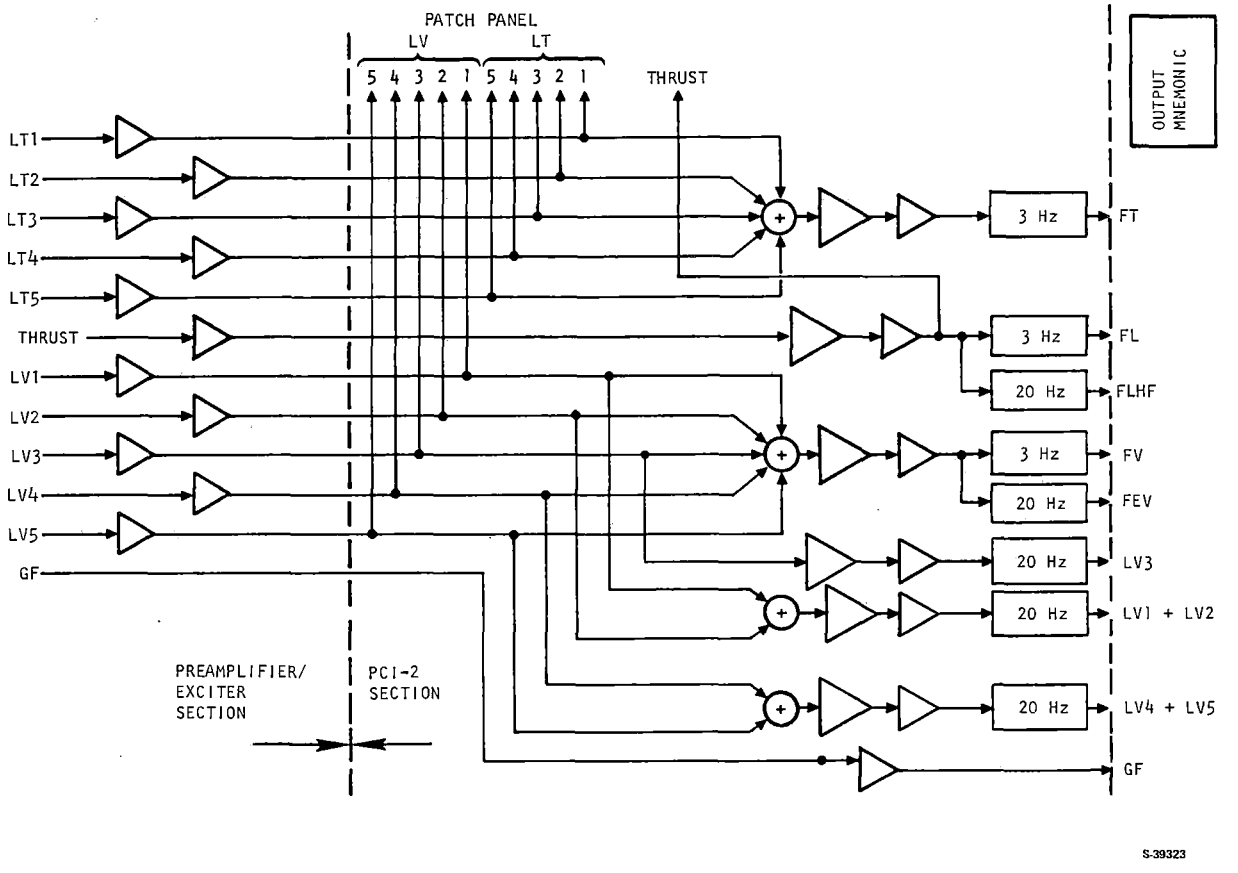

Figure C-4. SLIM Force Signal Conditioning System

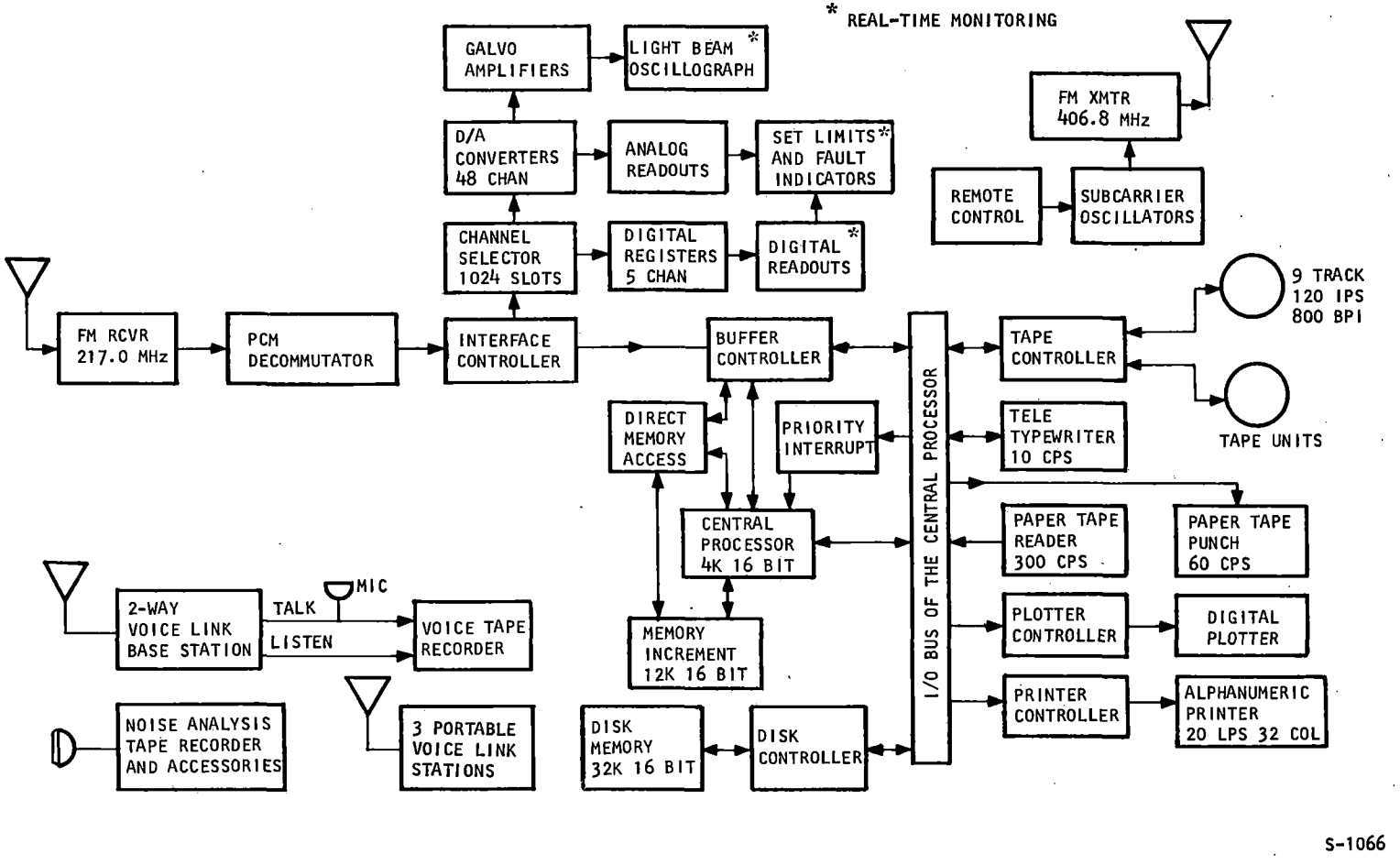

Figure C-5. Ground Station Data Acquisition and Remote Control System Functional Block Diagram

remote control via a 406.8-MHz FM/FM radio link with a power of 10 W.

A small computer (Varian Data Machines 620/I) in the data van, complete with peripheral hardware, is used online to format and store the incoming data in a computer-compatible configuration with interrecord gaps. The data stream enters the computer through a buffer controller and direct memory access and is assembled in core memory. Data storage in the core is divided into two parts, each with a capacity of 2048 16-bit words. When one core section is filled, the incoming data stream is transferred to the other storage area. The data in the first storage area is unloaded to magnetic tape and the cycle repeats. Interrecord gaps are thus generated between each record of 4096 8-bit words as they are recorded on tape, with no loss of incoming data.

Included with the central processor are 16k of core memory, a direct memory access feature, an 8-level priority interrupt option, and hardware multiply-and-divide equipment. The following peripheral devices of an input/output (I/O) nature are associated with the computer central processor by an I/O bus:

- Two tape transports and an associated controller are used for data recording, playback, and rerecording of converted data into modified BCD format. The tape transports are single-capstan driven. The controller operates such that when the tape on the first transport has been filled, the second transport starts automatically at the beginning of the next record, and the first tape is automatically rewound. A new tape is installed on the first transport for the automatic transfer back when the tape on the second transport is full. This process permits data to be recorded continuously during a lengthy test. Data is recorded in 9-track format with a character density of 800/in. and a tape transport speed of 120 ips.

- A 32k, 16-bit disk memory unit interfaces with the computer by means of a disk controller. The disk unit and controller are arranged to transfer data between the disk and computer memory in blocks of 128 16-bit words. The disk memory is used for storage of calibration data.
- A paper tape system consisting of a 300-character/sec optical reader, a 60-character/sec output punch, and a tape spooler is provided. Standard 8-in. reels on quick-release hubs are used. This system provides high-speed I/O access with the processor.
- A standard teletypewriter is used by the operator for initialization and real-time inputs to the processor.
- A 32-column, 40-character, alphanumeric printer operates at a maximum printing rate of 20 lines/sec. Through program control, the processor has the ability to update any column pair, write all spaces, or sense printer status. A digital plotter is installed to provide an onsite graphical data presentation. It has a plotting width of 12-7/8 in., a step size of 0.005 in., and a plot speed of 300 steps/sec. Resolution is 1 step.

2.3.1 Onsite Computer Software

Various programs have been written for the Varian 620/i computer and associated peripheral hardware. The main ones are listed below.

The data acquisition program accepts the incoming PCM data and records it in raw unprocessed form on magnetic tapes in binary format. Meaningful header records are recorded on the tape to separate the individual test runs. Prior to a test run, the program can be executed in the closed (or calibrate) mode to record sensor calibration data on the tape. During the test run, the program

is executed in the open (or run) mode to acquire actual data. The program automatically transfers appropriate information on header and update number to each tape being used during a long, continuous run.

A disk table generation program is used to generate the conversion tables necessary to translate the binary inputs to engineering units tapes in modified BCD format. A curve-fitting subroutine (for calibration tables) converts transducer curves into discrete readout points. This subroutine eliminates tedious manual calculations and possible errors each time a transducer is replaced or its characteristics are altered. The computer operator types in calibration points on the teletypewriter, i.e., raw data readings vs engineering units values. The program curve-fits these points, creates a calibration table of 256 discrete points, and punches this table out on paper tape. Up to 128 calibration tables, each consisting of 256 points in 4-character, 4-bit BCD can be stored in the 32k, 16-bit disk memory at any one time.

A calibration conversion processing program is used to process the raw binary PCM data tapes and produce calibrated output BCD magnetic tapes in engineering units. The program inputs define the data channel setup, the limit values, and the calibration values for that conversion. The output magnetic tape header contains information on the test run, as detailed in Section 4. During the conversion run, the printer can be used to read blocks of the BCD data being recorded on the EU tapes. The printer can be triggered through the teletype, or by setting desired upper and/or lower limit values on selected channels. Specific time words can also be used to turn the printer on and off.

A conversion table generation program provides editing capability for the operator in the form of table listings using the digital printer.

2.4 TORRANCE FACILITY COMPUTER EQUIPMENT

In Torrance the EU tape is processed with a general purpose laboratory computer, the Digital Scientific META4/1800. This computer system consists of a central processor with 64k of core memory, four magnetic tape drives, a 600 line/minute printer, a card reader, a digital plotter, and disk storage of 30 million bytes. Offline plotting is also available.

The computer operates under a real-time multiprogramming operating system, which allows real-time data acquisition tasks to execute concurrently with data reduction and program preparation tasks.

Data reduction programs are written primarily in the FORTRAN programming language. Bit and character manipulation subroutines are written in assembly language. A modular approach is followed in the design of the data reduction software. Each program module in the data reduction process will execute independently of other program modules.

2.5 COMPUTATIONS

As previously noted, the data output to the computer at Torrance is, for the most part, the output of onboard sensors, conditioned, filtered, and with calibration information incorporated. Some onboard computation is accomplished: phase and phase-belt powers, rms phase currents, vertical force summing, and voltage/frequency ratio. Table C-2 lists applicable constants and conversions. All other computations necessary for performance analysis are made by the computer. These computations are detailed in the paragraphs following. Note that the parameter numbers (e.g., P130) provide a reference to Table C-1, while the mnemonics will be used extensively in subsequent discussions.

TABLE C-2

CONSTANTS AND CONVERSIONS

Constant	Mnemonic	Value	Unit
Wheel circumference	CIRC	9.9762	ft
LIM weight	LIMW	2902	lb
Vertical force lever arm	VFLA	157.5	in.
Base current	BASI	1.4	kA
Base frequency	BASF	94.3	Hz

Conversion		
Multiply	by	to get:
inches	0.0254	meters
feet	0.3048	meters
meters per second	2.2369	miles per hour
miles per hour	1.46667	feet per second
pounds	0.4536	kilograms
pounds force	4.44822	newtons
kilonewtons	224.8	pounds force

2.5.1 Vehicle Speed, UVEL and VEL

Each revolution of one of the truck wheels generates 60 pulses. Every 60th pulse gates the count of an onboard 32-kHz signal. The count is binary and is transmitted as two 8-bit digital words, the most significant half and the least significant half of the count. An option for low-speed runs is available, whereby every 30th pulse gates the count, in which case the speed, as computed below, must be divided by 30.

VEL = UVEL = 32000 (wheel circumference)/count

VEL = UVEL = CIRC*.3048*32000./(256.*P129 + P130)

where UVEL = unfiltered vehicle speed, m/s

VEL = filtered vehicle speed (per para 2.5.19), m/s

CIRC = wheel circumference, ft

P130 = least significant half of count (multiple of 1)

P129 = most significant half of count (multiple of 256)

2.5.2 Generated Frequency, UFRE and FREQ

A pickup counts the number of pulses generated by a 66-tooth gear on the input shaft of the 81/31 speed decreasing gearbox to the alternator. Since the alternator produces 2 cycles per revolution, $\frac{66 \times 81}{2 \times 31}$ pulses per cycle are produced. If the number of pulses produced during 0.116 sec (obtainable from the DAS clock) is counted, it will be found that this number is equal to 10 times the generated frequency. This number is encoded into two 8-bit BCD words such that:

FREQ = UFRE = 10.*P134+.1*P135.

where UFRE = unfiltered frequency, Hz

FREQ = filtered frequency (per para 2.5.19), Hz

P134 = most significant half of count

P135 = least significant half of count

2.5.3 Slip, USLP and SLIP

Slip is determined by measuring the number of electrical cycles generated during the travel of a known distance. The known distance is the circumference of one truck wheel. The same gating pulse used in measuring vehicle speed (once per revolution) also gates a count of the number of cycles generated during this wheel revolution. The generated cycle is subdivided by means of a toothed gear on the high-speed (turbine) side of the main reduction gear. The count of pulses from the toothed gear is gated every revolution of the truck wheel.

Alternator = 4 poles = 2 cycles per generator revolution

Gearbox reduction ratio = 81/31

Teeth on turbine shaft = 66

LIM pole pitch = 14 in.

Wheel circumference = CIRC ft

Generated cycles per turbine revolution = 2*31/81

Cycles per tooth = cycles per count = 2*31/81/66

Cycles per gating period = 2*31/81/66 (count)

Synchronous inches per gating period (2*14)*2*31/81/66*(count) = Ds

Actual inches per gating period = 12*CIRC = Da

USLP = SLIP = (fe - fm)/fe = (Ds - Da)/Ds = 1-(Da/Ds)

= 1-CIRC*12*81*66/(2*14*2*31*count) = 1.-36.954*CIRC/count

USLP = SLIP = 1.-36.954*CIRC/(100.*P136+P137)

where USLP = unfiltered slip

SLIP = filtered slip (per para 2.5.19)

CIRC = wheel circumference, ft

P136 = most significant half of count (multiple of 100)

P137 = least significant half of count (multiple of 1)

2.5.4 Vertical Forces, FEV and DELV

The total vertical force produced by electrical (magnetic) attraction or repulsion, FEV, may be computed in kN as follows. A positive value represents an upward force.

FEV = P084+P128+P119+LIMW*.00444822

The differential of the vertical forces, which produces a pitching moment about the motor center, is designated DELV. A positive differential is defined as one tending to raise the front end. DELV is in kN. It is dependent upon the pole configuration of the motor:

For 10 poles, DELV = P084-P128.

For 5 poles leading, DELV = P084-P119-3.*P128-LIMW*.00444822.

For 5 poles trailing, DELV = 3.*P084+P119-P128+LIMW*.00444822.

2.5.5 Slip Frequency, DF

By definition, DF = FREQ*SLIP, Hz.

2.5.6 Corrected Thrust, CTHR; and Pitch Moment, MP

The measured thrust must be corrected for the effects of acceleration and DRAG to obtain the true developed force:

CTHR = FL + LIMW*ACCL + DRAG = P026+LIMW*P027*4.44822 E-3 + DRAG

where CTHR = corrected force, kN

LIMW = SLIM weight, lb

DRAG = aerodynamic and mechanical friction (see para 2.5.18)

The pitch moment is obtained by multiplying the vertical force differential by the lever arm (MP is in kNm when DELV is in kN):

For 10 poles, MP = DELV*VFLA*.0127.

For 5 poles, MP = DELV*VFLA*.00635.

2.5.7 Total Power, TAP

Total power, in kW, is equal to the sum of the phase powers:

TAP = P100+P101+P102

2.5.8 Average Current, AI

Average current, in kA, is equal to one-third the sum of the RMS phase currents:

AI = (P079+P080+P081)/3

2.5.9 Average Voltage, AV

Average voltage, in V, is equal to one-third the sum of the RMS phase voltages:

AV = (P085+P086+P087)/3

2.5.10 Power Factor

With power in kW and current in kA, power factor in percent is given by:

Phase-belt pf (typical): PF1A = 100.*P103/P088/POWL (See para 2.5.16 for definition of POWL.)

Average pf: APF = 100.*TAP/(3.*AI*AV)

A-phase pf: APFA = 100.*P100/(P079*P085)

B-phase pf: APFB = 100.*P101/(P080*P086)

C-phase pf: APFC = 100*P102/(P081*P087)

2.5.11 Efficiency, EFF

With force in kN and input power in kW, efficiency in percent is given by:

EFF = 100.*CTHR*VEL/TAP

NOTE: If CTHR 0, EFF = 0.

2.5.12 Current Ratio, RATI; and Frequency Ratio, RATF

RATI = AI/BASI

RATF = FREQ/BASF

2.5.13 Normalization

Computed Parameter (Normalized)	Mnemonic	Unit	Computation
Voltage	VN*	VRMS	VN = AV/(RATI*RATF)
Developed thrust	THRN	kN	THRN = CTHR/RATI**2
Vertical force	FVSN	kN	FVSN = FVS/RATI**2
Transverse force	FTN	kN	FTN = FT/RATI**2
Pitching moment	MPN	kNm	MPN = MP/RATI**2
Total power	PN	kW	PN = TAP/RATF/RATI**2
Vertical force	FEVN	kN	FEVN = FEV/RATI**2
A-ph current	IAN	kARMS	IAN = P079/RATI
B-ph current	IBN	kARMS	IBN = P080/RATI
C-ph current	ICN	kARMS	ICN = P081/RATI
A-ph voltage	VAN	VRMS	VAN = P085/RATI/RATF
B-ph voltage	VBN	VRMS	VBN = P086/RATI/RATF
C-ph voltage	VCN	VRMS	VCN = P087/RATI/RATF
Phase-belt voltage (typical)	AV1AN	VRMS	AV1AN = P088/RATI/RATF
A-ph power	PAN	kW	PAN = P100/RATF/RATI**2
B-ph power	PBN	kW	PBN = P101/RATF/RATI**2
C-ph power	PCN	kW	PCN = P102/RATF/RATI**2
Phase-belt power (typical)	P1AN	PU	P1AN = P103/RATF/RATI **2*100./PAN
Flux (typical)	F1V	Wb	F1V = F1*.346*POLE *FREQ/AV
Phase-belt kVAR (typical)	KR1AN	PU	KR1AN = (SQRT(((IAN*AV1AN) **2-(.01*P1AN*PAN) **2)/((IAN*VAN) **2-PAN**2))
Voltage-normalized current	IV	ARMS	IV = AI*.346*POLE *FREQ/AV

*Terminal character N indicates "normalized."

2.5.14 Normalized Velocity, VELN; and Normalized Efficiency, EFFN

Since VEL = fm*2.*(pole pitch) and fm = FREQ - DF, fm (normalized) = BASF - DF. So, VELN = 2.*14.*.0254*(BASF-DF) = .7112*(BASF-DF), in m/s.

Since EFF = 100.*CTHR*VEL/TAP, EFFN = 100.*THRN*VELN/PN

NOTE: If THRN <0, EFFN = 0.

2.5.15 Average Vehicle Speed, AVEL

AVEL shall be computed by averaging the value of VEL for all data points over a time interval equal to the printout interval, with the first data point after the time word located at the center of the data points to be averaged.

2.5.16 Miscellaneous

Computed Parameter	Mnemonic	Unit	Computation
Phase-belt current	POWL	kARMS	If H155 = 10000, POWL = P079 If H155 = 20000, POWL = P080 If H155 = 30000, POWL = P081
Average value of parameter in each selected data point group	AVG	-	AVG = (Σ parameter values)/20
Standard deviation in each selected data point group	SIG	-	SIG = SORT ((Σ(parameter value-AVG)**2)/19.)
Phase-belt power angle (typical)	AN1A	DEG	AN1A = ACOS (PF1A/100.)
Voltage-corrected thrust	THRV	kN	THRV = THRN*(POLE*.346*BASF/VN)**2
Excitation	V/HZ	V/Hz	V/HZ = AV/FREQ
Number of active poles	POLE	-	If H154 = 10, POLE = 10 If H154 = 05 or 55, POLE = 5

2.5.17 Track Position, POS; and Distance from Start, DIS

Every 500 feet along the track, aluminum plates are fastened to 12 consecutive ties in a manner that provides a BCD code for the track station number.

The position between station markers is determined by a wheel revolution counter that delivers 60 pulses per revolution. This count is reset at every station marker. Every 12th pulse thereafter is recorded. Since the wheel is very close to 10 feet in diameter, 2-foot intervals are recorded, with the first interval having an accuracy of -0, +2 in. The most significant half of the station marker is P131. The least significant half is P132. The revolution counter is P133. Thus:

POS = 100.*P131 + P132 + .02*P133 (station number)

DIS = (present POS - initial POS) *100.*.3048 (meters)

2.5.18 Drag, DRAG

In the case of SLIM, drag as measured during coasting is so low that it is obscured by resolution errors. Hence, DRAG = 0.

2.5.19 Filtered VEL, FREQ, and SLIP

The computed digital parameters VEL, FREQ, and SLIP, and parameters computed from them are subjected to a digital filtering process in the META4/1800 computer to ensure that they exhibit the same response characteristics as the electrical parameters. The digital filtering provides attenuation equivalent to two simple first-order filters, one with a break frequency of 1.5 Hz, and the other with a break frequency of 4.0 Hz.

2.5.20 Airgap, GF

Originally, proximity sensors were installed at both the front and rear of the SLIM to provide information on longitudinal variations of the airgap. Difficulty was experienced with the rear unit because of the high flux at that location. When high-speed motion pictures demonstrated the stiffness of the motor mounts, it was decided to use only the front airgap sensor.

2.6 COMPUTER OUTPUT

2.6.1 General

The DAS develops a large quantity of test data for each test condition. The quantity of test data available is a function of vehicle speed and operator skill. At low speeds, considerable time is available to establish test conditions and acquire data. Less time is available at high speeds due to limited track length. At low slips, thrust is most sensitive to vehicle speed. Because of this LIM characteristic, specified test conditions at low slip and higher thrust are more difficult to attain. Grade changes, headwind variations, and powerplant lags introduce additional difficulties in establishing a given test condition. Consequently, LIM performance data must be obtained at various excitation and slip frequencies under test conditions of varying degrees of stability.

The computer is therefore programmed to cull from the raw data the most representative and accurate data showing minimum deviation from the desired conditions.

2.6.2 Acceptable Frequency Range

In the first step of this automatic data selection process, the computer segregates all data points where the frequency is 94.3 $\pm$1 Hz. Errors resulting from normalization of test data to the base frequency are a function of the departure of test frequency from the base value. If the selected test data are restricted to a narrow band of frequencies centered around the base frequency, the frequency normalization error can be held to a small value. As the frequency band is reduced to minimize the frequency normalization error, the number of data points is also reduced. Prior test experience indicates that data points in the quantity required to provide statistical confidence in the results generally will be available if the frequency band is no less than $\pm$1 Hz.

2.6.3 Quiescence Criterion

Another basic requirement for optimal usage of the test data is that it be obtained during near steady-state operation.

Experience in analysis of data from the previous test series has been considered in the establishment of a quiescence criterion. This background indicates that if a requirement is imposed limiting the rate of change in frequency to approximately 3 Hz/s, reasonably steady conditions can be obtained. Under these conditions, acceptable quantities of data for other parameters can be acquired for subsequent analysis.

The computer is therefore programmed to reject all data frames where the 94.3 ±1 Hz criterion is not met for a minimum continuous period of about 0.64 sec.

2.6.4 Selected Data

The computer next examines all groups of quiescent data frames to determine whether certain other key parameters are also reasonably steady-state. It selects any 20 consecutive data frames (20 frames sampled at 31.25 samples per second provide 0.64 seconds of data) that meet the criteria of Table C-3.

TABLE C-3

ANOMALY CRITERIA

Parameter	Mnemonic	Permissible Departure from Group Median
Slip	DF	±0.5 Hz
Phase current	RATI	±2 percent
Thrust	THRN	±500 N
Phase voltage	VN	±2 percent full scale
Power	PN	±3 percent full scale

2.6.5 Selected Data Points

The values of important parameters are averaged over the 20-frame time span selected in accordance with para 2.6.4. These selected data points are printed out and stored in accordance with Table C-4. The data points, being essentially steady-state values, are the bases for the plots and analyses presented in the main body of this report.

2.6.6 Summaries

The computer can, upon request, print out time-based groupings of parameters, which permits detailed study of parametric relationships at any time during the run. Standard formats are available whose contents are described by their titles: Operating Parameters, Electrical Parameters, Phase-Belt Parameters, Mechanical Parameters, Performance Parameters, LIM Parameters, and Magnetic Parameters.

2.6.7 Plots

Most, if not all, of the plots contained in this report are computer-produced and utilize the selected data points.

TABLE C-4

STORED SELECTED DATA

Parameter	Mnemonic
Time of first of the 20 points	TIME
Slip	DF
Thrust	THRN
Average power factor	APF
Average of phase voltages	VN
Efficiency	EFFN
Thrust	THRV
Velocity	VELN
Total vertical force	FVSN
Pitching moment	MPN
Airgap	GF
Average of phase currents	RATI
Frequency	RATF
Total power	PN
A-phase current	IAN
B-phase current	IBN
C-phase current	ICN
A-phase voltage	VAN
B-phase voltage	VBN
C-phase voltage	VCN
A-phase power	PAN
B-phase power	PBN
C-phase power	PCN
Two LIM temperatures	LT1 and LT2
Average of phase currents	IV
Each phase-belt voltage	AV1AN (typical)
Each phase-belt power	P1AN (typical)
Each phase-belt KVAR	KR1AN (typical)
Flux at each pole and the wake flux	F1V (typical)

APPENDIX D

SELECTED AND SUMMARY DATA SYNOPSIS

Table D-1 lists the information derived from the tapes submitted to the Torrance computer. The data entries in the various columns are described below:

Column Heading	Description
Run	The run number, which corresponds to the AiResearch test log identification.
Type Test	The type of test performed.
EU	The serial number of the engineering units tapes submitted to the Torrance computer.
Roman numerals I through VII	Refer to the summary printouts discussed in Appendix C. An X indicates that the summary was printed.
S.D.	An X indicates that a selected data printout was obtained.
Status	Identifies the test point(s) that the selected data met. Where more than one data point was obtained during the run, the number of points is entered in parentheses. In the "Status" column, the following notations occur: Accept = used when a satisfactory test point was obtained that was not at a formal test point frequency. FZ = failure to meet the quiescence criterion. FS = failure to meet the slip criterion. FT = failure to meet the thrust criterion. FI = failure to meet the current criterion.
O-Gram	On some runs oscillographic recordings (oscillograms) were obtained, as indicated by an X.
^{o}C	States the reaction rail temperature in degrees Celsius.

Table D-2 cross references configurations with test run numbers.

TABLE D-1

SUMMARY OF PROCESSED DATA

Run	Type Test	EU	II	III	IV	V	VI	VII	S.D.	Status		O-Gram	°C	Remarks
981	10-pole baseline performance	201153	X	X		X	X		X	B212(2)		-	35	Erratic data
983	10-pole baseline performance	201143	X	X		X	X		X	B211		-	33	Erratic data
984	10-pole baseline performance	201143	X	X		X	X		X	B210		-	27	
985	10-pole baseline performance	201143												Recording failure
988	10-pole baseline braking	201143	X	X		X	X					-	40	
989	10-pole baseline performance	201155	X	X		X	X		X	FQ		-	43	
991	10-pole baseline performance	201148	X	X		X	X		X	B211	Accept	-	48	
992	10-pole baseline performance	201144	X	X		X	X		X	Accept		-	49	
993	10-pole baseline performance	201144	X	X		X	X		X	B208		-	48	
994	10-pole baseline performance	201154	X	X		X	X		X	B206		-	49	
995	10-pole baseline performance	201155	X	X		X	X		X	B205		-	49	
996	10-pole baseline performance	201155	X	X			X		X	B204		-	47	
997	10-pole baseline performance	201148		X	X	X	X		X	FQ		-	40	
998	10-pole baseline performance	201148	X	X	X	X	X		X	FQ		-	43	
999	10-pole baseline performance	201148	X	X	X	X	X		X	B202		-	43	
1000	10-pole baseline performance	201148	X	X	X	X	X		X	B200	B201	-	51	
1001	10-pole baseline performance	201149	X				X		X	B213		-	53	Phase C power erratic
1002	10-pole baseline performance	201151	X				X		X	FT, FS		-	53	
1003	10-pole baseline performance	201152	X				X		X	FT		-	53	
1004	10-pole baseline braking	201157							X					Recording failure
1008	10-pole baseline braking	201159	X	X		X	X		X	B205		-	36	
1009	10-pole baseline braking	201159	X	X		X	X		X	B207(2)		-	41	
1010	10-pole baseline braking	201159	X	X		X	X		X	B215		-	42	
1011	10-pole baseline braking	201159	X	X		X	X		X	B219		-	42	
1015	10-pole baseline braking	201161	X	X		X	X		X	B219		-	34	
1016	10-pole baseline braking	201161	X	X		X	X		X	B219(2)		-	42	
1017	10-pole baseline braking	201161	X	X		X	X		X	B218		-	46	
1018	10-pole baseline braking	201161	X	X		X	X		X	B217		-	45	
1019	10-pole baseline braking	201161	X	X		X	X		X	FI		-	46	
1021	10-pole baseline braking	201161	X	X		X	X		X	B221		-	43	
1022	10-pole baseline flux	201173	X	X		X	X	X	X	B506		-	20	
1023	10-pole baseline flux	201173	X	X		X	X	X	X	B505	Accept	-	27	
1024	10-pole baseline flux	201173	X	X		X	X	X	X	B504		-	30	
1025	10-pole baseline flux	201173	X	X		X	X	X	X	B502		-	33	
1026	10-pole baseline flux	201185	X	X		X	X	X	X	FQ		-	34	
1027	10-pole baseline flux	201185	X	X		X	X		X	B501		-	42	
1028	10-pole baseline flux	201185	X	X		X	X	X	X	B500		-	44	
1030	10-pole baseline flux	201172	X	X		X	X	X	X	FT		-	45	
1031	10-pole baseline flux	201167	X	X		X	X	X	X	Accept		-	44	
1033	10-pole baseline flux	201169	X	X		X	X	X	X	FQ		-	43	
1034	10-pole baseline flux	201169	X	X		X	X	X	X	FS		-	51	
1035	10-pole baseline flux	201169	X	X		X	X	X	X	FS		-	51	
1036	10-pole baseline flux	201169	X	X		X	X	X	X	B507		-	50	
1037	10-pole baseline flux	201169	X	X		X	X	X	X	Accept		-	51	Erratic data
1040	10-pole baseline braking	201177					X					-	23	
1041	10-pole baseline braking	201177					X					-	30	
1042	10-pole baseline braking	201177					X					-	33	
1043	10-pole baseline braking	201177					X					-	41	
1044	10-pole baseline braking	201177					X					-	43	
1045	10-pole baseline braking	201177					X					-	43	
1046	10-pole baseline drag	201177					X					-	43	
1049	5-pole trailing baseline performance	201179	X	X		X	X		X	B320		-	0	Phase C voltage measurement
1050	5-pole trailing baseline performance	201191	X	X		X	X		X	B319		-	0	Failed-backup channel utilized
1051	5-pole trailing baseline performance	201191	X	X		X	X		X	B318		-	0	Failed
1055	5-pole trailing baseline performance	201191	X	X		X	X		X	B317		-	8	Failed
1059	5-pole trailing baseline performance	201183	X			X	X		X	B320		-	22	Failed erratic data
1060	5-pole trailing baseline performance	201191	X	X		X	X		X	FQ		-	21	
1062	5-pole trailing baseline performance	201183	X	X		X	X		X	B324		-	18	Failed
1063	5-pole trailing baseline performance	201191	X	X		X	X		X	B323(2)		-	20	Failed
1064	5-pole trailing baseline performance	201191	X	X		X	X		X	B322		-	22	Failed

TABLE D-1 (Continued)

Run	Type Test	EU	II	III	IV	V	VI	VII	S.D.	Status	O-Gram	°C	Remarks
1065	5-pole trailing baseline performance	201191	X	X		X	X		X	Accept	-	26	Failed
1066	5-pole trailing baseline performance	201183	X	X		X	X		X	B316	-	25	Failed erratic data
1067	5-pole trailing baseline performance	201183	X	X		X	X		X	FQ	-	23	
1070	5-pole trailing baseline performance	201185	X	X		X	X		X	B316	-	25	Failed
1071	5-pole trailing baseline performance	201185	X	X		X	X		X	B314 B315	-	24	Failed
1072	5-pole trailing baseline performance	201250	X	X		X	X		X	B313	-	23	
1073	5-pole trailing baseline performance	201185	X	X		X	X		X	B312	-	22	Failed
1074	5-pole trailing baseline performance	201208	X	X		X	X		X	B310(2) B311	-	21	Failed
1075	5-pole trailing baseline performance	201191	X				X		X	B308	-	7	Failed
1076	5-pole trailing baseline performance	201191	X				X		X	B306	-	14	Failed
1077	5-pole trailing baseline performance	201191	X				X		X	B305	-	12	Failed
1079	5-pole trailing baseline performance	201188	X	X		X	X		X	FS	-	13	
1080	5-pole trailing baseline performance	201188	X	X		X	X		X	B303(2)	-	12	
1081	5-pole trailing baseline performance	201188	X			X	X		X	B302	-	12	
1082	5-pole trailing basleine performance	201190	X	X		X	X		X	B309	-	24	
1083	5-pole trailing baseline performance	201190	X	X		X	X		X	B301	-	22	
1084	5-pole trailing baseline performance	201190	X	X		X	X		X	B300(2)	-	21	
1085	5-pole leading baseline performance	201249	X	X		X	X		X	B414(2) B415(2)	-	3	
1086	5-pole leading baseline performance	201208	X	X		X	X		X	B413	-	16	
1087	5-pole leading baseline performance	201249	X	X		X	X		X	B412(2)	-	19	
1088	5-pole leading baseline performance	201207	X	X		X	X		X	B416	-	3	
1089	5-pole leading baseline performance	201196	X	X		X	X		X	B412(2)	-	31	
1090	5-pole leading baseline performance	201196	X	X		X	X		X	B411(3) B410	-	32	
1091	5-pole leading baseline performance	201196	X	X		X	X		X	B409(2)	-	30	
1092	5-pole leading baseline performance	201196	X	X		X	X		X	B408	-	32	
1093	5-pole leading baseline performance	201207	X				X		X	B407(2)	-	32	
1094	5-pole leading baseline performance	201203	X	X		X	X		X	B406(2)	-	18	
1095	5-pole leading baseline performance	201203	X	X		X	X		X	B405	-	18	
1096	5-pole leading baseline performance	201203	X	X		X	X		X	B403	-	17	
1097	5-pole leading baseline performance	201203	X	X		X	X		X	B402	-	15	
1098	5-pole leading baseline performance	201203	X	X		X	X		X	B401 B400	-	13	
1100	5-pole leading baseline performance	201203	X	X		X	X		X	FQ	-	23	
1101	5-pole leading baseline performance	201203	X	X		X	X		X	B419	-	30	
1102	5-pole leading baseline performance	201203	X	X		X	X		X	B418(2)	-	31	
1103	5-pole leading baseline performance	201204	X	X		X	X		X	B417	-	31	
1104	5-pole leading baseline performance	201202	X	X		X	X		X	B204	-	17	
1105	5-pole leading baseline performance	201202	X	X			X		X	B423	-	18	

TABLE D-1 (Continued)

Run	Type Test	EU	II	III	IV	V	VI	VII	S.D.	Status	O-Gram	°C	Remarks
1106	5-pole leading baseline performance	201202	X	X			X		X	B422(2) B421	-	17	
1108	5-pole leading baseline performance	201206	X				X		X	B407	-	13	Current overranged
1109	5-pole leading baseline performance	201206	X				X		X	B407	-	11	Current overranged
1111	5-pole leading baseline performance	201206	X				X		X	Accept	-	11	
1112	5-pole leading baseline performance	201206	X				X		X	B404(2) B406	-	6	
1117	10-pole baseline dc test	201214					X				-	20	
1118	10-pole baseline dc test	201214					Special				-	22	
1119	10-pole solid iron test	201216					Special				-	-	
1120	10-pole solid iron test	201216					Special				-	-	
1121	10-pole solid iron, 26 mm, performance	201219	X	X			X		X	S211	-	7	
1122	10-pole solid iron, 26 mm, performance	201219	X	X			X	X	X	Accept	-	-	
1123	10-pole solid iron, 26 mm, performance	201219	X	X			X	X	X	S210, S209, Accept	-	-	
1124	10-pole solid iron, 26 mm, performance	201219	X	X			X		X	S208(3)	-	-	
1125	10-pole solid iron, 26 mm, performance	201219	X	X			X		X	S207	-	-	
1126	10-pole solid iron, 26 mm, performance	201220	X	X			X		X	S206	-	18	
1127	10-pole solid iron, 26 mm, performance	201220	X	X			X		X	S205	-	13	
1128	10-pole solid iron, 26 mm, performance	201220	X	X			X		X	S204	-	12	
1129	10-pole solid iron, 26 mm, performance	201223	X	X		X	X	X	X	S210(2)	-	37	
1130	10-pole solid iron, 26 mm, performance	201223	X	X		X	X	X	X	FQ	-	38	
1131	10-pole solid iron, 26 mm, performance	201223	X	X		X	X	X	X	S206(2)	-	38	
1132	10-pole solid iron, 26 mm, performance	201223	X	X		X	X		X	S205	-	35	
1133	10-pole solid iron, 26 mm, performance	201224	X	X		X	X	X	X	S204(3)	-	38	
1137	10-pole solid iron, 26 mm, performance	201224		X		X	X	X	X	S202	-	11	
1138	10-pole solid iron, 26 mm, performance	201224		X		X	X	X	X	S202	-	12	
1139	10-pole solid iron, 26 mm, performance	201224	X	X		X	X	X	X	S201	-	24	
1140	10-pole solid iron, 26 mm, performance	201224	X	X		X	X	X	X	S200(2)	-	23	
1141	10-pole solid iron, 26 mm, performance	201224									-		Recording failure
1145	10-pole solid iron, 26 mm, performance	201231	X	X			X		X	FS	-	22	Stationary, ac, laminated secondary
1146	10-pole solid iron, 26 mm, performance	201231	X	X		X					-	39	Stationary, ac, solid secondary
1147	10-pole solid iron, 26 mm, performance	201231	X	X			X		X	S211	-	39	Stationary, ac, laminated secondary
1148	10-pole solid iron, 26 mm, dc test	201231	X				X				-	0	
1151	10-pole solid iron, 26 mm, performance	201232	X	X			X	X	X	FQ	-	34	
1152	10-pole solid iron, 26 mm, performance	201232	X	X			X	X	X	FQ	X	9	
1153	10-pole solid iron, 26 mm, performance	201231	X	X			X	X	X	FQ	X	11	
1154	10-pole solid iron, 26 mm, performance	201232	X	X			X	X	X	FQ	X	35	

TABLE D-1 (Continued)

Run	Type Test	EU	II	III	IV	V	VI	VII	S.D.	Status		O-Gram	°C	Remarks
1156	10-pole solid iron, 18 mm, performance	201237	X				X	X	X	185211(2)	Accept(2)	X	29	
1157	10-pole solid iron, 18 mm, performance	201237	X				X	X	X	185210		X	39	
1158	10-pole solid iron, 18 mm, performance	201237	X				X	X				X	37	Stationary, ac, laminated secondary
1159	10-pole solid iron, 18 mm, performance	201237	X				X	X				-	49	Stationary, ac, laminated secondary
1162	10-pole solid iron, 18 mm, performance	201237	X				X		X	185208(2)	185211(2), Accept	X	33	
1163	10-pole solid iron, 18 mm, performance	201238	X				X		X	185207(2)		X	37	
1164	10-pole solid iron, 18 mm, performance	201238	X				X		X	185206(4)		X	37	
1165	10-pole solid iron, 18 mm, performance	201238	X						X	Accept(2)	18509	X	33	
1167	10-pole solid iron, 18 mm, performance	201238	X						X	185200		X	22	
1168	10-pole solid iron, 18 mm, performance	201239	X				X		X	185201		X	18	
1169	10-pole solid iron, 18 mm, performance	201239	X				X		X	FQ		X	14	
1170	10-pole solid iron, 18 mm, performance	201241	X				X		X	185205		-	4	
1172	10-pole solid iron, 18 mm, performance	201241	X				X		X	185200		-	11	
1173	10-pole solid iron, 18 mm, performance	201241	X				X		X	FQ		-	12	
1174	10-pole solid iron, 18 mm, performance	201247	X				X	X				X	39	Stationary, ac, laminated secondary
1175	10-pole solid iron, 18 mm, performance	201247	X				X	X				X	39	Stationary, ac, solid secondary
1176	10-pole solid iron, 18 mm, performance	201247	X				X	X		185204		X	34	
1178	10-pole solid iron, 18 mm, performance	201247						X	X	FS		-	2	
1181	10-pole solid iron, 18 mm, dc test	201247					X					X	7	
1183	10-pole solid iron, 18 mm, dc test	201247					X					X	-	
1184	10-pole solid iron, 18 mm, dc test	201247					X					X	7	Vertical forces overranged
1185	10-pole solid iron, 18 mm, dc test	201247										X		
1186	10-pole solid iron, 18 mm, dc test	201250										X		
1187	10-pole solid iron, 18-mm, performance	201250	X				X	X	X	FQ		X	36	
1189	10-pole solid iron, 18 mm, performance	201248	X	X	X	X	X	X	X	185200		X	41	Summary I

TABLE D-2

SUMMARY OF DATA POINTS AND RUN NUMBERS

Test Run	Data Point
10-Pole Baseline	
981-1	B212 (ER) See Note.
981-2	B212 (ER)
983	B211 (ER)
984	B210
989	Failed quiescence criterion.
991-1	B211
991-2	Ok
992	Ok
993	B208
994	B206
995	B205
996	B204
997	Failed quiescence criterion.
998	Failed quiescence criterion.
999	B202
1000-1	B201
1000-2	B200
1001	B213 (ER)
1002	Failed thrust and slip criteria.
1103	Failed thrust criterion.
1108	B205
1109-1	B207
1109-2	B207
1010	B215
1011	B219
1015	B219
1016-1	B219
1016-2	B219
1017	B218
1018	B217
1019	Failed current criterion.
1021	B221
1022	B506
1023-1	B505
1023-2	Ok
1024	B504
1025	B502
1026	Failed quiescence criterion.
1027	B501
1028	B500
1030	Failed thrust criterion.
1031	Ok
1033	Failed quiescence criterion.
1034	Failed slip criterion.
1035	Failed slip criterion.
1036	B507
1037	Ok (ER)

Test Run	Data Point
5-Pole Trailing	
1049	B320*
1050	B319*
1051	G318*
1055	B317*
1059	B320* (ER)
1060	Failed quiescence criterion.
1062	B324*
1063-1	B323*
1063-2	B323*
1064	B322*
1065	Ok*
1066	B316* (ER)
1067	Failed quiescence criterion.
1070	B316*
1071-1	B315*
1071-2	B314*
1072	B313
1073	B312*
1074-1	B311*
1074-2	B310*
1074-3	B310*
1075	B308*
1076	B306*
1077	B305*
1079	Failed slip criterion.
1080-1	B303
1080-2	B303
1081	B302
1082	B309
1083	B301
1084-1	B300
1084-2	B300
5-Pole Leading	
1085-1	B415
1085-2	B415
1085-3	B414
1085-4	B414
1086	B413
1087-1	B412
1087-2	B412
1088	B416
1089-1	B412
1089-2	B412
1090-1	B411
1090-2	B411

Note: ER = Erratic reading
* = Phase C voltage measurement failed. High-speed channel used.

TABLE D-2 (Continued)

Test Run	Data Point
1090-3	B411
1090-4	B410
1091-1	B409
1091-2	B409
1092	B408
1093-1	B407
1093-2	B407
1094-1	B406
1094-2	B406
1095	B405
1096	B403
1097	B402
1098-1	B401
1098-2	B400
1100	Failed quiescence criterion.
1101	B419
1102-1	B418
1102-2	B418
1103	B417
1104	B424
1105	B423
1106-1	B422
1106-2	B422
1106-3	B421
1108	B407**
1109	B407**
1111	Ok
1112-1	B404
1112-2	B404
1112-3	B406

10-Pole Solid Iron (18 mm Airgap)

1151	Failed quiescence criterion.
1152	Failed quiescence criterion.
1153	Failed quiescence criterion.
1154	Failed quiescence criterion.
1157	18S210
1156-1	Ok
1156-2	18S211
1156-3	Ok
1156-4	18S211
1162-1	18S208
1162-2	18S208
1162-3	18S211
1162-4	Ok
1162-5	18S211

** = Phase currents overranged, otherwise ok.

Test Run	Data Point
1163-1	18S207
1163-2	18S207
1164-1	18S206
1164-2	18S206
1164-3	18S206
1164-4	18S206
1165-1	Ok
1165-2	18S209
1167	18S200
1168	18S201
1169	Failed quiescence criterion.
1170	18S205
1172	18S200
1173	Failed current criterion.
1176	18S204
1178	Failed slip criterion.
1189	18S200

10-Pole Solid Iron (26 mm Airgap)

1121	S211
1122	Ok
1123-1	S210
1123-2	S209
1123-3	Ok
1124-1	S208
1124-2	S028
1124-3	S208
1125	S207
1126	S206
1127	S205
1128	S204
1129-1	S210
1129-2	S210
1130	Selected data missing.
1131-1	S206
1131-2	S206
1132	S205
1133-1	S204
1133-2	S204
1137	S202
1138	S202
1139	S201
1140-1	S200
1140-2	S200
1145	Failed slip criterion.
1147	S211

APPENDIX E

SYSTEM LIMITATIONS

INSTRUMENTATION CERTIFICATION

The measurement systems for all of the parameters recorded during the SLIM test program were certified prior to the start of actual testing. At the conclusion of testing, those systems of major significance were recertified.

Since it was generally impracticable to apply a series of calibrated stimuli as inputs to the system transducers while they were mounted in the LIMRV, certification was accomplished as follows:

- The transducers were demounted and their calibrations checked either at the TTC Metrology Department, the AiResearch Metrology Laboratories, or the manufacturer's facility.
- With the transducer removed, calibrated signals were applied to the vehicle circuitry, simulating transducer outputs. The corresponding signal conditioner output was then recorded. The input and output measurement devices used are traceable to the National Bureau of Standards.
- A computer program combined the transducer and signal conditioner calibration, and produced tables wherein each of the 256 counts produced by the onboard analog-to-digital conversion was assigned a value in engineering units. These calibration tables were then applied to the recorded raw data in the course of producing the engineering units tapes.

MEASUREMENT ACCURACY

Objectives

- Determine at any test condition the expected error in the measured or computed parameters. This is in addition to expressing their errors as a percent of full scale.
- Estimate the errors in the onboard instrumentation and data acquisition systems.
- Develop error analysis techniques with which errors in the measured and computed data can be determined.

Assumptions

In determining measurement accuracy, the following conditions are assumed:

- Vehicle interior temperature range is 10° to 26.7°C (50° to 80°F).

- All instrumentation components meet or exceed applicable manufacturer specifications.
- All required calibrations have been performed.
- No systematic errors exist in the measurement or calibration techniques.

Statistical Techniques

The result of a measurement generally will be shifted from the true value. This shift, which may be considered a measurement error, may result from several sources. The objective of an error analysis is to evaluate the effect of component errors and estimate total measurement error.

The error in a component is generally random with respect to sign and magnitude and has a mean defined as:

$$\text{Mean} = m = \frac{\sum_{i=1}^{n} X_n}{n}$$

where X_n are the individual measurements. Furthermore, there is a statistical spread called a standard deviation, which is the root-mean-square (RMS) deviation from the mean error and is defined as:

$$\text{Standard deviation} = \sigma = \left[\frac{\sum_{i=1}^{n} (X_n - m)^2}{n}\right] 1/2$$

Also, if a system has a large number of component errors, its output error generally will exhibit a Gaussian distribution even though some of the individual components are non-Gaussian in nature. For systems of this type, 99.7 percent of all measurements will be within plus or minus three times the standard deviation (3σ) of the mean.

The root-sum-square (RSS) error is defined as the error equal to 3σ, and can be treated as the expected peak system error. The method of combining the component RSS errors of a system is:

$$3\sigma = [(3\sigma_1)^2 + (3\sigma_2)^2 + \ldots + (3\sigma_m)^2]^{1/2}$$

where σ_1, σ_2, ..., σ_m are the component system errors. Unless otherwise specified, the errors in the analyses are assumed to be RSS errors and therefore can be combined as shown in the foregoing equation of 3σ.

Values of 3σ determined from the analysis are specified in Table E-1, expressed as a percentage of full scale. The largest 3σ value, whether measured in pre-test or post-test calibration, is listed in Table C-1

TABLE E-1

DATA ACQUISITION SYSTEM ACCURACY

Parameter	No.	Unit	Full Scale	% Accuracy
Bolster position	001	in.	±2.4	±2.07
Bolster position	002	in.	±2.4	±2.07
Bolster position	003	in.	±2.4	±2.07
Bolster position	004	in.	±2.4	±2.07
Bolster position	005	in.	±2.4	±2.07
Truck accel	006	G	±10	±3.26
Truck accel	007	G	±10	±3.26
Truck accel	008	G	±10	±3.26
Truck accel	009	G	±10	±3.26
Vehicle accel	010	G	±1	±3.26
Vehicle accel	011	G	±1	±3.26
Vehicle accel	012	G	±1	±3.26
Journal bearing accel	013	G	±20	±3.35
Journal bearing accel	014	G	±20	±3.26
Journal bearing accel	015	G	±20	±3.26
Axle displacement	016	in.	±0.2	±2.07
Axle displacement	017	in.	±0.2	±2.07
Airgap	018	cm	±0.5	±4.28
LIM longitudinal accel, unfiltered	021	G	±0.3	Not used
Total transverse force	022	kN	±3.82	±4.28
Analog frequency	023	Hz	0-200	±1.04
Vertical force FV1, unfiltered	024	kN	±15	Not used
Vertical force FV2, unfiltered	025	kN	±15	Not used
LIM thrust	026	kN	±12.73	±1.66
LIM longitudinal accel, filtered	027	G	±0.3	±3.27
J52 throttle position, left	028	%	0-100	±2.47
J52 throttle position, right	029	%	0-100	±2.47
J52 speed, left	030	krpm	0-15	±1.53
J52 speed, right	031	krpm	0-15	±1.53
J52 temp, left, T5	032	k°F	0.032-1.5	±3.5
J52 temp, right, T5	033	k°F	0.032-1.5	±3.5
T64 temp, T5	034	k°F	0.032-1.5	±7.6
T64 gas generator speed	035	krpm	0-20	±5.12
T64 throttle position	036	%	0-100	±6.72
T64 temp, T2	037	°F	32-200	±2.67, -2.35
T64 torque	038	klb	0-1.5	±1.7
Brake pressure, front	039	psig	0-100	±3.6
Brake pressure, rear	040	psig	0-100	±3.6
Brake resistor bank temp	041	k°F	0.032-1.5	±5.75
Fuel quantity	042	%	0-100	±14.04
APU compartment temp	043	°F	32-500	±2.67, -2.35
Alternator temp	044	°F	32-500	+2.67, -2.35
Alternator vibration	045	G RMS	0-5	±8.6
400-Hz voltage	046	V RMS	0-132	±1.28
Vertical force FV3, unfiltered	047	kN	±15	Not used
Analog slip frequency	048	Hz	±20	±1.00
LIM flux #1	049	MWb	20	±2.61
LIM flux #2	050	MWb	20	±2.61
LIM flux #3	051	MWb	20	±2.61
LIM flux #4	052	MWb	20	±2.61
LIM flux #5	053	MWb	20	±2.61
LIM flux #6	054	MWb	20	±2.61
LIM flux #7	055	MWb	20	±2.61
LIM flux #8	056	MWB	20	±2.61
LIM flux #9	057	MWb	20	±2.61
LIM flux #10	058	MWB	20	±2.61
LIM flux #11	059	MWb	20	±2.61
Vertical force FV4, unfiltered	060	kN	±15	Not used
Total A-phase current	061	kA	±4	±1.06
Total B-phase current	062	kA	±4	±1.06
Total C-phase current	063	kA	±4	±1.06
Total A-phase voltage	064	kV	±1.2	±1.11
Total B-phase votlage	065	kV	±1.2	±1.11
Total C-phase voltage	066	kV	±1.2	±1.11

TABLE E-1 (Continued)

Parameter	No.	Unit	Full Scale	% Accuracy
Phase-belt voltage #1	067	V	±120	±1.11
Phase-belt voltage #2	068	V	±120	±1.11
Phase-belt voltage #3	069	V	±120	±1.11
Phase-belt voltage #4	070	V	±120	±1.11
Phase-belt voltage #5	071	V	±120	±1.11
Phase-belt voltage #6	072	V	±120	±1.11
Phase-belt voltage #7	073	V	±120	±1.11
Phase-belt voltage #8	074	V	±120	±1.11
Phase-belt voltage #9	075	V	±120	±1.11
Phase-belt voltage #10	076	V	±120	±1.11
Rms A-phase current	079	kA	0-3	±1.15
Rms B-phase current	080	kA	0-3	±1.3
Rms C-phase current	081	kA	0-3	±1.12
Thrust, unfiltered	082	kN	±15	Not used
Vertical force sum	083	kN	±28.7	±1.4
Vertical force FV1 + FV2	084	kN	±10	±5.7
RMS A-phase voltage	085	V	0-900	±1.17
RMS B-phase voltage	086	V	0-900	±1.17
RMS C-phase voltage	087	V	0-900	±1.17
RMS phase-belt voltage #1	088	V	0-90	±1.19
RMS phase-belt voltage #2	089	V	0-90	±1.12
RMS phase-belt voltage #3	090	V	0-90	±1.17
RMS phase-belt voltage #4	091	V	0-90	±1.18
RMS phase-belt voltage #5	092	V	0-90	±2.55
RMS phase-belt voltage #6	093	V	0-90	±1.14
RMS phase-belt voltage #7	094	V	0-90	±1.16
RMS phase-belt voltage #8	095	V	0-90	±3.38
RMS phase-belt voltage #9	096	V	0-90	±1.19
RMS phase-belt voltage #10	097	V	0-90	±1.28
Total A-phase power	100	kW	±1200	±1.33
Total B-phase power	101	kW	±1200	±1.36
Total C-phase power	102	kW	±1200	±1.36
Phase-belt power #1	103	kW	±120	±1.36
Phase-belt power #2	104	kW	±120	±1.94
Phase-belt power #3	105	kW	±120	±1.35
Phase-belt power #4	106	kW	±120	±1.43
Phase-belt power #5	107	kW	±120	±1.34
Phase-belt power #6	108	kW	±120	±1.34
Phase-belt power #7	109	kW	±120	±1.43
Phase-belt power #8	110	kW	±120	±3.07
Phase-belt power #9	111	kW	±120	±1.35
Phase-belt power #10	112	kW	±120	±1.36
Field current	115	A	0-200	±2.36
Alpha command	116	V	0-10	±1.02
Field PDR voltage	117	V	0-308	±2.64
Voltage/frequency ratio	118	V/Hz	0-5	Not used
Vertical force FV3	119	kN	±20	±6.2
Dynamic brake current	120	kA	0-2	± 2.5
LIM temp #1	121	°F	0-500	+2.67, -2.35
LIM temp #2	122	°F	0-500	+2.67, -2.35
Vertical force FV5, unfiltered	123	kN	±15	
Analog axle speed	127	mph	0-250	±1.02
Vertical force FV4 + FV5	128	kN	±10	±5.3
Speed, most significant half	129	Dgtl data		±1 count
Speed, least significant half	130	Dgtl data		±1 count
Station, most signicant half	131	Dgtl data		±1 count
Station, least significant half	132	Dgtl data		±1 count
Station subdivision	133	Dgtl data		±1 count
Frequency, most significant half	134	Dgtl data		±1 count
Frequency, least significant half	135	Dgtl data		±1 count
Slip, most significant half	136	Dgtl data		±1 count
Slip, least significant half	137	Dgtl data		±1 count
Parameter status	138	Dgtl data		On or off

Each channel in the LIMRV instrumentation system lacks the large number of component errors that the statistical technique under discussion requires to predict the error in that particular channel. The 3 errors generated in these analyses, however, are the best estimates of what can be generally expected from the system.

Scope of Error Analysis

Each parameter measurement system has been analyzed for factors that will contribute to measurement error. Manufacturer specifications as well as direct measurements are used to assign numerical values to each error source.

Among the types of errors considered in these analyses were:

- Transducer errors: nonlinearity, nonrepeatability, drift, environmental effects
- Calibration errors: errors in meters and gauges used in calibrations, readability effects
- Signal conditioning errors: nonlinearity, nonrepeatability, drift, environmental effects
- Data acquisition errors: digitizing errors and accuracy losses during transmission and recording
- Application errors: nonalignment of parameter axis with measurement axis under some operating conditions

EFFECT OF LIMRV POWERPLANT LIMITATIONS ON SLIM SATURATION TESTS

The LIMRV powerplant imposed the following limitations on SLIM testing (see Figure E-1):

- Maximum alternator output current (3 min) = 2500 A
- Maximum alternator field current = 200 A
- Maximum 10-pole SLIM excitation at 0.2 slip = 4.7 V/Hz
- Maximum 5-pole SLIM excitation at 0.2 slip (with current limit) = 3.0 V/Hz

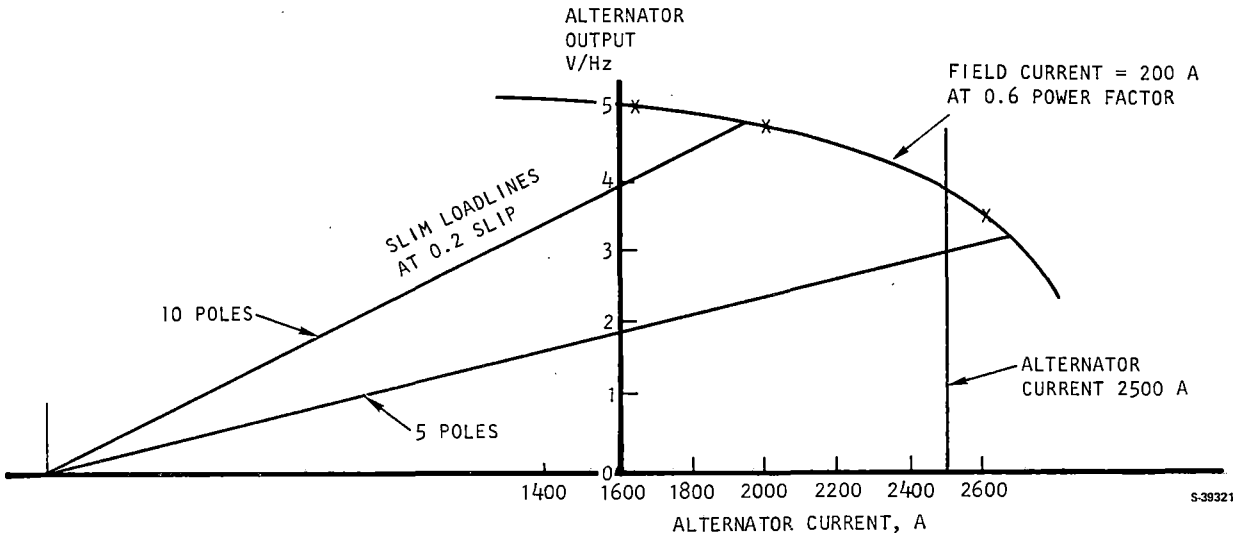

Figure E-1. Alternator Output

APPENDIX F

TRACK FLUX MEASUREMENT

In order to determine flux distribution within the solid backiron, a special laminated section was constructed, using three horizontally laminated sections. Around each section two one-turn search coils were wound, spaced one-half pole pitch apart. In addition, two search coils were similarly wound around the entire backiron. Figure F-1 shows the location of holes drilled for the purpose of attaching the section to the reaction rail base.

Figure F-2 shows the schematic arrangement of the search coils, together with details of search coil designators and relevant track dimensions. The north coil set (1) was located at Station 1715.8.

The output of each search coil was fed into an integrator, and the resultant signal was scaled in order to produce a uniform flux density-per-volt calibration for all search coils. The output of each integrator was automatically reset immediately prior to the primary passing over the track coils by an optical sensor placed 4.52 m before the first coil set.

Recording was accomplished by an FM tape recorder and subsequently played back into an oscillograph located in the data van.

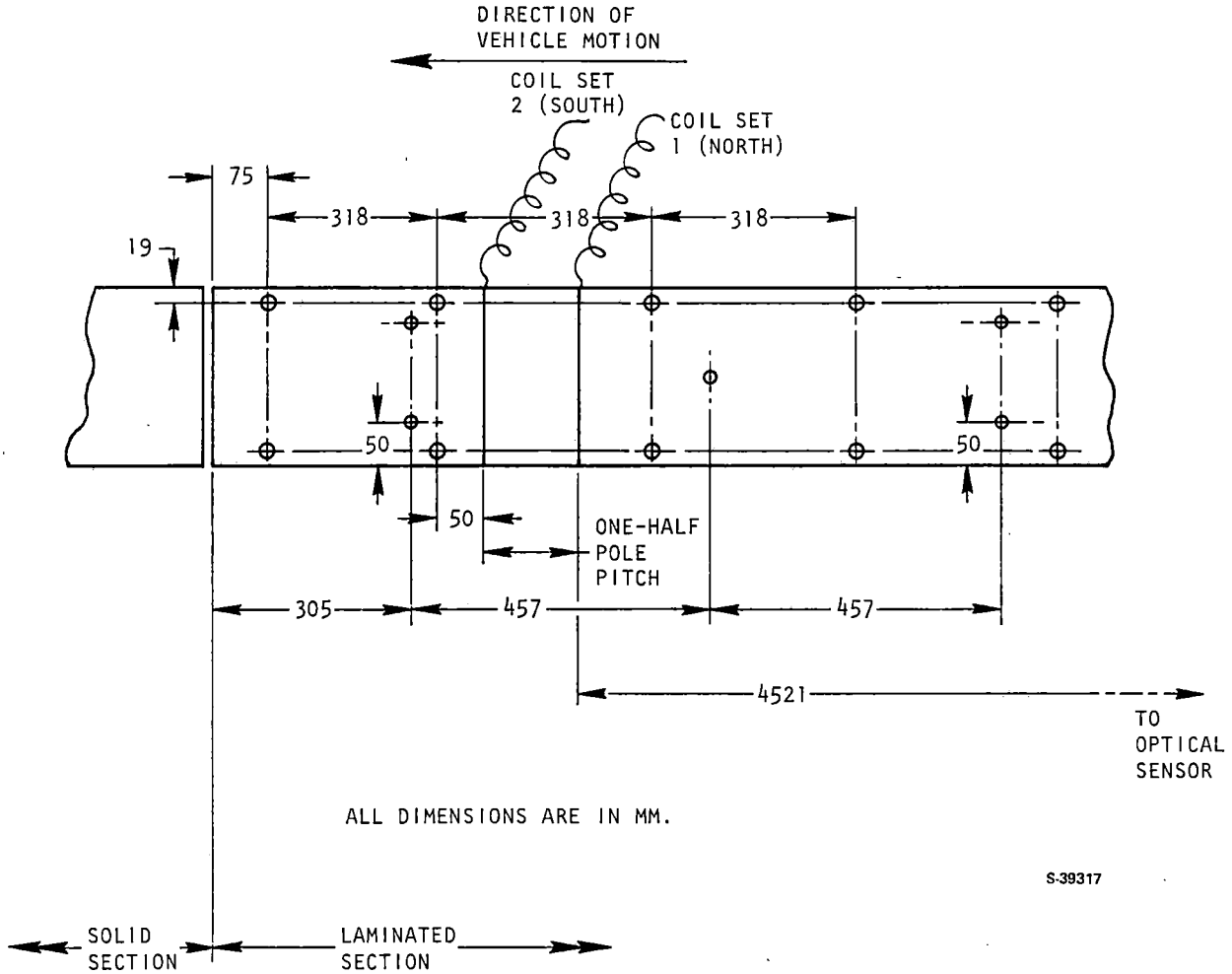

Figure F-1. Backiron Configured for Attachment to Reaction Rail Base

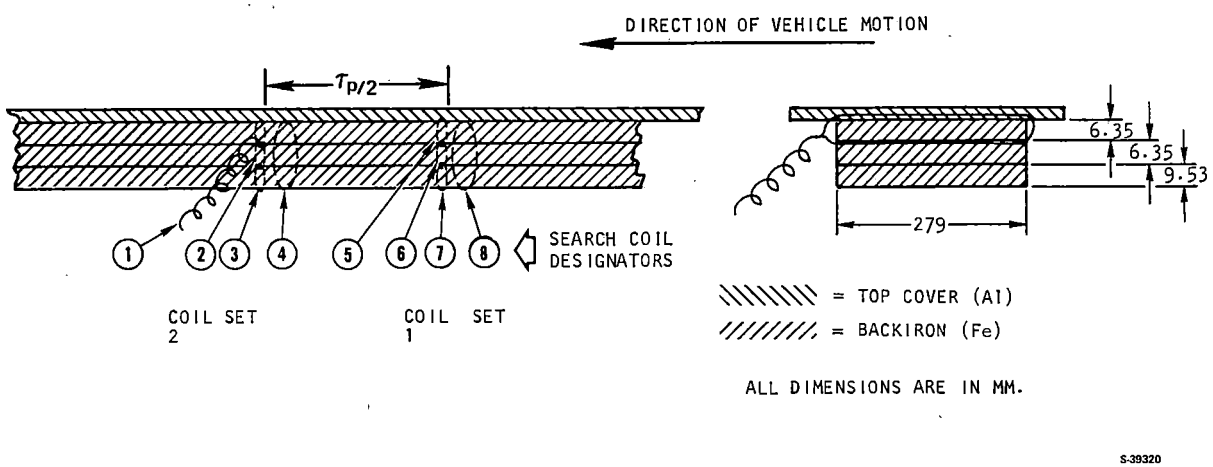

Figure F-2. Search Coil Installation

APPENDIX G

MEASUREMENT OF SLIM PHYSICAL AIRGAP

At the completion of testing (18S-series tests) the physical airgap of the motor was measured at station 1583. During the course of testing, adjustments were made in the motor installation, in particular, the force preloads of the five vertical support links. Changes in vertical force preload caused deflections in the motor poleface plane.

Figure G-1 shows the physical airgap along the length of the motor for three lateral positions. The average airgap was found to be 14.8 mm, corresponding to a recorded value of 18 mm (nominal) in the data acquisition system readout.

It can be seen from the measurements that the center support of the motor was comparatively in tension, which caused the center of the motor to bow upward. Also, the front end of the motor was lower than the rear end.

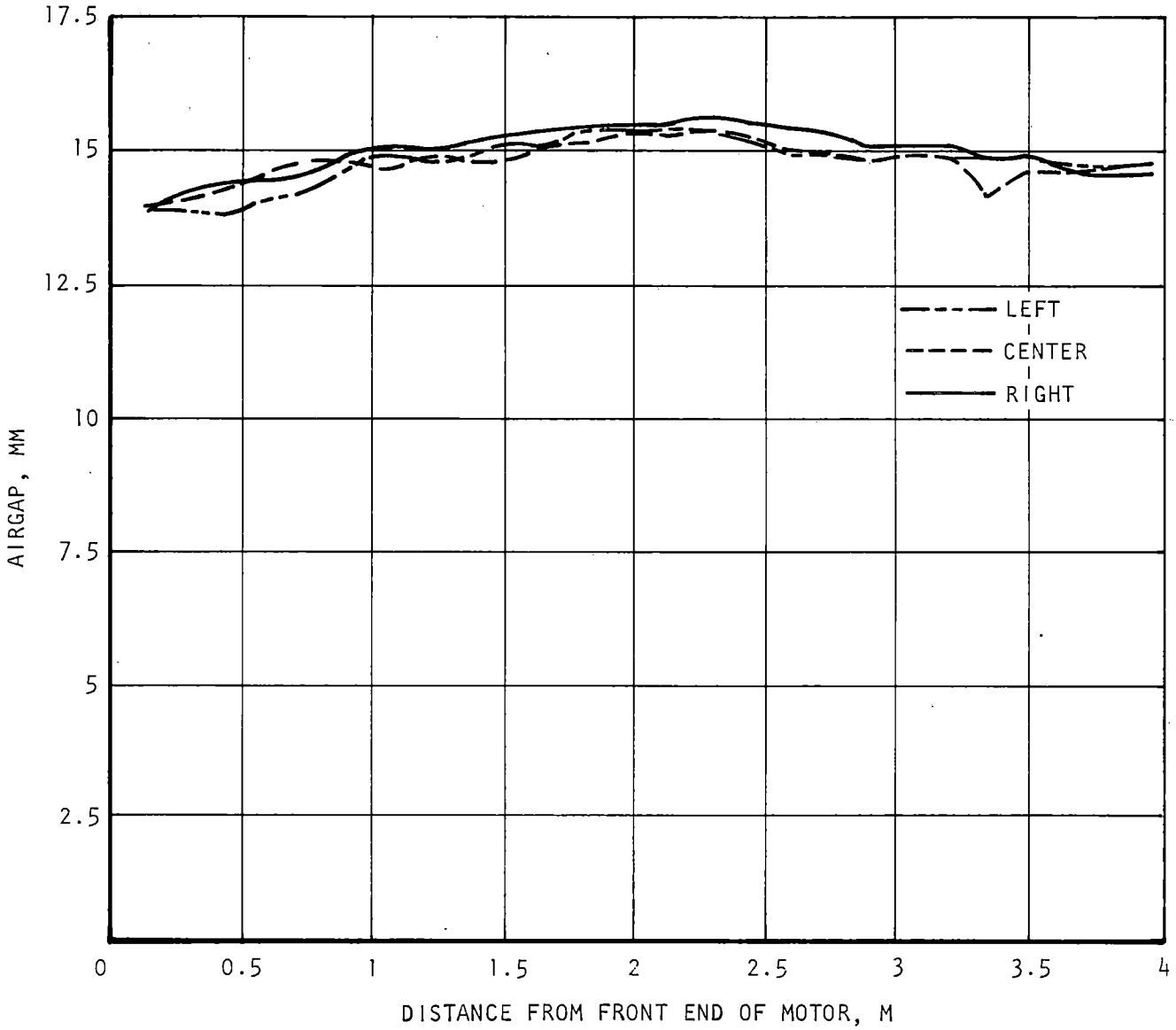

Figure G-1. Posttest Measurement of SLIM Physical Airgap

APPENDIX H

STATIC FLUX MEASUREMENT

In compliance with DOT direction, the following report is included herein:

"Static LIMRV/SLIM Airgap Flux Measurements"

by

Dr. J. J. Stickler
Electrical Power and Propulsion Branch
Vehicle and Engineering Division
Department of Transportation

The test data was obtained at the Transportation Test Center, Pueblo, Colorado, by Dr. Stickler, assisted by AiResearch test personnel.

Report No. SS-74-U-205-48

Date: June 22, 1979

STAFF STUDY

Static LIMRV/SLIM Airgap Flux Measurements

John J. Stickler

Approved for Distribution: Lawrence D. Zorio for
Frank L. Raposa, DTS-742

ELECTRICAL POWER AND PROPULSION BRANCH
VEHICLES AND ENGINEERING DIVISION
OFFICE OF GROUND SYSTEMS

U.S. DEPARTMENT OF TRANSPORTATION
TRANSPORTATION SYSTEMS CENTER
KENDALL SQUARE
CAMBRIDGE, MA 02142

STATIC LIMRV/SLIM AIRGAP FLUX MEASUREMENTS

1. INTRODUCTION

This report describes static airgap flux measurements made on the Linear Induction Motor Research Vehicle (LIMRV) single-sided LIM (SLIM) during the final phase of the electrical performance test program. The measurements were conducted at the Transportation Test Center (TTC), Pueblo, Colorado on February 8-9, 1979 and utilized a forty foot section of LIM test track located in the vicinity of the LIMRV terminal building.

The tests had two objectives. First, it was desired to have a record of the airgap flux distribution of the LIM in order to complete the characterization of the LIM electromagnetic properties. In addition to recording the flux signature of the LIM, the tests provide information on the Fourier spatial harmonics present in the airgap flux. From an analysis of the spatial flux distribution, one can independently check the amplitude and phase of the stator excitation waves and compare the results with that predicted by idealized LIM models. Second, it was anticipated that an analysis of the data would provide important information pertaining to the effective surface conductivity of the LIM reaction rail and permit an independent determination of the Goodness Factor(G) as defined by Laithwaite.[1]

These test objectives were generally met by the flux measurements. The data provided important information on the harmonic content of the flux distribution and, in particular, the magnitudes of the phase belt harmonics relative to the fundamental(excitation) harmonic. The interaction of these harmonic waves with the perturbation caused by the finite LIM width leads to an interesting study of coupled longitudinal,and transverse wave phenomena.

The valuable information acquired on the harmonic content of the airgap flux was partly offset by the increased complexity of the data analysis and the ensuing difficulty in evaluating the Goodness Factor of the LIM from the lateral flux distribution data. An additional problem arose due to lack of LIM symmetry caused by lateral offset of the LIM relative to the rail and nonuniform airgap between LIM stator and reaction rail. Further discussion of the test data is given in Section 5 of the report.

2. SCOPE OF MEASUREMENTS

The tests comprised four airgap flux measurements, three in the transverse direction and one along the center(longitudinal) axis of the LIM. The airgap flux at the surface of the rail was measured using the multi-probe fixture described in Section 4. To eliminate the problem of rail over-heating, the LIM power-plant (turbo-lternator) was run at 'idle' conditions which resulted in LIM phase currents of 35-36 amperes. At these low power levels, the power-plant frequency was 120-122 HZ. Table 1 presents a summary of LIM parameters as well as other parameters which define the test conditions.

TABLE 1

SUMMARY OF LIM PARAMETERS AND TEST CONDITIONS

LIM PARAMETERS:

Primary

Stack Width(in.)	= 10

Secondary

Aluminum Thickness(in.)	= .160
Aluminum Width(in.)	= 18
Backiron Thickness(in.)	= .875
Backiron Width(in.)	= 11

Airgap

Primary-to-Secondary(in)	= 15/16

TEST CONDITIONS:

Stator Phase Current(A)	= 35-36
Excitation Frequency(Hz)	= 121-122

Fig. 1 shows the locations of the test fixtures used in the four flux measurements. Configurations 1 and 2 describe the tests conducted on Feb. 7, 1979 to measure the basic properties of the transverse flux distribution. Configurations 3 and 4 give the positions of the test fixtures used on Feb. 8, 1979 to measure the longitudinal flux distribution and to give additional data on the transverse flux distribution. After each test, it was necessary to move the LIMRV (vehicle), reposition the test fixtures, and then return the LIMRV to it original position over the rail.

Fig. 2 shows a sketch of a cross-sectional view of the LIM and rail. The LIM was observed to have a one-half inch (lateral) offset relative to the center axis of the rail. Since the iron backing of the rail was eleven inches while the LIM stator stack width was only ten inches, this resulted in one edge of the LIM being directly over the edge of the rail backiron and the other edge of the LIM being displaced one inch from the other backiron edge. This lateral asymmetry caused a pronounced effect on the transverse flux distribution as discussed in Section 5.2.
An additional problem existed in the value of the airgap between the stator surface and rail. The LIM which was supported by the LIMRV truck was not exactly parallel with the rail surface. The airgap was observed to vary along both the width and length of the LIM yielding airgap reading which varied between 7/8 inch and 1 1/32 inch. In the end, an error was discovered in the calibration of the airgap sensor and the airgap was measured directly with calipers. A nominal airgap reading of 15/16 inch was obtained which represented the airgap at the center of the rail as measured in the region of the test fixtures. Further discussion of measurement techniques is given in Section 4 of the report.

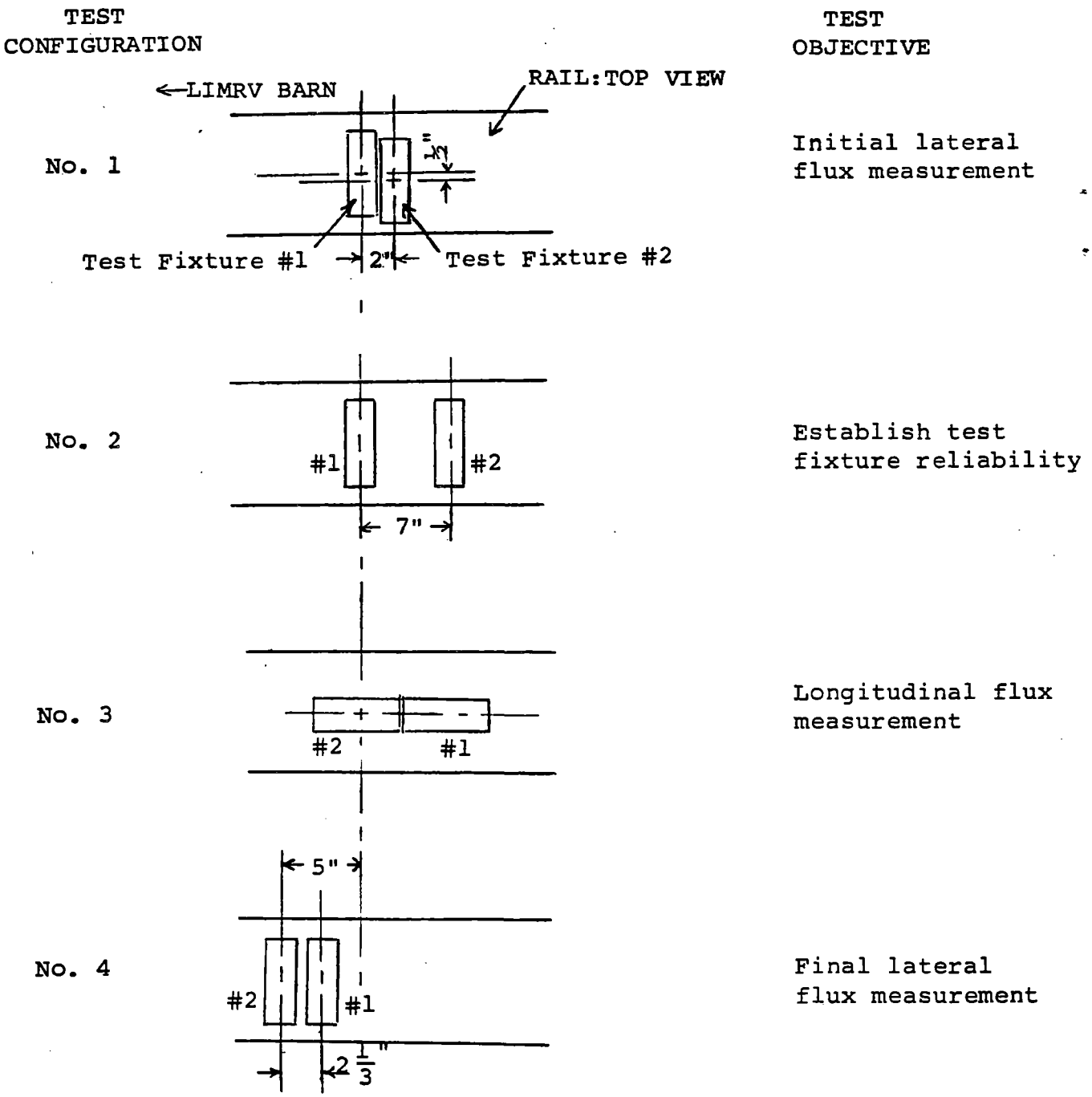

Figure 1 Sketch Showing Four Test Configurations Used in LIMRV Flux Measurements

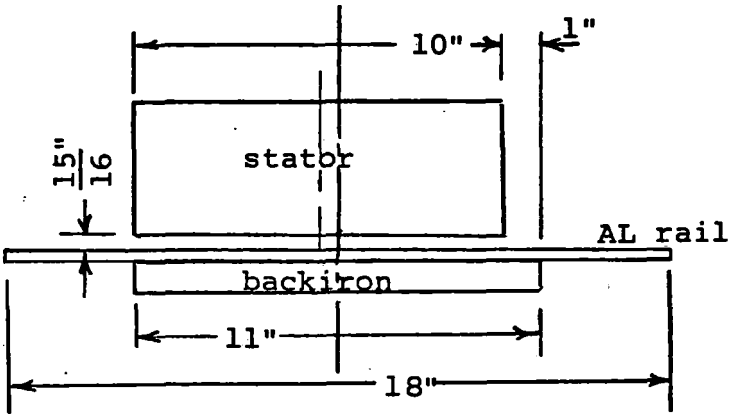

Figure 2. Sketch Showing LIM Crossectional View

3. THEORETICAL CONSIDERATIONS

Two factors contribute to the static flux distribution measured during these tests. These are the nature of the MMF excitation as determined by the stator winding distribution and the effect of the finite LIM width (transverse edge-effect) on the airgap flux. The latter factor is described theoretically by the Bolton treatment of transverse edge-effect[2] within certain limitations which are defined later. The longitudinal end-effect associated with the finite length of the LIM is negligible under the static test conditions and is therefore omitted in the analysis.

3.1 Primary Current Excitation

The primary current excitation, J_1, can be expressed in terms of a Fourier series of time, space harmonics according to,[3]

$$J_{1z} = \sum_{\nu} J_\nu e^{j(\omega t - \nu\pi x/\tau_p)} \qquad (1)$$

where J_ν is the magnitude of the νth harmonic current given by,

$$J_\nu = \frac{2\, N\, I_1 \sqrt{2}\, q\, m\, {}^{\nu}k_w}{\tau_p} \qquad (2)$$

N = turns per coil

I_1 = stator phase current, rms

q = slots per phase belt

τ_p = pole pitch

m = number of phases

${}^{\nu}k_w$ = winding factor

The winding factor for the ν th harmonic is given by,[3]

$$k_{w\nu} = \frac{\sin\frac{\nu\pi}{2m}}{q\sin\frac{\nu\pi}{2mq}} \sin\frac{\nu\pi}{2}\left(1 - \frac{\epsilon}{mq}\right) \qquad (3)$$

ϵ = number of half-filled slots at each end of LIM.

Table 2 gives the magnitudes of the winding factor for the first five non-zero harmonic amplitudes. A glance at the table shows that the harmonics beyond the 7th can be neglected with little error. In this case, Eq'n 1 can be rewritten as,

$$J_1 = \left(J^{(1)} e^{-jkx} + J^{(-5)} e^{+j5kx} + J^{(7)} e^{-j7kx}\right) e^{j\omega t} \qquad (4)$$

or,

$$J_1 = \left(J^{(1)} + J^{(-5)} e^{+j6kx} + J^{(7)} e^{-j6kx}\right) e^{j(\omega t - kx)} \qquad (5)$$

TABLE 2

WINDING FACTOR

ν	$k_{w\nu}$
1	.8285
-5	-.1732
7	.1249
-11	-.0316
13	.0295

Fig. 3 shows a plot of the primary current amplitude given by the term in brackets in Eq'n 5 . A stator phase current of 1000 A. is assumed. The presence of phase belt harmonics having periodicity of one-third pole pitch is clearly evident.

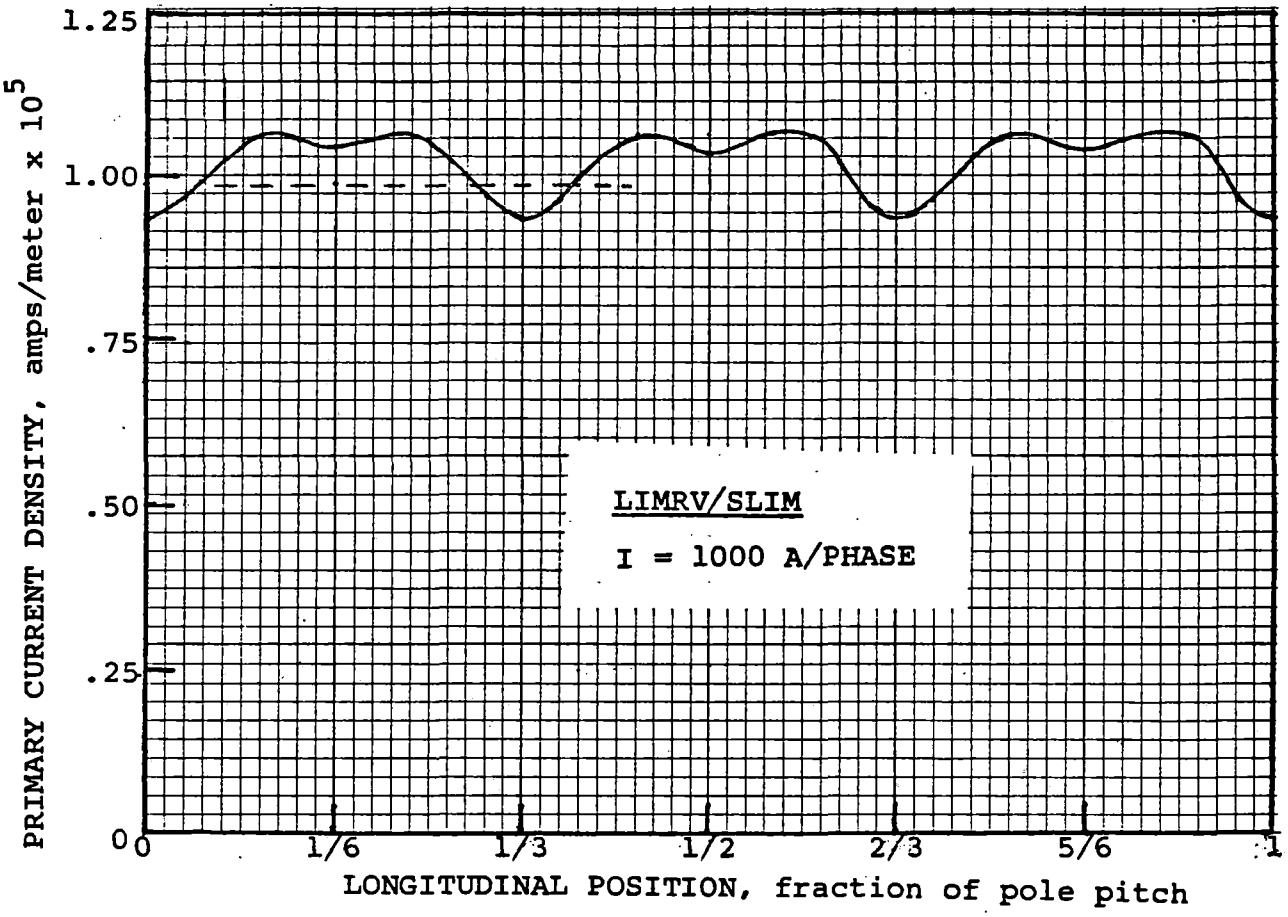

Figure 3 LIMRV Primary Current Density Amplitude

3.2 Transverse Edge-Effect

The Bolton theory of transverse edge-effect shows that the airgap flux for a LIM with a symmetrically positioned secondary is given by,

$$B(x,y) = (B_o + B_1 \cosh \alpha y)\ e^{j(\omega t - kx)} \tag{6}$$

where the amplitudes of the excitation and edge-effect waves are given respectively by,

$$B_o = -\frac{j \mu_o \tau_p J^{(1)}}{g \pi (1 + jGs)} \tag{7}$$

$$B_1 = B_o\ jGs \cdot \frac{\cosh \alpha y / \cosh \alpha a}{1 + \sqrt{1+jGs}\ \tanh \alpha a\ \tanh kb} \tag{8}$$

where,

g = primary-primary distance

s = slip

G = Goodness Factor

J^1 = primary linear current density

b = secondary thickness

Eq'n 6 assumes a number of important conditions: (1) the secondary thickness is assumed small compared with the skin depth, (2) the distance between primary and secondary is assumed small compared with the pole pitch, (3) the field outside the active region of the LIM is zero, and (4) a double-sided LIM configuration is assumed. The skin depth at the test conditions (see Table 1) is 8.7 mm or only about twice the thickness of the secondary. The factor $\pi\,\delta/\tau_p$ which relates the primary,secondary airgap, δ, to pole pitch, τ_p, is 0.21 which results in some error in the approximation $\cosh \pi\,\delta/\tau_p = 1$ used in the Bolton analysis. The assumption of zero field outside the active region leads to a boundary condition which overestimates the field at the edges of the LIM. The assumption of a double-sided LIM(DLIM) configuration is equivalent to an infinite backiron in the secondary. In spite of these important limitations in the application of the Bolton theory, the theory does describe the basic characteristics of the airgap flux distribution encountered in the LIMRV/SLIM flux measurements.

3.3 Transverse Edge-Effect with Phase Belt Harmonics

The inclusion of phase belt harmonics in the field description leads to the following equation for airgap flux density,

$$B(x,y) = (B_o^{(1)} + B_1^{(1)}\cosh \alpha y)\ e^{j(\omega t - kx)} + (B_o^{(-5)} + B_1^{(-5)}\cosh \alpha y)\ e^{j(\omega t + 5kx)} + (B_o^{(7)} + B_1^{(7)}\cosh \alpha y)\ e^{j(\omega t - 7kx)} \quad (9)$$

where B_o, B_1 are the driving (normal) and edge-effect flux density amplitudes respectively associated with the νth harmonic current excitation. This equation forms the basis for the analysis of the flux distribution data presented later in the report.

Table 3 gives the complex amplitudes of the flux density harmonics given by Eq'n 7,8 as a function of relative position y/a along the width of the LIM. The computed flux density at any position (x) along the length of the motor can be found by multiplying the complex amplitudes in Table 3 by their respective phase factors as defined by Eq'n 9 . Two important cases are considered, the first being the flux distribution along the longitudinal (center) axis of the LIM, and the second being the flux distribution along

TABLE 3

FLUX DENSITY HARMONIC AMPLITUDES

Relative Lateral Position y/a	$B^{(1)}$ tesla	$B^{(-5)}$ tesla	$B^{(7)}$ tesla
1.0	-.0415-j.0477	-.0048-j.0082	-.0052-j.0052
.9	-.0386-j.0143	-.0063-j.0057	-.0044-j.0042
.8	-.0273+j.0018	-.0065-j.0043	-.0040-j.0040
.7	-.0169+j.0067	-.0063-j.0036	-.0037-j.0039
.6	-.0102+j.0061	-.0061-j.0033	-.0036-j.0039
.5	-.0070+j.0039	-.0059-j.0032	-.0036-j.0039
.4	-.0060+j.0018	-.0058-j.0032	-.0036-j.0039
.3	-.0061+j.0004	-.0058-j.0032	-.0036-j.0040
.2	-.0065-j.0003	-.0058-j.0033	-.0036-j.0040
.1	-.0069-j.0006	-.0058-j.0033	-.0036-j.0040
.0	-.0071-j.0007	-.0058-j.0033	-.0036-j.0040

the lateral direction at two positions corresponding to maximum and minimum flux density positions along the length of the motor.

3.3.1 Longitudinal Flux Distribution

The longitudinal flux distribution, B(x,o), is found by substituting the values of the harmonic amplitudes given in Table 3 into Eq'n 9 and setting y equal to zero. Fig. 4 shows the longitudinal flux distribution computed for a LIM phase current of 1000 A. The large amplitude modulation predicted by the theory is the result of the constructive and destructive interference of the phase belt harmonics with the driving flux wave. A phasor description of the rotating field vectors is shown in Fig. 4 indicating the manner in which the phasors combine to produce peaks and valleys in the flux distribution. The positions of peak flux density are very closely given by x = 0, $\tau_p/3$, $2\tau_p/3$, etc.

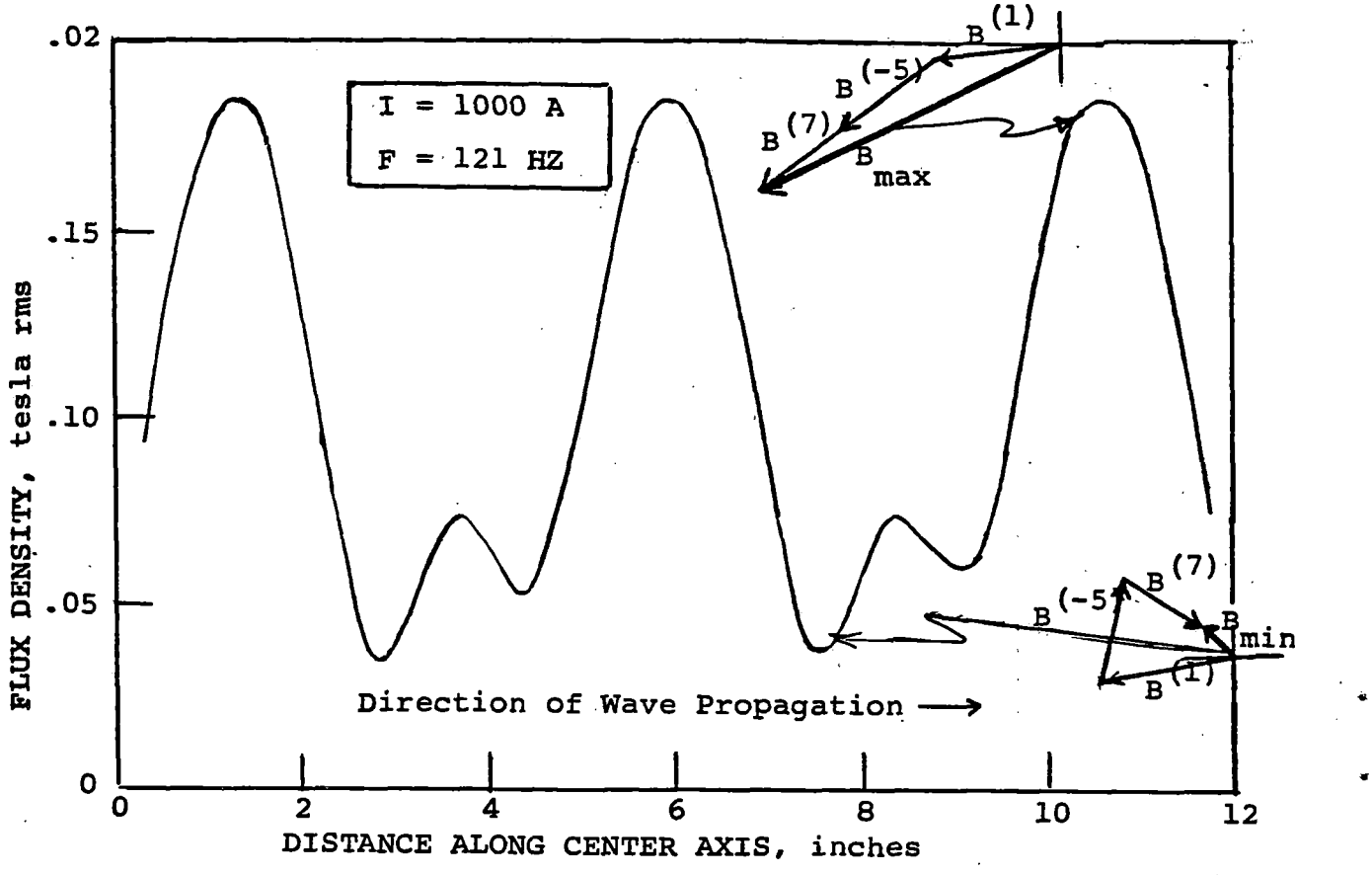

Figure 4. Computed Flux Density Along Center Axis of LIMRV

3.3.2 Lateral Flux Distribution

The lateral flux distribution at the positions of maximum and minimum field along the longitudinal direction is found by setting x = 0 and x = $\tau_p/6$ respectively into Eq'n 9 and computing $B(x_o,y)$ as a function of y. Note that the error introduced by assuming maximum flux density to occur at x = o is small. The predicted flux characteristics for the two positions along the LIM length are shown in Fig. 5. It is apparent from Eq'n 5 that the presence of the ν =-5, +7 harmonics of unequal amplitude

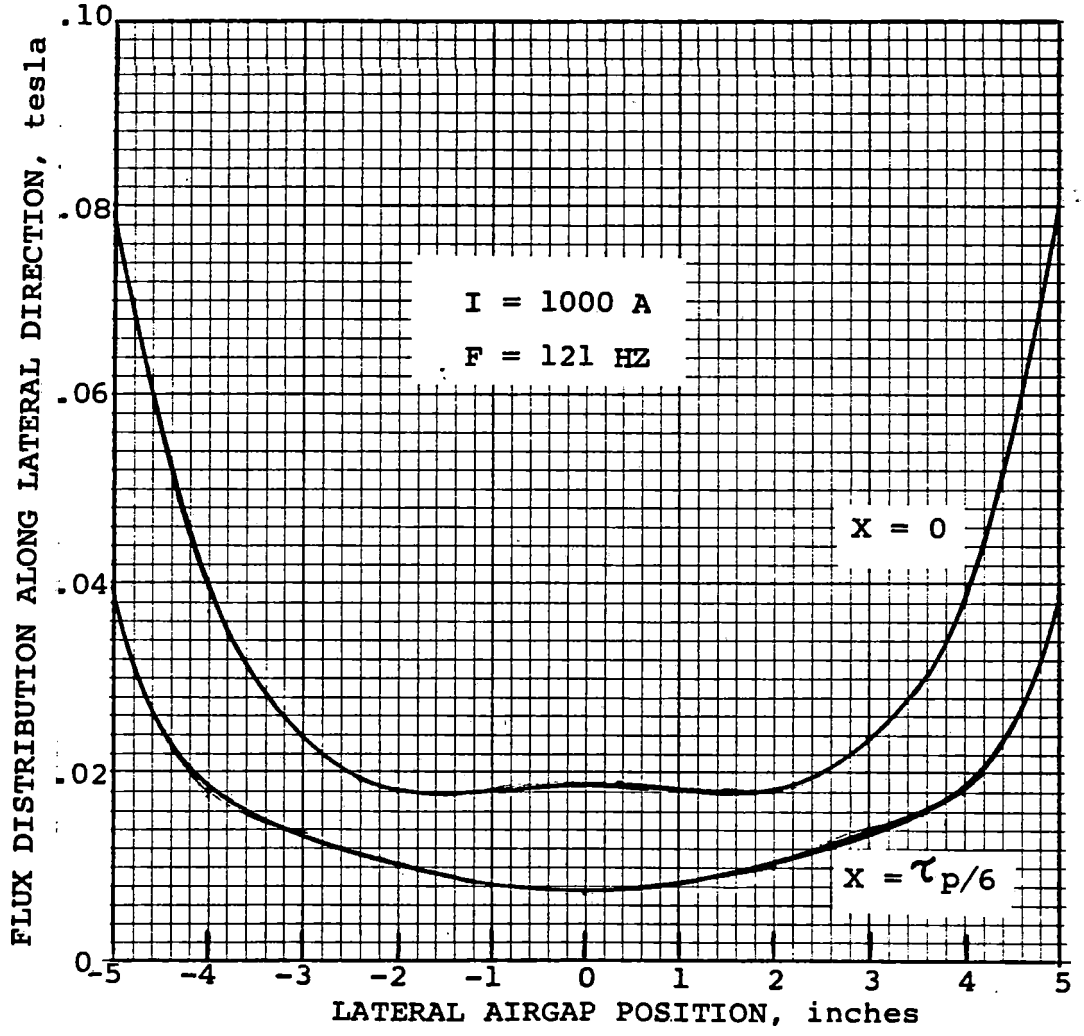

Figure 5. Computed Lateral Flux Distribution Including Phase Belt Harmonics

produces flux distributions which reflect the combined interactions of the fundamental plus phase belt harmonics. At no position along the LIM length can there be found a flux distribution which can be attributed to a pure normal wave. This leads to a problem in attempting to derive a value for the Goodness Factor based on the lateral distribution of the airgap flux, since the flux data reflects the Goodness Factors associated with the normal wave and phase belt harmonic waves. The results in Fig. 5 demonstrate the importance of including higher current harmonics in the LIM model and of treating edge-effects separately for all harmonics.

4. MEASUREMENT TECHNIQUE

The test fixtures (2) used in the flux studies consisted of a plexiglass support plate onto which 23 flux sensing coils were attached. Fig. 6 shows a sketch of the test fixture indicating the positions of the different coils. Each flux sensor was formed of eight turns of No. 30 copper wire having dimensions 3.7mm x 24.1mm. A single turn coil of dimensions 27.9cm x 24.1mm was used to measure the average flux density over an area spanned by one slot pitch. The coils were set into milled grooves 2.5mm deep and glued in place. Lead wires were twisted and inserted into shielded conductors to reduce pickup noise. A multi-contact switch was used to direct the coil pickup signals to a synchronous detector (Princeton Applied Research Lock-In Amplifier). Extraneous noise presented no problem in the measurements even at the small signal levels encountered in the tests.

The flux density (at the rail surface) was computed from the pickup coil voltage, V_c, according to,

$$B = \frac{V_c}{2 \pi f \, A_{coil} N_{coil}}$$

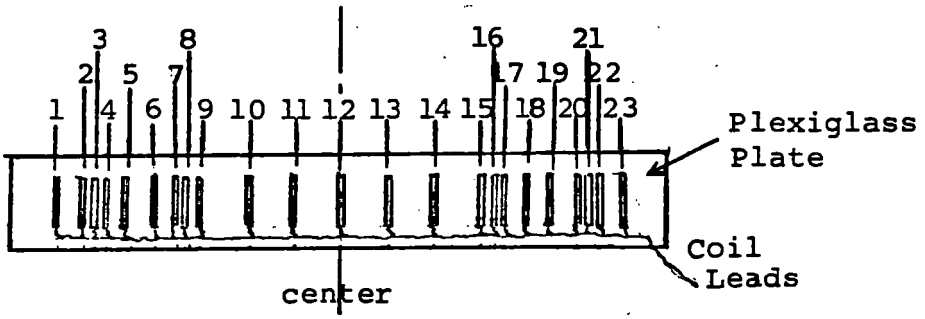

Coil No.	Position From Midpoint
1,23	6"
2,22	5½"
3,21	5¼"
4,20	5"
5,19	4½"
6,18	4"
7,17	3½"
8,16	3¼"
9,15	3
10,14	2
11,13	1
12	0

Figure 6. Sketch Showing Positions of Flux Sensors

4.1 Test Errors

The estimated errors in the measurement of the airgap flux density are given in Table 4.

TABLE 4

Measurement	Percent Error
Area of Flux Sensor (small coil)	5
Airgap Spacing	4
Frequency	.2
PAR Meter Reading	1

5. TEST RESULTS

Test data for the four flux measurements is given in Tables 5-8 showing the flux amplitude and phase for the different sensing coils. An additional column has been added giving the equivalent flux amplitude for a stator current of 1000A. All data presented in figures has been normalized to a stator current of 1000A.

5.1. Longitudinal Flux Distribution Data

Fig. 7 shows the measured flux density (normalized to 1000A) along the center longitudinal axis corresponding to Configuration No. 3 in Fig. 1. The data shows large modulation with periodicity one-third pole pitch which is associated with the phase belt harmonics as discussed in Section 3.3.1. The position of minimum flux density is not midway between the positions of maximum flux density but occurs closer to the one set of maximum flux densities. The direction of wave propagation as shown in the figure is from right-to-left, corresponding to the direction of thrust and decreasing phase of the propagating wave.

The computed longitudinal flux distribution is shown by the dashed curve redrawn from Fig. 4. The agreement in the magnitude of the flux density is good considering the approximations in the theory and possible errors in the measurements. The computed flux density shows a position of minimum field very close to that recorded in the measurements. The subsidiary peaks located between the main peaks in flux density would require better resolution in the field measurements to be detectable.

The asymmetrical character of the flux waveform (relative to the peak flux density position) presented problems in subsequent lateral flux studies and data interpretation. In the absence of more precise information on longitudinal flux distribution, it was

assumed that the minimum flux density positions were midway between the maximum flux density positions. The data presented in the next section giving the lateral flux distribution at two positions along the center axis illustrates this problem related to the error in locating the minimum flux density position.

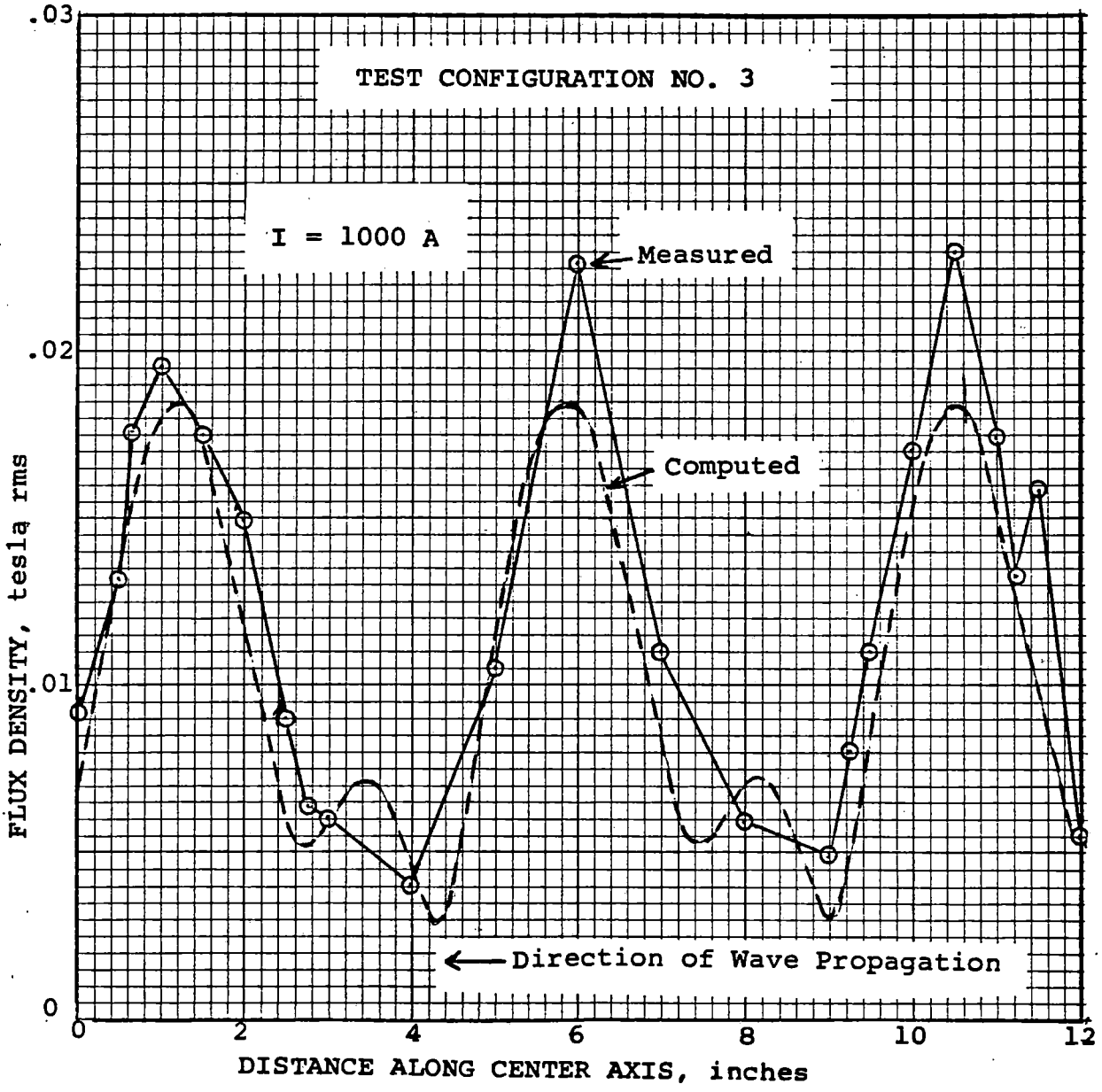

Figure 7. Comparison of Measured and Computed Airgap Flux Density Along Longitudinal LIM Axis

5.2 Transverse Flux Distribution Data

The measured flux distribution along the transverse axis of the LIM is shown in Fig. 8 for two positions along the length of the motor as indicated in Fig. 1, Configuration No. 4. The two positions corresponded to that of maximum flux density along the length of the LIM (upper curve) and a position midway between two positions of peak flux density (lower curve). The figure shows the large modulation of flux density along the length of the motor superimposed on the transverse edge-effect modulation. It is interesting to note the reduced edge-effect present in the upper flux density characteristic in the figure. This results from the fact that the flux density in the upper has a relatively large amount of phase belt harmonics present in it while the lower curve describes a flux distribution with a relatively small amount of phase belt harmonics present in it.

The computed transverse flux distribution based on the analysis given in Section 3.3.2 is shown in Fig. 8. Three computed flux characteristics are presented corresponding to different positions along the length of the LIM. These include positions for which the flux density is maximum and minimum along the center axis, and a position midway between adjacent maximum flux density peaks. A general correlation exists between the computed and measured flux characteristics both in terms of magnitude and shape of characteristics. The main difference lies in the magnitude of computed and measured flux density at the edges of the LIM, the computed flux density being roughly twice the measured flux density. The asymmetry in the test measurement (see Fig. 2) is noticeable in the flux distribution measured at the 'midway between B_{max} position' (lower curve). The large difference in the flux characteristics computed at a position

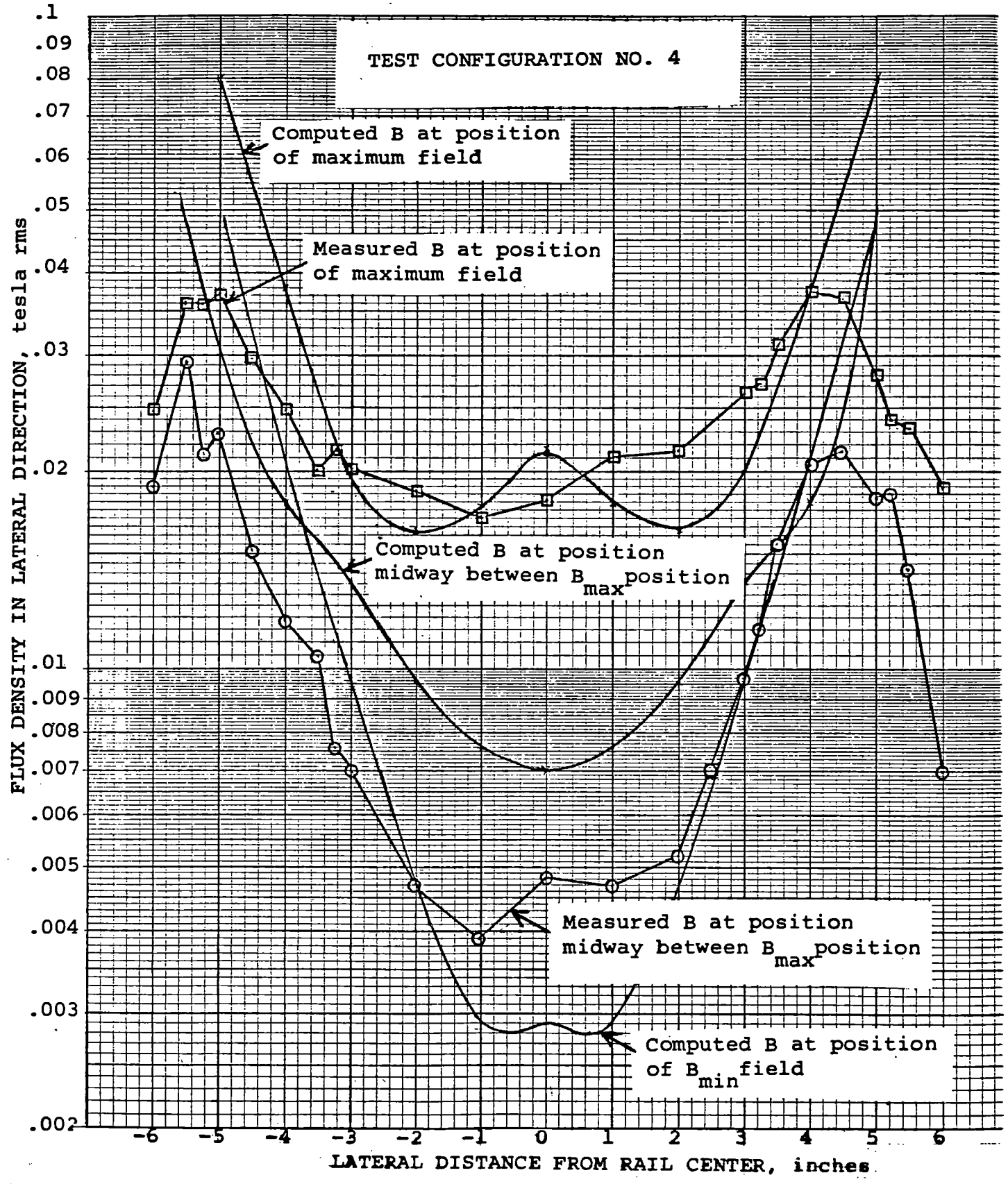

Figure 8. Comparison of Measured and Computed Lateral Flux Distribution

of B_{min} field and at a position between B_{max} peaks demonstrates the sensitivity of the data to the position along the LIM length at which the lateral flux is measured. It also suggests the difficulty which exists in attempting to use the lateral flux distribution data to derive values of Goodness Factor based on the slope of the lateral distribution characteristic.

5.3 Average Flux Density

The average flux density was measured using a search coil which spanned one tooth pitch over the lateral width of the rail backiron. Table 4 gives the measured and computed flux densities for two positions of the test fixture corresponding to maximum flux density and a position midway between the maximum flux density peaks. (See Fig. 1, Configuration 4.) The computed flux density includes the driving fundamental wave plus the ν =-5, +7 harmonics.

TABLE 4

AVERAGE FLUX DENSITY OVER LIM WIDTH

Test Fixture Position	B_{ave} Measured	B_{ave} Computed
B_{max} along long. LIM axis	.025 t.	.0262 t.
Midway between B_{max} positions	.013 t.	.0089 t.

A glance at Table 4 shows that the measured and computed flux densities are in good agreement for the maximum flux density configuration but deviate considerably in the case of the minimum flux density configuration. If one takes into account factors such as the neglect of leakage flux and the larger backiron width than stator stack width, the agreement in computed and measured flux densities is tolerably good.

5.4 Flux Density Phasor Description

The flux data along the longitudinal direction (Configuration No. 3, Fig. 1) was used to determine the phasor description of the spatial(airgap flux density)harmonic waves. Fig. 9a shows a plot of the locus of the magnetic field vector as determined from the flux coils at different positions along the center axis of the LIM. The locus describes an elliptical-like function, one end of which remains stationary while the other end shifts in angular position as shown in Fig. 9a. A vector from the point of origin to any point on the locus gives the amplitude and phase of the flux density wave. Note that the phase of the fundamental wave has been extracted from the locus plot so that the locus give the amplitude function given by the bracketted term in Eq'n 5.

Fig. 9b gives the phasor description based on the computed harmonic amplitudes given in Table 3 (y/a = 0). It is clear from Fig. 9b that the computed phasor locus gives rise to a phase modulation which is considerably larger than that observed as shown in Fig. 9a, even though the amplitude of the total phasor vector is comparable with the measured phasor amplitude. Fig. 9c shows the elliptical locus and phasor vectors for the case in which the finite airgap distance between stator and rail is taken into account. It is seen that while the net modulation of the phasor locus is comparable with the observed phase modulation in Fig. 9a, the amplitude of the phasor vector is smaller than observed. It must be concluded that the computed phasor harmonics, while describing the general character of the measured airgap flux density, do not yield the a complete description of airgap flux distribution. One factor which enters into the results is the fact that the flux sensing coils do not measure the flux at the exact surface of the secondary but measure it at a position approximately one and a half millimeters removed from the surface.

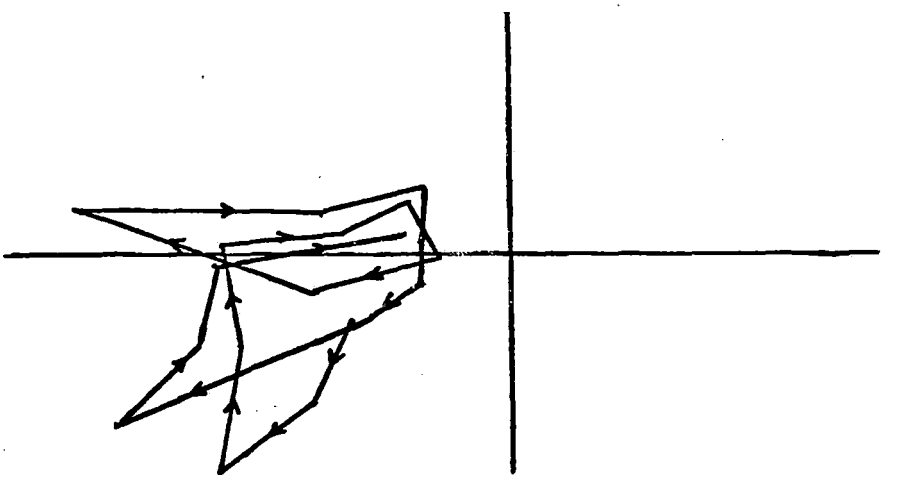

Figure 9a Measured Flux Density Phasor-Versus-Position Along Longitudinal Axis

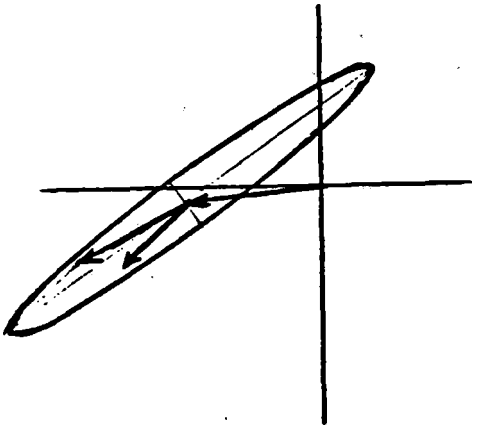

Figure 9b Computed Flux Density Phasor-Versus-Position Along LOngitudinal Axis, Neglecting Airgap Factor

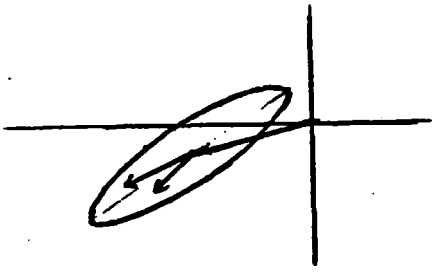

Figure 9c Computed Flux Density Phasor-Versus-Position Along Longitudinal Axis, Including Airgap Factor

6. ANALYSIS AND CONCLUSIONS

The data presented in this report demonstrates that the airgap flux density in the LIMRV under static conditions is strongly modulated in both the longitudinal and transverse directions. The modulation in the longitudinal direction is directly related to the higher harmonics present in current excitation. Superimposed on this modulation is the edge-effect which causes the flux density to peak at the edges of the LIM. The Bolton theory of transverse edge-effect combined with the superposition of primary excitation waves is able to describe the general character of the airgap flux. In addition, the average field computed using the Bolton theory is in reasonable agreement with test data.

The amplitude of the phase belt harmonic fields at the center axis position of the LIM is comparable with the amplitude of the main driving field. As a result, the constructive and destructive interference of these waves produces appreciable modulation of the airgap fields, in both amplitude and phase. While the computed amplitude variation along the longitudinal axis is in tolerable agreement with the test data, the computed phase modulation is much too large compared with the observed phase modulation. The results of the test data suggest that the phase belt harmonic (ν=-5,+7) fields are of smaller amplitude relative to the fundamental driving field than that computed from the analysis given in Section 3.3. However, if one takes into account the effect of the finite airgap on the effective field at the surface of the secondary (phase belt leakage) and recomputes the harmonic fields, one arrives at a new set of driving plus phase belt harmonic fields which yields the desired phase modulation characteristic. The peak amplitude of the flux density at the secondary is reduced due to the finite airgap and the flux density peak at the center axis is computed to be roughly sixty percent of the measured peak flux density.

This divergence between computed and measured flux density along the center (longitudinal) axis is in contrast with the good agreement in the computed and measured flux density averaged over the width of the LIM. (See Table 4)

It is apparent from the data analysis that many factors must be considered in the correlation of the test data with theory. In addition to the transverse edge-effect on the harmonic fields generated by the primary excitation, there exists the airgap factor which relates the net field at the secondary (surface) to the field at the primary (excitation) surface. The asymmetry of the LIM relative to the center axis of the rail causes asymmetry in the lateral flux distribution and leads to a longitudinal flux distribution which is 'distorted' from the distribution anticipated for a symmetrically positioned LIM.

The determination of the Goodness Factor associated with the driving excitation requires a careful analysis of the effect of harmonic fields on the flux distribution since, in effect, the higher harmonic fields must be 'removed' from the field description in order to study the fundamental driving field. Since the amplitudes of the $\nu = -5, +7$ harmonic fields are unequal, their vector sum in phasor representation describes an ellipse whose major and minor axes equal the sum and difference respectively of the harmonic amplitudes. At no point is there total cancellation of the harmonic fields leaving only the fundamental excitation. One cannot with certainty use the slope of the semilog plot of lateral flux distribution amplitude-versus-lateral position to determine the Goodness Factor.

REFERENCES

1. Laithwaite, E. R., Induction Machines for Special Purposes, Chemical Publishing Co., New York, N.Y. 1966

2. Bolton, H., "Transverse Edge Effect in Sheet-Rotor Induction Motors", Proc. IEE, Vol. 116, No. 5, May 1969, pp.725-731

3. Oberretl, K., "Three-Dimensional Analysis of the Linear Motor Taking into Account Edge Effect and the Distribution of the Winding", Archiv fuer Electrotechnik, Vol. 55, No. 4, 1973, pp. 181-190

TABLE 5

LIMRV LATERAL FLUX DATA: CONFIGURATION NO. 1

SENSOR NO. 1
I = 36 A
F = 120 HZ

Coil No.	Coil Sig. μv/10	B 1000A	B Phase
1	52.22	.0271	80.8
2	85.45	.0443	77.4
3	71.07	.0368	79.0
4	75.36	.0390	74.4
5	60.52	.0314	74.2
6	49.76	.0258	71.3
7	46.31	.0240	72.1
8	39.20	.0200	72.4
9	39.45	.0200	75.4
10	35.2	.0180	79.2
11	34.58	.0179	76.8
12	35.59	.0184	77.1
13	35.00	.0181	180± 76.0
14	35.47	.0184	76.0
15	48.00	.0249	77.5
16	52.79	.0274	80.0
17	61.42	.0318	77.3
18	71.96	.0373	84.5
19	65.74	.0341	91.4
20	46.07	.0240	67.4
21	42.77	.0220	61.2
22	33.94	.0176	57.9
23	14.64	.0076	51.6
24	468.	.0281	73.0

SENSOR NO. 2
I = 35 A
F = 120 HZ

Coil No.	Coil Sig. μv/10	B 1000A	B Phase
1	24.81	.0132	270± 8.5
2	30.91	.0165	13.0
3	37.04	.0197	20.0
4	43.87	.0233	0⁻
5	35.38	.0188	1.5
6	22.73	.0121	0± 83.5
7	13.43	.0072	66.8
8	15.00	.0080	62.7
9	11.85	.0063	57.8
10	8.65	.0046	52.5
11	5.28	.0028	49
12	8.1	.0043	59
13	12.00	.0064	0± 61.5
14	8.57	.0046	56.2
15	15.94	.0085	70.7
16	17.5	.0093	76.0
17	20.63	.0110	86.2
18	30.39	.0162	98.8
19	36.76	.0196	270± 17.7
20	39.71	.0212	17.0
21	36.00	.0192	13.0
22	34.62	.0184	17.0
23	25.00	.0133	0± 71.4
24	192.	.0119	84.7

TABLE 6

LIMRV LATERAL FLUX DATA: CONFIGURATION NO. 2

SENSOR NO. 1

I = 35 A
F = 122.1 HZ

Coil No.	Coil Sig. μv/10	B 1000A
1	45.80	.0227
2	78.75	.0390
3	68.24	.0338
4	76.56	.0379
5	64.92	.0322
6	54.23	.0268
7	49.26	.0244
8	42.00	.0208
9	41.28	.0204
10	37.00	.0183
11	35.57	.0176
12	36.60	.0181
13	35.80	.0177
14	35.47	.0176
15	46.00	.0228
16	50.76	.0251
17	58.68	.0291
18	70.10	.0347
19	71.28	.0353
20	56.54	.0280
21	52.13	.0258
22	40.95	.0208
23		
24	480.	.0266

SENSOR NO. 2

I = 34 A
F = 122.5 HZ

Coil No.	Coil Sig. μv/10	B 1000A	B Phase
1	28.36	.0152	90+ 49.0
2	41.82	.0224	50.7
3	39.35	.0211	49.0
4	36.32	.0195	49.5
5	26.89	.0144	47.5
6	18.18	.0097	42.6
7	10.37	.0056	33.2
8	12.80	.0069	31.4
9	10.93	.0059	28
10	8.17	.0044	26.6
11	5.28	.0028	26.4
12	7.80	.0042	31.0
13	12.40	.0066	33.0
14	9.39	.0050	31.0
15	19.27	.0103	42
16	19.70	.0106	43
17	25.83	.0138	44.4
18	26.96	.0144	54.7
19	39.70	.0213	64.0
20	34.80	.0186	52.7
21	32.00	.0171	43.3
22	30.29	.0162	48.5
23	18.02	.0097	28.2
24	138.	.0078	43.0

TABLE 7

LIMRV LATERAL FLUX DATA: CONFIGURATION NO. 3

SENSOR NO. 1
I = 35 A
F = 121.6 HZ

Coil No.	Coil Sig. μv/10	B 1000A	B Phase
1	18.82	.0099	270+ 41
2	31.45	.0165	42
3	24.24	.0127	42
4	32.57	.0171	47.5
5	41.50	.0218	62
6	32.28	.0170	52
7	23.06	.0121	41
8	16.05	.0084	35
9	6.14	.0032	41
10	6.88	.0036	0+ 57
11	17.32	.0091	65
12	37.70	.0198	88
13	21.18	.0111	84.5
14	8.00	.0042	0+ 41
15	12.90	.0115	270+ 98.3
16	8.24	.0043	67.5
17	17.45	.0092	0+ 11.
18	19.69	.0104	26
19	34.54	.0182	39
20	39.50	.0208	39
21	32.51	.0171	40
22	25.90	.0136	39
23	15.26	.0080	27
24	148.	.0090	85

SENSOR NO. 2
I = 35 A
F = 120.6 HZ

Coil No.	Coil Sig. μv/10	B 1000A	B Phase
1	17.50	.0093	90.+ 93.
2	24.82	.0132	180+ 26.5
3	33.33	.0176	29.5
4	36.98	.0196	36
5	33.02	.0175	39
6	28.18	.0149	25
7	16.94	.0090	7
8	12.20	.0064	90+ 84.5
9	11.30	.0060	81
10	7.5	.0040	180+ 38
11	19.81	.0105	75
12	42.00	.0227	88
13	20.80	.0110	180+ 60
14	11.22	.0059	48
15	9.33	.0049	270+ 28
16	15.19	.0081	35.5
17	20.83	.0110	42
18	32.35	.0171	44.5
19	43.63	.0230	48.3
20	32.84	.0174	48.5
21	25.00	.0132	46
22	29.81	.0158	41.5
23	10.42	.0065	29
24	145.	.0095	180+ 69

TABLE 8

LIMRV LATERAL FLUX DATA: CONFIGURATION NO. 4

SENSOR NO. 1

I = 35 A
F = 121.6 HZ

Coil No.	Coil Sig. μv/10	B 1000A	B Phase
1	36.95	.0194	0+ 45.
2	56.00	.0294	46
3	40.10	.0211	45
4	43.66	.0229	41
5	28.80	.0151	39
6	22.35	.0118	32
7	19.70	.0104	26
8	14.50	.0076	23.5
9	13.30	.0070	24
10	9.00	.0047	28
11	7.51	.0039	27.5
12	9.10	.0048	30.-
13	9.00	.0047	0+ 21
14	9.85	.0052	24
15	18.50	.0097	39
16	21.83	.0115	41.5
17	29.44	.0155	41.2
18	38.66	.0203	46
19	40.96	.0215	47.8
20	34.55	.0181	41.7
21	35.11	.0185	39.5
22	27.13	.0142	40
23	13.40	.0070	33
24	218	.0133	38.5

SENSOR NO. 2

I = 35 A
F = 122.1 HZ

Coil No.	Coil Sig. μv/10	B 1000A	B Phase
1	46.63	.0245	0+ 31-
2	68.18	.0359	33.5
3	67.59	.0355	34.5
4	70.75	.037	36
5	56.60	.0298	35.5
6	47.27	.0248	32
7	38.43	.0200	32
8	41.00	.0216	31.3
9	38.89	.0204	33
10	35.58	.0187	35.5
11	32.55	.0171	37.5
12	34.50	.0181	37.0
13	40.00	.0121	0+ 33.5
14	40.82	.0215	35
15	50.00	.0263	32
16	52.88	.0278	32.5
17	59.38	.0312	34
18	71.57	.0376	36.7
19	69.61	.0366	39
20	53.43	.0280	33.5
21	46.00	.0240	23
22	44.23	.0232	27
23	22.71	.0119	270+ 82
24	452	.0250	34.5

APPENDIX I

MODELING OF TRACK FLUX

ANALYSIS OF FLUX DIVISION FOR THE LAMINATED SECTION

The equivalent circuit in Figure I-1 shows the model used in this analysis. Symbols used in this section are defined as follows

R_g main airgap reluctance (includes contribution from top lamination eddy current loss)

R_t reluctance of top layer of backiron

R_{g1} reluctance of airgap between top and middle layers

R_{et} Reluctance due to middle lamination eddy current loss

R_m reluctance of middle layer of backiron

R_{g2} reluctance of airgap between middle and lower layers

R_{em} reluctance due to lower lamination eddy current loss

R_b reluctance of lower layers of backiron

B_s average magnetic flux density

B_o flux density at outermost edge

α depth of penetration = $\sqrt{\frac{2}{\mu w \gamma}}$

μ magnetic permeability assumed uniform and constant

ω frequency in radians per sec

γ electrical resistivity

b one-half the thickness of the infinitely large thin lamination

ℓ length of magnetic path

A cross-sectional area of magnetic circuit

τ_p pole pitch

ϕ flux

In Figure I-1 R_g represents the reluctance of the main airgap. R_t R_m, and R_b represent the effective reluctances of the backiron, (corrected for the skin effect of flux distribution), of the top, middle, and bottom layers, respectively. R_{g1} and R_{g2} represent the reluctances of the clearance gap between the top and middle, and between the middle and bottom layers. R_{et} represents the ampere-turns drop due to eddy current when the fluxes in the middle and bottom layers penetrate the top layer. R_{em} represents the ampere-turns drop when the bottom layer flux penetrates the middle layer.

The average magnetic flux density in a thin laimination is given by the formula*:

$$B_s = 2B_o \frac{\alpha}{b}\sqrt{\frac{\cosh\frac{2b}{\alpha} - \cos\frac{2b}{\alpha}}{\cosh\frac{2b}{\alpha} + \cos\frac{2b}{\alpha}}}$$

B_o = flux density at the outermost edge

= uniform flux density if there is no eddy current

The reluctance for dc flux or for ac flux in a magnetic circuit with no electric conductivity is given by

$$R = \frac{\ell}{\mu A}$$

The reluctance for ac flux in a magnetic circuit with finite values of μ and ν is:

$$R = \frac{\ell}{\mu A} \cdot \frac{b}{2\alpha}\sqrt{\frac{\cosh\frac{2b}{\alpha} + \cos\frac{2b}{\alpha}}{\cosh\frac{2b}{\alpha} - \cos\frac{2b}{\alpha}}}$$

assuming that μ and ν are constant and uniform throughout the magnetic circuit.

Assume that:

1. Airgap between layers is 0.254 mm (0.01 in.).

2. In calculating both the airgap reluctance and the equivalent reluctance for flux penetration, the areas are taken as 1/4 τp x width of the backiron.

3. The length of path for the flux in the top layer is assumed to be 3/8 τ_p; those for the middle and bottom layers are assumed to be 1/2 τ_p.

---

*Jiri Lammeraner and Milos Stafl, "Eddy Currents," English translation edited by G. A. Toombs, CRC Press, Cleveland, 1966.

For the solid backiron case, the equivalent circuit is:

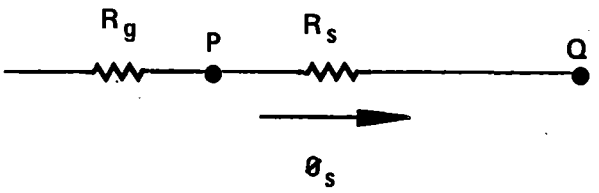

Using the same formula for ac reluctance to calculate R_s.

$$R_s = 9.03 \times 10^5 \text{ AT/Wb}$$

Assume the potential difference between P and Q is still 3800 AT for the laminated case.

$$\phi_s = 4.2 \text{ mWb (test value = 3.85 mWb)}$$

This simple model therefore provides a reasonable approximation.

Reasons for discrepancies include:

1. The magnetic permeance is not uniform in the backiron, nor is it constant with time (sinusoidal variation of flux density with time).

2. The length of path is difficult to determine.

3. Many of the equivalent reluctances are calculated on the basis of uniform flux distribution. This is not the case in the actual situation.

4. In this approach, the three layers are assumed to be isolated electrically.

5. The airgaps between layers are unknowns.

6. The values of μ for different layers and for the solid backiron are only estimated values.

AMPERE-TURNS DROP WHEN AN AC FLUX PENETRATES A CONDUCTING PLATE

When ac flux penetrates a conducting plate (Figure I-2), eddy currents are produced. Assuming that the impedance for the eddy current is purely resistive, there will be ampere-turns directly opposing the ampere-turns generating the flux. This ampere-turns drop can be represented by an equivalent reluctance.

Consider a rectangular plate of thickness δ, dimensions $2\ell_1 \times 2\ell_2$ and an electric resistivity ρ (see Figure I-3). Assuming:

1. The flux distribution is uniform and perpendicular to the surface of the plate with a frequency f Hz.

2. Induced current is rectangular, as shown in Figure I-3. Total flux is ϕ_T. The flux inside the dotted area is $\left(\frac{x}{\ell_1}\right)^2 \phi_T$.

The voltage induced in the strip ABCD with width dx is:

$$e = 4.44 \times 10^{-8} f \left(\frac{x}{\ell_1}\right)^2 \phi_T.$$

The strips between D and A or B and C have an elementary width of dx. The strips between A and B or C and D have an elementary width of $\frac{\ell_2}{\ell_1}$ dx.

The resistance of the four strips together is:

$$R = 2\rho \frac{2x}{\frac{\delta \ell_2 \, dx}{\ell_1}} + 2\rho \frac{2\ell_2}{2\ell_1} \times \frac{x}{\delta dx} = 4\rho \frac{x}{\delta dx} \left(\frac{\ell_1}{\ell_2} + \frac{\ell_2}{\ell_1}\right)$$

The elementary current in the slip will be:

$$di = \frac{e}{R} = \frac{4.44 f \phi_T \left(\frac{x}{\ell_1}\right)^2}{4\rho \frac{x}{\delta dx}\left(\frac{\ell_1}{\ell_2} + \frac{\ell_2}{\ell_1}\right)} = \frac{1.11 \, \delta f \, \phi_T \, x}{\rho \ell_1^2 \left(\frac{\ell_1}{\ell_2} + \frac{\ell_2}{\ell_1}\right)} dx$$

Since this elementary current opposes only part of the flux, its equivalent total opposing ampere-turn is:

$$dM = \left(\frac{x}{\ell_1}\right)^2 di = \frac{1.11 \, \delta f \, \phi_T \, x^3}{\rho \ell_1^4 \left(\frac{\ell_1}{\ell_2} + \frac{\ell_2}{\ell_1}\right)} dx$$

Integrate the above expression:

$$M = \int_{x=0}^{x=\ell_1} dM = \frac{1.11 \, \delta f \, \phi_T}{\rho \ell_1^4 \left(\frac{\ell_1}{\ell_2} + \frac{\ell_2}{\ell_1}\right)} \int_0^1 x^3 dx = \frac{0.278 \, \delta f \, \phi_T}{\rho \left(\frac{\ell_1}{\ell_2} + \frac{\ell_2}{\ell_1}\right)}$$

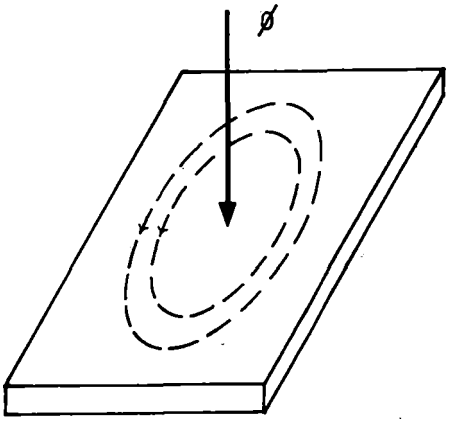

Figure I-2. Induced Eddy Currents in a Conducting Plate

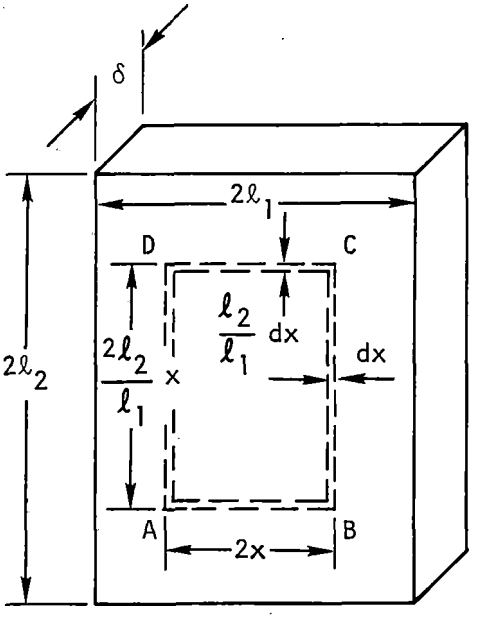

Figure I-3. Elementary Current Path in a Rectangular Plate

The equivalent reluctance to represent this ampere-turn drop is:

$$R_{eq} = \frac{M}{\phi_T} = \frac{0.278\ \delta f}{\rho\left(\frac{\ell_1}{\ell_2} + \frac{\ell_2}{\ell_1}\right)} \quad AT/Wb$$